Modelling of sound attenuation by periodic, rectangular structures

Thesis

Modelling of sound attenuation by periodic, rectangular structures

August 2019 (Revised April 2020) Thesis of,

Stephen Mellish

for the degree of Doctor of Philosophy.

The Open University, Milton Keynes, UK.

Certificate of Originality

I certify that I am responsible for the work submitted in this thesis, that the original work is my own except as stated in acknowledgements, in text or in references and that neither the thesis nor the original work contained therein has been submitted to this or any other institution for a degree.

Signed _____ (Steve Mellish)

on the _____ day of the month of _____ in the year _____

SUPERVISORS

Dr. Shahram Taherzadeh, Senior Lecturer.

Prof. Keith Attenborough. Research Professor.

Both of the Acoustics Research Group, Department of Engineering and Innovation,

The Open University, Milton Keynes, United Kingdom.

ABSTRACT

The problem of noise reduction in outdoor environments is the subject of significant research effort because of the wide reaching impact it has on the population, especially those in urban areas. From existing outdoor and laboratory data it has already been established that periodic structures embedded into the ground may be tuned to significantly reduce transported noise at nuisance frequencies. Such structures possessing rectangular section are of particular interest due to the relative ease with which they can be implemented. While significant data is available, it has traditionally been a time consuming task to model and simulate such structures due to the need to apply complex numerical methods to do so. Finding simplified modelling methods is the aim of this research.

Modelling of these structures will be considered in detail, culminating in the presentation of a novel analytic model with application in practical acoustic engineering and environmental planning. Existing general methods are explored before moving on to consider simpler techniques which may be employed by applying the simplifying assumption that all cavities within the periodic structure are rectangular in nature. By considering the structure as an effective impedance a novel analytic model is presented to conclude the thesis.

ACKNOWLEDGEMENTS

My sincere appreciation goes to both of my supervisors Shahram and Keith, who have guided me on the journey from fundamentally clueless but enthusiastic to a reasonable approximation of an Acoustic Physicist. It has truly been a pleasure and I look forward to continuing our work together and many more hours of enjoying ourselves chewing the acoustic cud.

I must thank Alec Goodyear for watching over proceedings as third party monitor and Anton Krynkin of Sheffield University for freely handing us his impressive 3d BEM software.

Many measurements made by Imran Bashir for his thesis were used in this study, so thanks to him for good quality data and for saving us having to do them!

Finally, I would like to thank my wife Marie, for her unconditional love and support as well as for her practical help in generating many of the diagrams and for collating the final thesis. Also for force feeding me when the sugar levels crashed.

Table of Contents

List of Figures

List of Tables

LIST OF SYMBOLS

The following is a list of specific symbols and their definition utilised throughout this thesis and are presented in the approximate order in which they appear for ease of reference. All SI units are assumed unless otherwise stated.

CHAPTERS 1 to 3

L_T	Source tube length
Δx_{SR}	Source to receiver straight line distance
A_V	Amplifier gain
z_S	Source height above top surface
z_R	Receiver height above top surface
$SIGLEN$	Array length of measurement sample block
F_{c0}	Speed of propagation factor
c_0	Speed of sound in ideal air
t_{START}, t_{STOP}	Sampling period start and stop times
n_p	Number of pulses per signal burst
f_S	Sampling frequency
W_{START}, W_{END}	Beginning and end sample index of sample data window
EA	Excess-Attenuation

CHAPTER 4

R	Bounded region of space
ϕ	The field variable (pressure, velocity etc.)
k	propagation constant
$s(R)$	Field equation for region R
c	Arbitrary speed of sound
$G(R_j, R_k)$	General solution to field equation in region R
C	Bounding contour of R
L_P, L_C, L_S	Plane, Cylindrical and Spherical reflection coefficient
f_C	Field function on curve C
$\mathbf{n}$	Contour or Surface normal unit vector
$\mathbf{F}$	General Vector function
B	Inner boundary within C
R_1	Inner region bounded by B
ρ_0	Standard density of air
A	Bounding surface of enclosed area
Ω	Porosity

CHAPTER 5

d	Spacing between grating features
a	Width of aperture of rectangular cavity
h	Depth of cavity
O	Origin
n	Cavity mode or index thereof
m	Free-space mode or index thereof
v	Acoustic particle velocity
v_x, v_y, v_z	Component velocity in x, y and z
$v_i, v_r, \hat{v}_m$	Particle velocity of incident, reflected and mode-m waves
p	Acoustic pressure (general)
p_i, p_r, p_m	Incident, reflected and m-modal pressure
p_{sct}, p_{tot}	Scattered and total pressure
t	Time
f	Temporal frequency
ω	Angular frequency
Z_S	Surface Impedance
$\mathbf{x}, \mathbf{y}, \mathbf{z}$	Unit vectors in axes x, y and the z-direction
e_n	Characteristic function of mode n
$\hat{e}_m$	Characteristic function of mode m
^	Indicates modal quantity relaing to free-space as opposed to grating region
k_{xn}, k_{yn}, k_{zn}	Propagation constant of cavity mode n in x, y and z
$\hat{k}_{xm}, \hat{k}_{ym}, \hat{k}_{zm}$	Propagation constant of free-space mode m in x, y and z
Z_n	Impedance for mode n
$\hat{Z}_m$	Impedance for mode m
Z_C	Characteristic impedance of free-space

CHAPTER 6

Ψ	Arbitrary wave function
α_m, β_m	Propagation constant in x and z for mode m
$\hat{V}_i, \hat{V}_r$ *or* $\hat{V}^i, \hat{V}^r$	Complex velocity amplitude for incident and reflected wave
$V_n, \hat{V}_m$	Complex velocity modal amplitude for mode n and m
$\hat{I}_i, \hat{I}_r$	Complex pressure amplitude for incident and reflected wave
$I_n, \hat{I}_m$	Complex pressure modal amplitude for mode n and m
$\delta_x, \delta_y, \delta_z$	Infinitesimally small increment in x, y or z
M	Truncation of m-modes
N	Truncation of n-modes
R_{inc}	Direct distance between source and receiver
R_A	Direct distance from source to point of specular reflection
R_B	Direct distance from point of specular reflection to receiver
R_{ref}	Total reflected ray path length
x_S	The horizontal position of the source
x_R	The horizontal position of the receiver
$O = O(0,0,0)$	Coordinate system origin
$S = S(x_S, y_S, z_S)$	Location of source
$R = R(x_R, y_R, z_R)$	Location of receiver
$G = G(x_G, y_G, 0)$	Centre point of grating structure
$G_1 = G_1(x_{G1}, y_{G1}, 0)$	Starting point of grating
$G_2 = G_2(x_{G2}, y_{G2}, 0)$	End point corner of grating
ΔG	Horizontal extent of finite grating

CHAPTER 6 Continued

Δ_{SR}	Horizontal distance from source to receiver
Δ_{S}	Horizontal distance from origin to source
Δ_{R}	Horizontal distance from origin to receiver
Δ_{Gx}, Δ_{Gy}	Linear size of grating in x and y
θ	Angle of incidence (AOI)
θ_{mx}	Propagation angle of mode m projected in x
θ_{my}	Propagation angle of mode m projected in y
$\theta_1 = (\theta_{1x}, \theta_{1y})$	Angle from start of grating (in x or y) to receiver
$\theta_2 = (\theta_{2x}, \theta_{2y})$	Angle from end of grating (in x or y) to receiver
$\Delta_{D1} = (\Delta_{D1x}, \Delta_{D1y})$	Horizontal distance from start of grating (in x or y) to receiver
$\Delta_{D2} = (\Delta_{D2x}, \Delta_{D2y})$	Horizontal distance from end of grating (in x or y) to receiver
φ	Azimuthal angle
Z_{eff}	Arbitrary effective impedance, usually of a surface
Z_{SP}	Impedance given by Slit-Pore model
Γ_P, Γ_S	Planar and Spherical reflection coefficients
f_{LS}	Frequency at and above which scattering occurs
$f_{EA\min}$	Frequency of the first EA minimum
$\lambda_{EA\min}$	Wavelength of the first EA minimum

CHAPTER 7

d_x, d_y	Pitch of lattice in x and y directions
a_x, a_y	Aperture width of lattice cavities in x and y
φ	Azimuthal angle
α_x, α_y	Horizontal progapation constant in x and y directions
n_x, n_y	Cavity mode or index thereof in x and y
m_x, m_y	Free-space mode index thereof in x and y

CHAPTER 8

Z_{Seff}	Effective surface impedance prediction of Simplified Causal model
Z_{Heff}	Effective surface impedance prediction of Heuristic model
Z_{effs}	Effective surface impedance of Heuristic model with slit-pore zeroth term
C_n	Amplitude weighting function for mode n
p_n	Complex pressure for modal component n
v_n	Complex particle velocity for modal component n
$f_{\max}$	Upper usable frequency limit of simplified model
h^H	Hurd corrected groove or cavity depth
W_n	Weighting function for modal component n
Λ_n	Wavelength adjustment factor for mode n

Note that sub or superscripts may be combined where appropriate, for instance v_{xi} will refer specifically to the x-axis component of particle velocity for the incident wave.

CHAPTER 1 – Introduction

1.1 The Problem

The relentless expansion of modern society has widely accepted consequences for the environment we occupy. Noise pollution is one such side effect and whilst it poses no physical or environmental danger, evidence does indicate adverse health effects [32]. It is a worsening problem as our population and its density increase, particularly in cities. With modern vehicles having quiet power-trains but wide tyres and heavy construction, the majority of such noise has its origin in the contact between the tyres and the road which tends to be focused within the approximate range of 900-2000 Hz.

We may consider that the noise we perceive from a road some distance away is the combination of sound which has reached our ears via two distinct paths. A component of the noise will reach us directly and another will do so after reflection from the ground in between. The difference in path-length between the direct and reflected components will cause a relative phase difference and hence a periodic cycle of constructive and destructive interference phenomena throughout the frequency spectrum. The magnitude of the reflected component will depend upon the relative impedance of the ground surface which if manipulated, would affect the location of constructive and destructive interference events across the frequency band. Engineering the effective ground impedance thus allows destructive interference minima to be located at frequencies most effective at minimising the level of perceived road noise to the listener. One method of achieving this is through periodic ground surface structures which manipulate the reflection characteristics. The analysis of such structures consisting of rectangular grooves or pores is to be the subject of this research.

There exists significant knowledge and research into grooved or latticed passive structures for noise reduction but conventional approaches for predicting their performance rely upon computationally intensive methods such as Boundary-Element-Methods (BEM) or Finite-Element-Analysis (FEA) whose complexity precludes their routine use in urban planning and infrastructure design. This research proposes to investigate modelling such structures with the aim of yielding a practical model that may be routinely used by engineers and planners to design-in and simulate these rectangular periodic structures.

1.2 Context

A gap in existing knowledge and capability has been identified which this research has been designed to address. That of having a simple acoustic model for predicting the response of periodic rectangular passive ground structures. Such structures are known to have scattering properties and so existing impedance based acoustic models do not lend themselves to simple adaptation to this problem. Therefore we are currently restricted to modelling with complex and time consuming numerical methods.

1.3 Research Questions

Can the acoustic response of rectangular periodic ground surface structures be successfully modelled as an effective impedance or by a specific reflection coefficient expression?
Hence,
Can such a model be applied to everyday use by engineers for the design and modelling of noise attenuating structures in urban landscaping applications for propagation angles near grazing?

1.4 Application

It is hoped that the results of this project will aid the proliferation of passive noise reducing structures to benefit local amenities by providing engineers and planners with a simple model they can use to predict the performance of periodic structures and thus integrate them into the urban environment.

As a precursor the point-to-point acoustic model often used to represent environmental noise propagation is introduced in figure 1.1. In this instance it is applied to a road and settlement separated by a region of reasonably flat ground.

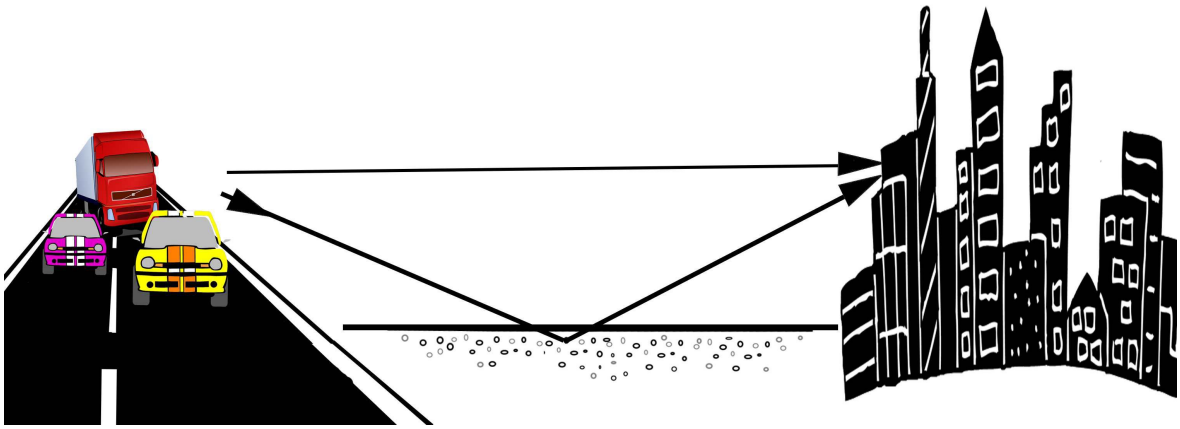

Figure 1.1 Noise from a nearby road when separated by flat ground.

The total sound at the settlement is the addition of the sound received directly from the road and a component which is reflected from the ground surface. The ground surface may then be modelled as a lumped effective impedance Z_{eff}, calculated from an appropriate model for the ground type, for instance grassland, forest or tarmac. By applying this to the appropriate reflection coefficient and including the ray path-length difference of the two components the total sound field at the receiving point is estimated. Generally the ground can be considered to be homogeneous, modelled by its bulk physical properties and so reflection will be specular as the feature sizes of the ground are small when compared with the incident wavelength. Attenuation phenomena throughout the frequency spectrum will be caused primarily by destructive interference between the direct and reflected components.

The rectangular periodic structures which are the subject of this research are intended to be built into the ground surface in the space between a road and inhabited area as per figure 1.2, in order to scatter some of the acoustic energy away from the settlement. Due to the structure being comprised of feature sizes comparable to the wavelength of the incident wave it cannot be considered to be a homogeneous surface and so will exhibit diffractive properties which may not be modelled by existing impedance models. This behaviour will be considered as the basis of our research.

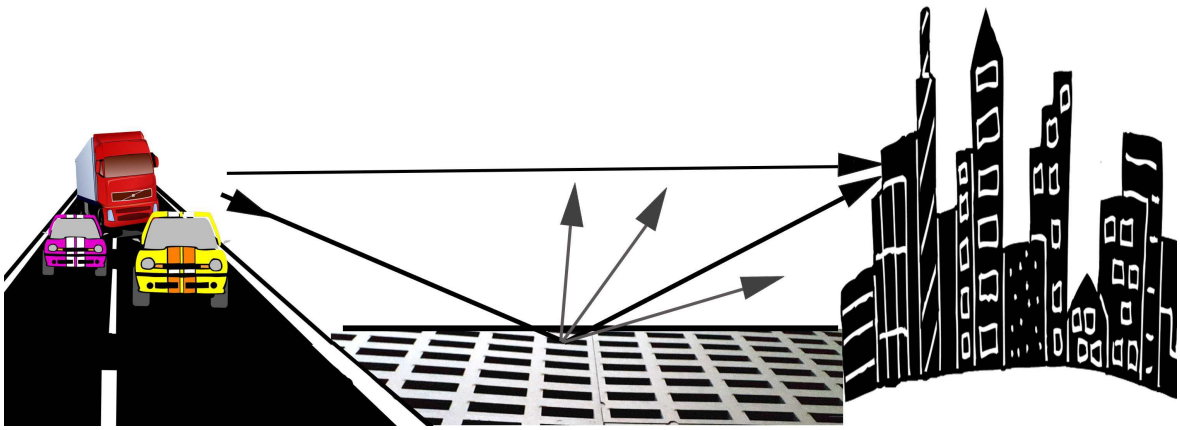

Figure 1.2 Noise reduced by the scattering effect of the latticed ground surface.

Practical tests on the noise reducing properties of rectangular pore lattice structures have been conducted by the Acoustics department at the Open University [33]. The following presents results from the limiting case of the lattice where the pore width in one dimension is infinite, which simplifies to a 2d structure consisting of equally spaced parallel walls and the full lattice, both constructed from house bricks. Figure 1.3 presents the sound level results for car drive-by tests with and without the 2d groove-grating structure in place. Here an insertion-loss of 2.7 dB is obtained from the grooved structure.

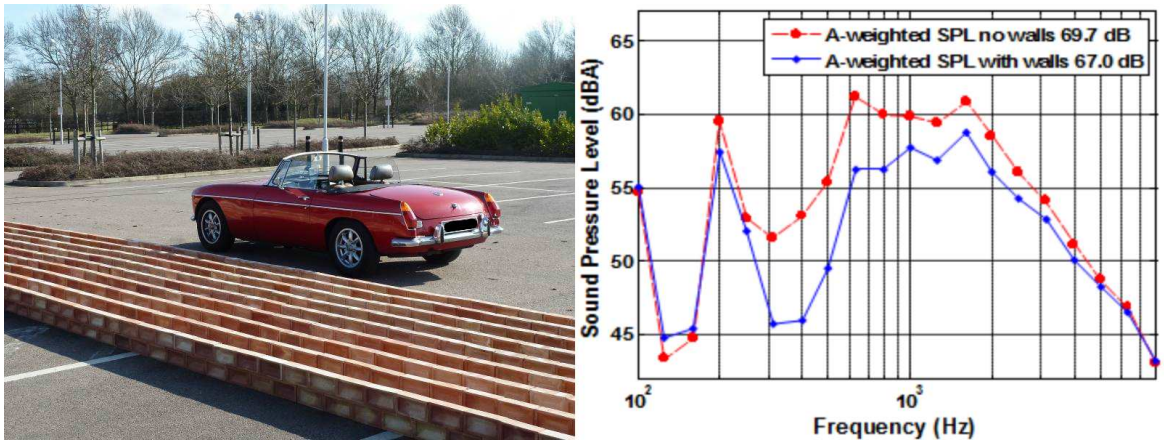

Figure 1.3 Test results from Parallel Walled groove-grating, 2.3 m wide and 0.2 m tall. (Photograph and data courtesy of The Open University, Acoustics Research Group)

Figure 1.4 shows the same results but for a full 3d lattice structure. An insertion loss of

2.6dB is obtained in this instance.

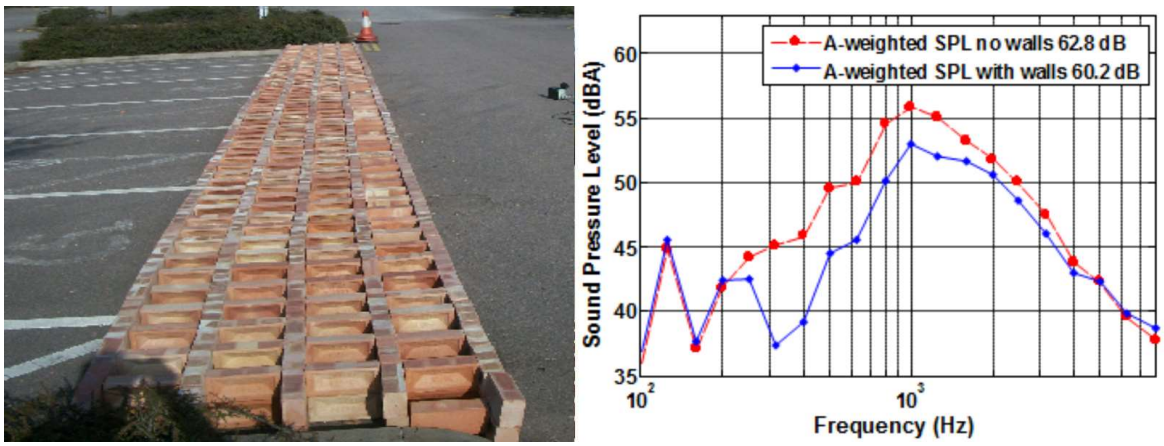

Figure 1.4 Test results from Lattice structure, 1.18 m wide and 0.2 m tall.
(Photograph and data courtesy of The Open University, Acoustics Research Group)

Although the results are similar in noise reduction magnitude the width of the lattice structure is much smaller than the grooved, indicating that the lattice may be more effective per unit surface area than the 2d grooved structure. This is potentially due in part to the lattice scattering more effectively over a greater range of horizontal source-receiver angles than the groove structure. The groove is likely to be most effective when the source-receiver ray path is perpendicular to the grooves with scattering performance falling off as this angle reduces due to the sound propagating along the grooves rather than over them. The 3d structure of the lattice will present a scattering periodic structure in both planes and so is expected to perform better over the range of source-receiver horizontal azimuthal angles.

1.5 Thesis organisation

The thesis is arranged in a progressive manner beginning with existing methods and knowledge and then building upon this throughout the thesis in a structured manner, introducing author contributions along the way.

A literature review begins the body of the thesis in chapter 2, which sets the scene and puts this work into context. An overview of key works relating to this thesis is presented along with historical time lines of broadly how the current state of the art has been reached. The

literature review focuses upon two branches of research, based upon understanding interactions with periodic surfaces from a wave mechanics point of view and from a Newtonian standpoint. Both branches of research have been progressing for over a century and this work seeks to utilise methods from both.

This work is largely theoretical in nature but even so it is necessary to test any theory against data and so reference is made throughout to measurements taken in the laboratory, which are compared, where practical, to theory. In chapter 3 the measurement process used for gathering data is explained with limitations or shortcomings being discussed. In some cases existing data was available and it was unnecessary to repeat the measurements, so for such cases the source of the data is stated. The measurement setup is presented and the exact methods of processing the data explained with the aid of diagrams and process flow-charts.

As well as measurements, the theories put forward in this work are also tested against other proven theoretical methods which in this case is predominantly the Boundary Element Method, or BEM for short. It is a complex numerical model based upon advanced mathematics which are briefly covered in chapter 4, but is a powerful tool in the analysis of acoustic fields because it is a comprehensive model which is not abstracted from the fundamental wave processes. Many forms of BEM exist but for our purposes the steady-state time-independent method is used to produce spatial field magnitudes for given geometries in the presence of a particular ground surface. Both 2d and 3d versions of BEM are discussed but due to computational limitations we are only able to call upon results from 2d simulations. The computing resources required to run 3d BEM simulations of sufficient resolution are enormous (at the time this thesis was authored) and the human resource required to understand and implement more advanced BEM methods to alleviate the resource limitations, prohibitive.

Chapter 5 offers a simple appraisal of how waves interact with a rectangular groove. It is a subject with widespread coverage in literature which delves into far greater detail than we shall do here. However the fundamentals are required to be fresh in the mind in order to be able to explore the wave field theories presented thereafter. The waveguide theory of wave propagation in a rectangular grooved will be discussed along with the notion of the resulting impedance relationships, formed periodically within the groove. The problem

will be considered in terms of wave mechanics in an ideal medium as opposed to fluid flow with thermo-viscous effects and their associated losses.

Progressing onto chapter 6 reveals the modal-model of plane-wave interaction with an infinite array of regularly spaced grooves of rectangular cross-section. This model was originally devised to tackle an equivalent problem in the electromagnetic domain for a 2-dimensional problem with invariance in one dimension. It was subsequently adapted for acoustics several decades later as the wave mechanics of the electromagnetic domain are similar to that of the inviscid acoustic field. Therefore the process of transferring the technique across to acoustics was more a stroke of excellent lateral thinking than it was of technical complexity. Work with the modal-model underpins this research and so a thorough treatment of the technique is made which includes its step-by-step derivation from first principles with a commentary as to the physical meaning of each element of the model. Up until now and to the author's knowledge, the modal-model has not been applied to the problem of point-to-point acoustic propagation, which we go on to achieve in this chapter. The method is to use the 2d modal-model to predict the effective impedance of a given rectangularly grooved ground surface under plane-wave excitation. The effective impedance is then applied to a ground plane above which lay a point source and receiver. Then utilising an appropriate reflection coefficient, the field at the receiver may be approximated for spherical or cylindrical wave excitation. The implementation of these methods is then thoroughly discussed, culminating in the presentation and analysis of extensive results. The method is compared to BEM, data and the most appropriate existing effective impedance model which is known as the slit-pore model. The method is found to be generally effective but with typical computation times far less than for BEM.

The modal-model is extended to 3 spatial dimensions in chapter 7. This does not significantly affect the complexity of the model but it does have a large impact upon the time it takes to solve. Adding the 3rd dimension does however allow the analysis of doubly-periodic ground structures so long as they are rectangular in section. Lattice like structures are explored in this chapter and compared with measurements made in the laboratory on an equivalent sample. Agreement with data is found to be questionable but in the absence of another method with which to compare the results it is difficult to narrow down the cause. More work would be required to refine the method for lattice like structures in 3d.

Returning once more to the case of 2d rectangular grooved gratings, learnings from the modal-model are applied in chapter 8 in order to construct simplified analytic models capable of predicting an effective impedance directly from the given geometry of the problem; a key research goal. Simplifying assumptions are applied to derive analytic approximations by decoupling the mutual half-space field dependencies within the modal-model which necessitate its numerical solution. Each groove is also considered in isolation and the wave motion therein considered as a superposition of discrete modes. The results are weighted series approximations to the effective impedance of the surface that are functions of the geometry of the problem alone and simple enough for practical everyday use by acoustic engineers. Turning full circle back to the literature review we were then able to link the two branches of study together in a small way by using Newtonian based models as a term in the resulting series approximations to provide an approximate impedance model based primarily in wave motion theory but with a thermo-viscous term deriving from Newtonian methods.

The diagram of figure 1.5 shows an overview of how the thesis flows and how each chapter interrelates. It has been organised in a progressive and logical manner in order that the reader will be gradually introduced to increasing complexity with the intention that the relevant concepts will fresh in the mind.

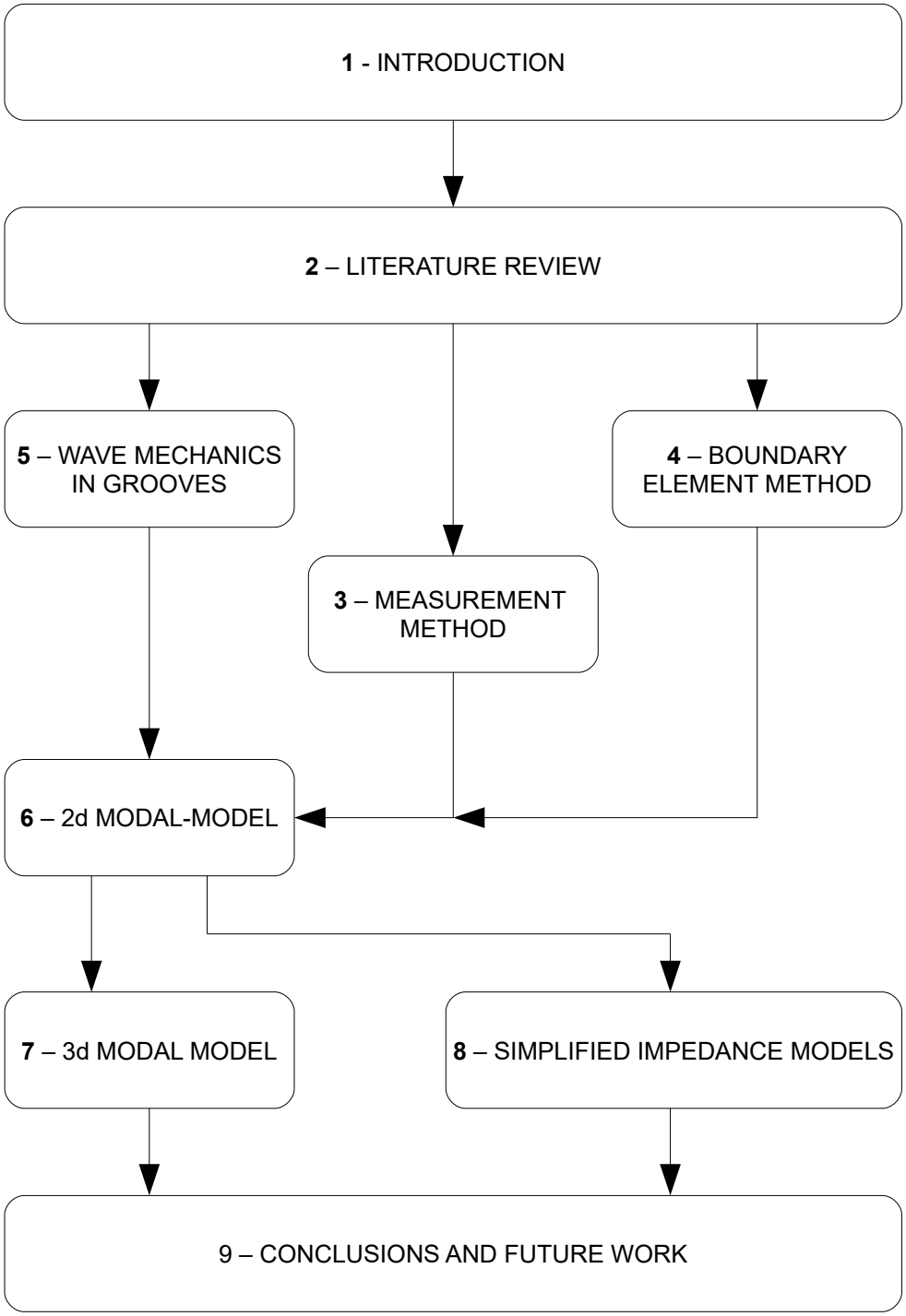

Figure 1.5 Thesis organisation

1.6 Claims of originality and author contributions

Much of the information presented within this thesis is either existing knowledge, novel work or a varying mixture of the two. It is therefore difficult and cumbersome for the reader to have continual commentary upon this during the body of the thesis and so a chapter-by-chapter summary of the origins of the work is given here.

Chapters 1 and 2 – These are simply introductory chapters and do not discuss technical detail.

Chapter 3 – Contains discussions of measurement technique, which contains widely known methods and practices for measurement. Measurements presented in this section were performed by the author. The sole original contribution from the author for this chapter was the laser cut lattice structure!

Chapter 4 – The author understands the complexities of BEM but the concepts are all existing knowledge. The 2d program used throughout this thesis was written in Fortran by Dr. Taherzadeh of The Open University. For the 3d BEM program however, the author significantly modified an existing 'C' program kindly supplied to us by Dr. Krynkin of Sheffield University to meet our needs. This necessitated a good understanding of the concepts and application of the BEM.

Chapter 5 – This chapter is all based upon existing knowledge and concepts but the author devised this chapter with little reference to literature, to best suit the theme of this work.

Chapter 6 – Fundamentally the core of the modal-model is existing knowledge but the author had to consolidate its derivation from two sparsely detailed technical papers [6,8]. To the best of our knowledge the methods of taking the results from the modal-model and applying to a point-to-point propagation model via an effective impedance are original. Another contribution is probing the limits of validity of representing the parallel groove or strip surface as that of a slit-pore model to a greater extent than hitherto and to explore the onset of scattering.

Chapter 7 - The extension of the modal-model to 3d was derived independently and in isolation by the author, later to discover that similar although not identical, work had already been published [39]. The methods to apply to point-to-point acoustic propagation are again, believed to be original.

Chapter 8 – The outcomes of this chapter are, to the best of the author's knowledge, original work.

CHAPTER 2 – Literature Review

The aim of this research is to formulate an effective impedance model for large feature groove or lattice structures in the ground plane. Thus far satisfactory impedance models for such surfaces where the feature size of the surface is comparable to the wavelength of the incident wave are not available to acousticians. Existing impedance models are primarily based around the assumption that the ground is homogeneous and so the ground can be considered as uniformly porous rather than discrete in its structure. This requires the notion that the constituent features of the ground, such as pores, air gaps etc., are small in comparison with the incident wavelength. An assumption which cannot be invoked in this research.

In acoustics the current state of the art in terms of modelling the effects of a ground plane structure upon the free-space sound field are divided into two distinct branches separated according to the geometries of the problem. Where the ground can be considered homogeneous, bulk properties are applied to the ground surface from which a single effective impedance can be calculated given the geometry of the problem. However when features of the ground structure become large enough in scale that the bulk property approximation is no longer valid, then the problem becomes one of scattering. Again, many models exist which can predict the sound field for this class of problem but as yet, to the authors knowledge, they do not satisfactorily account for scattering. Kelders, Allard & Lauriks [8] allude to an effective impedance but simplify so as to preclude scattering. The literature map following is a chronology of major contributions to theory relevant to this project with two distinct branches relating to the two main approaches. For scattering problems where the surface features are comparable to incident wavelength, wave or modal models have been used to tackle the problem. Whereas the problem has been approached in a Newtonian manner where the features are small and scattering does not occur, so the fluid may be considered within individual characteristic tubes or cavities in isolation and then lumped to form an effective impedance for the surface as a whole. Our research intends to bridge a gap between the two approaches by using wave theory to deduce a lumped effective impedance model for the rectangular periodic structures.

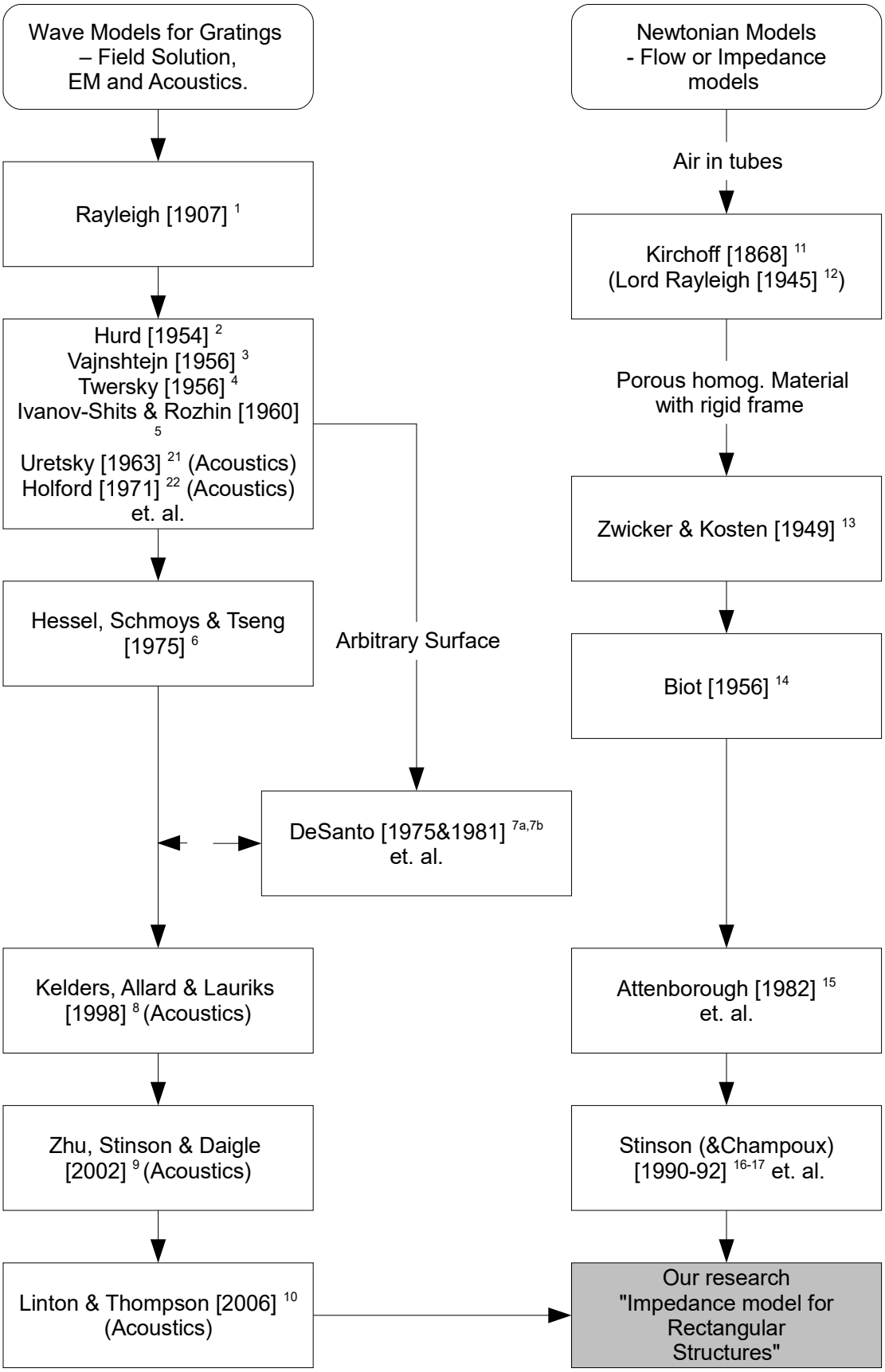

Figure 2.1 Literature map.

Consider each type of model in turn beginning with impedance models whose roots go back to the work of Kirchoff [11]. He solved the flow of air in tubes by solving the fundamental conservation equations. The solutions yielded positional solutions of the state quantities and also of flow velocity and pressure. This laid the foundations of being able to calculate the equivalent impedance of simple porous structures from rigorous application of Newtonian mechanics and Thermodynamic laws. Lord Rayleigh [12] built upon this work in his 1945 Theory of Sound. Although the Kirchoff theory was exact it is complicated and time consuming to solve and so Zwicker and Kosten [13] addressed this by deriving simplifications of the exact theory to yield approximations for complex density and complex compressibility. It then became simple to apply these approximations to yield an equivalent acoustic impedance within the given range of geometries where the Zwicker and Kosten [13] approximations held. Useful as this is it still was not capable alone of modelling many typical ground structures with a porous structure which comprise of cavities embedded is a solid structure. Biot [14] addresses this in his 1956 paper by incorporating the complex density and compressibility equations into a wider model assuming a porous ground to be a fluid-saturated porous structure within a solid rigid frame. Biot had proposed a prototype model which was to form the basis of the models used today for predicting the equivalent surface impedance of porous ground. Many academics then built upon this adding extra physical parameters such as Attenborough [28] et al. with their slit-pore model which accounted for tortuousity of the pores as well as flow-resistivity to improve correlation with experiments for specific groups of ground type, but the fundamentals of approximating the impedance with complex density and compressibility equations remains. In the early 1990's Stinson & Champoux [16-17] revisited the fundamental theories of Kirchoff and Zwicker and Kosten validating the approach and extending the analysis to pores of different shapes beyond just circular. The aforementioned models make the general assumption that incident acoustic waves have wavelengths much greater than the cross-sectional magnitude of the tubes or pores which reduces the problem to plane wave modes and precludes scattering. Reflection being only specular. The 2013 thesis of Bashir [31] offered a comprehensive appraisal of the state of the art of rough ground surface modelling, considering a vast array of different surfaces and the current techniques best suited to model them. Our research will be adding to this branch of impedance modelling by attempting to deduce an effective impedance model useful for grating type structures of magnitude beyond where the ground can be considered

homogeneous and the problem essentially becomes one of complex scattering as opposed to specular reflection from a bulk surface.

The related problem is the effect of periodic ground surfaces whose features are comparable in size to the wavelengths of the incident source. In such cases the ground cannot be considered as homogeneous. The problem becomes one of scattering as opposed to specular reflection from an impedance plane. The roots of this type of problem begin in earnest with Rayleigh in 1907 [1] with his theory of diffraction from a sinusoidal surface. He expanded the scattered field above and on the surface with a set of only up going and evanescent waves. Broadly, this assumption that the scattered field can be completely defined by an expansion containing only up going waves and without down going components is known as the 'Rayleigh Hypothesis'. Its range of validity and finer points remain a topic for discussion today and are out of the scope of this report but see [18-20] as further reading. However the work of Rayleigh remains a cornerstone of the subject.

Subsequent work on modelling perfectly reflecting diffraction gratings continued [2-5], with the majority of work applied to the electromagnetic domain or purely theoretical generic analysis. Subtly different approaches evolved but with a general theme of modelling the scattered field using modal expansions as Fourier series, Bloch-wave or associated expansions. Uretsky's paper of 1963 [21] is a definitive paper in the application of diffraction theories to the subject of Acoustics as is the contribution from Holford of Bell Labs in 1971 [22]. Uretsky used a Fourier expansion of the acoustic field and related the set of amplitudes to integrals over the surface. Waterman 1975 [23] also studied the acoustic application of diffraction gratings and used a Bloch-wave expansion to model the scattered field. DeSanto [7] produced a milestone work on the subject where he derived an exact solution to the problem, initially for a periodic sinusoidal surface and latterly to other forms, without invoking the Rayleigh hypothesis. Once again he used Bloch-wave expansions to model the scattered field but used Greens Theorem to express the line integral equations bounding one cell of the periodic surface. This work further confirmed the validity of the Rayleigh hypothesis within certain geometric bounds, which in essence states that the hypothesis is valid up to a critical slope of the surface. DeSanto did not specifically consider rectangular groove surfaces and it would be possible apply his method directly to such surfaces. However, useful assumptions can be introduced when limiting the surface to rectangular grooves in that waveguide theory can be applied to

model the wave behaviour inside the grooves which allows significant simplifications to expansion based diffraction models. This leads to the work of Hessel 1975 [6] who solved the problem of scattering of electromagnetic waves above a rectangular grooved surface using a modal approach. Worthy of note also is the work of Zhu, Stinson & Daigle 2002[9] whom considered a rectangular-groove structure by relating the scattered field to the tangent velocity across the groove walls. This approach is novel but has the limitation that the walls between grooves are assumed infinitely thin. This is not an assumption we can use for our research which has a practical application and structures with thin walls are not practical.

Hessel [6] considered the Bloch-wave modal expansion of a diffracted field from a rectangular groove grating in his work of 1975. Although his work was in the electromagnetic domain, it addressed every aspect required to apply the model to rectangular groove gratings in acoustics. Tolstoy [41] produced a comprehensive study comparing and contrasting the major works on the subject of scattering surfaces such as they were when he published in 1984. Of particular relevance to this research is his distinguishing between surface modes which are an artefact of an incident field and boundary or surface waves which may be sustained by a periodic surface alone in the absence of an incident field. Specific application of Hessel's model to acoustics was proposed by Kelders, Allard & Lauriks 1998 [8]. The Kelders, Allard & Lauriks work focused upon the study of surface waves and so expressing the free-space field was not specifically explored, although implicit in the model. Our work is concerned with the free-space field, so the model will be expanded to this end with the algorithms required to combine the modal components for given acoustic source-receiver geometries. These works are of particular relevance to our research because they consider a rectangular grooved surface. Therefore our research will be a direct continuation of Hessel and Kelders, Allard & Lauriks work on the subject. A unique aim will be to further the work to focus upon the free-space field and hence derive an effective ground surface impedance model. Allard, Kelders & Lauriks [39] expanded their work to consider surface waves above a doubly periodic grating (a latticed structure) but again did not consider the free space field specifically and limited the pores to square in section. Assuming invariance in one spatial dimension and consider rectangular grooves as opposed to doubly periodic lattices simplifies the problem considerably due to the fact that the modal expansions of the field can be considered as planar waves propagating in the plane of the problem and the

structure exhibits periodicity in just one-plane and invariance in another.

Boulanger et al. [34] investigated the effectiveness of the Boundary Element Method (BEM) and Twersky's [4] boss theory which assumes arrays of different shaped roughness elements, with measurements for periodic and randomly spaced scattering elements. Boulanger at.al. [35] went on in 2005 to build upon work of Linton & Martin [61] to study the problem of arrays of semi-cylindrical scattering elements laid upon a hard surface, using wave field theory to predict the scattered field from such a surface. Similarly in 2007 Linton et al. [10] continued with the problem of plane-wave excited arrays of cylindrical scattering elements upon a hard surface using a modal wave field approach in order to investigate modal resonances which lead to the Woods [60] anomaly and the exchange of energy between diffracted modes. A laboratory appraisal of rib-like structures, which are the limiting case of rectangular grooved gratings with infinitely thin side walls, was undertaken by Bougdah et al. [36] in 2006 and proposed that quarter-wave resonance within each cavity contribute to scattering phenomenon.

Worthy of particular mention due to their similarity with the concepts considered in this work are profiled diffusers. They are carefully designed structures consisting of arrays of rectangular grooves with varying depths, tuned in order to maximise their diffusive or absorptive properties. They were proposed by Schroeder [62] in the 1970’s and have found widespread use in concert halls to improve the acoustics. Following studies by Cox, Lam et al. [63-65] considered these structures in detail and present similar concepts to those in Chapter 5 such as considering the phase change impedance of grooves to express an effective impedance [64-65] and the assumptions behind their Fraunhofer model [63] bear close resemblance to the simplified causal model presented in Chapter 8.

Although this work does not seek to consider surface waves specifically, their influence cannot be ignored due to their significance when dealing with periodic surfaces which support them. The surface wave term is implicit in an effective impedance representation and so the spherical reflection coefficient of Chien and Sorokka [37] will be used extensively throughout this work and consideration will be made to the similar formulation of Thomasson [52] but where the surface wave component is expressed as a separate term. The work of Embleton [68] considers not only the phenomenon of surface waves but also that of modelling acoustic problems as a point source and receiver above a ground plane,

both of which he tackles in a highly practical manner. This model will be made use of extensively in this thesis due to its broad application to acoustics propagation problems.

In the interests of brevity, references in this study where the content is not specifically drawn upon represent a starting point for the 'state of the art' at the given time so the author infers reference to the papers cited therein.

CHAPTER 3 – Measurement method

The measurements referred to throughout this thesis were performed in the same manner and explained henceforth. Measurements were made in an anechoic chamber with a personal computer running a single MATLAB script as a host to generate the signal waveforms and to collect and post process the data via a National Instruments data acquisition module (DAQ) connected by USB. The sound source comprised of a Tannoy driver that is acoustically coupled to a 22 mm diameter copper tube with length L_T of 2.2 m and driven by the signal from the DAQ via an audio amplifier whose gain was set manually at the beginning of each session to ensure a good signal level without saturating the DAQ at any time. This approximates a point source and ensures that only the plane wave mode will be excited within the tube to improve the omni-directionality of the source. A short pulse is used to excite the sound source and the long length of tube ensures that the internal reflection caused by the open end does not interfere with the incident wave and can be removed from the measured results by simple time windowing of the measured data. The pulse must be of short enough duration and the tube length long enough relative to the separation distance of the source and receiver to ensure that the effects due to the layer under test have reached the receiver before the reflected pulse itself is re-emitted and re-received. Since any surface waves may travel significantly slower than their free-space counterparts, the tube should be longer than one may initially expect to allow for this. Distant stray reflections from inside the chamber itself or by the apparatus are also mitigated by time windowing the data. The receiver was a Brüel & Kjær 0.5” free field microphone cartridge type 4966 with a preamp type 2669 and connected to a Brüel & Kjær microphone power supply type 5935, which is battery powered to improve noise characteristic and reduce the risk of electrical ground loops. The analogue output from the preamplifier is sampled by the DAQ with the digitised data stream being acquired by the host computer via the USB link for post processing. A block diagram of the hardware set-up used to make the measurements is given in figure 3.1.

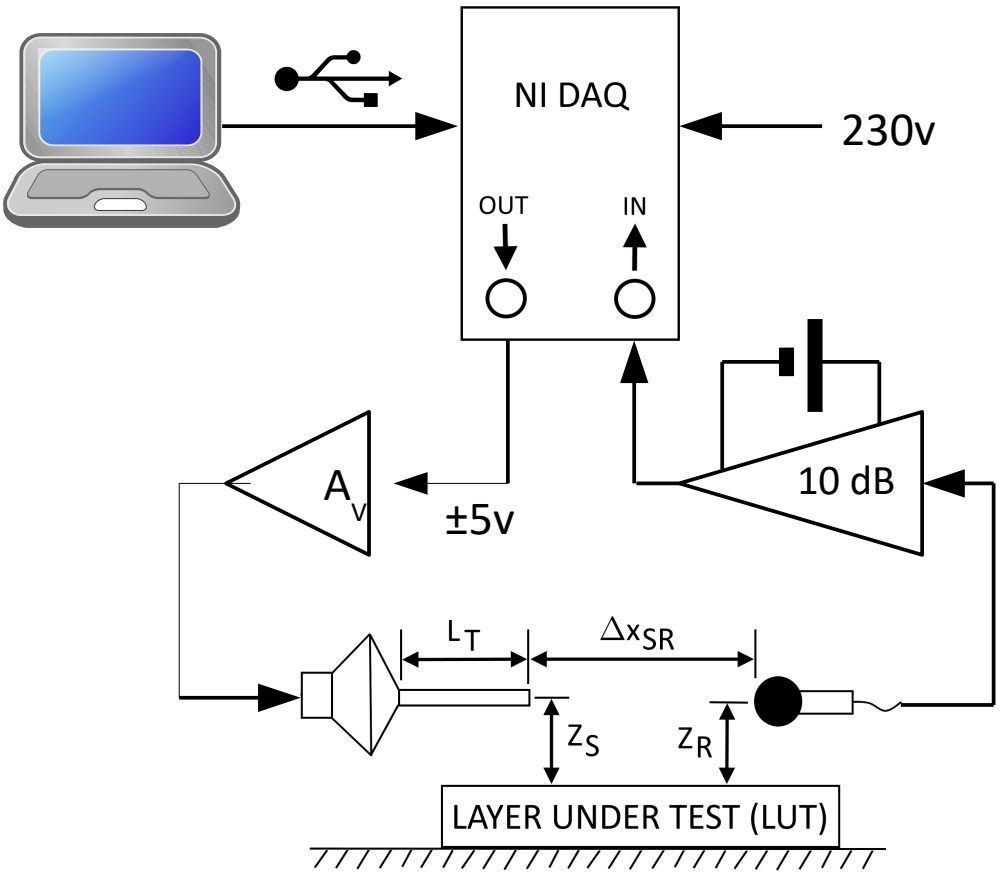

Figure 3.1 Measurement setup.

3.1 The measurement process

The measurement method is best understood in terms of the processes involved without unnecessary regard to the specific implementation. Figure 3.2 shows the logical sequence of processes in our measurement method.

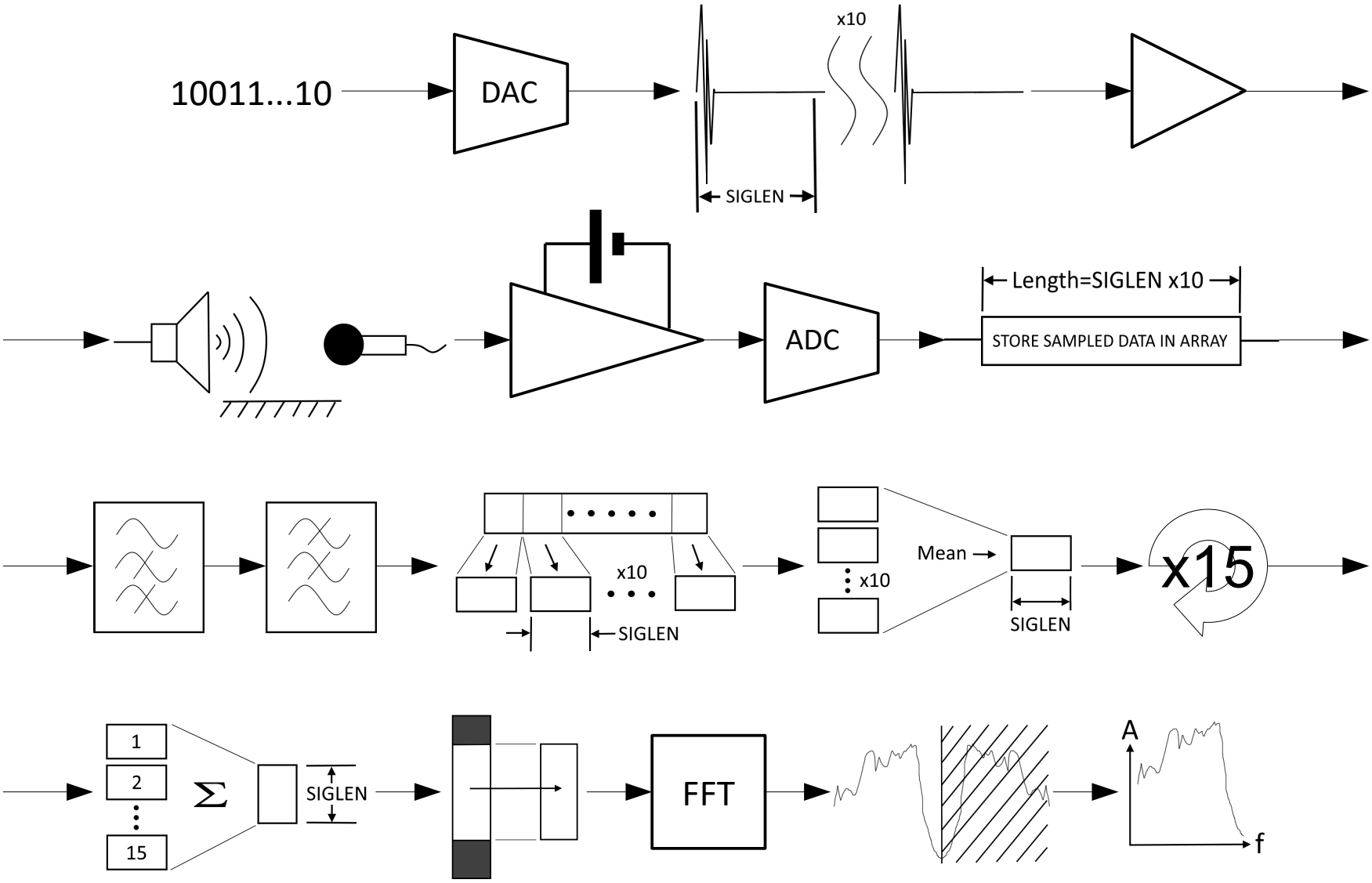

Figure 3.2 Measurement process.

This process begins within the MATLAB script of the host computer feeding the 16-bit digital representation of the driving signal to the DAQ module via the USB connection. The DAQ then converts the digital samples to an analogue signal at the rate of f_S=75472 samples per second and with a peak amplitude of approximately ±5 volts. The signal consists of a pulse train of n_P=10 pulses, each an approximation to an impulse. Each pulse has a length *SIGLEN*, of 4000 samples giving a total sample length for the pulse train of 40000 samples, or just over 0.5 s in time at the given sample rate. In their ideal form an impulse is an infinitely short pulse whose spectral characteristic is flat throughout the entire bandwidth. Theoretically, excitation of a system with such a pulse would yield the impulse response whose spectrum is then the frequency response of said system. The pulse train, each of which an approximation to an impulse, was sampled directly from an old audio analyser system which will no longer operate on modern computer equipment. This method was adopted in order to maintain consistency with previous measurements made with the old system [31]. The analogue signal from the DAQ is amplified by a good quality consumer audio power amplifier whose gain A_V, is set manually at the start of each set of measurements to ensure that the received signal is within the signal level limits of the DAQ input. The amplifier is connected to the sound source to produce the audio signal to excite the layer under test (LUT) which in our case is either the grooved grating or latticed structure. The length of the tube of the sound source L_T, is set such that the reflections within it do not interfere with the measurement. A 'safe' minimum length may be given approximately by the following relation of Eq. (3.1) which ensures that all incident effects have reached the receiver by the time the first reflected pulse within the tube has reached the radiating aperture. This does however require some estimation as to the minimum propagation speed of the slowest component in the system (liable to be any ground surface waves) which will be expressed as a factor $F_{c0}\,(min)$ of the free-space propagation speed c_0.

$$2L_T > \frac{\Delta x_{SR}}{F_{c0}}$$
$$2 \times 2.2 > \frac{1}{F_{c0}} \therefore F_{c0} > \frac{1}{4.4} \tag{3.1}$$

The 2.2 m length of L_T and Δx_{SR} of no greater than 1 m used throughout this research ensures that the measurements will not be affected in this regard unless any acoustic wave components posses a propagation speed less than about one quarter that of c_0.

Once the pulse train emanates from the source it will interact with the ground layer and the

resulting dynamic sound field at the receiver location will be measured for a given period of time. The analogue signal from the microphone is amplified by a dedicated power supply with a gain facility of up to 40 dB and is battery powered to provide good electrical isolation as the raw signal from the microphone is very low level and highly susceptible to electrical noise and interference. A 10 dB gain is applied by the amplifier and the signal then fed straight into the input of the DAQ module which will convert the analogue signal to a digital stream at a sample rate of f_S and bit depth of 16-bit. Because of the time-of-flight delay of the audio waves, the signal from the microphone must continue to be sampled by the DAQ and subsequently stored, for a period of time after the source signal has been transmitted from the source in its entirety. Conversely it is not necessary to begin sampling until the signal first reaches the radiating aperture of the source. The sampling period start and stop times, t_{START} and t_{STOP} respectively, are given by the following, assuming that t=0 is when the signal is first output from the DAQ and that there are no delays in the signal process or amplification chain.

$$t_{START} \leq \frac{L_T}{c_0} \approx \frac{2.2}{343} \approx 6\,ms$$

$$t_{STOP} \geq \frac{L_T}{c_0} + \frac{SIGLEN.n_P}{f_S} + \frac{\Delta x_{SR}}{F_{c0}(\min).c_0} \approx 6\,ms + \frac{4000 \times 10}{75472} + \frac{1}{1/4.4 \times 343} \approx 550\,ms \qquad (3.2)$$

In our case this yields $t_{START} \leq 6$ ms and $t_{STOP} \geq 550$ ms given that $F_{c0}\,(min)$ is one quarter. Within the DAQ module there is provision to include filtering to the sampled signal and for our purposes both a low and high-pass filter are applied. They are both 4th order filters and have their cut-on and cut-off frequencies set to 350 Hz and 35000 Hz respectively. The low-pass filter reduces any DC offset, low frequency ripple and mains noise while the high pass filter is set below the Nyquist frequency to avoid aliasing as a result of the analogue to digital conversion and high frequency interference. All functionality is built into the DAQ module and the filters are configured simply by programming the DAQ appropriately via the USB interface.

Once the sampling window is complete the filtered data is stored within the DAQ and retrieved by the host computer via the USB connection. It is then processed on the host computer using the MATLAB script in the following manner. Firstly the measured data array is dissected into n_P discrete arrays each of *SIGLEN* in length which correspond to the response from each one of the individual pulses present within the source signal. Due to

the fact that the signals are impulse like, the significant 'quiet' time of approximately 6 ms between each pulse should be such that all relevant waves should have reached the receiver by the time the next pulse is transmitted for our given setup. However the 6 ms gap may not be sufficient with a factor $F_{c0}\,(min)$ of one quarter, as under this condition the time between pulses should in fact be in excess of 11 ms to ensure a safe margin for any surface waves to traverse the gap between source and receiver. But the one quarter value for $F_{c0}(min)$ has been calculated based upon a safe margin given the geometry of the setup and in reality any waves travelling this slowly are very unlikely to be significant or even present as most surface waves are estimated to have speeds no slower than around 280-300 m/s. The mean of all n_P arrays is then taken, resulting in a single array of length *SIGLEN* which is the mean response to an individual source pulse and consequently a loose approximation to the impulse response of the acoustic environment including the layer under test. The whole process is then repeated 15 times and the mean of each mean is taken to provide a final result which is the mean response of some 150 pulses. The purpose of this averaging is to improve signal to noise ratio and to minimise uncorrelated noise or transient events which may spoil an individual measurement.

Subsequently the averaged response is windowed to extract the salient response and help to exclude unwanted artefacts. A given number of samples are excluded at the beginning of the array due to the time-of-flight delay of the signal being emitted from the receiver and the first desired effects being detected by the microphone. Aside from trivial delays in the DAQ and analogue audio chain, the measured data is time aligned with the source signal and so the first sample in the measured data corresponds to the first sample of the driving signal being fed to the source. Hence the maximum number of samples which can blanked at the start of the measured data for Δx_{SR}=0.7 m is,

$$W_{START} \le f_S\left(\frac{L_T}{c_0}+\frac{\Delta x_{SR}}{F_{c0}(\max).c_0}\right)\approx 75472\times\left(\frac{2.2}{343}+\frac{0.7}{1\times 343}\right)\approx 638 \tag{3.3}$$

where $F_{c0}\,(max)$ is the maximum speed of sound factor for the fastest propagating signals that are desired to be captured in the measurements. For instance non-linear large signal disturbances such as sonic booms may travel faster than c_0. In our case these are not of interest so $F_{c0}\,(max)$=1 and around the first 640 of the 4000 (SIGLEN) samples may be safely removed and set to zero for Δx_{SR}=0.7 m. The data is also truncated at the end from sample number W_{END} onwards, for the purpose of removing the reflections caused by the

source tube and other stray reflections which may occur from nearby objects. Setting this is somewhat subjective and will only be optimised by trials as the stray reflection effects are too complex to accurately predict. However, a minimum bound may be defined such that the truncation will not encroach on relevant data. One must also consider the reflections from inside the source tube which will re-emit an ever decreasing portion of the source signal each time the periodic reflection reaches the aperture of the source tube. This will introduce a maximum requirement upon W_{END}. Given that the pulse is very few samples long it can be considered to have zero time duration, leading to the bounds,

$$
\begin{aligned}
&f_S\left(\frac{3L_T}{c_0}+\frac{\Delta x_{SR}}{c_0}\right) >\sim W_{END} >\sim f_S\left(\frac{L_T}{c_0}+\frac{\Delta x_{SR}}{F_{c0}(\min).c_0}\right)\\
&75472\times\left(\frac{3\times 2.2}{343}+\frac{0.7}{343}\right) >\sim W_{END} >\sim 75472\times\left(\frac{2.2}{343}+\frac{0.7}{0.25\times 343}\right)\\
&1606 >\sim W_{END} >\sim 1100
\end{aligned}
\qquad (3.4)
$$

where the first term accounts for the removal of tube reflections and the second, the requirement to capture a long enough time period to include all relevant data. Hence both conditions of Eq. (3.4) must be met to ensure usable data and if both conditions cannot be satisfied then the parameters of the measurement setup must be changed. For our case and with Δx_{SR} =0.7m, W_{END} should lie approximately in the region 1100-1606. In practice for the measurements made for this research values of 649 and 1711 were adopted for W_{START} and W_{END} giving a truncated data length of 1063 samples. The latter being in excess of that calculated because it was tuned during experimentation to an apparent optimum value.

Applying a Fast Fourier Transform (FFT) to the processed measurement data array and truncating by half to remove the resulting alias, will yield the frequency response of the acoustic environment combined with that of the measurement system itself. Isolating the response of the Layer Under Test (LUT) from its surroundings and measurement system will be achieved in the next section and is not part of the measurement process itself. A 2048 point FFT was applied to the measurement data which consisted of 4000 points. After removing the upper 1024 samples from the resulting FFT to remove the alias response which manifests in this process, a frequency response with 1024 points is obtained which is enough to provide a bandwidth from 36 Hz up to $f_S/2$ of nearly 38 kHz at our sampling rate of 75472 Hz. For the measurements made by Bashir [31] and reproduced in 6.3.9, a half Blackman-Harris window was applied prior to the FFT in order to minimise the spectral spreading which would otherwise occur, due to the start and end point

discontinuities of the time truncated signal. For the measurements made specifically for this work in 7.3.1 no window was used because the surface wave tends to overlap and follow the direct and reflected arrivals and pre-windowing might curtail its contribution. A result of not pre-windowing is the presence of related artefacts such as spectral spreading and Gibbs oscillations.

Figure 3.3 shows a plot of the signal waveforms at each key stage of processing for one *SIGLEN* length slice of data. The blue trace is the raw signal from the analogue to digital conversion. The red trace is post filtering, which has clearly removed the large DC offset present on the raw signal. Finally the black trace is the fully processed signal which has been averaged and the windowing process applied. It can be seen in this case that a slightly smaller value of W_{END} would have been desirable as a small portion of the reflection from the source tube has been included, which can be seen clearly in the red and blue traces between samples 1500-2000. The second reflection can be seen between samples 2500-3000, but this has been removed completely by the windowing process. The window at the beginning appears ideal as it has removed the initial signal delay due to time-of-flight from source to receiver without losing relevant data.

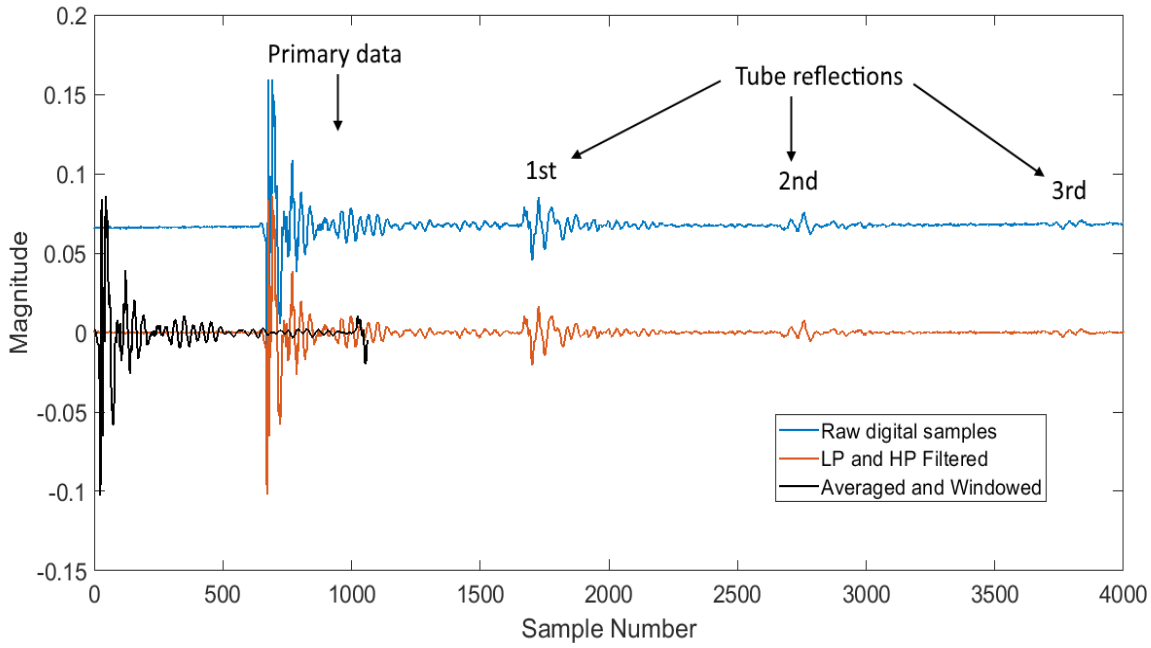

Figure 3.3 Raw, filtered and fully processed signals.

3.2 Obtaining the excess-attenuation spectrum

It is required that the excess-attenuation (EA) spectrum of the LUT be obtained. This is achieved by taking two sets of measurements and taking their ratio to yield the EA of the LUT alone. It is critical that the measurement system settings are unaltered between measurements including the gain of the amplifiers as the method relies upon repeatability of measurement. Any settings must be determined initially by experiment to find their optimum and then once stable, the measurements taken in succession without further alteration. First the response of the system is measured without the LUT in place and the source and receiver placed as close as possible over the hard ground to ensure interference phenomenon between direct and reflected paths are pushed beyond the bandwidth of interest. Incidentally neither the source nor receiver may touch the ground as this will cause seismic coupling and will taint the results. This is a reference measurement to characterise the measurement system on the assumption that the ground is acoustically hard.

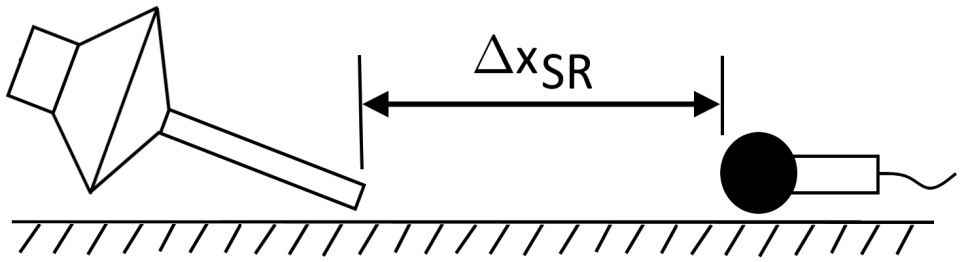

Figure 3.4 Reference measurement setup.

The setup is restored to that of interest and a further measurement made to obtain the full frequency response of the entire system.

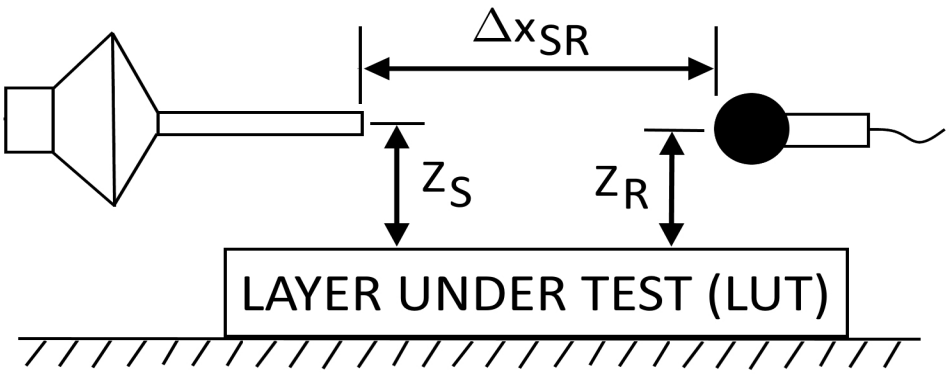

Figure 3.5 Full measurement setup.

It would also be possible to use the setup of figure 3.5 but with the LUT removed as a reference as opposed to that of figure 3.4. However this would mean that the ground reflection interference phenomena would lay within the bandwidth of interest and would be part of the reference characteristic causing these events to not be present in the spectra once the LUT is re-inserted. We wish to see these hard ground reflection phenomena in our excess-attenuation spectra for the LUT and so the reference is taken as in figure 3.4 where any ground reflection interferences occur beyond the audio bandwidth of interest. Another alternative is referencing with respect to the free field, where measuring it requires removing the surface or moving the source and the microphone far away from the surface. Neither are practical in our anechoic chamber without risk of disturbing or significantly repositioning the measurement apparatus introducing potential errors because of uncertainty in source-receiver position. Using the field above the hard surface as in figure 3.4 has the advantage that the source-microphone system is repositioned only slightly thereby reducing potential for errors. If the source and microphone are close enough to the surface, which is the normal case, the resulting reference field is just the same as the free field but with a 6 dB offset due to the ground reflection component. The downside to this is that it assumes that the hard surface is indeed acoustically hard which of course is not possible in practice.

Taking the sample wise quotient of the full and reference measurement frequency responses isolates the insertion loss of the LUT which by definition is the EA spectrum, hence.

$$EA(LUT)_{dB} = 20\log_{10}\left(\frac{\text{Full measurement}}{\text{Reference measurement}}\right) \quad dB \tag{3.5}$$

3.3 Summary

The measurement process used to obtain the results presented in this thesis has been explained. The setup is that of a point like source and receiver, separated by a given distance and placed above a ground surface, which in this work is a periodic series of grooves or lattices. Many of the measurements used in this work were made by others [31] using this method and to ensure continuity with existing work, the same process was used for new measurements made by the author. All measurements were undertaken in the laboratory and within the same anechoic chamber at the Open University to reduce as much a practical environmental effects such as ambient noise or reflections in order that the effect of the grooved grating is observed.

CHAPTER 4 – Relevant theoretical methods

4.1 The Boundary Element Method (BEM)

The Boundary Element Method, or BEM for short, is a numerical technique for solving spatial field problems for which an analytic solution is either cumbersome or is not known to exist. The method evolved in the 1970's and gained momentum as computing power became more accessible for its implementation, but the underlying mathematics predate all of this by quite some time. In its fundamental form BEM is posed in the frequency domain and is used extensively in physics to solve complex time independent spatial field problems across a wide range of disciplines such as thermostatics, electrostatics and of course acoustics. The problem is posed in terms of a time independent governing equation describing the behaviour of the process involved, such as the Helmholtz equation for wave field problems and the heat diffusion equation for thermostatics and a set of boundary conditions which relate to the spatial domain of the problem and often, but not always, enclose the domain of the problem. The boundary is subsequently disctretised into individual elements of finite size to approximate the geometry of the problem. The governing equation is then solved numerically to satisfy the set of given boundary conditions, the results of which define the field on the boundary which in turn analytically defines the field at every point in the domain. A major advantage of BEM over finite difference methods such as Finite Element Analysis (FEA) is that the problem need only be discretised in one dimension less than the problem at hand whereas other methods would require discretisation in all spatial dimensions. This has significant advantages in terms of lower computation times and demand upon computing resources. Furthermore, for unbounded half space problems only the obstacles require meshing with the BEM whereas the equivalent problem in FEA would require an infinitely large mesh or a perfectly matched layer. The former being impractical and the latter, troublesome to achieve. The BEM is often better suited to solving acoustic field problems than FEA because for a given discretisation step size the BEM will involve less discrete elements and does not require that the field equations be linearised.

The BEM implementation used throughout this work assumes an ideal and homogeneous air medium, precluding atmospheric turbulence, refraction and other related real world phenomenon which affect outdoor acoustics. However, the modelling of such non-idealities has been considered by Taherzadeh et al. [65] using a boundary integral method

but its implementation is not necessary for this study. For thorough consideration of the fundamentals of BEM and its application the reader is referred to texts by Whye-Teong Ang [43] for general consideration and Chandler-Wilde and Langdon [54] for a comprehensive review of BEM for acoustics applications, but a brief introduction to the fundamental methods relating specifically to our application of acoustic wave propagation is offered henceforth.

4.1.1 An introduction to the BEM for acoustic wave fields

Before introducing the mathematical detail of BEM it is worth mentioning some of the fundamental premises which underlie the method. The field equation $s(R)$ must be linear as the BEM relies upon the superposition principle. Examples of which are the Helmholtz equation for wave propagation, the thermal diffusion equation and many potential field equations. The divergence theorem of Gauss-Ostrogradskii is applied to transform a spatial domain problem into one which may be solved at the boundaries, effectively removing one spatial dimension from the resulting equations and affording significant benefits in terms of the computing resources required. A general solution for $s(R)$ is required which shall be termed $G(R_1,R_2)$ along with its normal derivative $\delta G(R_1,R_2)$ and are usually referred to as the 'Green's' functions in recognition of the mathematician George Green's work on the solution of differential equations.

A typical problem is shown in figure 4.1 which consists of a region of space R for which the field is required to be known. The region R is bounded by the curve C.

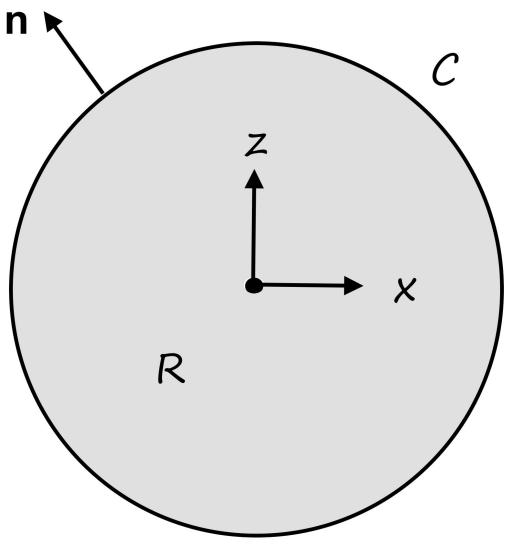

Figure 4.1 Simple spatial field problem.

The choice of surface normal direction pointing inwards or outwards is arbitrary and authors do differ in convention. This causes no problems so long as the chosen convention is adhered to and consistently applied. The field must obey a governing equation $s(R)$ throughout R and on the boundary, which for acoustic wave fields in an inviscid air medium is the homogeneous Helmholtz equation,

$$\nabla^2 \cdot \phi + \frac{1}{c^2}\phi = 0 \tag{4.1}$$

where the divergence in space is,

$$\nabla^2 \cdot \phi = \frac{\delta^2 \phi}{\delta x^2} + \frac{\delta^2 \phi}{\delta y^2} + \frac{\delta^2 \phi}{\delta z^2} \tag{4.2}$$

The Green's functions in this case are the fundamental solution to the Helmholtz differential equation of Eq. (4.1) and give the field at point R_2 anywhere within R caused solely by the field present at point R_1. Suppose a simple problem with a single source at location R_1 and receiver at R_2 in free-space. The function $G(R_1,R_2)$ would give the field at the receiver due to the free-space propagation of acoustic energy from the source. Green's functions are linear and superposition holds so in the case of n sources, the field at R_2 would be the n-term summation $\Sigma G(R_n,R_2)$ for all n sources at location R_n. This principle is

key to BEM as will be seen, because the field at any point within R is the summation of all sources within R and contributions from all points on C, where each point on C is considered as if it were a discrete source of amplitude $\phi(C)$. Similar in concept to the Huygens principle in the time domain.

$$G(R_1, R_2) = \phi(R_1)\, L\, H_0^{(1)}\left(ik\left[\left(R_{1x} - R_{2x}\right)^2 + \left(R_{1z} - R_{2z}\right)^2 \right]^{\frac{1}{2}} \right) \tag{4.3}$$

$$\delta G(R_1, R_2) = \frac{\delta}{\delta \mathbf{n}} G(R_1, R_2) \tag{4.4}$$

where,

$$L_C = \frac{1}{2\pi\left[\left(R_{1x} - R_{2x}\right)^2 + \left(R_{1z} - R_{2z}\right)^2 \right]^{\frac{1}{4}}}$$

$$L_S = \frac{1}{4\pi\left[\left(R_{1x} - R_{2x}\right)^2 + \left(R_{1z} - R_{2z}\right)^2 \right]^{\frac{1}{2}}}$$

Where the factors L_C and L_S respectively represent a cylindrical and a spherical source. Care must be taken to ensure that the correct term is used throughout. For representing contour elements the source will generally be assumed cylindrical or spherical depending upon the dimensions and assumptions of the problem but if a specific source term is included in the problem (to be discussed later) it may be also be of homogeneous plane-wave type.

The unknown field ϕ in R will have the boundary conditions on the boundary contour C thus,

$$\begin{aligned} \phi &= f(C) \\ \frac{\delta\phi}{\delta \mathbf{n}} &= \delta f(C) \end{aligned} \tag{4.5}$$

where the field amplitude $f(C)$, its derivative $\delta f(C)$ or linear combination of the two are given as part of the problem conditions. The unknown field amplitude or its derivative is given by the solution of the Boundary Integral Equation (BIE) which is the core equation of the BEM and is derived according to this procedure. Solution of which fully defines the field ϕ on C and hence at any point within R.

As well as ϕ being a solution to the Helmholtz equation, then by definition so must the

Green's function G, leading to the statement,

$$\nabla^2 \cdot G + \frac{1}{c^2} G = 0 \quad R1 \neq R2 \tag{4.6}$$

Multiplying Eq. (4.1) by G and Eq. (4.6) by ϕ yields the coupled equations below.

$$\phi\left(\nabla^2 \cdot G\right) + \phi\left(\frac{1}{c^2} G\right) = 0 \tag{4.7}$$

$$G\left(\nabla^2 \cdot \phi\right) + G\left(\frac{1}{c^2} \phi\right) = 0 \tag{4.8}$$

Subtracting Eq. (4.8) from (4.7) leads to,

$$\phi\left(\nabla^2 \cdot G\right) + \phi\left(\frac{1}{c^2} G\right) - G\left(\nabla^2 \cdot \phi\right) - G\left(\frac{1}{c^2} \phi\right) = 0$$

$$\phi\left(\nabla^2 \cdot G\right) - G\left(\nabla^2 \cdot \phi\right) = 0 \tag{4.9}$$

Since G and ϕ are constant with respect to $d\mathbf{n}$ then they may be absorbed into any order of differentiation with respect to $d\mathbf{n}$. Exploiting this and expanding the second order differential allows Eq. (4.9) to be expressed thus,

$$\frac{\delta}{\delta \mathbf{n}}\left[\phi \frac{\delta G}{\delta \mathbf{n}}\right] - \frac{\delta}{\delta \mathbf{n}}\left[G \frac{\delta \phi}{\delta \mathbf{n}}\right] = 0 \tag{4.10}$$

Let R be a 2d area in the x-z plane with invariance in y making the boundary C a 1d line contour in the same plane. Integrating Eq. (4.10) over R yields the area integral,

$$\oiint_R \frac{\delta}{\delta \mathbf{n}}\left[\phi \frac{\delta G}{\delta \mathbf{n}}\right] - \frac{\delta}{\delta \mathbf{n}}\left[G \frac{\delta \phi}{\delta \mathbf{n}}\right] dx dz = 0 \tag{4.11}$$

The Gauss-Ostrogradskii divergence theorem states that for a well defined vector function $\mathbf{F}$,

$$\oint_C \mathbf{F}.\mathbf{n}\, d(x,z) = \oiint_R \nabla.\mathbf{F}\, dx dz \tag{4.12}$$

Applying this to Eq. (4.11) leads to Green's first theorem as follows, which lowers the order of integration on the right hand side by one dimension and expresses ϕ in terms of its boundary values upon C.

$$\iint_R \frac{\delta}{\delta \mathbf{n}}\left[\phi \frac{\delta G}{\delta \mathbf{n}}\right] - \frac{\delta}{\delta \mathbf{n}}\left[G \frac{\delta \phi}{\delta \mathbf{n}}\right] dxdz = \oint_C \phi \frac{\delta G}{\delta \mathbf{n}} - G \frac{\delta \phi}{\delta \mathbf{n}} d(x,z) \tag{4.13}$$

However, the Green's function of Eq. (4.3) and (4.4) will equate to infinity when $R_1 = R_2$ causing the integral to also saturate. Intuitively this is because at point R_1 there is assumed to be an equivalent point source and so at R_1 anything other than a zero amplitude will result in an infinite energy density. Clearly this is not not sensible so to avoid this situation R_1 is excluded from the region R by an additional circular boundary of radius r_B which resides fully within C, as shown in figure 4.2.

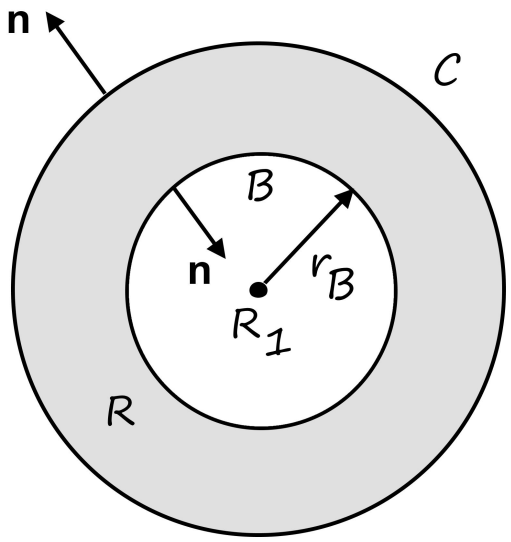

Figure 4.2 Additional boundary 'B' to avoid integral saturation.

The surface normal of the inner boundary B is opposite to the major boundary C and so by definition the net flux due to the effective source at R_1 within R is zero, where R is now the space between B and C. The example once again is posed in 2d but the principles are the same for 3d, where R becomes a volume and B and C enclosed surfaces. This scheme gives rise to the equation,

$$\oint_C \phi \frac{\delta G}{\delta \mathbf{n}} - G \frac{\delta \phi}{\delta \mathbf{n}} d(x,z) + \oint_B \phi \frac{\delta G}{\delta \mathbf{n}} - G \frac{\delta \phi}{\delta \mathbf{n}} d(x,z) = 0 \tag{4.14}$$

Letting the radius of B, r_B tend to the limit of zero and evaluating the resulting integrals yields the results below. The details of which have been omitted for clarity but the reader is

referred to pages 14 and 15 of [43] for the full process.

$$\phi(R_{1x}, R_{1z}) = \oint_C \phi \frac{\delta G}{\delta \mathbf{n}} - G \frac{\delta \phi}{\delta \mathbf{n}} d(R_{2x}, R_{2z}) \tag{4.15}$$

This equation states that the field at point R_1 is equal to the sum of all other points on C given by R_2, where C is considered as a contour of an infinite number of individual source elements superposed by the integral to give the resultant field at location R_1. The field throughout R is therefore determined by the field and its derivative on the boundary C. However to evaluate Eq. (4.15) the condition that B lie wholly within the bounds of C is broken because point R_1 will lie upon C and so B by definition will protrude beyond C. Taken in the limit of $r_B \rightarrow 0$ then C will approximate to a straight line bisecting the diameter of B and so half of B will be within and half will be outside of C. This gives rise to a leading factor $\lambda(R_1)$ which when applied to Eq. (4.15) gives the boundary integral equation (BIE) for this example problem of,

$$\lambda(R_{1x}, R_{1z})\phi(R_{1x}, R_{1z}) = \oint_C \phi \frac{\delta G}{\delta \mathbf{n}} - G \frac{\delta \phi}{\delta \mathbf{n}} d(R_{2x}, R_{2z}) \tag{4.16}$$

where,

$$\lambda(R_1) = \begin{Bmatrix} 1 \text{ if } R_1 \text{ within } C \\ \frac{1}{2} \text{ if } R_1 \text{ lies on } C \\ 0 \text{ if } R_1 \text{ oustide } C \end{Bmatrix}$$

The BIE will vary depending upon the governing field equation (Helmholtz for our time independent acoustic application) and the specific geometry chosen, but the derivation process remains the same for other physical problems and the form of the equation will likely be similar. The demanding aspect is finding the appropriate Green's functions which is often not a trivial task. Further insight into this process is offered for a range of problems in [43] and for acoustics specifically in [54].

It is worth clarifying that so far the field has been assessed in the absence of a source within the bounds of C, hence the resultant flux out of or into the boundary has been zero. Sources outside of C will however be implicit in the definition of ϕ or $\delta\phi$ on the boundary as part of the problem initial conditions. A source term within C will be considered in the next section when the BEM is applied to the acoustic case of point-to-point propagation.

4.1.2 Solving the BIE numerically

In all but the simplest of cases the BIE cannot be solved analytically and so it must be reposed in a discrete form to allow numerical solution. This involves truncation in both space and numerical precision so the solution will be approximate. Choosing truncations inappropriately causes significant error and it is all too easy to obtain results which bear no resemblance to reality. It is therefore critical that the greatest practical number precision is used both for storage and in the calculations in order to avoid accumulation errors. As part of the process the boundary C is segmented into a discrete mesh and this must be discretised finely enough to give sufficient spatial resolution otherwise discretisation error will ruin the result. A less obvious pitfall may occur when calculating $\phi(R)$ at distance comparable or less than the mesh size of C away from C itself which can cause numerically instability and unreliable results.

Let C be represented by M straight line segments as shown in figure 4.3, with vertices at the intersections of each segment. Here it is assumed that the field along each m'th segment C_m is constant and takes on the value as at the mid-point.

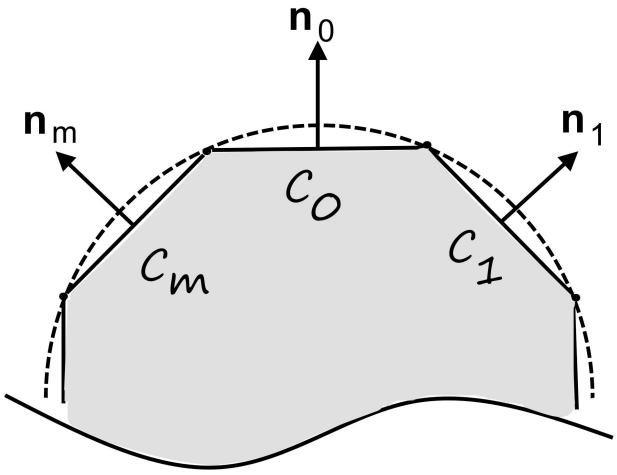

Figure 4.3 Discretised boundary.

To form a discrete BIE which may solved numerically, the field upon the boundary is taken at the mid-point of each segment C_m giving M field values upon the discrete boundary of ϕ_m and $\delta\phi_m$. Hence the discrete form of the BIE in Eq. (4.16) is Eq. (4.17), noting that the leading factor λ will remain at ½ as all field points lie upon the boundary. Since ϕ_m and $\delta\phi_m$ do not vary along each segment C_m, they may be taken out of the segment integral as a

constant factor. The Green's functions of Eq. (4.3) and (4.4) outside of the remaining integrals are evaluated at the midpoint of each segment C_m.

$$\frac{1}{2}\phi_m = \sum_{m\dagger=1}^{M}\left(\phi_{m\dagger}\oint_{C_{m\dagger}}\frac{\delta G}{\delta \mathbf{n}}d(x,z) - \frac{\delta\phi}{\delta \mathbf{n}}\oint_{C_{m\dagger}} G(C_m, C_{m\dagger})d(x,z)\right) \tag{4.17}$$

We are now left with the two continuous integrals which must be evaluated across the length of each segment m. The complexity of these integrals will depend upon the problem at hand and so it is not possible to consider a general case. However numerical approximations of integrals are widely published in literature for most applications, ranging from simply multiplying the mid-point value at C_m by the length of the segment to involved methods which may be required in complex problems or for greater accuracy. Evaluating the integrals for self-interaction and near-neighbour interactions are the most challenging and require special treatment in most cases. Once a numerical approximation has been applied for the two remaining integral terms, then Eq. (4.17) may be formed into a system of M equations and solved numerically for the unknown ϕ_m or $\delta\phi_m$ upon the boundary. From the numerical solution all terms on the right hand side of Eq. (4.17) become known allowing the field at any given point R_1 to be expressed analytically by,

$$\lambda(R_1)\phi(R_1) = \sum_{m\dagger=1}^{M}\left(\phi_{m\dagger}\oint_{C_{m\dagger}}\frac{\delta G}{\delta \mathbf{n}}d(x,z) - \frac{\delta\phi}{\delta \mathbf{n}}\oint_{C_{m\dagger}} G(C_m, C_{m\dagger})d(x,z)\right) \tag{4.18}$$

4.1.3 Application to acoustic problems

The boundary element method will be applied to point-to-point acoustic problems starting with a simple source and receiver in free-space and building upon this to include ground surfaces and arbitrary structures.

4.1.3.1 Point source and receiver in free-space

Consider initially the simple case of a point source at location R_S and point receiver at R_R in free-space and suppose we wish to know the field magnitude at the receiver due to the source. This is a trivial case which has the solution given merely by applying the Green's function of Eq. (4.3) with $G(R_s, R_R)$. However the BEM will be applied to this simple problem to establish the process for such acoustic problems and complexity will be

introduced in stages.

Thus far the BIE has assumed that no source is present within the boundary but in this acoustic problem a source has been introduced. This requires the addition of a source term to the right hand side of the BIE which is given in this case by the Green's function $G(R_s,R_R)$ of Eq. (4.3). The BIE of Eq. (4.17) then becomes,

$$\frac{1}{2}\phi_m = \sum_{m\dagger=1}^{M}\left(\phi_{m\dagger} \oint_{C_{m\dagger}} \frac{\delta G}{\delta \mathbf{n}} dC_{m\dagger} - \frac{\delta \phi}{\delta \mathbf{n}} \oint_{C_{m\dagger}} G(C_m, C_{m\dagger}) dC_{m\dagger} \right) + G(R_S, R_R) \tag{4.19}$$

To apply the BEM, either ϕ or $\delta\phi$ must be defined on the boundary. This raises a problem, where is the boundary as we are occupying an infinite free space and what would be the conditions imposed by such a hypothetical boundary? This problem of unhindered propagation into free space was solved by Sommerfeld with the so called Sommerfeld radiation condition below, the derivation of which is left as further reading [54].

$$\begin{aligned} &\phi(r) = O\left(r^{-(d-1)/2}\right) \\ &\frac{\delta \phi}{\delta r}(r) - ik\phi(r) = o\left(r^{-(d-1)/2}\right) \end{aligned} \tag{4.20}$$

Given that r is the radial distance from the source and d the number of spatial dimensions the qualitative implications of this are that the field in two or more dimensions must vanish as $r\rightarrow\infty$ and the wave appears locally as if it were a plane wave. Consequently the free-space may be modelled as a closed circular contour C with an infinite radius, upon which the field and hence its derivative, must vanish. Applying this to the BIE of Eq. (4.17) causes the ϕ_m or $\delta\phi_m$ terms to equate to zero, removing any contribution from the summation. The BIE thus becomes,

$$\frac{1}{2}\phi_m = \sum_{m\dagger=1}^{M}\left(0 * \oint_{C_{m\dagger}} \frac{\delta G}{\delta \mathbf{n}} dC_{m\dagger} - 0 \oint_{C_{m\dagger}} G(C_m, C_{m\dagger})\, dC_{m\dagger} \right) + G(R_S, R_R) \tag{4.21}$$

The field ϕ at a point R anywhere in free-space because the radius of C is infinite, reduces to the trivial case of,

$$\phi(R) = G(R_S, R_R) \tag{4.22}$$

without any need to solve the BIE. The practical implication of this results is that when

formulating the problem only impedance boundaries need be contoured in the BIE summation as the contour at radius ∞ representing lossless free-space propagation is implicit.

4.1.3.2 Point source and receiver above a hard ground plane

Consider now the point source and receiver in free space but above an acoustically hard ground plane in the *x*-*z* plane at *z*=0 which extends infinitely as shown figure 4.4. The half space above *z*=0 will be free-space and so the Sommerfeld radiations apply so this region need not be considered in the BIE. Ordinarily, impedance boundaries such as the ground surface would require discretising into a mesh but because of the symmetry around the origin the field in the upper half space can be represented by an image source at $-z_S$.

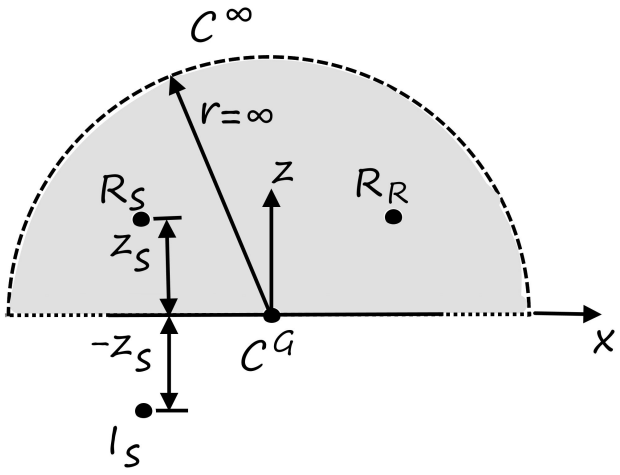

Figure 4.4 Source-receiver above a ground plane.

Due to the simplicity of the problem the image source may be fully represented by just modifying the Green's function to accommodate it. In fact any geometry may theoretically be represented by the appropriate Green's function without the need to discretise or solve the BIE, but in practice all but the most trivial of geometries such as in this case, would possess a Green's function far too complex to ever derive and so discretising the geometry as a mesh and solving the BIE is the only viable option. Adding the image source term to the standard free-space Green's function of Eq. (4.3) is intuitive and results in the Green's function which implicitly accounts for a hard ground surface of,

$$G_{\dagger}(R_S, R_R) = A\,L\exp\left(ik\left[\left(R_{Sx} - R_{Rx}\right)^2 + \left(R_{Sz} - R_{Rz}\right)^2 \right]^{\frac{1}{2}} \right)$$
$$+ A\,L\exp\left(ik\left[\left(R_{Sx} - R_{Rx}\right)^2 + \left(-R_{Sz} - R_{Rz}\right)^2 \right]^{\frac{1}{2}} \right) \qquad (4.23)$$

where A is the source strength, usually assumed unity for simplicity as the absolute value simply scales the field in this instance. If multiple sources were present then the relative scaling of each source would become important.

Once again the BIE simplifies to just the Green's function because of the absence of a tangible contour, which for this example is $G_{\dagger}$ of Eq. (4.23). The solution is therefore analytic and simply calculated without the need to solve the BIE.

4.1.3.3 Point source and receiver above a shaped ground surface

A more complex ground surface will now be introduced which will form part of the overall boundary C. Up to now the boundary has been comprised of the hard ground surface contour element C^G and the upper half space bound C^{∞} given by the Sommerfeld conditions. In this case a rectangular grooved structure will be placed upon the hard ground surface and will be expressed as the contour C^R as shown in figure 4.5 and described by a surface impedance relation.

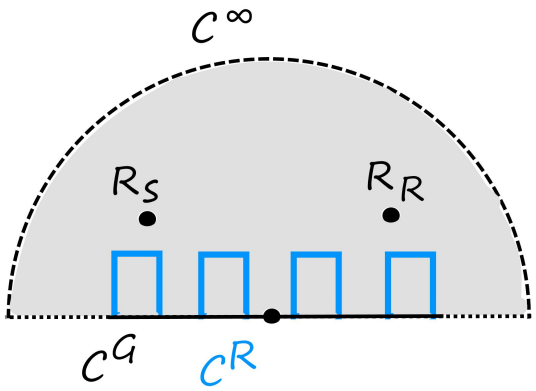

Figure 4.5 Source-receiver above a hard ground plane and periodic rough surface.

The first step in the solution of this problem is to discretise the rough ground element

contour C^R into a discrete mesh of the form shown in figure 4.3. The number of mesh elements must be chosen such that the distance between each mesh element is small enough for the maximum frequency of interest to ensure sufficient resolution commensurate with accurate results which are free of spatial aliasing. Evidently the finer the mesh the better the results may be, but computation time is increased, so a reasonable rule-of-thumb for acoustics problems is that the mesh pitch distance be no greater than around 1/10th of the minimum wavelength involved. Elements of the structure which are coincident with the hard ground surface need not be discretised because they will already be accounted for by the Green's function of Eq. (4.22). The boundary conditions are then defined at the centre point of each m element C^R_m by the field value of ϕ_m, its derivative $\delta\phi_m$ or linear combination of the two. The impedance of the surface Z_m is defined on each element m according to the well known acoustic impedance boundary condition of the following, assuming that ϕ is the acoustic pressure field.

$$i\omega\rho_0\phi_m + Z_m\frac{\delta\phi_m}{\delta\mathbf{n}} = 0 \tag{4.24a}$$

$$\therefore \quad \frac{\delta\phi_m}{\delta\mathbf{n}} = -\frac{i\omega\rho_0\phi_m}{Z_m} \tag{4.24b}$$

By substituting Eq. (4.24b) for $\delta\phi_m/\delta\mathbf{n}$ into Eq. (4.19) gives the BIE for the case of figure 4.5 with C_R defined by an impedance Z_m, of,

$$\frac{1}{2}\phi_m = \sum_{m\dagger=1}^{M}\left(\phi_{m\dagger}\oint_{C_{m\dagger}}\frac{\delta G_\dagger}{\delta\mathbf{n}}dC_{m\dagger} + \frac{i\omega\rho_0}{Z_m}\phi\oint_{C_{m\dagger}}G_\dagger(C_m, C_{m\dagger})dC_{m\dagger}\right) + G_\dagger(R_S, R_R) \tag{4.25}$$

Once again the field values of ϕ_m and $\delta\phi_m$ have been assumed constant along the length of each segment m, in order that these terms may reside outside of the integrals and be discrete in m. Upon numerical solution of the BIE the field within R is calculated analytically using Eq. (4.25) but without the leading ½ factor as the field point will reside within R (see Eq. (4.16)). For the specific case of an acoustically hard surface where $Z_m=\infty$ and the normal derivative of pressure $\delta\phi_m$ must vanish, the BIE reduces to,

$$\frac{1}{2}\phi_m = \sum_{m\dagger=1}^{M}\left(\phi_{m\dagger}\oint_{C_{m\dagger}}\frac{\delta G}{\delta\mathbf{n}}dC_{m\dagger}\right) + G(R_S, R_R) \tag{4.26}$$

Given the discrete mesh and the boundary conditions there upon, the integral must be

evaluated across the extent of each m-th element which as discussed previously may be approximated numerically using an appropriate method or in its simplest form as the value of the field at each segment centre point C_m. Evaluating the integral is an entire subject in itself and the method will depend upon the particular application, so detail is omitted here in favour of clarity.

An existing BEM program written by Dr. Taherzadeh in the programming language Fortran was used for all 2d BEM simulations during this research. For the predictions following in this thesis a structure like figure 4.5 is assumed and a BIE of the form of Eq. (4.26) solved within Dr. Taherzadeh's program to produce the results. Cylindrical source spreading was used for all simulations which approximates to a 3d situation where invariance in the 3rd dimension may be assumed. The process of implementing a BEM simulation is complex and this chapter offers only an insight into the fundamental principles underlying the method. The Fortran program is significantly longer than this chapter!

4.1.4 3d BEM simulations

Aims of this research include investigating doubly periodic ground structures with rectangular cavities that require consideration of all three spatial dimensions. The existing BEM programs available to us were in 2d only and so a 3d version was desirable in order to provide a theoretical reference with which to compare our work. Dr. Anton Krynkin from Sheffield university kindly supplied us with a 3d BEM program written in C++ for calculating the field due to closely spaced arrays of cylinders. This program already had much of the functionality required for our purposes including the BEM solution engines and critically, support to import 3d meshes for the boundary contours. From the imported 3d file the program would discretise the mesh and assign each surface normal vector in the correct direction which is a precise task. However many adaptations were required to repose the BIE into the form that we required for the point-to-point geometry of figure 4.5. Furthermore modifications were made to the presentation of the results to allow sectional slice plots of a 3d field and excess attenuation plots for a fixed receiver location. The process for the BEM in 3d is identical to that described in the previous section except that the number of dimensions is raised by one, so line contours in 2d become surfaces in 3d and surfaces in 2d become volumes in 3d. The BIE of Eq. (4.26) for the 2d solution to the point-to-point propagation problem of figure 4.5 above an acoustically hard ground structure becomes as follows in 3d.

$$\frac{1}{2}\phi_m = \sum_{m\dagger=1}^{M}\left(i\omega\rho_0\phi_{m\dagger}\iint_{A_{m\dagger}}\frac{\delta G}{\delta \mathbf{n}}dA_{m\dagger}\right) + G(R_S, R_R) \tag{4.27}$$

This is the equation that the 3d BEM program was adapted to solve, assuming spherical source spreading throughout. Although the impact of going from 2d to 3d on the complexity of the code required to solve the BIE is not significant, the increase in demand upon computational resources is.

After significant work it was unfortunate that the resolution required to represent a useful 3d ground surface was such that the resulting mesh was large and although the program would run, it quickly ran out of memory even on a computer with 32 GB RAM. Solving this limitation would have required advanced BEM techniques such as the multipole method [55], but no such programs were available to us and writing our own was beyond the scope and bounds of this research project. Nonetheless the principles of our 3d BEM program were proven on a somewhat simpler problem, that of a hard sphere in space above a hard ground plane, given a single point source located at R_S. The field was plotted at each point on a fine grid in the upper half-space to give the spatial field. A cross-sectional slice at y=0 was then taken and with the following result, where the geometry of the problem has been superimposed onto the image for clarity. The wave-number k of the source at point R_S is 30 and the medium has been assumed to be inviscid air.

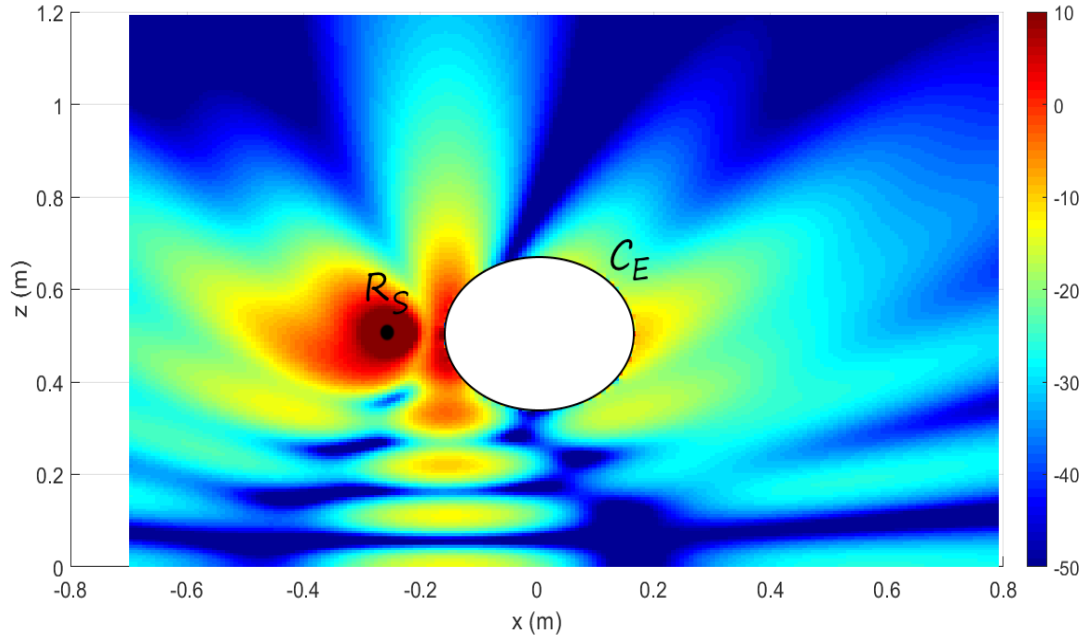

Figure 4.6 Cross-sectional slice of 3d BEM pressure field solution (in dB) of hard sphere above a hard ground plane.

The problem contains two contours. Firstly that of the implied Sommerfeld propagation conditions at infinity, intersected by the acoustically hard ground plane which is implicit with the Green's function of Eq. (4.23). The sphere is then discretised as a self contained contour C_E within the spatial boundaries of the outer contour with its surface normal pointing in the opposite direction because this element is known as an exterior boundary as the field is wished to be known outside of the boundary and not within it. As mentioned before the linear nature of the problem allows superposition in this way and so highly elaborate geometries may be expressed and solved with the BEM.

4.1.5 Summary

A brief overview of the Boundary Element Method (BEM) has been presented for applicaiton to acoustic field problems, specifially those involving a single point source above a ground surface of abitrary form. Results from BEM will be used extensively as a reference method with which to compare the techniques discussed henceforth using an existing program written by Dr. Taherzadeh of the Open university. This program is restricted to 2d problems and so a 3d program supplied by Dr. Anton Krynkin from Sheffield university was adapted in an attempt to tackle 3d problems involving the doubly periodic latticed ground surfaces. However, the computational resources required were unrealistic as was the implementation of suitable optimisations and as such could not be applied as a reference method. In this chapter, merely the fundamentals of BEM have been discussed, as the body of knowledge surrounding this method is vast.

4.2 Slit-pore effective impedance model

The slit-pore model is an established homogeneous ground impedance model which assumes the ground surface to be comprised of small, when compared to incident wavelength, parallel walled slits of a given depth backed by an acoustically hard layer. The slit-pore model yields a normalised impedance from specific complex compressibility $C(\omega)$ and density $\rho(\omega)$ functions thus,

$$Z_{SP}(h)=\left(\frac{1}{\rho_0 c_0}\sqrt{\frac{q}{\Omega^2}.\frac{\rho(\omega)}{C(\omega)}}\right)\coth\left(-i\omega h\sqrt{q\rho(\omega)C(\omega)}\right)$$

where for slit-pores,

$$\rho(\omega)=\frac{\rho_o}{1-\left((a/2)\sqrt{\omega/c_0}\sqrt{-i}\right)^{-1}\tanh\left((a/2)\sqrt{\omega/c_0}\sqrt{-i}\right)}$$

$$C(\omega)=(\gamma P_o)^{-1}\left(1+\frac{(\gamma-1)}{\sqrt{-iN_{pr}}(a/2)\sqrt{\omega/c_0}}\tanh\left(\sqrt{-iN_{pr}}(a/2)\sqrt{\omega/c_0}\right)\right)$$

N_{pr} = Prandtl Number ≈ 0.708

γ = Adiabatic gas constant ≈ 1.41 (4.28)

The derivation of this model is complex and omitted here in the interests of brevity but the reader is referred to [28] for a thorough explanation. The parameters used for the grooved grating structure are as follows,

Porosity, $\Omega = a/d$

Tortuosity, $q = 1$

Tortuosity is unity in accordance with the straight parallel rectangular grooves and the flow resistivity is calculated for slit shaped pores according to the equation,

$$R_S=\frac{2\mu q^2 s_0}{\Omega r_h^{\,2}}$$

μ = dynamic viscosity coefficient of air = $1.811e^{-5}$

s_0 = shape factor for slit-pores = 1.5

r_h = hydraulic radius for slit-pore = $a/2$ (4.29)

The slit-pore model is derived from analysing the thermo-dynamic behaviour of a plane wave propagating a closed bottomed grooved cavity. It therefore models two fundamental phenomenon which are the interference of the reflected wave with the incident wave at the aperture for the plane wave mode giving rise to an imaginary impedance and the losses due to thermo-viscous effects which manifest as a real part to the effective impedance. The interference effects are dependent upon the incident wavelength λ and the depth of the groove *h* and will exhibit peaks of destructive and constructive pressure interference at integer multiples of $h = \lambda/4$ and $h = \lambda/2$ respectively. These will manifest as an imaginary and hence lossless part of the effective impedance. The thermo-viscous effects will dominate in the realm where $\lambda >> a$ due to the relative extent of the boundary layers set up

on the sides of the groove. The porosity ratio a/d is applied as a factor to scale the effective impedance of the grooves to account for the hard top ledges either side of the grooves and provide a bulk effective impedance for the surface which will apply under the assumption that $\lambda >> a$ where the grooved structure can be considered as a homogeneous effective fluid.

4.3 Predicting the surface wave magnitude

For this work it is required to know the magnitude of the resulting surface that would be induced upon spherical wave excitation of a surface with normalised effective impedance Z_{eff}, in order to provide a reference with which to compare this particular aspect of the methods presented in due course. Ideally suited to this task is the work of Thomasson [52], who proposed a form of spherical reflection coefficient which includes a separate term describing the surface wave alone and given by,

$$|p|(x_R, z_R) = \frac{1-C(H)}{4} \cdot \frac{k}{Z_{eff}} \exp\left(\frac{-ik(z_S+z_R)}{Z_{eff}}\right) J_0\left(k\, z_S \sqrt{1-(1/Z_{eff})^2}\right)$$

$$\text{where } C(H) = \begin{cases} 1 \text{ if } \angle H < \pi/4 \\ -1 \text{ else} \end{cases}$$

$$\text{and } H = \sqrt{ikR_{ref}\left(\left(-\frac{z_S+z_R}{R_{ref}} \cdot \frac{1}{Z_{eff}} + \sqrt{1-\left(\frac{1}{Z_{eff}}\right)^2} \cdot \sqrt{1-\left(\frac{z_S+z_R}{R_{ref}}\right)^2}\right)-1\right)}$$

$$\text{and } c_{SW} = \text{Re}\left(\frac{c_0}{\sqrt{1-(1/Z_{eff})^2}}\right) \text{ and } k_{zSW} = \sqrt{k^2-(\omega/c_{SW})^2} \qquad (4.30)$$

The result is the pressure magnitude |p| of the surface wave component alone at the receiver location (x_R,z_R), given the source-receiver geometry and effective impedance of the ground surface Z_{eff}. The location of the source is at the co-ordinate (x_R,z_R) while R_{ref} is the reflected ray path length. The terms c_0, ω and k are the speed of sound in the medium, the angular frequency $2\pi f$ and propagation constant respectively.

CHAPTER 5 – Principles of sound propagation within a groove grating structure

In order to explore effective impedance models and to better understand modal-models it is necessary to understand the fundamental mechanisms by which wave motion is supported in the grooves of rectangular grating structures of the form shown in figure 5.1 [64-65]. Inviscid conditions will be assumed throughout this chapter so visco-thermal effects may be neglected which reduces the discussion to that of lossless wave-motion. Furthermore all surfaces will be assumed acoustically hard.

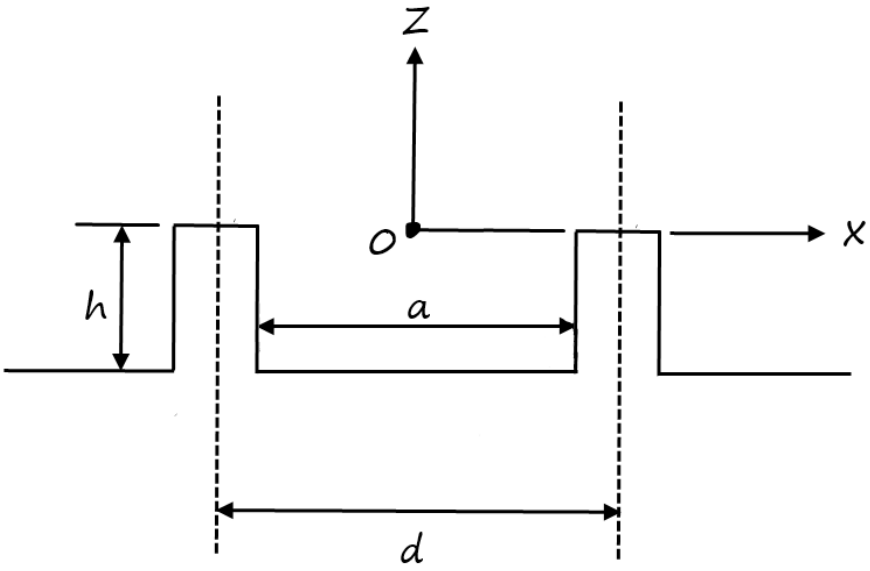

Figure 5.1 Periodic rectangular grooved surface.

For the infinitely periodic groove grating structure the excitation of modes within the grooves, termed '*n'* modes, by an incident source is complex. It depends not only upon the incident wave but also upon the free-space modes supported by the periodicity *d* of the structure and their interaction with the *n*-modes within the grooves at the aperture. The response also depends upon the impedance the groove presents at the aperture for each *n*-mode which is defined solely by the geometry in terms of the depth of the groove *h* and the *z*-direction wave number of mode *n*. The amplitude of each *n*-mode is affected by the incident wave and by the infinite set of free-space modes, but the free-space mode amplitudes are themselves dependent upon the set of *n*-modes along with their impedance and so on ad-infinitum to form a circular dependence between the free-space and groove bound *n*-modes. Non-orthonormality between the free-space and *n*-modes means that

each individual *n*-mode affects every one of the infinite set of free-spaces mode and vice versa. The complications resulting from the interdependence means that the modal model is solved numerically. The time convention of *exp(-iωt)* will be assumed but omitted for brevity throughout this thesis.

Each groove is akin to a waveguide and as such waveguide theory will apply to this problem [29]. Due to the boundary conditions imposed by the side walls and bottom surface of a groove only a discrete set of modes are supported for a given geometry. With the assumption that all surfaces are acoustically hard then normal velocity must vanish at the inside surfaces of the groove as must the derivative of normal pressure as in Eq. (5.1) where $d\mathbf{n}$ is the surface normal unit vector pointing into the surface [38].

$$v \bullet d\mathbf{n} = 0$$
$$\frac{dp}{d\mathbf{n}} = 0 \tag{5.1}$$

This enables the definition of the boundary conditions for each surface of the groove. Incidentally, the hard surface boundary conditions of Eq. (5.1) are the limiting cases of the general impedance condition of Eq. (5.2) for infinite surface impedance $Z_s=\infty$.

$$i\omega\rho_0 v \bullet d\mathbf{n} + \frac{dp}{d\mathbf{n}} = 0$$
$$v \bullet d\mathbf{n} = p / Z_s,$$
$$\therefore\ i\omega\rho_0 p + Z_s \frac{dp}{d\mathbf{n}} = 0 \tag{5.2}$$

The horizontal ledges either side of each groove $d/2>|x|>a/2$ at $z=0$ are hard flat surfaces requiring total reflection of any incident wave across their extent to meet the boundary conditions of Eq. (5.1). The response within the aperture of the groove at $z=0$ is more complex as it is the combination of the down-going waves excited by an incident source and the corresponding up-going components reflected from the bottom surface. This requires the wave solution of the boundary conditions of the groove side walls and bottom surface to yield the wave motion the groove is able to support while simultaneously accounting for how such sets of waves will be excited by an incident source across the groove aperture.

5.1 Infinite depth groove, h=∞

Consider first the boundary conditions of the groove side walls by assuming that $h=\infty$ so the bottom surface has no effect and only the down-going waves excited by a source at $z=0$ will exist within the groove. For the left hand side wall with reference to figure 5.1 the boundary conditions are,

$$-v \bullet \mathbf{x} = 0$$
$$-\nabla p \bullet \mathbf{x} = \frac{dp}{-d\mathbf{x}} = 0 \tag{5.3}$$

and for the right hand side groove wall,

$$v \bullet \mathbf{x} = 0$$
$$\nabla p \bullet \mathbf{x} = \frac{dp}{d\mathbf{x}} = 0 \tag{5.4}$$

Where the two are equivalent because the sign of the surface-normal vector does not matter due to the relevant quantities being equal to 0. Due to the vanishing normal pressure gradient at the walls, only standing wave solutions in x are admissible so it may be inferred that the groove will support an infinite set of discrete wave modes across the groove in the x-direction whose gradient vanishes at $|x|=a/2$. The solution to the side wall boundary conditions within the groove is satisfied by the function,

$$e_n(x) = \cos\left[\left(\frac{n\pi}{a}\right)\left(x+\frac{a}{2}\right)\right] \quad n = 0,1,2... \tag{5.5}$$

Standing waves may be considered as the superposition of pairs of identical travelling plane-waves propagating in opposite directions in the standing wave axis, x in this case. Each mode n is formed from a pair of plane-waves propagating the groove at a constant angle to the groove walls but with opposing directions in the standing axis. The result is a standing wave pattern perpendicular to the to the major axis of the groove (z in this example) as they reflect back and forth off the side walls while traversing the groove. As both waves propagate the groove in the same down-going direction the wave motion in z is that of a travelling wave with wave-number given by Eq. (5.6). The first five supported modes are shown in figure 5.2 where the dotted line represents a single ray-trace path of each plane wave and the colour gradient the time independent magnitude within the groove for each mode. Pure blue represents 0 magnitude whereas signal red is a magnitude of 2

signifying points of maximum destructive and constructive interference respectively as the modal wave pair traverses the groove. The total response within the groove is the linear superposition of all modes which will be excited with magnitude according to the incident source.

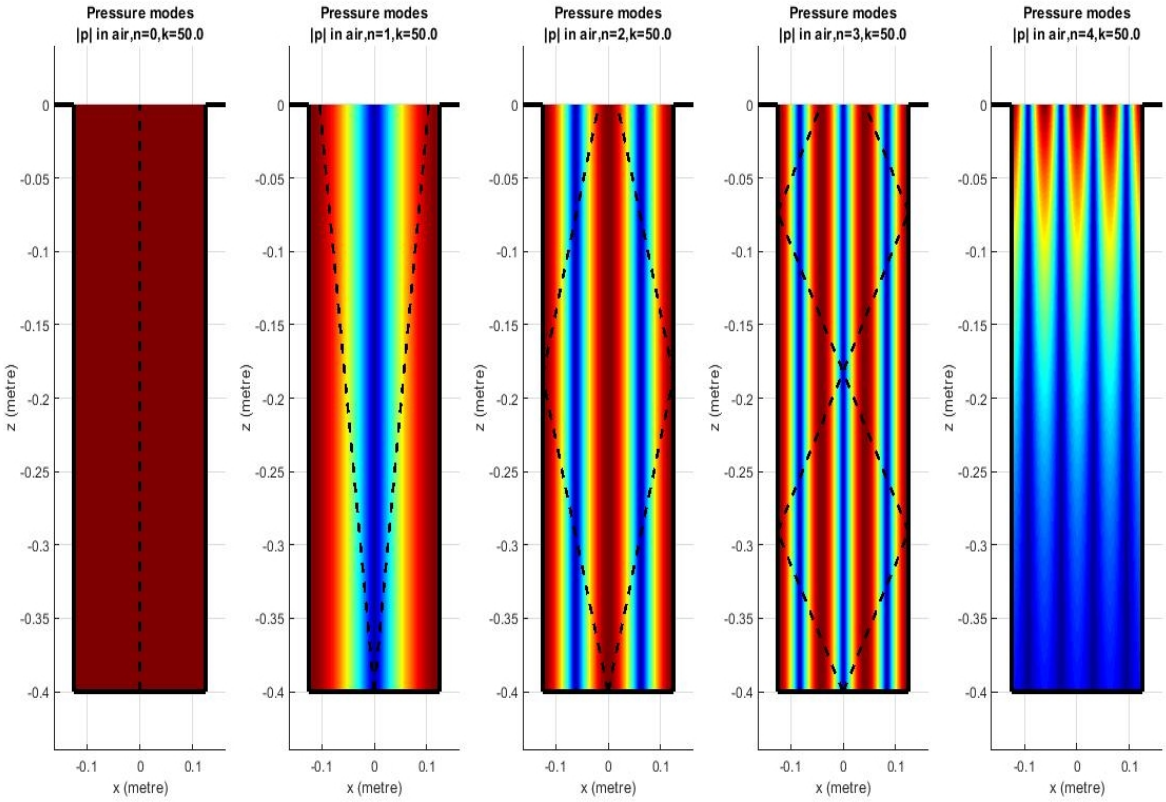

Figure 5.2 Horizontal Modes n=0 to n=4 supported by the h=∞ groove.

The medium within the groove is assumed to be that of the free space and so the resultant wave-number of each mode must be that of free space, *k.* The standing direction *x* and propagating direction *z* wave-number components k_{xn} and k_{zn} respectively, for each mode are given by,

$$k_{xn} = \frac{n\pi}{a}$$
$$k_{zn} = \pm\sqrt{k^2 - \left(\frac{n\pi}{a}\right)^2} \tag{5.6}$$

The positive signed case of k_{zn} refers to an up-going wave component in $+z$ and the negative case a down-going component in $-z$. Notice that when k_{xn} is greater than k_0, the propagating direction wave-number k_{zn} becomes imaginary and the mode no longer propagates the groove, instead decaying exponentially downwards from the aperture at

z=0. It is then said to be evanescent in z. The frequency at which a mode changes from being evanescent to propagating is known as it's cut-off frequency because below this frequency the mode is incapable of propagating in the groove and no sign of it's existence will be apparent at h=∞. Whereas all propagating modes will traverse the groove unhindered and indefinitely, given the inviscid assumption. As each mode traverses the groove at a specific angle given by the geometry of the groove and the order of the mode n, the group velocity will be different for each mode, always being less than that in free-space and being the slowest for the highest order modes due to the greater transverse component.

To explore the excitation of modes within the groove for which h=∞ consider a forced rigid source with normal velocity v_z function $s(x)$ across the top aperture of the groove at z=0. Examples are a rigid piston or vibrating membrane which forces v_z across the aperture to be that of the source which ensures that all energy is transmitted into the groove because reflections at z=0 are precluded by the rigid nature of the source. The combined response of the modes within the groove $v_z(x)$ must match that of the forcing source at z=0 and so the modal response within the groove to the forced source will be the Fourier series,

$$s(x) = \sum_n A_n \, e_n(x) = v_z(x) \quad n = 0,1,2... \tag{5.7}$$

where the infinite set of amplitude coefficients A_n are given by the inner product of the forcing source function $s(x)$ and the n'th modal characteristic e_n,

$$A_n = C \int_{-a/2}^{a/2} s(x)\, e_n(x)\, dx \equiv C < s(x), e_n > \quad n = 0,1,2...$$

where,

$$C = a^{-1/2} \quad n = 0$$

$$C = \left(\frac{2}{a}\right)^{1/2} \quad n > 0 \tag{5.8}$$

The constant C is to normalise A_n in order that it be unity when $s(x)$ and $e_n(x)$ are equivalent functions. The resultant acoustic pressure p, at the aperture will be given by the superposition of all n-modes multiplied by their v_z related impedance as given by,

$$p(x) = \sum_n A_n \, Z_n \, e_n(x) \quad n = 0,1,2... \tag{5.9}$$

Where Z^O_n relates the v_z of each mode to the resultant pressure p at any given point and is given by,

$$Z_n^O = Z_c \frac{k}{k_{zn}} \tag{5.10}$$

where $Z_c=\rho_0 c_0$ and is the characteristic impedance of the inviscid air medium. Remember that this applies only to the case where $h=\infty$ and so only down-going modes are present with no bottom surface reflections.

For many problems the source is itself an incident wave which does not successfully approximate to a rigid piston or membrane. Replacing a forced source with an incident wave source complicates the problem because a proportion of the incident energy will now be reflected at the aperture and a proportion transmitted into the groove and the inner product relation of Eq. (5.8) no longer holds. This is because the v_z function at the aperture is no longer fixed by a rigid source and hence the resultant v_z and pressure at the aperture on $z=0$ will be given by the combination of the incident, transmitted and reflected components. The latter two components being given by the resultant impedance of the groove at $z=0$. For problems comprising solely of one groove mode ($k<<a$ for instance where only $n=0$ is dominant) all wave components within the groove share a common spatial frequency across the aperture meaning that the impedance across the aperture is in invariant in x. In such cases the groove impedance Eq. (5.10) may be applied to an appropriate reflection coefficient formula [37] to obtain the reflected and transmitted components to solve for the pressure and v_z fields. However when multiple groove modes are considered the impedance across the mouth of the groove aperture will not be constant due to the combination of different spatial frequencies across the aperture so the impedance across the mouth of the groove is dependent upon x and the reflection coefficient of [37] doesn't strictly apply. Furthermore the magnitude of excitation of each groove mode also depends upon the modal component present in the incident source which creates a highly interdependent and complex problem primarily involving $\langle s(x), e_n \rangle$ and Z_n for each mode n meaning that the modal-model is solved numerically.

5.2 Finite depth groove, h<∞

If the bottom of the groove is at $z=-h$ there will be reflections of the down-going modes, forming a set of equivalent up-going modes with the same propagation characteristics save

for a sign inversion of k_{zn}. This creates a standing wave pattern in z with a node in v_z and anti-node in pressure at z=-h for each mode n due to the boundary conditions imposed by the hard bottom surface of,

$$-v \bullet \mathbf{z} = 0$$
$$-\nabla p \bullet \mathbf{z} = \frac{dp}{-d\mathbf{z}} = 0 \tag{5.11}$$

Combined with the reflections of the side walls there now exists standing wave patterns within the groove in both x and z directions. This is shown in figure 5.3 as an idealised pressure magnitude plot of the supported modes within a lossless closed end rectangular cavity of given dimensions. In addition a representative ray-trace path of the wave fronts are included to provide insight in to the various angles of propagating plane wave components.

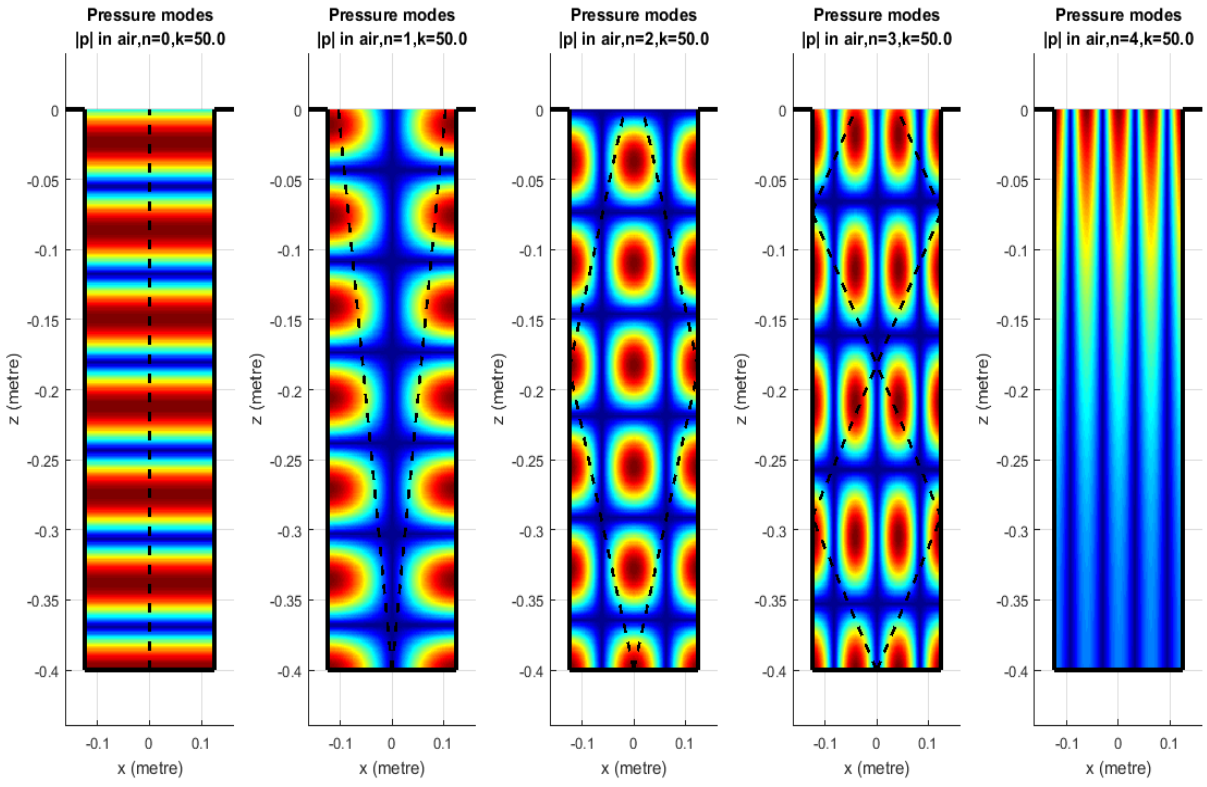

Figure 5.3 Pressure magnitudes within cavity of dimension a=0.25, h=0.4 at 2730 Hz.

Mode n=0 is the only axial mode, propagating solely in z where higher order modes are transverse having both x and z components. In this example the mode n=4 is evanescent, which does not propagate in the groove as the incident frequency in this case is below the

cut-off frequency of mode n=4. At this frequency of 2730 Hz the wavelength is approximately 0.126 m representing just over half the aperture width hence the four propagating modes. Each mode has a horizontal x-axis component with a wavelength multiple of 2a. In this illustration mode n=4 is close to propagating and would do so once the incident wavelength contracts below (2a)/4.

The effect the closed bottom has on the effective impedance at the aperture z=0 will be discussed. The impedance across the aperture at z=0 for each mode n is given by the superposition of the normal velocity v_z and pressure p down-going and up-going plane wave mode components within the groove as,

$$Z_n = \frac{p_n^- + p_n^+}{(v_{zn}^- + v_{zn}^+) \bullet d\mathbf{n}} \quad z = 0,\ h < \infty \tag{5.12}$$

The up and down-going components are denoted by + and – superscripts respectively. Unity amplitude is assumed for each component which is valid as the model is lossless and ratio-metric in terms of characteristic. Each term is expanded in turn beginning with the down-going velocity component at z=0,

$$\begin{aligned} v_{zn}^- &= \exp(ik_{zn}^- z) \\ &= 1 \qquad z = 0 \end{aligned} \tag{5.13}$$

The down-going pressure component can be deduced from v_{zn}^- and its impedance relationship of Eq. (5.10) thus,

$$p_n^- = v_{zn}^- Z_C \frac{k}{k_{zn}^-} \quad z = 0 \tag{5.14}$$

The up-going components are the reflections from the bottom surface of the groove and hence will have travelled the full depth of the groove twice. The reflected component of velocity is expressed as follows where the -1 factor accounts for the phase inversion upon reflection from the bottom and the two '*exp*' phase factors accounting for the downward and upward traverse respectively,

$$\begin{aligned} v_{zn}^+ &= \exp(ik_{zn}^-(-h))\exp(ik_{zn}^+ h)(-1) \\ &= -\exp(ik_{zn}^+ 2h) \quad z = 0 \end{aligned} \tag{5.15}$$

The expansion is completed with the reflected pressure component where the $Z_C(k/k_{zn}^+)$ term remains positive as this component is up-going,

$$\begin{aligned} p_n^+ &= v_{zn}^+ Z_C \frac{k}{k_{zn}^+} \\ &= v_{zn}^+ Z_C \frac{k}{k_{zn}^+} \quad z = 0 \end{aligned} \tag{5.16}$$

Substituting these expansions into Eq. (5.12) gives the impedance at the aperture of the groove z=0 for each mode n,

$$Z_n = \frac{Z_C \frac{k}{k_{zn}^-} - \exp(ik_{zn}^+ 2h) Z_C \frac{k}{k_{zn}^+}}{\left(1 - \exp(ik_{zn}^+ 2h)\right) \bullet d\mathbf{n}} \tag{5.17}$$

Noting that $\bullet d\mathbf{n}$ equates to -1 because v_z is already normal velocity so all that is required is a sign inversion to account for the impedance being defined as normal velocity into the surface [38] which is -z in this model. Factoring as well then yields,

$$Z_n = \frac{Z_C k}{k_{zn}^+} \frac{-1 - \exp(ik_{zn}^+ 2h)}{-1 + \exp(ik_{zn}^+ 2h)} \tag{5.18}$$

noting that the leading unity term in the numerator is negated because we have factored with the positive k_{zn}^+ term whereas the leading numerator term relates to the negative k_{zn}^- and the relationship of k_{zn}^+ to k_{zn}^- is just -1. Making use of trigonometric identities the equation for the surface impedance at z=0 across the aperture of the groove for each mode n is,

$$Z_n = i \frac{Z_C k}{k_{zn}^+} \cot(k_{zn}^+ h) \tag{5.19}$$

This equation appears frequently in literature as the normalised impedance for a hard-backed layer. Figure 5.4 shows the normalised Impedance Z_n of a propagating mode (real k_{zn}) as a function of frequency for a groove. The impedance is purely imaginary. Notice that as $k_{zn}/h \rightarrow 0$ the response $Z_n \rightarrow \infty$ as would be expected as the phase shift of the mode traversing the groove tends to zero and so the impedance at the groove aperture appears as a hard surface at z=0. This is especially relevant for the zeroth mode as it propagates under

all conditions. As the resultant phase shift at the aperture becomes significant the response exhibits the periodic '*cot*' like features as the interference of the down-going and up-going components cycles periodically between constructive and destructive. When the phase shift between up- and down-going components k_{zn}/h, equals $m\pi$ (m=0,1,2...) then Z_n will exhibit a maximum as the pressure will constructively interfere while the velocity which changes direction at the bottom of the groove will be at a minimum. Conversely Z_n will be zero when $k_{zn}/h=m\pi+\pi/2$ where the pressure cancels and the velocity constructively interferes at z=0.

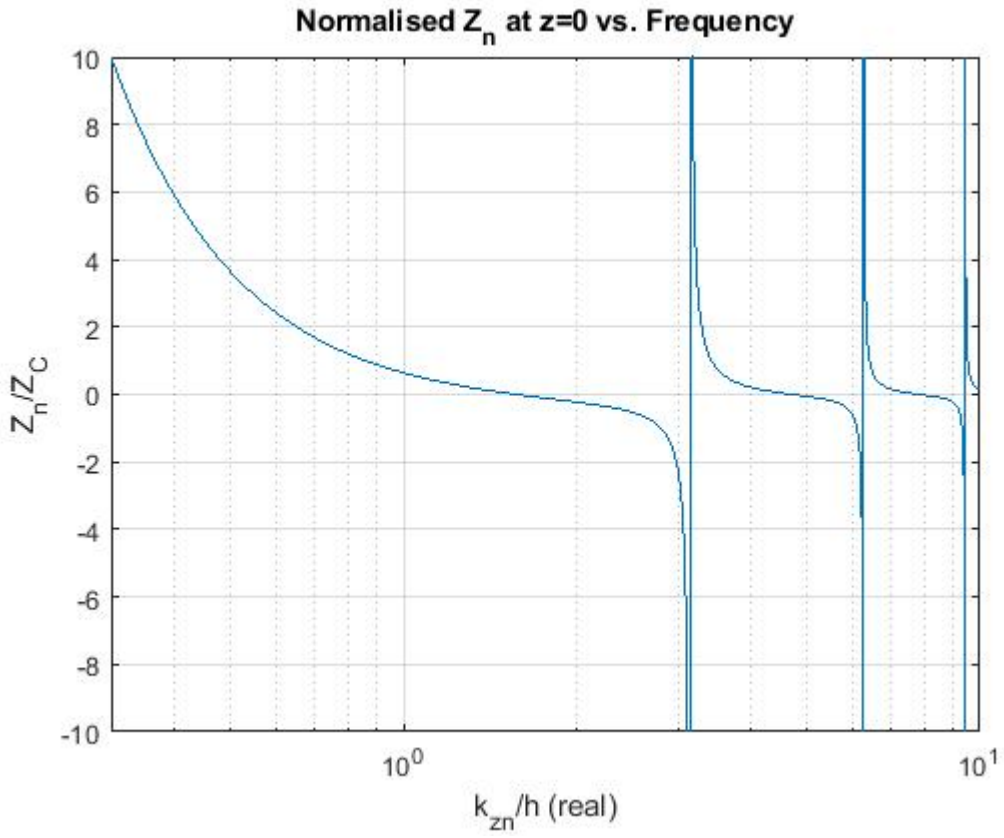

Figure 5.4 Normalised groove Impedance at z=0 assuming mode is propagating (real k_{zn}).

In summary, closing the bottom of the groove has introduced the '*i cot()*' term into Z_n which accounts for the periodicity of the impedance function caused by the standing wave pattern in z and the imaginary component introduced because of the interaction with the down-going and up-going vector velocity but scalar pressure components. The periodicity for each mode n being dependant upon h and k_{zn}. The equation for Z_n holds regardless of whether k_{zn} is real valued and propagating or imaginary and evanescent. Intuitively the

impedance of the lossless closed bottom groove must be purely imaginary as for all cases when $h<\infty$ energy inflow must equal energy outflow otherwise it would indicate a loss or energy accumulation within the groove. Whereas for the open bottom case when $h=\infty$ the impedance would have a real component caused by modes which propagate the groove and appear as a loss as they traverse the infinite groove downwards in $-z$ while evanescent modes contribute an imaginary part to the impedance as all energy must be reflected back out of the groove albeit with a phase shift as energy is transferred between the free-field and evanescent mode.

5.3 Evanescence

When the frequency of the incident wave is below the cut-off frequency for mode $n>0$, then that mode will not propagate the groove and will be evanescent in z. The evanescent mode does not propagate in z and as such energy does not traverse the groove in a geometric manner. However energy is transferred from the incident wave into the exponentially decaying disturbance and subsequently released into free-space as a reflected wave at a later time. The energy transfer between incident and reflected waves via the energy temporarily stored in the evanescent wave, causes a phase shift of the reflected wave and is known as the Goos-Hänchen effect [44].

For a given mode $n>0$ at a frequency much less than its cut-off frequency, the evanescent decay will be rapid with a short evanescent wave that leads to the aperture acting increasingly like a zero impedance pressure release surface as frequency decreases. Conversely as the frequency approaches cut-off the evanescent length tends to infinity and the impedance will be infinite at cut-off and the aperture behaves as a hard surface. Figure 5.5 shows the impedance for mode $n=1$ in its evanescent realm for a range of groove depths, h.

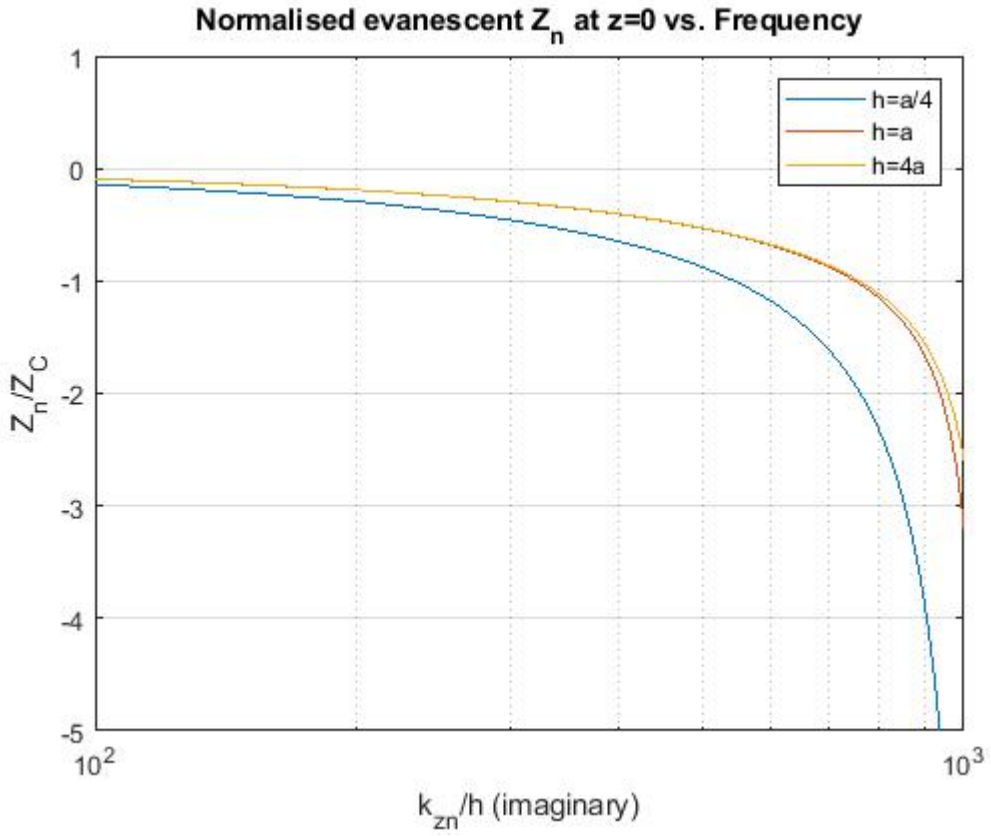

Figure 5.5 Normalised groove Impedance at z=0 in the evanescent region (imaginary k_{zn}).

Notice when *h* is small that the bottom surface of the groove is exerting a large influence over the impedance as the evanescent disturbance is reflected from the bottom surface and interferes with itself at the aperture resulting in an increase in the magnitude of Z_n. The evanescent mode does not propagate in the *z*-direction and so all interference between the primary and reflected components must be constructive as there will be no phase variation in *z*. The phase of the evanescent mode varies only in *x* as it 'creeps' along the impedance boundary at *z*=0 in synchronisation with the free-space field which could be an incident source or a surface wave propagating in the absence of source excitation. As *h* is increased the impedance will tend to that of an open bottomed groove and the effect of *h* diminishes as the reflection from the bottom surface has less and less effect due to the attenuation of the evanescent mode with distance. The deeper the groove the lower the amplitude of the evanescent reflection due to the imaginary wave-number in *z*.

5.4 Cavity resonance

The closed bottomed groove will act as a resonant cavity when excited by a source, which

in this case is an incident wave at the aperture with wavelength λ. Incident energy will excite modes within the groove as discussed which if propagating will reflect from the bottom surface and form a standing wave within the groove and interfere with the incident wave at the aperture. When the *z*-axis wavelength of the propagating mode within the groove (see figure 5.1 and as given by $2\pi k_{zn}$) is an integer multiple of $4h$, the lowest frequency of which is the quarter wavelength resonance, then the pressure interference at the aperture will be destructive but will be constructive for odd integer multiples of $2h$. The up-going pressure wave reflected from the bottom of the groove will encounter a pressure release surface at the aperture and a portion will be reflected back into the groove.

However, the pressure wave reflected by the impedance mismatch at the aperture will not be abrupt and will in fact penetrate the free-field to some extent. The pressure wave at the aperture may be considered to be an oscillating piston exciting the free-field with an effective complex radiation impedance [45]. The portion of imaginary impedance represents reflection and the creation of evanescent field in free-space which decays exponentially with radial distance from the aperture and the real portion represents a component radiated into the free-field as a propagating wave. The apparent reflection at the aperture on $z=0$ will therefore exhibit a phase shift due to evanescent field [44] which can be modelled as an apparent increase in h proportional to the aperture width a. The apparent overall length for the calculation of resonant responses becomes $h=h+Ka$ where Ka is known as the end correction factor. Such interaction can be considered as an extra column of fluid akin to an increase in length. This effect is often known as 'organ pipe' resonance because the tubes used for musical pipe organ notes are in fact shorter than would be expected due to this effect. It is a well documented concept [49] which need not be repeated in detail here.

It has been suggested by Berry et al. [56] that there is a direct connection between the resonant frequencies of a cavity, which are ‘organ pipe’ resonances and the frequency of the surface waves supported by a periodic grating structure of such cavities.

In contrast to the end-correction just discussed which adds to the effective length of a cavity in isolation, the work of Hurd [2] explored electromagnetic surface waves above an array of closely spaced rectangular grooves and found the opposite to be true, that the effective length of the each groove shortens. Under the conditions of $a=d$ and considering

only the plane wave mode within the groove by assuming that $\lambda >> a$, then the effective depth of an individual groove h, is foreshortened in a manner related to the ratio a/h. Specifically it leads to the result that the effective depth h^H for the purposes of calculating resonant effects of rectangular grooved gratings may be approximated by,

$$h^H = h - \frac{a}{\pi}\log(2) \tag{5.20}$$

This correction was proposed in modelling the acoustic impedance of closely spaced grooves by Kelders-Allard et al. [8] and will be applied successfully later in this thesis. However Hurd's correction will always yield an effective reduction in the effective length (h in this case) of the groove which is at odds with the classic 'organ pipe' resonance effect.

Once many cavities are placed in close proximity to form a periodic structure, the interaction between adjacent cavities becomes significant and it seems that one can then no longer rely solely upon a simple length correction alone such as the 'organ pipe' effect to predict the combined effect, even for 'long' length ($h >> a$) cavities. In fact the problem becomes so complex that numerical models such as BEM or modal-models are required to solve the resulting fields from arrays of closely spaced uniform cavities. The aforementioned techniques inherently consider the mutual interaction between the cavities and the free-field, which facilitates coupling via the free-field of adjacent cavities. This is why the complex models such as BEM or modal-model successfully predict the response even at the extremes of 'short' ($h << a$) cavities whereas the simple impedance based models such as those presented in this thesis cannot, so require depth corrections to improve performance, namely that suggested by Hurd [2]. The Hurd correction was derived for an equivalent problem in electromagnetics for arrays of closely spaced cavities whereas the 'organ pipe' effect is an acoustic one for a cavity in isolation. The assumption of an inviscid air medium which is free from viscous and inertial effects is akin to the electromagnetic case whereas the 'organ pipe' effect is an inertial phenomenon due to the particle displacement in acoustic waves. Bougdah et al.[36] considered many factors involved in the complex response of closely placed cavities including quarter-wave resonance effects, but it may be concluded that the response cannot be successfully explained by any one phenomenon alone as is often possible for a single cavity in isolation.

5.5 Summary

Within this chapter the acoustic propagation within an ideal rectangular groove has been presented from first principles. The groove is considered to behave as an acoustically hard waveguide with a hard bottom and so the resulting impedance at the aperture of the groove is the combination of the incident wave and the components reflected from the bottom. Due to the nature of the structure, an infinite set of discrete modes will be supported, each with its own propagation characteristic. All but the lowest order modes will be evanescent and the effect or such modes is considered. Furthermore, existing end correction methods have been considered both for a groove in isolation and for an array of closely spaced grooves which locally interact.

CHAPTER 6 - The two dimensional modal model

6.1 Theory

6.1.1 Introduction

The aim is to calculate the field scattered by a perfectly conducting rectangular groove grating from a single incident plane wave. The grating structure is periodic and consists of a linear array of identical cells where each cell is one cycle of the structure as shown in figure 6.1. The structure is assumed to extend infinitely in $\pm x$. Furthermore the structure is considered invariant in y so that the structure extrudes without bound in $\pm y$. Given this and the assumption that the incident wave propagates in the x-z plane allows the problem to be reduced to one of 2-dimensions. The modal-model is numerical as closed form solutions are not known.

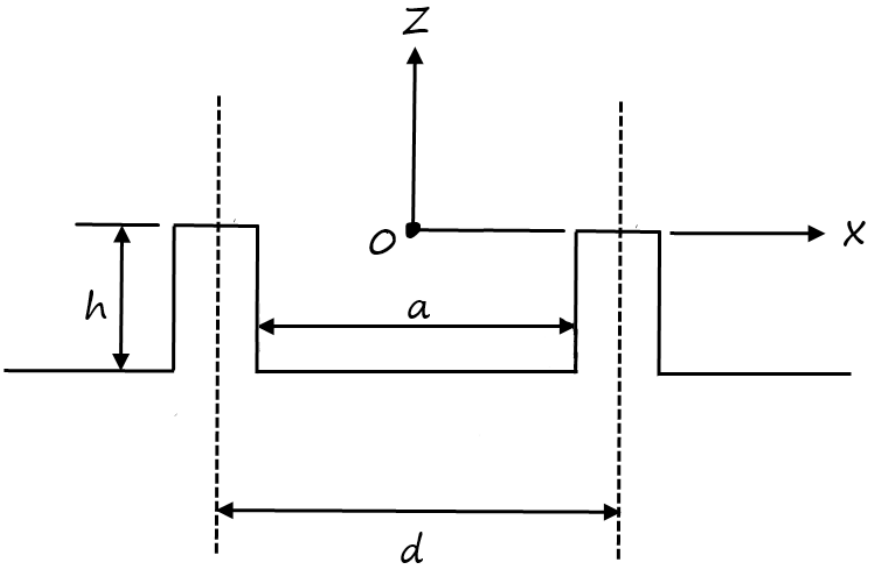

Figure 6.1 Rectangular groove grating structure.

The groove will behave in a waveguide like manner. The plane wave mode will be the sole propagating mode at incident wavelengths much greater than the aperture feature size a, with higher order modes being excited as the wavelength becomes comparable to or less than a. This causes the incident wave to set-up standing modes within the groove. The grating pitch d, will dictate the geometry of the scattered field while the complex nature of the modes within the waveguide like groove will affect the complex amplitude

of the diffracted field. Propagating modes traversing within the groove will be reflected at the bottom surface, $z=-h$ and diffracted at the surface $z=0$ into free space $z>0$ at the aperture. The diffraction pattern will be complex in nature and exact analysis is not required for the purposes of this investigation. The reader is referred to the Huygens-Fresnel principle [24,25] for further insight. Due to the periodic nature of the structure and continuity of the incident wave in x, then each cell will behave in the same way save for a phase shift proportional to the feature pitch, d. It is known that interference between the fields scattered by each cell will combine to produce a discrete set of infinite diffraction modes in free-space, $z>0$.

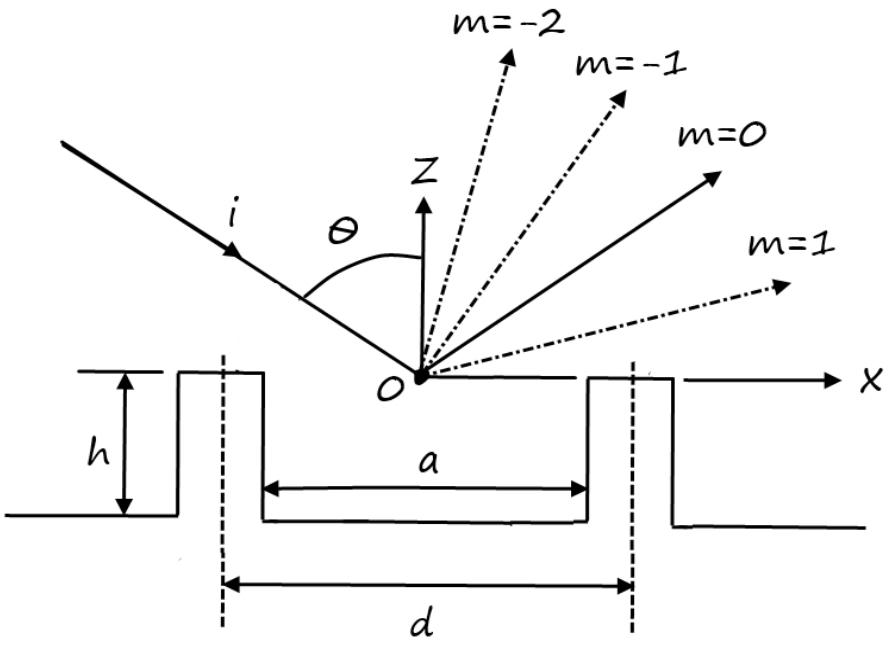

Figure 6.2 Diffraction modes scattered by grating surface.

This type of problem has been studied for Electromagnetic waves for over a century and many approaches have been taken to solve the resulting fields. In this chapter the modal model will be based upon the analysis presented by Hessel in 1975 [6] for the electromagnetic case and adapted to Acoustics by Kelders-Allard and Lauriks in 1998 [8]. This method is founded on the principle that the problem is periodic and can be described by orthonormal Bloch wave modes which can be superposed to form an approximate solution to the free space field. It is also possible through periodicity of the problem to solve by considering just the behaviour of one cell in isolation which simplifies the computational requirements. Furthermore, plane-wave incidence is assumed.

The known quantities of the problem are the characteristics of the incident wave having wave-number k and angle of incidence θ, along with the geometry of the grating structure. From this the amplitudes of the standing wave modes within the apertures of the groove at $z=0$, known as n-modes, excited by the incident wave can be computed using numerical methods. The infinite set of harmonic n-modes within the aperture provide the boundary conditions at z=0 within the aperture of the groove where $|x|<a/2$. For the remainder of the cell outside of the aperture window, $d/2>|x|>a/2$, the boundary conditions at z=0 are simply those of a perfectly reflecting surface. These combined yield the boundary conditions for a cell of the grating structure.

The free-space field is modelled as an infinite set of free-space diffraction modes, termed m-modes, describing the field in free space where $z>0$. The infinite set of n-modes provide the complete set of boundary conditions to which the free-space m-mode amplitudes are matched at the boundary z=0 to yield the free-space field solution. Therefore the solution to the problem is the calculation of the set of complex amplitudes for all n and m-modes. The m-modes are pseudo periodic Bloch waves [26] with periodicity of the cell period, d, multiplied by a common phase term due to the variation of the incident wave in x. This represents a Floquet type problem with periodicity in x as,

$$\Psi(x+Cd) = \exp(i\,k_{xm}\,x)\psi(x+Cd) \quad C = 0,1,2...\infty \tag{6.1}$$

Where the *exp()* term is the periodic in d term representing the modes induced by the grating with wave-number k_{xm} and $\psi()$ the incident term which is not periodic in d.

The complex amplitude of each m-mode is calculated so that the set of m-modes combine to satisfy the boundary conditions at z=0 as given by the n-modes where $|x|< a/2$ and the reflective surface element where $d/2>|x|>a/2$. The orthonormal nature of the problem allows each m-mode to be approximated by the inner product its own mode function and sum of all n-modes. Following the definitions given by Hessel [6] and Kelders et al. [8] the inner product of functions *f(x)* and *g(x)* is defined in Eq. (6.2), where *f(x)* and *g(x)* are spatial functions of an m or n mode [1]. Where the integration limits are the extents of the aperture a and not the full grating pitch d, because the hard ground portions outside of the aperture contribute nothing to the integral as the n-mode velocity component will be zero

1 This differs from the standard inner product definition where *g(x)* is conjugated, but is used to ensure continuity with previous work.

in this region of the groove ledges.

$$< f(x), g(x) >= \int_{-a/2}^{a/2} f(x).g(x)\, dx \tag{6.2}$$

The complete set of complex amplitude coefficients of the *m*-modes, which can be considered as the basis functions of the free-space region $z>0$, yield the free-space field solution due to the scattering of the incident wave by the grating. In Hilbert space [27], which this problem occupies, the infinite set of basis functions can be combined to produce any other function within that space. It requires that the basis functions, *m*-modes in this case, are orthonormal. Which indeed they are. The geometry of the diffraction modes (see figure 6.2) is governed by the period *d*, of each cell and the angle of incidence and propagation constant of the incident wave. Most *m*-modes will be surface waves which are evanescent in *z*. Under appropriate conditions some *m*-modes will propagate into free space which correspond to the diffraction modes detailed in figure 6.2. Where $m=0$ is usually termed the 'specular reflected' component as angle-of-Incidence equals angle-of-reflection for this mode even though the concept of specular reflection needs careful qualification where the feature dimensions are larger or comparable to the wavelengths involved.

The problem is divided into considering the fields in free-space $z>0$, and lower waveguide space where $z<0$, separately. Continuity is maintained by equating the resultant surface-normal velocity of the complete set of free space *m*-modes with the boundary conditions given by the cell structure and *n*-modes, also posed in terms normal velocity, at $z=0$ and across the *x*-extents of a periodic cell. The free-space scattered field may be expanded as the superposition of the infinite set of *V* amplitude weighted Bloch-Floquet plane-wave *m*-modes ψ_m as,

$$\Psi(x,z) = V_i\psi_i + V_r\psi_r + \sum_{m\neq 0} V_m\psi_m \quad z \geq 0, t = 0$$
$$\Psi(x,z) = V_i \exp\left(ik\left[x\sin\theta - z\cos\theta\right]\right) + V_r \exp\left(ik\left[x\sin\theta + z\cos\theta\right]\right) + \sum_{m\neq 0} V_m \exp\left(i\left[\alpha_m x + \beta_m z\right]\right) \tag{6.3}$$

where the sub or super scripts '*i*' refers to a parameter of the incident wave, '*r*' the $m=0$ specular reflected component with α and β being the modal wave number components in *x* and *z*. The Floquet periodic nature the problem is such that the field at $z=0$ exhibits a

periodicity in *d,* combined with a phase constant term of the incident wave, evident in the definition of α and β.

$$\alpha_m = k\sin\theta + \frac{2m\pi}{d}$$
$$\beta_m = \sqrt{k^2 - \alpha_m{}^2} \tag{6.4}$$

This model is purely linear with a homogeneous plane-wave source meaning that all modes will have the same temporal frequency and wave-number as the source. Deviations in temporal frequency could only be caused by non-linearities of which there are none in this model as we assume an invariant ideal inviscid air medium which has a constant speed of sound and our boundary surfaces are linear in nature. The resultant magnitude at a given point in the free-space field is the vector sum of all modes, which can be considered as phasors. As one moves in space, the total field magnitude will vary due to the phasor relationships between the modes because each mode will exhibit its own combination of *x* and *z*-axis wave-number components depending upon its angle of propagation. However, at a given point in space the phasor relationships between all modes remains fixed because the value of each phasor is a function of space and their relative relationships will not change with time. Bringing in the time dependence will cause each modal phasor to rotate around the complex circle at the rate ω, but because of our linear assumptions each phasor must rotate at the same rate, maintaining a constant relative relationship between all phasors and causing the magnitude of the resultant vector to remain constant and invariant in time. The instantaneous field magnitude will be given by the Real part of the vector sum but the time invariant portion is given by just its magnitude which is a function of space but not time. This assumption could not be made were the model composed of modes with different temporal frequencies.

The modal-model must be solved numerically due to the complex interdependence of the parameters therein. Specifically because of the coupling between the free-space *m*-modes and groove-space *n*-modes supported by the given geometry. Although the *m* and *n*-modes are locally orthonormal within themselves (one mode does not excite any other within the set) they are not orthonormal to each other which is why the modal-model model cannot be solved analytically. The magnitude of every mode within the system is dependent upon every other so they cannot be isolated and solved independently. The non-orthonormailty between the two modal sets causes local orthonormality within each set to break down.

Each mode within a set becomes coupled to every other within the same set through its interaction with the other set. For instance an excitation of mode n=1 will effect every mode within the m-mode set due to non-orthonormality. Because each m-mode will then effect every n-mode we have effectively coupled mode n=1 to every other n-mode via the non-orthonormal interaction with the m-mode set. This in turn then affects each m-mode once more, coupling all m-modes within the set due to their interaction with the n-modes. The cycle then continues ad-infinitum.

6.1.2 Forming the linear matrix – The 2d modal model for acoustic applications

Given our discussions in the introduction to this method it is apparent that the modal method may and has been applied to acoustics. To reiterate, the fundamental premise of the method remains; plane waves are assumed throughout requiring that no sources or sinks exist in the domain of the problem. Furthermore we assume a lossless system. Periodicity of the structure means that the fields in each cell are identical save for a phase shift of $kd\ sin\ \theta$ per cell. This allows the problem to be reduced to that of solving for one cell in isolation with extent $d/2 \geq x \geq -d/2$ so as to be evenly symmetric about the origin at $(x,z)=(0,0)$.

For the application of the modal model to acoustics we must build the model from the fundamental consideration of the boundary conditions given by a single cell of the grating structure which consists of the groove itself which is flanked by flat 'ledges' either side. The structure is defined to be continuous in the x-axis and so the boundary conditions will be posed in terms of continuity of z-axis velocity v_z at z=0. The primary focus will be on velocity components normal to the structure boundary at z=0 and pressure then related to this via impedance relationships later in the process. Therefore the incident wave and all of the m and n-modes will be formed in terms of v_z. The boundary conditions for velocity are hence,

$$\begin{aligned} &v_z(x,0-\delta_z) = v_z(x,0+\delta_z) \quad |x| < a/2 \\ &v_z(x,0) = 0 \quad d/2 > |x| > a/2 \end{aligned} \tag{6.5}$$

where δ_z represents an infinitesimally small increment in the z-axis. Qualitatively this is simply stating that the v_z particle velocity must be continuous at the boundary z=0 within the waveguide aperture and vanish at the acoustically hard boundary ledges either side of

this. The x-component of velocity v_x, which is the tangential part need not be constrained as we are assuming an inviscid fluid with no viscous forces. The lack of shear force at the boundary z=0 allows the tangential slip to be undefined and therefore unbounded in magnitude.

The boundary condition for acoustic pressure within the aperture is continuity of pressure as otherwise a discontinuity would have an infinite pressure gradient inferring an impossible discontinuity in velocity. Outside of the aperture at the hard boundary a vanishing pressure gradient in z is required. Expressing this boundary condition for pressure gives,

$$\begin{aligned} &p(x,0-\delta_z) = p(x,0+\delta_z) \quad |x| \le \frac{a}{2} \\ &\frac{d}{dz}p(x,0) = 0 \quad d/2 > |x| > a/2 \end{aligned} \tag{6.6}$$

where p is the scalar acoustic pressure.

As an interesting comparison between the acoustic and electromagnetic case, the acoustic wave velocity has been substituted for the electric field and pressure allied to the magnetic field. This may at first appear counter intuitive as we are equating a force to an effective flow and vice versa but in fact the transposition is arbitrary as the EM and Acoustic cases are separate and valid in their own cases so long as the correct relative relationships are maintained, specifically via impedance.

The modal model constitutes a linear system and as such all component waves have the same time frequency f, as the incident wave and hence $\omega=2\pi f$ is a constant throughout. Henceforth a time dependence convention of $exp(-i\omega t)$ will be adopted in line with Kelders-Allard-Lauriks work [8] and as commonly used by physicists.

6.1.3 Acoustic free space field, z>0

The free-space field in the realm z>0 is modelled as a superposition of the incident wave, with known amplitude and angle of incidence θ, and the infinite set of Bloch-Floquet [26] spatial harmonics, m-modes. These are eigenmodes of the cell period d, multiplied by the phase term related to the spatial frequency of the incident wave. Solving the complex

amplitude $\hat{V}_m$, of each *m*-mode is the aim of the modal-model as this yields the solution to the free-space field. By convention and to avoid confusion, free-space field variables will be denoted by the hat '^' to distinguish them from their namesakes applying to the lower waveguide space of $z<0$ (to be defined in the next section). The free-space field can therefore be expressed in terms of the *z*-component of acoustic particle velocity v_z thus,

$$v_z(x, z \geq 0) = \hat{V}_0^i \hat{e}_0 \exp(-i \hat{k}_{z0} z) + \hat{V}_0^r \hat{e}_0 \exp(i \hat{k}_{z0} z) + \sum_{m \neq 0} \hat{V}_m \hat{e}_m \exp(i \hat{k}_{zm} z) \tag{6.7}$$

Where the '*i*' and '*r*' annotations (incident and reflected) have moved to superscript to avoid confusion with set indices *m* or *n*. At the surface $z=0$ this equation reduces to;

$$v_z(x, 0) = \hat{V}_0^i \hat{e}_0 + \hat{V}_0^r \hat{e}_0 + \sum_{m \neq 0} \hat{V}_m \hat{e}_m \tag{6.8}$$

The $\hat{e}_m$ in the above equation is the *z*-component of the acoustic particle velocity for mode *m* at $z=0$, defined and discussed subsequently in Eq. (6.15). $\hat{V}_m$ is the *z*-direction velocity amplitude for mode *m* and is a complex quantity giving magnitude and a spatial phase offset relative to the origin $x=0$. $\hat{k}_{zm}$ is the *z*-axis wave-number of mode *m* given by,

$$\hat{k}_{zm} = +\sqrt{k^2 - \alpha_m{}^2} \tag{6.9}$$

where *k* is the wave-number of the incident wave and $\hat{k}_{zm}$ is always positive because propagation of scattered modes from the boundary at $z=0$ will be into free-space in the $+z$ direction. Mode $m=0$ represents the combination of the incident wave and specular reflected component whom share the same wave number magnitudes, which in *x* is given by the $k \sin \theta$ term. It tends to zero at normal incidence and to *k* at grazing incidence. At normal incidence $\theta=0$, there is no *x* component propagation of the incident wave whereas at grazing incidence $\theta=pi/2$ the incident wave propagates solely in *x* leading to zero *z*-direction velocity component.

It is evident that for $|m|>0$ the subtraction term in Eq. (6.9), which is the *x*-component wave-number of the *m*-mode, may exceed $|k|$ causing $\hat{k}_{zm}$ to be positive imaginary. This signifies an evanescent wave in *z* because the *x*-component wave-number exceeds *k* which precludes propagation in the *z*-direction. Otherwise $\hat{k}_{zm}$ will be positive real denoting a propagating wave in the $+z$ direction with phase velocity c_0. Due to $k=\omega/c$ relationship, the

phase velocity c, of an evanescent mode in the x-direction is less than the free field velocity c_0. This characteristic is consistent with a surface wave [28] although these evanescent m-modes are merely surface modes, existing and sustained only as a result of the incident field whereas true surface waves are capable of propagating in isolation and in the absence of an incident field [41 *p19*]. However, Kelders-Allard [8] do use the modal model matrix to solve for the characteristics of a true surface wave that could be supported by given groove grating geometry but this is a particular solution and outside of our scope. As part of the infinite m-mode set there will be modes propagating in both $+x$ and $-x$ directions which is expected qualitatively if one considers their origin as diffraction from the groove aperture.

The $\hat{k}_{zm}$, corresponding to mode m, will either be positive real denoting a wave propagating in z or negative imaginary where the mode is evanescent in z. The x-component velocity is inferred through the impedance relationships defined later which in turn is a defined by the incidence or diffraction angles. It is only the z-component of acoustic wave velocity which is of direct concern because the boundary conditions for the acoustics case are posed entirely in the normal axis which in this case is z. The x-component of the acoustic wave will be automatically satisfied by the composition of the final equations and inherent conservation of wave number constraints.

The wave-number in x is given by the m'th harmonic of the grating period d in addition to the phase term of projected the incident wave,

$$\hat{k}_{xm} = k\sin\theta + \frac{2m\pi}{d} \quad m = \ldots -3, -2, -1, 0, 1, 2, 3 \ldots \tag{6.10}$$

The $k \sin\theta$ term is the phase term of the incident wave m=0, projected on the x-axis and at z=0. The $\sin\theta$ term will vanish at normal incidence with no wave motion in the x-direction. Conversely at grazing incidence the wave will propagate entirely in x and the $\sin\theta$ term will accordingly be unity. The resulting m-mode x-axis wave-number $\hat{k}_{xm}$, may be positive or negative signifying the $+x$ or $-x$ direction of propagation. Both will occur due to the diffraction of the modes from the groove aperture. The unity amplitude characteristic of the m-mode function will therefore be of the form,

$$\exp(i\hat{k}_{xm}x).\exp(i\hat{k}_{zm}z) \tag{6.11}$$

where the complex exponential form is given as the spatial phase of the *m*-modes is not constrained by any boundary conditions in *x,* unlike the modes within the groove aperture which by nature are constrained to be standing waves. It just remains to normalise the modal function in order that its own inner product over the cell period *d*, is unity to ensure correct scaling of the final amplitude solutions. The reasoning behind this will become apparent in the later section when the set of system equations are defined. The normalising factor is derived thus, given that the self inner product of all of the *m*-mode functions is,

$$\int_{-d/2}^{d/2} \exp(i\hat{k}_{xm}x).*\exp(i\hat{k}_{xm}x)\,dx = d \tag{6.12}$$

Introducing a constant A and noting the conjugation in the second term,

$$\begin{aligned}
&\int_{-d/2}^{d/2} A\exp(i\hat{k}_{xm}x).A\exp(-i\hat{k}_{xm}x)\,dx = dA^2 \\
&\int_{-d/2}^{d/2} A^2\left(\exp(i\hat{k}_{xm}x).\exp(-i\hat{k}_{xm}x)\right)dx = dA^2
\end{aligned} \tag{6.13}$$

The normalising process must force the integral to evaluate to unity giving the normalising constant A of,

$$\begin{aligned}
A^2 &= \frac{1}{d} \\
A &= d^{-\frac{1}{2}}
\end{aligned} \tag{6.14}$$

The normalised mode function $\hat{e}_m$ introduced in Eq. (6.8) is given by,

$$\hat{e}_m = d^{-\frac{1}{2}}\exp\left(i\left[k\sin\theta + \frac{2m\pi}{d}\right]x\right) \quad z = 0 \tag{6.15}$$

The amplitude of each *m*-mode is given by the primary unknown set $\hat{V}_m$ and so the instantaneous value for mode *m* will be given at z=0 by $\hat{V}_m\hat{e}_m$. To provide a complete solution for the acoustic field both velocity and pressure components must be considered. Pressure can be deduced from the impedance relation,

$$\hat{p}_m = \hat{Z}_m \hat{V}_m \hat{e}_m \quad z = 0 \tag{6.16}$$

noting that each free-space *m*-mode has a unique impedance Z_m, which is implicit from the relationship between its *x* and *z* wave-number components. We must pause for a moment to consider a subtlety which occurs in the application of the modal model to acoustics. Due to only the *z*-component of velocity being defined in the mode functions (6.15) the resultant scalar pressure and hence impedance, must be dependent upon then angle of incidence θ in order to implicitly account for the *x*-component of velocity. At normal incidence θ=0 the acoustic velocity will exist only in *z* and so the pressure will be related to the velocity simply by the characteristic impedance Z_C, of the free-space medium,

$$Z_C = \rho_0 c_0 \tag{6.17}$$

where ρ_0 is the density and c_0 the speed of sound of air. As the angle of incidence is increased, relating the ratio of scalar pressure to v_z by just Z_C will result in a falsely low pressure due to the *x*-component of velocity being neglected. As the *z* and *x* wave-number components are co-sinusoidally related, a factor of $1/\cos\theta$ must be applied to the characteristic impedance to account for the vector nature of the velocity which is expressed in its simplest form as,

$$\hat{Z}_0^i = \frac{-Z_C}{\cos\theta} \quad 0 < \theta < \pi/2 \tag{6.18}$$

with Z_0^i being the impedance relationship of the incident wave, given by the free-space air medium. It is also assumed that a positive wave-number component in any axis denotes the wave component propagating in the positive direction of said axis. The impedance is therefore negative for the incident wave because in *z* the incident wave is propagating in the negative direction, which is downwards with reference to figure 6.1. Strictly speaking this is valid only for the *z*-direction as the wave could propagate in either direction in *x*. However for this application we are considering only the *z*-component of velocity and accounting implicitly for the magnitude of the *x*-component so its direction doesn't matter at this stage for the resulting pressure magnitude. We will assume that the incident wave propagates in the positive *x*-direction, left to right as in figure 6.1. Due to the change in *z*-direction upon reflection at the *z*=0 boundary, the reflected wave impedance is simply the negative of the incident,

$$\hat{Z}_0^r = -\hat{Z}_0^i \tag{6.19}$$

which results in a positive impedance magnitude due to the propagation of the reflected component in the positive direction in z.

The impedance for non-zero m-modes $\hat{Z}_m$, relates the z-direction wave-number $\hat{k}_{zm}$, to the resultant pressure which implicitly includes the x-axis component of velocity through the ratio of the incident wave-number k and the $\hat{k}_{zm}$ as follows. Given the relationship,

$$\hat{k}_{zm} = \frac{\omega}{c_m} \tag{6.20}$$

where $\omega=2\pi f$ and c_m is the phase velocity of mode m. Noting that,

$$\begin{aligned} &\omega = k\, c_0 \\ &Z_C = \rho_0 c_0 \\ &\therefore\ c_m = \frac{\hat{Z}_m}{\rho_0} \end{aligned} \tag{6.21}$$

allows the following recomposition to yield an expression for Z_m in terms of the known quantities of the problem.

$$\begin{aligned} \hat{k}_{zm} &= \frac{k\, c_0}{\hat{Z}_m / \rho_0} \\ &= \frac{k\left(Z_C / \rho_0\right)}{\hat{Z}_m / \rho_0} \\ &= \frac{k\, Z_C}{\hat{Z}_m} \\ \therefore\ \hat{Z}_m &= Z_C \frac{k}{\hat{k}_{zm}} \end{aligned} \tag{6.22}$$

Incidentally Kelders-Allard-Lauriks [8] state the following expression (their equation 20) for the incident wave impedance $\hat{Z}_0^i$,

$$-\hat{Z}_0^i = \frac{i\, Z_C}{\sqrt{\sin^2\theta - 1}} \tag{6.23}$$

which in the range $0<\theta<\pi/2$ between normal and grazing incidence, is equivalent to Eq. (6.18) except for the leading negative sign as Kelders-Allard-Lauriks [8] assume the opposite sign convention for the z-axis and is derived as follows. It allows evanescent surface wave solutions for the incident wave.

$$\hat{Z}_m = \frac{Z_C k}{\hat{k}_{zm}} = \frac{Z_C k}{\sqrt{k^2 - \left(k\sin\theta + \frac{2m\pi}{d}\right)^2}}$$

for $m = 0$,

$$\hat{Z}_0 = \frac{Z_C k}{\sqrt{k^2 - (k\sin\theta)^2}}$$

$$\left(\hat{Z}_0\right)^2 = \frac{{Z_C}^2 k^2}{k^2 - k^2\sin^2\theta}$$

$$\hat{Z}_0 = \frac{Z_C}{\sqrt{1-\sin^2\theta}}$$

$$\therefore \quad -\hat{Z}_0^i = \frac{i Z_C}{\sqrt{\sin^2\theta - 1}}$$

for $0 < \theta < \pi/2$,

$$\hat{Z}_0 = \frac{Z_C}{\cos\theta} = -\hat{Z}_0^i = \hat{Z}_0^r \tag{6.24}$$

For our application we will always assume an incident wave with a real angle of incidence so the simpler expression of Eq. (6.18) will suffice.

Continuing the convention that $\hat{k}_{zm}$ is nominally positive due to propagation in the positive z direction, which is upwards with reference to figure 6.1 it can be seen that when $\hat{k}_{zm}$ is imaginary the mode m is evanescent and the resulting impedance will be purely imaginary whereas when the m-mode is propagating in z (real $\hat{k}_{zm}$) the impedance will also be real. From the impedance relationship the amplitudes of the non-zero order pressure m-modes $\hat{I}_m$ are defined as,

$$\hat{I}_m = \hat{Z}_m \hat{V}_m \quad m \neq 0 \tag{6.25}$$

The pressure amplitude for mode m=0 requires special attention due to this mode being unique, composed of both the incident and its specular reflected component. These components have opposite propagation direction in z which is denoted by the sign of the impedance so need careful attention when considering the amplitude of mode m=0. The

incident wave amplitude $\hat{V}_0^i$ is a defined quantity given as part of the initial conditions of the model. The mode m=0 pressure and velocity amplitudes, $\hat{I}_0$ and $\hat{V}_0$, are the resultant pressure and velocities from the superposition of both the incident and reflected wave components at z=0. The $\hat{V}_0^i$ represents the downward -z propagating incident wave and $\hat{V}_0^r$ the m=0 reflection component often tenuously referred to as the 'specular reflection' component due to its angle of reflection equalling the angle of incidence. This is what makes $\hat{I}_0$ a special case. Eq. (6.18) and (6.19) are used to compose the mode m=0 impedance $\hat{Z}_0$, whereas Eq. (6.22) is used for the impedance all other m-modes. The m=0 pressure amplitude $\hat{I}_0$, at z=0 is therefore,

$$
\begin{aligned}
&\hat{I}_0^i = \hat{Z}_0^i \hat{V}_0^i \\
&\hat{I}_0^r = \hat{Z}_0^r \hat{V}_0^r \\
&\hat{I}_0 = \hat{I}_0^i + \hat{I}_0^r \\
&\quad = \hat{Z}_0^i \hat{V}_0^i + \hat{Z}_0^r \hat{V}_0^r \\
&\text{as } \hat{Z}_0^i = -\hat{Z}_0^r \\
&\hat{I}_0 = \hat{Z}_0^i \hat{V}_0^i - \hat{Z}_0^i \hat{V}_0^r \\
&\quad = \hat{Z}_0^i \left(\hat{V}_0^i - \hat{V}_0^r \right)
\end{aligned}
\tag{6.26}
$$

Worthy of note is a sanity check on the sign of $\hat{I}_0^i$ pressure amplitude. Given a positive incident wave velocity amplitude $\hat{V}_0^i$, the negative signed impedance $\hat{Z}_0^i$ yields a negative pressure amplitude $\hat{I}_0^i$. Intuitively this is correct as consider a point in space and time where the velocity is negative in z. The pressure at this point must be positive to be consistent with the -z propagating component of the incident wave.

The expression for the free space pressure field is then,

$$
p(x, z \geq 0) = \hat{I}_0^i \hat{e}_0 \exp\left(-i \hat{k}_{z0} z \right) + \hat{I}_0^r \hat{e}_0 \exp\left(i \hat{k}_{z0} z \right) + \sum_{m \neq 0} \hat{I}_m \hat{e}_m \exp\left(i \hat{k}_{zm} z \right) \tag{6.27}
$$

which at the boundary z=0 reduces to,

$$
p(x, 0) = \hat{I}_0^i \hat{e}_0 + \hat{I}_0^r \hat{e}_0 + \sum_{m \neq 0} \hat{I}_m \hat{e}_m \tag{6.28}
$$

Equations Eq. (6.7) and Eq. (6.27) together describe the acoustic free-space field. The unknowns which require solving are the amplitudes $\hat{V}_m$ of the complete set of m-modes. These are dependent upon the fields in the waveguide region $z<0$ as described in the following chapter.

As an aside the normalising constant of $d^{-0.5}$ for the $\hat{e}_m$ modes may be omitted when plotting the free-space field as it will represent just a scaling factor at this point. This improves clarity when implementing the model and then ensures that the mode functions $\hat{e}_m$ become unity amplitude and the $\hat{V}_m$ amplitude set then referenced to unity amplitude which may ease implementation.

6.1.4 Acoustic waveguide region, z<0

Moving on to the lower space acoustic field region $z<0$, the effect of the waveguide like grooves must be considered. To avoid ambiguity, field variables relating to this space where $z<0$ will be referred to without annotation to distinguish them from the '^' denoted variables of the free-space field where $z>0$. The groove can be considered as a closed bottom waveguide with the plane wave mode being the only mode able to propagate when the incident wavelength is large in comparison with the width of the groove aperture a. When a is in the order of or larger than the incident wavelength we observe that high order waveguide modes become excited within the grooves. The field at $z=0$ within the groove aperture, $|x|<a/2$, will consist entirely of standing waveguide modes of v_z which shall be termed n-modes. Where n is an integer and each mode consists of n half-cycles within the aperture. The full derivation of these waveguide principles is beyond the scope of this paper but is a widely published topic should the reader choose to delve deeper [29].

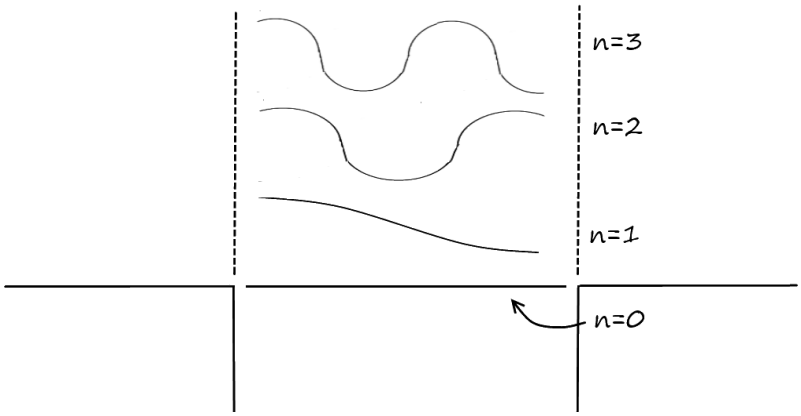

Figure 6.3 Example waveguide modes at z=0.

Boundary conditions within the waveguide dictate that only a discrete set of modes may exist within the aperture. The characteristics of the modes are given solely by aperture dimensions which in our two dimensional case is the width, a. The complex amplitude V_n of each mode n then depends upon the incident wave characteristics, the depth of the groove, h and also more subtly d. Any n-mode harmonic content present in the incident wave will tend to excite that mode in the waveguide. The magnitude of V_n is the amplitude of the mode n while the phasor angle describes its temporal phase relationship with other modes and time zero. Each n-mode is a standing wave within the aperture, imposed by the boundary conditions and as a result of the interference between the lateral interference of reflected waves off each side wall and the incoming and outgoing waves traversing vertically. The value of each n-mode at any given time will be expressed by the real part of the n-mode function multiplied by V_n. The trivial case of zero groove depth h=0, will cause the amplitudes of all n-modes to vanish. The amplitude of every n-mode will be dependent upon h whilst their characteristic form are dependent only upon the aperture width a.

To obtain normalised mode functions describing the z-axis acoustic velocity with respect to x for the waveguide modes we apply the boundary conditions within the groove. At the side walls of the groove the normal velocity must vanish as must the normal pressure gradient. Otherwise a non-zero normal pressure gradient at a wall surface would infer a velocity across the boundary material which is precluded by the assumption of acoustically hard boundaries. Confining this principle to the n-mode function across the aperture at z=0, the normalised z component of acoustic velocity is derived as follows. The boundary conditions allow an infinite set of discrete solutions to the mode functions within the aperture whose spatial frequency in x is given by,

$$k_{xn} = \frac{n\pi}{a} \quad n = 0,1,2...\infty \tag{6.29}$$

Given the chosen origin at x=0 centred upon the waveguide aperture the mode function must be co-sinusoidal because the vertical velocity is not bounded by the aperture walls and inviscid conditions allow an unbounded tangential velocity gradient. Furthermore we know that the pressure gradient must vanish in x at the boundary walls, exerting no accelerative force upon the air particles. The modal characteristic function is therefore of the form given below,

$$\cos\left(k_{xn}\left[x+\frac{a}{2}\right]\right)=\cos\left(\left[\frac{n\pi}{a}\right].\left[x+\frac{a}{2}\right]\right)$$
$$\text{when } n=0,$$
$$\cos(0)=1 \tag{6.30}$$

Finally the mode function must be normalised to the aperture to ensure that its inner product with itself across the aperture width a, is unity to allow the inner product method to be used to fit the m-modes with the n-modes with correct scaling. Starting with the self inner product of the mode n characteristic function of Eq. (6.30) for $n>0$,

$$\int_{-a/2}^{a/2}\cos\left(k_{xn}\left[x+\frac{a}{2}\right]\right).\cos\left(k_{xn}\left[x+\frac{a}{2}\right]\right)dx=\frac{a}{2} \tag{6.31}$$

noting the 'd' signifying an 'infinitesimally small increment of' as in dx, is not to be confused with the grating pitch d throughout the following explanation. Introducing a constant B,

$$\int_{-a/2}^{a/2}B\cos\left(k_{xn}\left[x+\frac{a}{2}\right]\right).B\cos\left(k_{xn}\left[x+\frac{a}{2}\right]\right)dx=\frac{a}{2}B^2$$
$$\int_{-a/2}^{a/2}B^2\cos^2\left(k_{xn}\left[x+\frac{a}{2}\right]\right)dx=\frac{a}{2}B^2 \tag{6.32}$$

In order to force the integral to evaluate to unity,

$$B^2=\frac{2}{a} \tag{6.33}$$

Giving the modal function normalising constant of,

$$B=\sqrt{\frac{2}{a}}\quad n>0 \tag{6.34}$$

For n=0 where the characteristic mode function is spatially constant across the aperture there is a special case of the normalising constant due to the invariance of the function with x. The self inner product of the non-periodic n=0 mode which evaluates to 1 for all x is,

$$\int_{-a/2}^{a/2}(1).(1)\,dx=a\quad n=0 \tag{6.35}$$

Introducing a constant C,

$$\int_{-a/2}^{a/2} 1C.1C\,dx = aC^2$$
$$C^2 \int_{-a/2}^{a/2} 1^2\,dx = aC^2 \tag{6.36}$$

In order to force the integral to unity requires the definition of C thus,

$$C^2 = \frac{1}{a} \tag{6.37}$$

Giving the normalising constant for n=0 of,

$$C = \sqrt{\frac{1}{a}} \quad n = 0 \tag{6.38}$$

Bringing this together gives the normalised mode function for each n-mode thus,

$$\begin{aligned} e_n &= B\cos\left(\left[\frac{n\pi}{a}\right]\left[x+\frac{a}{2}\right]\right) && |x| \le \frac{a}{2},\ n > 0 \\ e_0 &= C && |x| \le \frac{a}{2},\ n = 0 \\ e_n &= 0 && |x| > \frac{a}{2} \end{aligned} \tag{6.39}$$

Outside of the aperture $|x|>a/2$ the modal function is zero in order to satisfy the $v_z=0$ boundary condition on the ledges. The n=0 plane wave mode, reduces to a spatial constant because its field is invariant in x as it describes a plane wave perpendicular to the x axis. Given a time dependence then the n=0 mode would be seen to oscillate uniformly in x with angular frequency ω and amplitude V_0. The n>0 modes describe the standing waves of v_z set up within the aperture of the groove. Assuming a purely sinusoidal incident wave then each n-mode can be propagating in the groove only when the incident wave is in excess of the cut-off frequency for the n-th mode. Below the cut-off frequency the mode may still be excited but it will be evanescent in z. For complex incident waveforms, excitation of the n-modes will also depend upon the harmonic content in the incident wave but in this case a purely sinusoidal incident wave is assumed.

To complete the model of the waveguide space z<0, the impedance within the aperture at

the boundary z=0 must be defined. The impedance at z=0 for each n-mode is given by the interaction of the down-going modal component with that of the up-going reflected component from the bottom of the groove. Assuming that the mode is propagating as signified by a real z-axis wave number the impedance will be purely imaginary. The phase difference between the two waves will be governed by the transit time to traverse the waveguide, a distance in z of 2h. Given the depth of the waveguide h and the z-axis wave-number for mode-n of k_{zn}, the transit time and hence phase shift is known. Dependence on k_{zn} will create a discrete impedance for each n-mode and is given by,

$$Z_n = -i\frac{Z_C k}{k_{zn}}\cot(k_{zn}h) \tag{6.40}$$

The negative sign is introduced to conform to our axes and z-axis propagation sign conventions so because the incident n-mode will be propagating in the -z direction into the groove it will have a negative signed impedance. The reflected component of course will be propagating in the +z direction but this inversion will be satisfied by the *cot* relationship. The z-axis wave-number k_{zn} for each waveguide mode n is given by,

$$k_{zn} = \pm\sqrt{k^2 - \left(\frac{n\pi}{a}\right)^2} \tag{6.41}$$

Modes with a real k_{zn} wave number will propagate the groove in z and excite mode n as a standing wave pattern throughout the vertical extent of the groove. Whereas evanescent modes will not propagate the groove and decay exponentially away from z=0. The negative case of k_{zn} indicates the modal component propagating downwards in -z within the groove while positive denotes the reflected component propagating upwards in +z and out into free-space. For the purposes of matching the waveguide and free spaces at z=0 it is not critical which sign is used for k_{zn} as the two are theoretically equivalent at z=0 and will produce the same result for Z_n because the sign of the $Z_c k/k_{zn}$ term in Eq. (6.40) opposing the '*cot'* term to ensure the same Z_n sign in either case. For convention however, the positive case will be used. Imaginary values of k_{zn} will represent an evanescent mode that will not propagate the groove due to the incident wave being below the cut-off frequency for that mode [29]. Due to us assuming a lossless model then k_{zn} will not possess a real part.

6.1.5 Acoustic boundary conditions and equations at z=0

For this model a medium of inviscid air is assumed with characteristic impedance $Z_c=\rho_0 c_0$. This is a far-field model where the propagating waves are planar, assumed to propagate unimpeded in free space and with the pressure and velocity components in phase (lossless). Consider now a plane wave reaching an acoustically hard material at normal incidence. Boundary conditions will dictate that the normal velocity at the boundary be zero and the impedance infinite. This demands that normal acoustic velocity must vanish everywhere on the boundary as total reflection will occur with no transmission into the boundary medium. The steady state situation can be considered as an incident wave and a reflected wave propagating in opposite directions with the free-space impedance given by the superposition of incident and reflected components. The acoustic pressure is a scalar quantity so the resultant pressure at any point will be the numerical sum of the incident and reflected waves causing a standing pressure wave in the *z*-direction with an anti-node at the boundary *z*=0. The velocity however is a vector with both magnitude and direction so the resultant acoustic velocity is the vector sum of the velocities of incident and reflected waves. At the boundary the magnitude of the velocity for the two waves is equal, due to perfect reflection, but the direction normal to the boundary is opposite causing cancelling of normal velocity at the boundary surface. The resultant free-space acoustic velocity field is a standing wave in the *z*-axis with a node at the boundary. The superposition of the incident and reflected waves produces a phase shift of 90 degrees between the standing pressure and velocity fields. Therefore the free-space characteristic impedance for the summation of incident and reflected waves will be imaginary and will exhibit spatial periodicity in *z*. By applying the principle that a pressure gradient will tend to create acoustic acceleration to this situation we can conclude that the normal pressure gradient at the boundary must be zero to ensure a vanishing surface normal component of velocity. The boundary conditions at an infinitely hard boundary can thus be stated,

$$\begin{aligned} \nabla p \bullet d\mathbf{n} &= \frac{dp}{d\mathbf{n}} = 0 \\ v \bullet d\mathbf{n} &= 0 \end{aligned} \tag{6.42}$$

where $d\mathbf{n}$ is the unit vector normal to the boundary surface and pointing into the surface which in our case is *-z*.

Using the characteristic equations presented for the upper and lower spaces the complete

boundary condition set can be described for the problem at the space boundary z=0. Remembering that the solution is obtained by matching the free-space m-modes with the waveguide n-modes within the waveguide like groove aperture and hard boundary conditions outside of the aperture. For our acoustic application it is continuity of v_z and pressure which must be maintained. Therefore the z-direction velocity continuity condition at z=0 is,

$$\begin{aligned} &\hat{V}_0^i \hat{e}_0 + \hat{V}_0^r \hat{e}_0 + \sum_{m\neq 0} \hat{V}_m \hat{e}_m = \sum_n V_n e_n \qquad |x| \le a/2 \\ &\hat{V}_0^i \hat{e}_0 + \hat{V}_0^r \hat{e}_0 + \sum_{m\neq 0} \hat{V}_m \hat{e}_m = 0 \qquad d/2 > |x| > a/2 \end{aligned} \tag{6.43}$$

Continuity of pressure within the groove aperture is expressed at z=0 as,

$$\begin{aligned} &\hat{I}_0^i \hat{e}_0 + \hat{I}_0^r \hat{e}_0 + \sum_{m\neq 0} \hat{I}_m \hat{e}_m = \sum_n I_n e_n \qquad |x| \le a/2 \\ &\frac{d}{d\mathbf{n}}\left(\hat{I}_0^i \hat{e}_0 + \hat{I}_0^r \hat{e}_0 + \sum_{m\neq 0} \hat{I}_m \hat{e}_m \right) = 0 \qquad d/2 > |x| > a/2 \end{aligned} \tag{6.44}$$

Pressure boundary conditions outside of the aperture and at z=0 are that the pressure gradient in z vanish.

Due to the orthonormal nature of the problem as discussed in the previous section and with consideration to Eq. (6.45 and 6.46) each m-mode acoustic velocity amplitude can be expressed as the Hermitian inner product of the set of n-mode basis functions and vice versa. Thus, noting the conjugation of the $\hat{e}_m$ term in (6.45),

$$\hat{V}_m = \sum_n V_n < e_n, {}^*\hat{e}_m > \tag{6.45}$$

$$V_n = \sum_m \hat{V}_m < e_n, \hat{e}_m > \tag{6.46}$$

This is valid in this model as we assume a Hilbert space [27] where the inner product is always defined and any complex function can be described by a weighted linear combination of orthonormal basis functions where the m and n-modes represent the basis function in our space for z>0 and z<0 respectively. This function has the effect of correlating a single m-mode with every n-mode in turn to yield an overall weighted

amplitude for mode m. The limits of integration theoretically should extend from -d/2 to d/2 to correlate the m and n modes across the complete structure period. But because the n-modes will always vanish outside of the aperture to account for boundary conditions on the groove ledges which causes a zero contribution to the integral and permits truncation of the limits to -a/2 to a/2. The real and imaginary parts of each m-mode will provide correlation for both the even co-sinusoidal and odd sinusoidal components respectively.

The fundamental equations of the problem will henceforth be formulated. In order to make the solution complete the acoustic pressure must be considered as well as v_z which is achieved via the impedance relationships Z_n and $\hat{Z}_m$. Eq. (6.46) may be reposed in terms of the acoustic pressure by multiplying through by the corresponding impedance thus,

$$Z_n V_n = \sum_m \hat{Z}_m \hat{V}_m < e_n, \hat{e}_m >$$

$$Z_n V_n = \hat{Z}_0^i \left(\hat{V}_0^i - \hat{V}_0^r \right) < e_n, \hat{e}_0 > + \sum_{m \neq 0} \hat{Z}_m \hat{V}_m < e_n, \hat{e}_m >$$

as $I = ZV$,

$$I_n = \hat{I}_0 < e_n, \hat{e}_0 > + \sum_{m \neq 0} \hat{I}_m < e_n, \hat{e}_m > \qquad (6.47)$$

where the zeroth mode pressure amplitude $\hat{I}_0$, once again has to be separated initially from the major summation due to its uniqueness in containing incident and reflected components which have impedances of opposing sign. $\hat{I}_0$ accounts for the incident wave propagating by definition in the negative z-direction and the reflected component propagating in positive z. This equation can be tidied by including the case of m=0 in the major summation. Inclusion of m=0 with the $\hat{Z}_0\hat{V}_0$ term in the major summation is balanced by subtracting the same term post summation. Within the major summation the $\hat{Z}_0\hat{V}_0$ term will use Eq. (6.22) to calculate the complex impedance $\hat{Z}_m$, for each mode where as the correct terms for the zeroth mode m=0 are in fact Eq. (6.18 and 6.19) or (6.23). This leads to another subtlety when balancing the inclusion of the m=0 term in the major summation. The post summation subtraction of $\hat{Z}_0\hat{V}_0$ must use Eq. (6.22) as in the major summation. Eq. (6.22) used to calculate impedance which in turn uses Eq. (6.9) to give a z-axis wave number, assumes a positive propagation in z and so when m=0 this will give the wrong direction for the incident wave. Therefore the incident impedance component must be inverted when considering the $\hat{Z}_0\hat{V}_0$ term as used in the major summation. Adding the m=0 term to the

major summation and subtracting it outside as explained earlier in the paragraph gives,

$$\text{for } m=0,\ \hat{Z}_0\hat{V}_0=\hat{Z}_0\left(\hat{V}_0^i+\hat{V}_0^r\right) \text{ and } \hat{Z}_0=-\hat{Z}_0^i=\hat{Z}_0^r$$

$$\therefore\ \hat{Z}_0\hat{V}_0=-\hat{Z}_0^i\hat{V}_0^i+\hat{Z}_0^r\hat{V}_0^r=-\hat{Z}_0^i\hat{V}_0^i-\hat{Z}_0^i\hat{V}_0^r \tag{6.48}$$

so adding this result into the major summation of Eq. (6.47) and subtracting it from outside to retain balance leads to,

$$\begin{aligned} I_n &= \left[\hat{Z}_0^i\left(\hat{V}_0^i-\hat{V}_0^r\right)-\left(-\hat{Z}_0^i\hat{V}_0^i-\hat{Z}_0^i\hat{V}_0^r\right)\right]<e_n,\hat{e}_0>+\sum_m \hat{Z}_m\hat{V}_m<e_n,\hat{e}_m> \\ &= \left[\hat{Z}_0^i\hat{V}_0^i-\hat{Z}_0^i\hat{V}_0^r-\left(-\hat{Z}_0^i\hat{V}_0^i-\hat{Z}_0^i\hat{V}_0^r\right)\right]<e_n,\hat{e}_0>+\sum_m \hat{Z}_m\hat{V}_m<e_n,\hat{e}_m> \\ I_n &= 2\hat{Z}_0^i\hat{V}_0^i<e_n,\hat{e}_0>+\sum_m \hat{Z}_m\hat{V}_m<e_n,\hat{e}_m> \end{aligned} \tag{6.49}$$

It now remains to recompose the boundary continuity equation to allow the V_n set to be numerically solved from the set of known variables. Substituting Eq. (6.45) into Eq. (6.49) eliminates $\hat{V}_m$ giving a form with V_n as the only unknown,

$$\begin{aligned} I_n &= 2\hat{Z}_0^i\hat{V}_0^i<e_n,\hat{e}_0>+\sum_m \hat{Z}_m\left(\sum_{n\dagger} V_{n\dagger}<e_{n\dagger},*\hat{e}_m>\right)<e_n,\hat{e}_m> \\ &= 2\hat{Z}_0^i\hat{V}_0^i<e_n,\hat{e}_0>+\sum_{n\dagger} V_{n\dagger}\left(\sum_m \hat{Z}_m<e_{n\dagger},*\hat{e}_m><e_n,\hat{e}_m>\right) \end{aligned} \tag{6.50}$$

Because of the substitution of Eq. (6.45) there now exists an n and $n\dagger$, due to the fact that we are solving for a single n mode but within this calculation it is required to sum over all n. The latter being denoted $n\dagger$. Therefore n is the mode we are solving for whereas $n\dagger$ is just an index used within the calculation to sum all n-modes. It is apparent that this will require iterative numerical solving as each value of n will depend upon every other in the complete set.

By making use of $I_n=Z_nV_n$ then Eq. (6.40) for Z_n can be substituted into Eq. (6.50) for $Z_{n\dagger}$. In the n=0 case k/k_{zn} equates to unity and the mode propagates the groove purely in z so k must equal k_{zn} for n=0,

$$-i\frac{Z_C k}{k_{zn}}\cot(k_{zn}h)V_n = 2\hat{Z}_0^i \hat{V}_0^i < \hat{e}_n, \hat{e}_0 > + \sum_{n\dagger} V_{n\dagger}\left(\sum_m \hat{Z}_m < \hat{e}_{n\dagger}, {}^*\hat{e}_m >< \hat{e}_n, \hat{e}_m >\right)$$

subtracting $2\hat{Z}_0^i \hat{V}_0^i < \hat{e}_n, \hat{e}_0 >$ and adding $i\frac{Z_C k}{k_{zn}}\cot(k_{zn}h)$ to both sides gives,

$$-2\hat{Z}_0^i \hat{V}_0^i < \hat{e}_n, \hat{e}_0 > = i\frac{Z_C k}{k_{zn}}\cot(k_{zn}h)V_n + \sum_{n\dagger} V_{n\dagger}\left(\sum_m \hat{Z}_m < \hat{e}_{n\dagger}, {}^*\hat{e}_m >< \hat{e}_n, \hat{e}_m >\right) \tag{6.51}$$

The finishing touch to this equation will be to absorb the '*cot*' term into the primary summation over $n\dagger$ to allow the neat formation of a linear equation matrix. Notice though that the '*cot*' term applies only to n and not $n\dagger$, meaning that this term is evaluated only when $n=n\dagger$. This can be achieved mathematically by use of the Kronecker delta which by definition is,

$$\delta_b^a = \begin{bmatrix} 0 \text{ if } a \neq b \\ 0 \text{ if } a = b \end{bmatrix} \tag{6.52}$$

We thus obtain our final set of linear equations,

$$\sum_{n\dagger} V_{n\dagger}\left(\sum_m \left[\hat{Z}_m < \hat{e}_{n\dagger}, {}^*\hat{e}_m >< \hat{e}_n, \hat{e}_m >\right] + \delta_n^{n\dagger} i\frac{Z_C k}{k_{zn}}\cot(k_{zn}h)\right) = -2\hat{Z}_0^i \hat{V}_0^i < \hat{e}_n, \hat{e}_0 > \tag{6.53}$$

Due to the fact that $\hat{Z}_{m=0}=\hat{Z}_0^r$ the summation in 'm' can be left intact because it is the $\hat{Z}_0^r$ term required when m=0 as this relates to the reflected mode which propagates in $+z$. This equation can then be solved numerically to yield the V_n set. The infinite integer set of n-modes must be truncated as must the range of the $\pm m$-mode set. Rearranging this into a matrix form of Eq. (6.54) and truncating the infinite sets of n-modes to $0 \leq n \leq N$ and m-modes to $|m| \leq \pm M$ allows numerical solving for the unknown set V_n. From this solution the $\hat{V}_m$ set is then calculated analytically from the inner product relationship of Eq. (6.45). Remember that the variables denoted by the hat '^' signify upper-space variables such as $\hat{e}_m$, $\hat{I}_m$ and $\hat{V}_m$ and without the hat refer to the lower-space variables relating to the waveguide like groove space such as e_n, I_n and V_n.

$$\begin{bmatrix} \left(\sum_m \left[\hat{Z}_m < e_0, {}^*\hat{e}_m >< e_0, \hat{e}_m >\right] + i\frac{Z_C k}{k_{z0}}\cot(k_{z0}h)\right) & \left(\sum_m \left[\hat{Z}_m < e_1, {}^*\hat{e}_m >< e_0, \hat{e}_m >\right]\right) & \cdots + \left(\sum_m \left[\hat{Z}_m < e_n, {}^*\hat{e}_m >< e_0, \hat{e}_m >\right]\right) \\ \left(\sum_m \left[\hat{Z}_m < e_0, {}^*\hat{e}_m >< e_1, \hat{e}_m >\right]\right) & + \left(\sum_m \left[\hat{Z}_m < e_1, {}^*\hat{e}_m >< e_1, \hat{e}_m >\right] + i\frac{Z_C k}{k_{z1}}\cot(k_{z1}h)\right) & \cdots + \left(\sum_m \left[\hat{Z}_m < e_n, {}^*\hat{e}_m >< e_1, \hat{e}_m >\right]\right) \\ \vdots & \vdots & \vdots \\ \left(\sum_m \left[\hat{Z}_m < e_0, {}^*\hat{e}_m >< e_n, \hat{e}_m >\right]\right) & + \left(\sum_m \left[\hat{Z}_m < e_1, {}^*\hat{e}_m >< e_n, \hat{e}_m >\right]\right) & \cdots + \left(\sum_m \left[\hat{Z}_m < e_n, {}^*\hat{e}_m >< e_n, \hat{e}_m >\right] + i\frac{Z_C k}{k_{zn}}\cot(k_{zn}h)\right) \end{bmatrix} \begin{bmatrix} V_0 \\ V_1 \\ \vdots \\ V_n \end{bmatrix} = \begin{bmatrix} -2\hat{Z}_0^i \hat{V}_0^i < e_0, \hat{e}_0 > \\ -2\hat{Z}_0^i \hat{V}_0^i < e_1, \hat{e}_0 > \\ \vdots \\ -2\hat{Z}_0^i \hat{V}_0^i < e_n, \hat{e}_0 > \end{bmatrix}$$

(6.54)

As an aside the methods proposed by DeSanto [7] and Zhu, Stinson & Daigle [9] for solving a similar problem are also of interest for further reading. Slightly differing methods are used to compose the set of equations although the fundamental principle of breaking the scattered field down into a set of modes is similar to the modal method presented.

6.2 Implementation

6.2.1 Introduction to implementation

This section is dedicated to taking the modal-model equations as derived and applying them to the task of simulating a realistic acoustic field. Specifically the Excess-Attenuation spectrum will be produced for acoustic point to point propagation above the grating structure ground. It is also a primary aim of this research to explore effective impedance models for grating structures and so the effective impedance will be calculated from the modal-model acoustic field. The whole process is as follows.

Initially the process of solving the modal-model matrix will be tackled which will yield the complex amplitudes of the scattered free-space modes that superpose to form the acoustic field.

The next stage is to apply simple approximations to improve the agreement of the model with 2d boundary element method (BEM) simulations which employs cylindrical waves and finite ground structures.

Given that the free-space pressure field has been solved, an effective impedance for the grating-structure can be calculated algebraically from the plane-wave reflection coefficient.

Finally, the effective impedance of the grating structure can be applied into the spherical or cylindrical reflection co-efficient equation to produce the wave acoustic field for our point to point propagation above a ground plane structure problem. This will provide the excess-attenuation spectrum for the given geometry.

6.2.2 Forming the linear matrix

Recall that the 2d modal-model matrix of linear equations is composed in terms of the truncated set of unknown waveguide mode amplitudes V_n. The matrix is solved

numerically to yield the V_n set. From which the truncated set of free-space mode amplitudes, $\hat{V}_m$ are calculated from inner-products due to the basis function [27] properties of the V_n and $\hat{V}_m$ mode sets.

The matrix has the form,

$$\begin{bmatrix} A_{0,0} & A_{0,1} & \cdots & A_{0,n\dagger} \\ A_{1,0} & A_{1,1} & \cdots & A_{1,n\dagger} \\ \vdots & \vdots & & \vdots \\ A_{n,0} & A_{n,1} & \cdots & A_{n,n\dagger} \end{bmatrix} \begin{bmatrix} V_0 \\ V_1 \\ \vdots \\ V_n \end{bmatrix} = \begin{bmatrix} X_0 \\ X_1 \\ \vdots \\ X_n \end{bmatrix} \tag{6.55}$$

Where the V_n set are the unknown n-mode amplitudes which must be truncated to produce a finite matrix. For our acoustic applications the truncation is in the order of N=5 [6,8]. Furthermore the infinite $\hat{V}_m$ set must also be truncated which generally will be of magnitude M=25, however the truncations are application and resource dependant and are addressed in detail later in this chapter. Remember that the V_n and $\hat{V}_m$ sets are the v_z amplitudes for the n and m-mode sets respectively.

The following flow diagram of figure 6.4 shows the process for populating the matrix using the equations derived in previous sections. It shows the process in its simplest form with a logical progression for ease of comprehension. There are no optimisations and so it does not necessarily represent the most efficient implementation. Simple optimisations to reduce computational time will be introduced in due course once the fundamental methods have been established. Remember that capital N and M are the truncation constant values used for the set of n and m-modes while the lower-case n and m are used to denote the index within the sets.

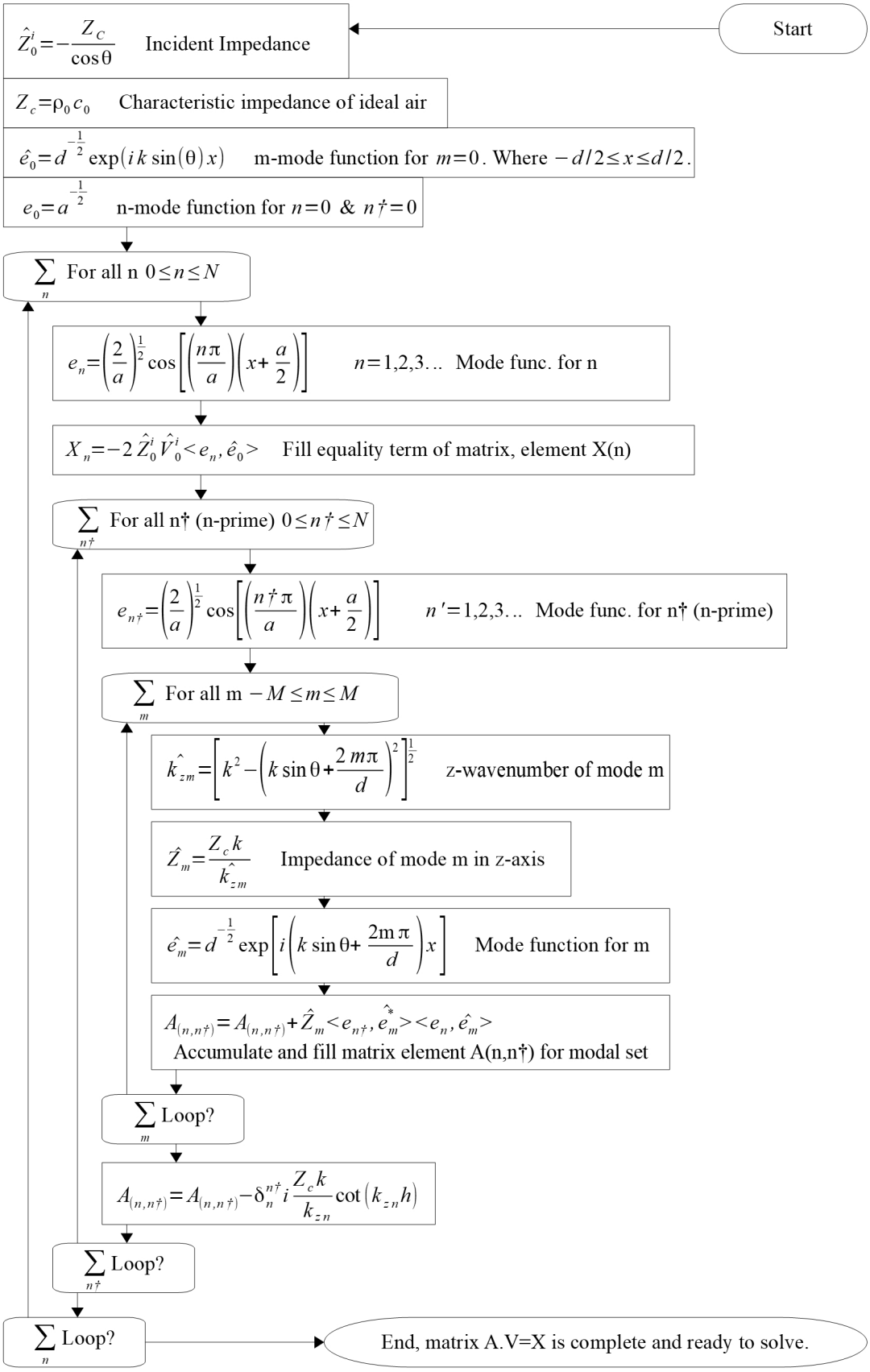

Figure 6.4 Solution process for the modal model.

With the matrix fully populated it can be solved numerically to yield the set of V_n amplitudes which completes the model of the waveguide space below the boundary z=0. Completing the model requires the last set of unknowns, the m-mode amplitude set $\hat{V}_m$. This is achieved by matching the m-modes to the waveguide space n-modes at then boundary z=0. This is achieved analytically by the inner product relation introduced previously in the theory section,

$$\hat{V}_m = \sum_n V_n < e_n, * \hat{e}_m > \tag{6.56}$$

which applies due to the orthonormality of the modal set. The logical process for solving this is as shown in figure 6.5.

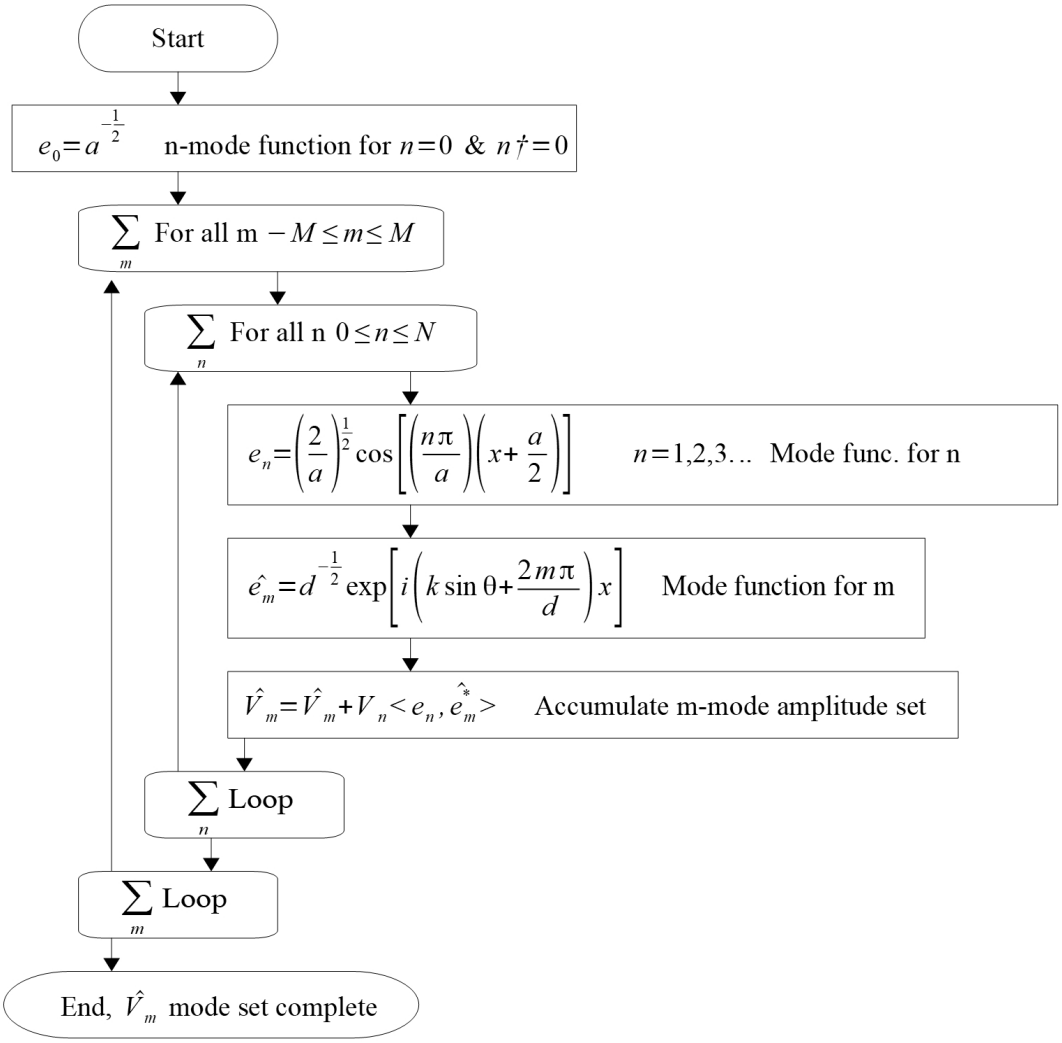

Figure 6.5 Calculating the $\hat{V}_m$ set.

This completes the process of implementing the modal model. It now remains to plot the free-space field as required for the application. From this point on concern is only with the free-space field where $z>0$ and all free-space field relationships are posed in terms of the m-mode set.

6.2.3 Truncating the modes

In order for the modal model to be solved, the infinite sets of n and m-modes must be truncated to N and $\pm M$ respectively. The chosen truncations of N=5 and M=25 are partly applied to maintain consistency with previous works [6,8] but are also justified as sensible for this application in this section. The N set may have a more severe truncation than M

because the influence of each *n*-mode is related to its cut-off frequency in the groove. However the *m*-modes are a series representation of the free space field which at the boundary z=0, has field discontinuities at the aperture walls and so high order modes are required of sufficiently high spatial frequency to satisfactorily reproduce the resulting field. Furthermore the computation cost of additional *m*-modes is low as they are just summated, but additional *n*-modes increase the matrix size and subsequent solution time. Figure 6.4 shows a sweep of *N* and *M* truncations for a large scale geometry with high *a*/*d* ratio which is where the truncations are likely to be at their most sensitive due to the lower cut-off frequency of the *n*-modes when compared with smaller scale geometries or low *a*/*d* ratios. The *m*-modes are less sensitive to the groove size because the dominant factor is the discontinuity either side of each groove aperture which is independent of the scale. The blue, cyan and green traces and the yellow, magenta and red traces of figure 6.4 are so similar as to be indistinguishable for the majority of the spectrum.

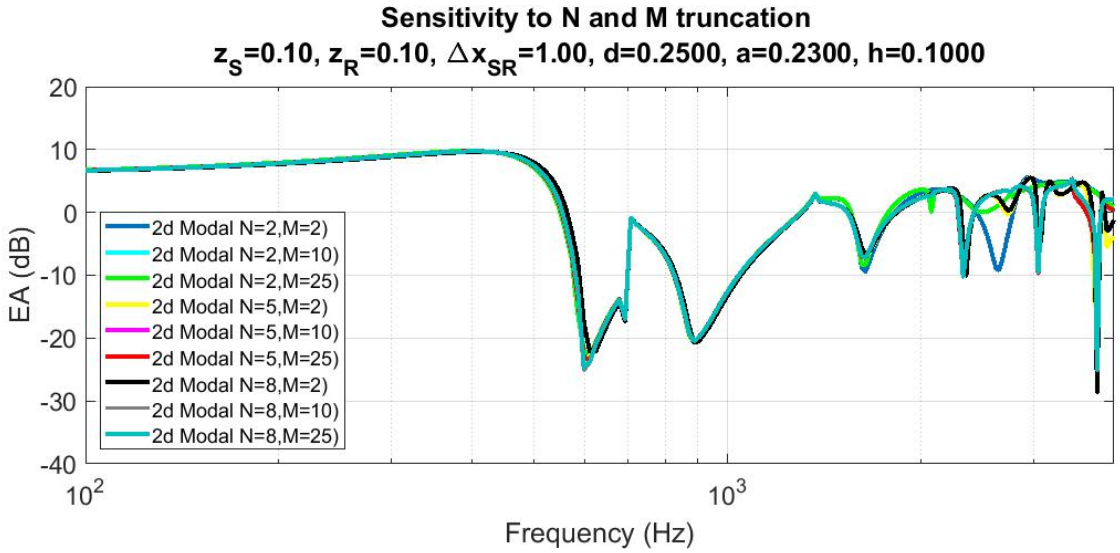

Figure 6.6 Sensitivity to N and M truncation.

At low frequencies all truncations agree closely, but beyond 2 kHz the N=2 case diverges because the modal wave structure within the grooves is no longer faithfully represented beyond this frequency and the result is a de-featuring of the response, tending to more of a flat line. For N=5 the result converges with those for which N=8, suggesting that N=5 is a sensible truncation. Over truncating *M* causes false minima to occur with the true minima features being missed. This is due to the failure of the *m*-mode set to realistically represent the free space field because of a lack of modal, and hence spatial, resolution. It can be seen that the result converges for M≥10, therefore, truncations of N=5 and M=25 are sufficient

for the results presented henceforth.

6.2.4 Plotting the time-independent free-space field

Taking the solution of the modal-model allows the plotting of the resulting acoustic field. For this case it is the time independent field magnitude at time t=0. However, should a time dependant model be required then the modal expansions presented can be multiplied by the exponential factor of $exp(-i\omega t)$. All time dependence is once again omitted but may be assumed.

The pressure field for each mode in free-space can be calculated using the $\hat{Z}_m$ impedance relationship and the v_z amplitude $\hat{V}_m$. The product of the two with $\hat{e}_m$ will give the scalar pressure at a given field point. To recap, the impedance quantity $\hat{Z}_m$ relates the acoustic velocity component in z to the acoustic pressure at a point, implicitly accounting for the x velocity component via the wave-number conservation used when deriving the equations in previous sections. Attention must be paid to the signs of the quantities to retain correct propagation direction and pressure-velocity direction relationships. The resultant acoustic pressure amplitude p, for a given free-space field point (x,z) is the superposition of all m-modes. It will become useful later in the model to break the pressure field into its component parts which are the incident wave, the reflected mode and the rest of the scattered field components. The $d^{-0.5}$ normalising constant is omitted which was included to ensure the correct relative scaling of the m and n-modes when correlated via the inner products in the modal model solution. It need not be included when calculating the fields because the $\hat{V}_m$ set of amplitudes relates to the unity amplitude. However the normalising constant can still be included if desired as it just scales the field uniformly retaining the relative relationships but it makes sense to remove it for ease of implementation. This gives for the incident pressure field component,

$$p_i(x, z > 0) = \hat{Z}_0^i \hat{V}_0^i \exp\left(ikx \sin\theta\right).\exp(-i\hat{k}_{z0} z) \tag{6.57}$$

and the 'specularly reflected' m=0 mode is,

$$p_r(x, z>0) = \hat{Z}_0^r \hat{V}_0^r \exp\left(ikx\sin\theta\right).\exp(i\hat{k}_{z0}\, z)$$

where $\hat{V}_0 = \hat{V}_0^r + \hat{V}_0^i$ so $\hat{V}_0^r = \hat{V}_0 - \hat{V}_0^i$

$$\therefore\ p_r(x, z>0) = \hat{Z}_0^r\left(\hat{V}_0 - \hat{V}_0^i\right)\exp\left(ikx\sin\theta\right).\exp(i\hat{k}_{z0}\, z) \tag{6.58}$$

The pressure field components for the scattered *m*-mode set are,

$$p_m(x, z>0) = \hat{Z}_m \hat{V}_m \exp\left(i\left[k\sin\theta + \frac{2m\pi}{d}\right]x\right).\exp(i\hat{k}_{zm}\, z) \quad m \neq 0 \tag{6.59}$$

So the total pressure field in free-space is the addition of the incident wave, the reflected wave and the scattered field caused by the grating structure,

$$p_{tot}(x, z>0) = p_i + p_r + \sum_{m\neq 0} p_m \quad -M \le m \le M \tag{6.60}$$

As will become evident later, it is also useful to define the pressure field contributions caused only by the scattering surface which in this case requires the addition of all of the modal components but excludes the incident pressure as this is not an artefact of the grove-grating structure. This scattered field will be termed p_{sct} as follows and in this instance includes the *m*=0 reflected component,

$$p_{sct}(x, z>0) = p_r + \sum_{m\neq 0} p_m \quad -M \le m \le M \tag{6.61}$$

where *M* is the truncation value for the *m*-mode set. As such it should be re-emphasised that this is an approximate solution not an exact one due to the truncation of modes.

The velocity is a vector field so the 2-dimensional space will be formed from orthogonal *x* and *z* components. The amplitude of the *z*-direction velocity v_z, for each mode *m* is given by $\hat{V}_m$. For the incident wave v_z is given by,

$$v_{zi}(x, z>0) = \hat{V}_0^i \exp(ikx\sin\theta).\exp(-i\hat{k}_{z0}\, z) \tag{6.62}$$

The v_z of the reflected mode (*m*=0) is,

$$v_{zr}(x, z>0) = \left(\hat{V_0} - \hat{V_0^i} \right) \exp(ikx\sin\theta).\exp(i\hat{k}_{z0}\, z) \tag{6.63}$$

and the remaining scattered modal-field is therefore,

$$v_{zm}(x, z>0) = \hat{V_m} \exp\left(i\left[k\sin\theta + \frac{2m\pi}{d} \right] \right).\exp(i\hat{k}_{zm}\, z) \quad m \neq 0 \tag{6.64}$$

with the overall *z*-direction velocity field being given by the following superposition,

$$v_z(x, z>0) = v_{zi} + v_{zr} + \sum_{m\neq 0} v_{zm} \quad -M \le m \le M \tag{6.65}$$

The '$k \sin\theta + 2m\pi/d$' terms describe the wave-number of each *m*-mode in the *x*-direction and $\hat{k}_{zm}$ the modal wave-number in *z*.

The *x*-component amplitude of velocity $\hat{V}_{xm}$, for each mode *m* will be given by the ratio of the *x* and *z* wave-numbers thus,

$$\hat{V}_{xm} = \frac{\hat{V}_m \hat{k}_{xm}}{\hat{k}_{zm}}$$
$$\text{where } \hat{k}_{xm} = k\sin\theta + \frac{2m\pi}{d} \tag{6.66}$$

The *x*-direction velocity field is again made up of the superposition of the incident, reflected and scattered modes. The incident component having the *x*-velocity relationship,

$$v_{xi}(x, z>0) = \frac{\hat{V_0^i}\hat{k}_{x0}}{\hat{k}_{z0}} \exp(ikx\sin\theta).\exp(-i\hat{k}_{z0}\, z) \tag{6.67}$$

and that of the reflected component,

$$v_{xr}(x, z>0) = \frac{\left(\hat{V}_0 - \hat{V_0^i} \right)\hat{k}_{x0}}{\hat{k}_{z0}} \exp(ikx\sin\theta).\exp(i\hat{k}_{z0}\, z) \tag{6.68}$$

with the remaining scattered field having v_x of,

$$v_{xm}(x,z>0)=\frac{\hat{V}_m\hat{k}_{xm}}{\hat{k}_{zm}}\exp\left(i\left[k\sin\theta+\frac{2m\pi}{d}\right]\right).\exp(i\hat{k}_{zm}z)\quad m\neq 0 \tag{6.69}$$

So the total field in terms of x-direction acoustic velocity is,

$$v_x(x,z>0)=v_{xi}+v_{xr}+\sum_{m\neq 0}v_{xm}\quad -M\leq m\leq M \tag{6.70}$$

The model co-ordinate space (x,z) assumes that the point of m=0 'specular reflection' is located at x=0 and the surface boundary at z=0. All of the scattered modes and the incident wave are defined with reference to this origin (0,0) and so absolute co-ordinates are used when plotting the field and choosing the notional source and receiver location points once the problem is applied to that of point-to-point propagation.

6.2.5 Pseudo-finite grating approximation

The modal-model is based upon the assumption that the grating structure extends infinitely in $\pm x$. The source is modelled as an infinite plane-wave which exists in all free-space where z>0. These assumptions simplify the model significantly and lead to a periodic field which itself extends infinitely in $\pm x$ and $+z$. A drawback of this is that most of the real-world situations are best modelled in 2-dimensions by spherical sources giving rise to non-homogeneous fields. A significant difference between plane and spherical wave sources is that the notion of a source at a point does not apply to plane waves whereas is does for spherical waves. However for many source-receiver geometries and ground configurations solving the modal-model for plane waves and then applying some techniques to transfer the results to a spherical point-to-point propagation problem will be shown to provide satisfactory results.

A consequence of the infinite extent of the ground structure are that all scattered modes must reach the receiver, regardless of angle-of-incidence because there are no geometrical conditions or limits imposed by the geometry of the model. Whereas this is theoretically valid it does not represent a typical real-world scenario where the source is generally assumed to be point like. An approximation is presented to model a pseudo-finite grating structure with a point source in which the grating structure is assumed to exist only in the horizontal extent between a fictitious point source and the receiver point. For the 2d problem with invariance in y our fictitious point source located at (x_S,z_S) is actually a line

source emitting cylindrically in the *x*-*z* plane and invariant and infinite in *y*. However both spherical and line sources can be modelled by using either the spherical or cylindrical spreading equation as described later. For clarity we will therefore refer to the generic point source as the source.

Propagating scattered modes (real *z*-axis wave-number $\hat{k}_{zm}$) whose angle-of-propagation would cause them to not intersect the receiver are removed from the field summation and hence neglected. Consider this concept with the aid of the diagram below.

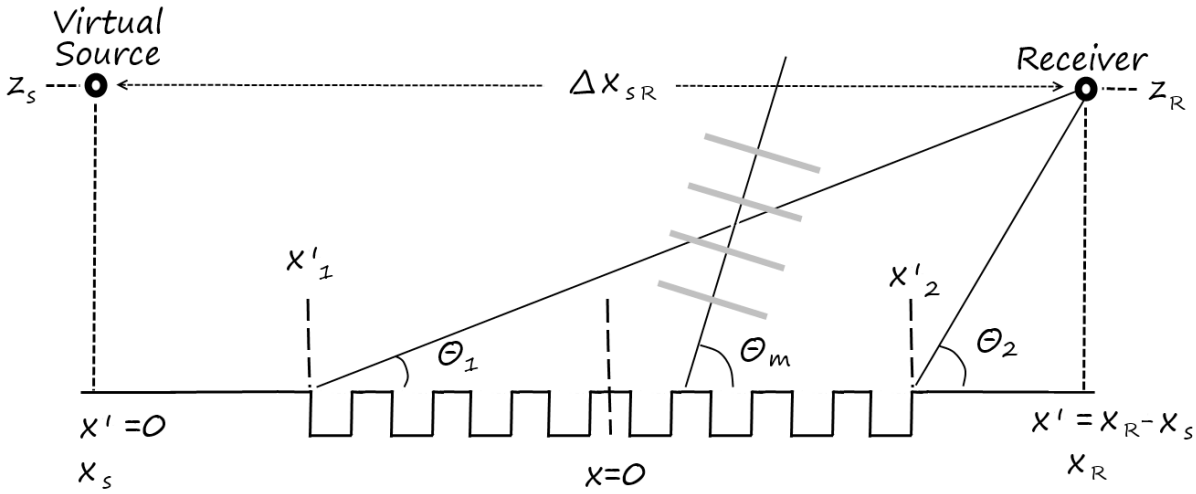

Figure 6.7 Geometric modal cut-off scheme.

For this process only and to simplify the geometry a new *x*-axis co-ordinate space, *x*-prime, will be used. In this space the virtual point source is assumed to reside at $x'=0$ and the grating horizontal dimensions and the x' coordinate of the receiver are then defined as absolute co-ordinates in x'. The reasoning for this is that when the model is implemented the geometry of the complete problem can be defined simply by the horizontal source-receiver distance, source and receiver height and the absolute extents of the grating x'_1 and x'_2. This transformation is arbitrary and x is related to x' by,

$$x = x' + x_S \tag{6.71}$$

where x_S is the *x*-coordinate of the virtual point source which will lie within $x \leq 0$. The conditions for determining whether a propagating free-space *m*-mode would reach the

receiver are mathematically,

$$\delta_{\theta 1}^{\theta 2}(\theta_m) = \begin{bmatrix} 1 \text{ if } \Re\left(\hat{\mathrm{k}}_{\mathrm{zm}}\right) > 0 \text{ and } \theta_2 \geq \theta_m \geq \theta_1 \\ 1 \text{ if } \Im\left(\hat{\mathrm{k}}_{\mathrm{zm}}\right) > 0 \\ 0 \text{ else} \end{bmatrix}$$

where,

$$\theta_m = \cos^{-1}\left(\frac{\hat{k}_{xm}}{\sqrt{\hat{k}_{zm}^{\,2} + \hat{k}_{xm}^{\,2}}}\right)$$

$$\theta_1 = \tan^{-1}\left(\frac{z_R}{x'_R - x_1}\right)$$

$$\theta_2 = \tan^{-1}\left(\frac{z_R}{x'_R - x_2}\right) \tag{6.72}$$

With the added condition in the case of a surface wave mode (imaginary $\hat{k}_{zm}$), that if the receiver is not perpendicularly within the *x*-bounds of the pseudo-finite grating then the surface mode will be neglected in the field calculation. Like the free-space modes, the surface modes are plane waves which will not diminish in amplitude with distance, hence arriving at the receiver unabated, which isn't realistic when applied to the point-to-point case and so they may overwhelm the results in some instances if not removed from the summation, especially for low receiver heights. For a lossless model where the wave-number will either be entirely imaginary or entirely real this is mechanism is expressed thus,

$$\delta_{x2}(\hat{k}_{zm}, x_R) = \begin{bmatrix} 1 \text{ if } \Im\left(\hat{k}_{zm}\right) > 0 \text{ and } x_2 > x_R \\ 1 \text{ if } \Re\left(\hat{k}_{zm}\right) > 0 \\ 0 \text{ else} \end{bmatrix} \tag{6.73}$$

Combining these conditions yields the pseudo-finite grating approximation equation for accumulating the free-space pressure field at any given field point (*x,+z*),

$$p'_{tot}(x, z > 0) = p_i + p_r + \sum_{m \neq 0} \delta_{\theta 2}^{\theta 1}(\theta_m)\, \delta_{x2}(\hat{k}_{zm}, x_R)\, p_m \quad -M \leq m \leq M \tag{6.74}$$

With the scattered components of the modified field given by and annotated with a prime to denote it includes the finite grating approximation.

Finally the location of a virtual point source is given from the assumption that the model origin at x=z=0 is also the point of specular reflection where angle of incidence equals angle of reflection for the incident and reflected (m=0) modes. By convention we will always assume the model is constructed 'left-to-right' therefore our point source must lie somewhere in the quadrant -x,+z and the receiver in +x,+z. In fact if the z co-ordinate height of the source and receiver are equal then the source and receiver will be symmetric about x=0. The source-receiver horizontal separation Δx_{SR} and the z-axis heights of the source z_S and receiver z_R are given as model parameters. Therefore the x co-ordinates of the source and receiver x_S and x_R respectively, relative to the origin are given from the numerical solution of the following,

$$\frac{x_R}{z_R} - \frac{x_S}{z_S} = 0 \text{ and } x_R + x_S = \Delta x_{SR}$$

which in matrix form is,

$$\begin{bmatrix} \frac{1}{z_R} & - & \frac{1}{z_S} \\ 1 & + & 1 \end{bmatrix} \begin{bmatrix} x_R \\ x_S \end{bmatrix} = \begin{bmatrix} 0 \\ \Delta x_{SR} \end{bmatrix} \tag{6.75}$$

It is obvious that such a severe geometric cut-off will not provide a true representation of the field at the edges of the grating and a more sophisticated approach would be an improvement. For instance a problem similar to this has been considered by Hargreaves et al. [67] where the field surrounding a finite flat plate under plane wave excitation was solved using boundary element techniques. It shows that the field at the edges is highly complex and so solving the boundary integral equation is the benchmark solution, although too complex and computationally expensive for implementation in this work which is seeking computationally efficient approximations rather than perfect solutions.

Another problem which the hard cut-off simplification will create are artefacts in the cut-off regions or geometric inclusion/exclusion of scattered free space modes which in reality would be somewhat smoothed due to non-plane wave excitation, non-ideal geometry, atmospheric effects (refractive and diffractive) and the lack of true point sources and receivers. A clear example of this may be seen in figure 6.12a at the cut-off frequency of the first scattered mode m=-1 at just under 600 Hz. The sudden inclusion of the first

scattered mode has caused a discontinuity in the curve which is not seem in the BEM prediction which fully considers the resulting field.

However it is evident from later results, that the edge effects are not dominant for the types of problem considered in this work because consistently good agreement is maintained with reference to the BEM solution.

6.2.6 Path length difference gain approximation

The next approximation to be added to the model is for cylindrical or spherical spreading losses. This will account for the relative spreading-loss differences between the incident and reflected components caused by the difference in path length between the components. For spherical waves the amplitude spreading loss (not to be confused with energy spreading loss) will be proportional to $1/R$ where R is the equivalent ray-path length from source to receiver. Once again this is an approximation being applied for spherical/cylindrical principles to a purely plane-wave model so the processes will not be exact and analogies awkward, but as will be discussed in due course such methods can improve the correlation with existing BEM models. Furthermore this approximation is founded upon the ray geometry of the 'specularly reflected' m=0 component, remembering of course that the concept of specular reflection does not strictly apply in a scattering model. The geometry of the approximation is shown in figure 6.8.

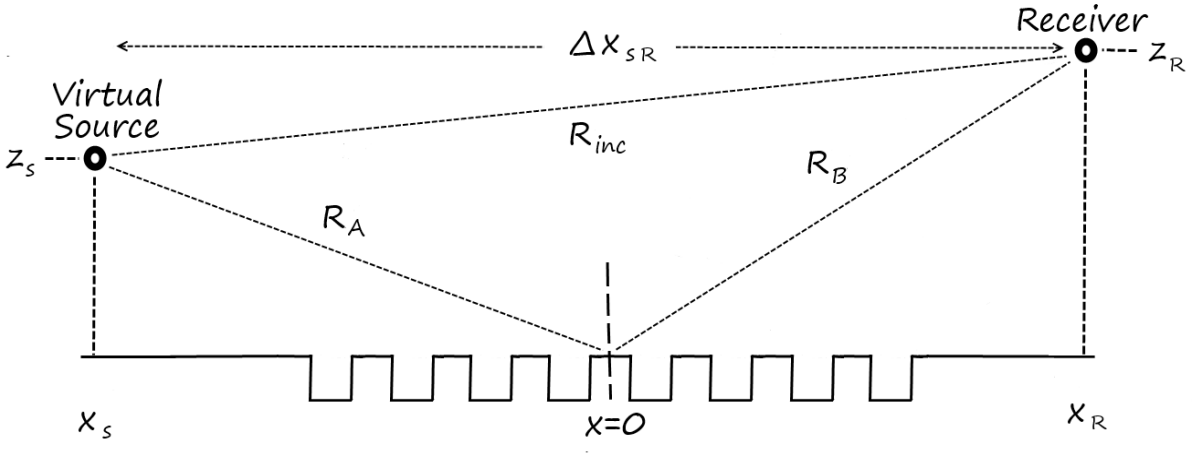

Figure 6.8 Path-length difference approximation geometry.

The ray-path length R_{inc} of the incident wave is given by,

$$R_{inc} = \sqrt{\Delta x_{SR}{}^2 + (z_R - z_S)^2} \tag{6.76}$$

With the 'specularly reflected' component ray-path length R_{ref} being,

$$R_{ref} = R_A + R_B = \sqrt{(-x_S + z_S)^2} + \sqrt{(x_R + z_R)^2} \tag{6.77}$$

Ordinarily the relative amplitude difference between the incident and specularly reflected components due to the spreading-loss would simply be the ratio of the two distances. For the spherical case the amplitude spreading loss factor is proportional to $1/R$ and for cylindrical spreading to $R^{-0.5}$. For this application though the incident amplitude is defined at the origin x=z=0 and consequently this defines the amplitudes of all of the modal components. Being plane-waves, they do not suffer from spreading losses and so their amplitudes are invariant with distance and one may assume their value at the receiver point is the same as at the origin. Using this as a reference, then apparent incident amplitude can be modified at the receiver to approximate spreading losses caused by the path-length difference. Because the reflected mode is the reference, the apparent amplitude of the incident wave must be increased at the receiver to simulate its shorter path to the receiver. The final approximation in this method is that due to the amplitudes being defined at the origin and not at the source point itself. The path length spreading-loss will apply only over the path from the origin (point of specular reflection) to the receiver for the reflected component. For most typical geometries R_A is approximately equal to R_B and so for simplicity the total source to receiver distance can be halved (see factor of ½ in Eq. (6.78)). The reflected wave path length difference is then referenced from the origin to receiver, but no such apparent point can be defined for the source location as the relationship between planar and spherical/cylindrical waves breaks down. Given that the geometry of typical acoustic problems of this nature generally have a small vertical source-receiver separation when compared with the horizontal distance it will suffice to assume that the source-receiver distance is also halved. This assumes that the apparent source is now located above the origin. This is expressed as follows as a scaling factor to the incident wave component α.

Let the path length loss ratios between the incident and reflected compontents be,

$$\frac{1/R_{inc}}{1/\left(R_A+R_B\right)}=\frac{R_{ref}}{R_{inc}} \quad \text{for spherical spreading and,}$$

$$\frac{1/\sqrt{R_{inc}}}{1/\sqrt{R_A+R_B}}=\frac{\sqrt{R_{ref}}}{\sqrt{R_{inc}}} \quad \text{for cylindrical spreading.}$$

An emperical factor of 1/2 to approximate the displacement of the source strength definition to the point of specular reflection as mentioned in the preceeding text is added and the equation is scaled to be a factor of the incident pressure amplitude to give,

$$\alpha_S \approx \frac{1}{2}\left(\frac{R_{ref}}{R_{inc}}-1\right)+1 \quad \text{for a spherical source and,} \tag{6.78a}$$

$$\alpha_S \approx \frac{1}{2}\left(\frac{\sqrt{R_{ref}}}{\sqrt{R_{inc}}}-1\right)+1 \quad \text{for a cylindrical source.} \tag{6.78b}$$

Applying this to the acoustic pressure field equation solution for the whole of free-space gives the new equation denoted by a double-prime,

$$p''_{tot}(x,z>0)=\alpha_s\, p_i + p_r + \sum_{m\neq 0}\delta_{\theta 2}^{\theta 1}(\theta_m)\,\delta_{x2}(\hat{k}_{zm},x_R)\,p_m \quad -M\le m\le M \tag{6.79}$$

A spherical source will be applied henceforth to allow direct comparison with the results of Bashir [31] in section 6.3.9 which assume a spherical source. Furthermore a spherical source is often utilised in point-to-point acoustic propagation problems involving 2d structures. An example being the situation of a localised stationary noise source with the ground structure extending far in the perpendicular direction to the source-receiver, allowing the problem to be tackled in 2d in the plane of the source-receiver. However the choice is arbitrary and for other applications cylindrical line source would be more appropriate, such as when the noise source is like a busy road.

6.2.7 Calculating effective impedance

From the equations derived for the pressure field is it possible to calculate an effective impedance Z_{eff} of the groove-grating surface which is normalised to the characteristic impedance of air Z_C. The modal-model assumes plane-waves throughout so given the plane-wave reflection coefficient [37] it is a straightforward algebraic task to rearrange

this in terms of Impedance. The plane-wave reflection coefficient, Γ_P, is given by,

$$\Gamma_P = \frac{\cos\theta - 1/Z_{eff}}{\cos\theta + 1/Z_{eff}} \tag{6.80}$$

Applying this to the point-to-point propagation problem of the form of figure 6.8 but assuming plane wave propagation along the direct and ground reflected ray paths, the total pressure field at the receiver for a unity amplitude source is therefore,

$$p(x_R, z_R) = \exp(ikR_{inc}) + \Gamma_p \exp(ik\left[R_A + R_B\right] \tag{6.81}$$

The reflection coefficient will be proportional to the ratio of the scattered field plus the reflected component and the incident wave. However for this application a phase term for the path length difference between the incident and reflected rays must be included to obtain the reflection coefficient of the surface alone. Otherwise the phase difference due to the geometric path length difference would be erroneously included in Γ_p. This leads to the plane-wave reflection coefficient below, where it is simpler to add the path-length difference to the incident wave rather than subtract from the scattered as the incident is just one term whereas the scattered field is the complete modal set.

$$\Gamma_P = \frac{p_r(x_R, z_R) + \sum_{m\neq 0} p_m(x_R, z_R)}{p_i(x_R, z_R).\exp(ik\left[(R_A + R_B) - R_{inc}\right])} \tag{6.82}$$

The *exp*() term is the phase term corresponding to the phase difference due to path-length difference. The pressure terms at the receiver point are known from the free-space field solution to the modal-model.

This analysis is based upon specular reflection and so the resulting impedance is merely an effective value, valid only for the given pressure field obtained from the modal-model for the geometry and frequency with which it was solved. The effective impedance of the groove grating can therefore be considered as non-locally reacting where the impedance will depend upon angle of incidence and also the geometry for which the modal-model was solved. Rearranging Eq. (6.80) to find Z_{eff} from the reflection coefficient calculated from the results of the modal-model gives,

$$Z_{eff} = \frac{(1+\Gamma_P)\sec\theta}{1-\Gamma_P} \tag{6.83}$$

The scattered and incident fields may be expressed with or without the finite-grating and spreading-loss approximations, although these approximations will later be found to improve correlation with BEM models.

The advantage of deriving the impedance for the surface as opposed to just manipulating the pressure fields to yield the required information is that the effective impedance Z_{eff}, is approximately independent of the wave type so the effective impedance of the surface remains valid whether planar, spherical or cylindrical waves are assumed. This allows the plane-wave assumption to be decoupled from from further analysis and manipulation. The model will be locally reacting and so the impedance must be recalculated for any change in angle-of-incidence or geometry.

As a matter of interest were the modal-model cylindrical/spherical then the spherical reflection coefficient would have to be solved to yield impedance which would not be a trivial algebraic task as it is for the plane-wave form.

6.2.8 The excess-attenuation spectrum

The effective impedance derived from the modal-model will now be used to provide a model for predicting the behaviour of cylindrical or spherical waves for point-to-point acoustic propagation problems.

The excess-attenuation spectrum is a quantitative measure of how a ground surface affects the sound field when compared to the ambient free-field situation without the ground surface. It is similar in principle to the insertion-loss of a component in electronics. The excess-attenuation, or EA for short, curve is generally expressed in dB relative to the free-field conditions. The free-field conditions with no ground surface are just the incident pressure p_{inc}. The acoustic ground surface under test is the groove structure at z=0. The EA plot will therefore show the gain/attenuation in the free-field caused by the presence of the ground where the free-field conditions are considered as the 0 dB reference. The plots will be in terms of acoustic pressure.

The EA spectrum will be calculated from the known source-receiver geometry and the effective impedance Z_{eff} calculated from the extended modal-model. The model-geometry is that of a point source-receiver above an impedance plane as shown in figure 6.9,

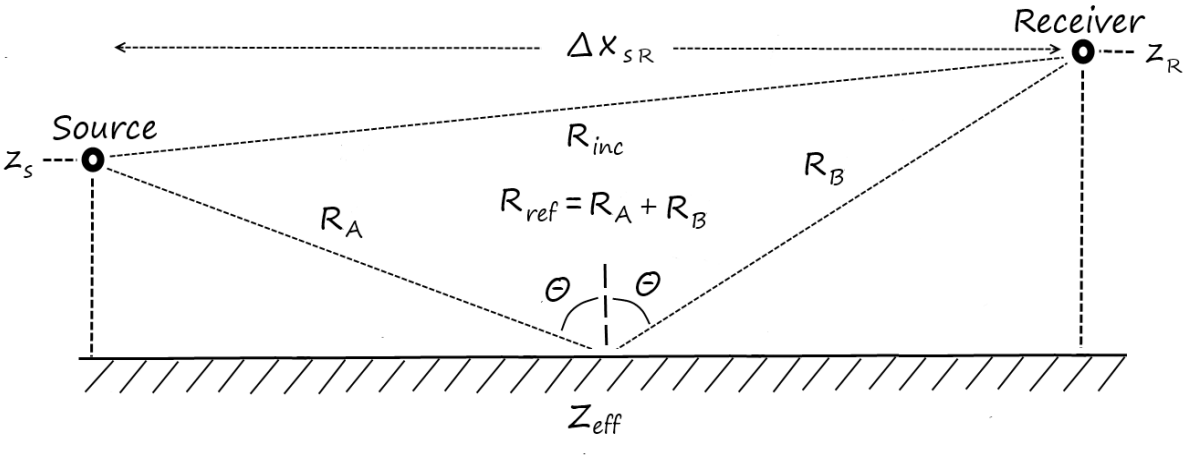

Figure 6.9 Point-to-point acoustic propagation above an impedance ground plane.

This is a widely applied model for outdoor acoustics problems because many situations can be modelled by such a scheme (see section 1.4). A single point source and receiver are located above a ground surface at heights z_S and z_R respectively and separated by the horizontal distance Δx_{SR}. Either spherical or cylindrical spreading may be applied to the source depending upon the application, where spherical spreading would be suitable for localised noise sources such as a compact compressor or individual vehicle whereas the cylindrical case would infer a line source more suited to busy roads or large towns. An effective impedance Z_{eff} is used to characterise the ground surface and with that comes the assumption of homogeneity and that the surface features are small enough when compared to the exciting wavelength so as to preclude scattering and cause only specular reflection. On this assumption the total field at the receiver is the combination of an incident component which has traversed the path of length R_{inc} (given by Eq. 6.76) and a specularly reflected component, having taken the path $R_{ref}=R_A+R_B$ (as in Eq. 6.77) and been reflected by the ground with coefficient Γ. The angle-of-incidence upon the ground from the incident component will be given by,

$$\theta = \tan^{-1}\left(\frac{\Delta x_{SR}}{z_S + z_R}\right) \tag{6.84}$$

The path-lengths of the incident and reflected paths provide the magnitude of the cylindrical/spherical spreading losses while the impedance of the ground surface defines the magnitude and phase of the reflection via the reflection coefficient Γ. For this work we will apply henceforth, the spherical reflection Γ_S of Chien and Sorokka [37] as defined in

Eq. (6.85).

$$\Gamma_S = \Gamma_P + (1-\Gamma_P)F(w)$$

where,

$$F(w) = 1 + i\sqrt{\pi}.w.erfc(w)$$

and w known as the numerical distance is,

$$\text{w}=1+\left(i\sqrt{\frac{i}{2}k\left(R_A+R_B\right)}\right)\cos\theta+\frac{1}{Z_{eff}} \tag{6.85}$$

where *erfc*() is the complementary error function and Γ_S is often referred to as the spherical wave reflection coefficient. The wave-number k is that of the source as given by,

$$k=\frac{\omega}{c_0}=\frac{2\omega f}{c_0} \tag{6.86}$$

Where as before c_0 is the speed of sound in the medium, assumed to be inviscid air in this instance and f is the temporal frequency of the source.

The spreading-loss factors for pressure amplitude for each wave form are as follows, where R is the ray-path distance.

$$L_P = 1 \text{ for plane waves (no spreading loss)}$$

$$L_C(R)=\frac{1}{2\pi\sqrt{R}} \text{ for cylindrical waves } (\propto 1/\sqrt{R})$$

$$L_S(R)=\frac{1}{4\pi R} \text{ for spherical waves } (\propto 1/R) \tag{6.87}$$

The Intensity or energy spreading losses would be the square of each of these but the EA spectra are being expressed with respect to acoustic pressure. Bringing this altogether and assuming spherical waves for the 2d case gives the expression for EA in decibels of,

$$EA_{dB}(f)=20\log\left(\left|1+\frac{\Gamma_S L_S(R_{ref})\exp(ikR_{ref})}{L_S(R_{inc})\exp(ikR_{inc})}\right|\right) \tag{6.88}$$

The EA given by this equation will provide the acoustic response at each given frequency point and so sweeping the required frequency range will produce the full EA curve over the chosen bandwidth. Because this equation involves a ratio the absolute amplitude of the source is not important, it is simply the ratio between the incident and reflected amplitudes at the receiver which is of interest. As the two paths originate from the same source the

amplitude and phase relationships are automatically conserved. A spherical source is shown in Eq. (6.88) but for a cylindrical source L_S can be substituted for L_C.

6.2.9 Justifying the method

The rationale for the approach of characterising the grooved structure as Z_{eff} is clear to see in figure 6.10, which shows a comparison between the results obtained from simply plotting the plane wave field obtained directly from the modal model versus doing so via an effective impedance in the point to point model for spherical spreading. In the plane wave plot the surface wave which would be induced by the grating under spherical/cylindrical excitation is not present whereas it is when using the method presented in this chapter. This is because the evanescent modes in the plane wave field are simply boundary modes [41] (or ground waves [68]) which exist only in the presence of the incident wave in order to satisfy the boundary conditions of the grating and do not propagate in isolation as does a true surface wave. The plane wave is not exciting a surface wave and will not do so in the vast majority of cases [68]. However, the surface wave component is implicit in Z_{eff} as a pole in the reflection coefficient Γ_S and therefore will be present in the prediction of the point to point propagation model.

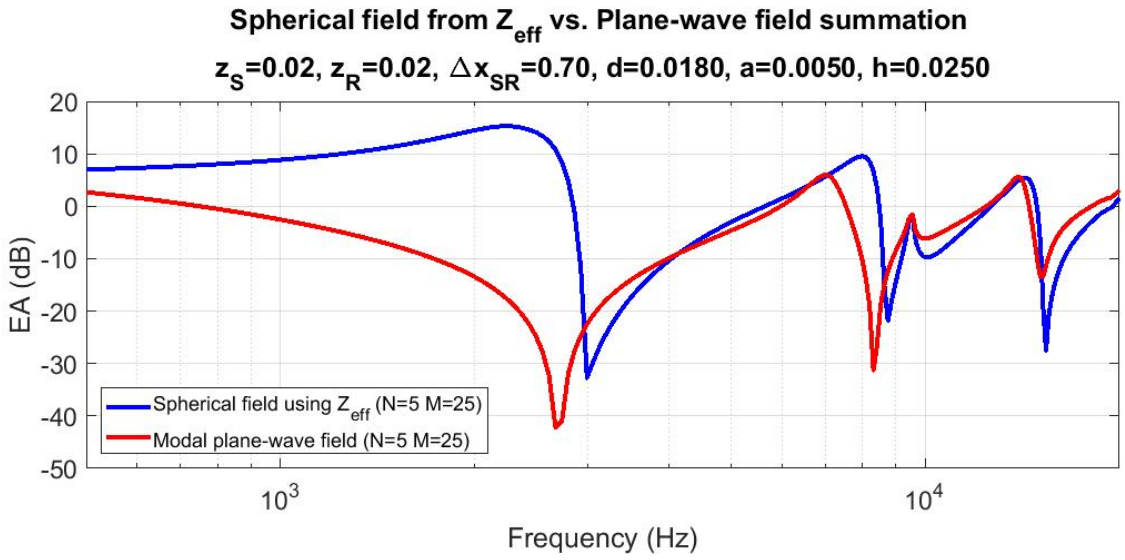

Figure 6.10 Z_{eff} approach versus direct plane wave summation.

As the plane wave summation fails to predict the surface wave, with peak frequency of

around 2.2 kHz in this example, there is no similarity between the methods in the low frequency range upto the first minima. Beyond this though, at frequencies where the surface wave has lost its influence, the agreement is fair and it may be argued that the direct plane wave summation could have some relevance to the point to point propagation problem in specific circumstances such as at high frequencies or geometries where the surface wave is not dominant such as high source-receiver heights but its potential application is too restrictive to warrant further study in this research.

6.3 Results

6.3.1 Introduction to results

The results from the extended 2d modal-model are presented henceforth which has application in outdoor acoustics. The results are in the form of excess-attenuation spectra for point-to-point propagation above a ground plane with effective impedance Z_{eff}. The geometry of the problem is as described in previous sections. The values enclosed in '[ ]' within the legend of forthcoming plots are standard errors (SE) for each model prediction with reference to the BEM model unless otherwise stated and using the following formula,

$$SE = \sqrt{\frac{1}{n}\sum_{f_n}\left|EA_{reference}(f_n) - EA_{predicted}(f_n)\right|^2} \tag{6.89}$$

The standard error was chosen as it is a widely accepted method for quantitively assessing the goodness of fit between two data sets. For qualitative appraisal we are particularly interested in the accuracy with which excess-attenuation minima and maxima are predicted because these are often tuned in acoustics applications to remove particular nuisance frequencies and so need to be predicted accurately. The magnitude agreement at minimum points is not so critical because these are sensitive to small errors because the pressure levels in these regions are very low. In the low frequency region, the prediction of the slope and magnitude of the surface wave will be of particular interest because many applications involve analysis and manipulation of the surface wave induced in a periodic surface. Also the agreement in characteristic curve shape is important because it gives some suggestion that the fundamental phenomena are being modelled accurately.

To begin with, results showing the effect of the grating structure pitch *d*, aperture width *a*

and groove depth h for a given geometry will be presented in order to provide an insight into the effect of each of the grating parameters. This also has the effect of varying the ratios between the parameters. The simulations were run with 500 frequency points as this gives good definition around the EA minima which can be sharp, so fine detail is easily lost with too few frequency steps. Subsequent sections present results for varied source-receiver geometries and were run with the reduced resolution of 100 frequency steps as this was sufficient to capture all relevant phenomena for the cases shown. For all simulations the number of m-modes M and n-modes N were defined as 25 and 5 respectively. The solve time for the extended 2d modal model was in the order of 15 seconds for the lower resolution plots and around 60 seconds for the greater number of frequency steps on a 2010 vintage mid-range personal computer.

The bulk of the plots have a frequency span of 20 Hz to 4 kHz and the speed of sound has been defined as 343.2 ms^{-1}. For the purposes of the pseudo-finite grating approximation, as defined in the 'Implementation' section, the grating structure has been defined to begin at the x-location of the source and end at the x-coordinate of the receiver unless otherwise stated. All boundaries of the grating structure and ground have been defined as acoustically hard, having infinite impedance.

For each plot the results obtained from the modal-model derived impedance will be compared with predictions from BEM and the Attenborough slit-pore model [28] for the given geometry. Both methods have been presented in Chapter 4. The slit-pore has been included as a reference method because it has been shown by Bashir [31] to successfully approximate closely spaced rectangular grooves within given constraints that will be explored later.

For the BEM simulations and unless otherwise specified, 100 frequency steps were used with a mesh size of 0.008 m and hard ground assumption, giving solve times ranging from 10 s up to many minutes.

The final reference on each curve is a cursor line that represents the cut-off frequency for mode m=-1 which near grazing incidence will be the first scattered mode to propagate free-space. Below this frequency only the specularly reflected mode m=0 will propagate in free space and all other free-space modes will be evanescent in z. This is included as it is

expected that the Slit-pore model will perform less well above this frequency because of its assumption of homogeneous ground which assumes the incident wavelength is much greater in magnitude than the feature sizes of the ground and hence no scattering.

6.3.2 Discussion

It is prudent to summarise the key attributes of the modal, BEM, slit-pore models in order to provide intuition into how they may be successfully applied and to add context to the forthcoming results. Thermo-viscous losses are implicit only in the slit-pore model whereas the other models are inviscid. For this reason the slit-pore may be expected to be the most accurate at frequencies far below the onset of scattering f_{LS} and where the viscous boundary layers are comparable to a which occurs as $\lambda >> a$. However for decreasing λ with respect to a the visco-thermal contributions of the slit-pore model Eq. (4.28) will become increasingly negligible for a given d and h and the response will tend to simple lossless *coth*() periodicity. In this case the slit-pore equation will simply be modelling the impedance due to the lossless time-of-flight interaction of the plane wave mode within the grooves and hence will be unreliable especially near the onset of scattering or when more than just the plane wave mode propagates the grooves. The slit-pore model assumes only homogeneous plane wave motion within a homogeneous ground structure with the assumption $\lambda >> a$, precluding scattering effects which will occur as $\lambda \approx d$ (and a via inference from d). In fact the slit-pore model is inherently incapable of predicting losses due to scattering because they occur as $\lambda \approx a$ and persist as $\lambda < a$ (for given a/d) but the thermo-viscous losses reduce as λ/a decreases and so in the region of scattering the slit-pore model will tend towards lossless. The slit-pore model is expected to be effective outside of the $\lambda >> a$ assumption under certain circumstances where the effective impedance of the grooved grating surface is dominated by the time-of-flight of the plane wave mode within the grooves and when the frequency band of interest is far below the onset of scattering where diffractive scattering losses are negligible and the dominant process is the behaviour of the plane wave mode within the grooves. Bashir [31] also suggests that the slit-pore model may become unreliable when $a < h$ because of the near field effects which dominate at the aperture when the depth is small when compared with the aperture width a.

The modal model is a non-homogeneous model, comprising a continuum of discrete grooves, whose phase terms interfere constructively and destructively to approximate the complex scattered field. BEM also accounts inherently for scattering which will occur as

the wavelength of the incident wave becomes comparable in magnitude to the pitch of the grating structure *d.* For a given angle of incidence and grating pitch *d*, scattering begins as the frequency increases beyond a critical value or conversely for a given frequency, as *d* is increased beyond a critical length. One would therefore expect the modal and BEM models to be the most accurate for problems involving scattering. Also for a given geometry, thermo-viscous losses diminish with increasing frequency further aiding the accuracy of the modal and BEM models for high frequency or large *d*.

From this discussion it is clear that the slit-pore model may cease to hold if any scattered mode is free-space propagating because it assumes purely specular reflection. If $|\alpha_m|$ (the *x*-axis wave number of mode *m*) exceeds $|k|$ then the mode is evanescent in *z* with an imaginary *z*-axis wave number β_m and thus not free space propagating, providing a general condition of validity for the slit-pore of,

$$\left|\alpha_m\right| \le \left|k\right| \quad M \ge m \ge -M \wedge m \ne 0 \tag{6.90}$$

where *M* is the truncation parameter of the free-space *m*-mode set of the modal model. For a given geometry this represents a high frequency scattering limit f_{LS}, above which scattering will occur and the homogeneous ground assumption, upon which the slit-pore model relies, will cease to hold. At near grazing incidence, every scattered field exhibiting free-space propagation will include the *m*=-1 mode. As a consequence the condition of Eq. (6.90) can be simplified further at near grazing incidence to,

$$\left|\alpha_{-1}\right| \le \left|k\right| \quad \pi / 2 > \theta > 0 \tag{6.91}$$

which is dependent solely upon the relative magnitudes of α_m and the pitch of the grating, *d*. The groove depth *h* and aperture width *a*, will affect the magnitude of the scattered components but not their propagation characteristics. Therefore the slit-pore model may hold outside of the limits imposed by Eq. (6.90) if the magnitudes of scattered components are negligible, such as when $h \to 0$, $a \to 0$ or $a/d \to 0$. The f_{LS} condition is not exhaustive as the effectiveness of slit-pore model was found by Bashir [31] to be dependent also upon porosity which is the ratio of *a*/*d*.

6.3.3 The effect of grating pitch, *d*

The effect of varying the grating feature pitch d is explored which is akin to varying the ratio a/d while keeping a constant. A sweep from 0.1 m to 0.5 m was applied while keeping the aperture width a and groove depth h constant. The source-receiver locations will be kept constant at heights of 0.2 m with a horizontal separation of 2 m.

The modal-model and BEM results agree well. The slit-pore model also agrees well in the first result due to the fact that throughout the majority of the spectrum the incident wavelength is much larger than d and the ratio of a/d is high, so in this region the ground will behave predominantly as a hard ground surface at $z=-h$. The low-frequency response (below the onset of scattering) is therefore dominated by the simple time-of-flight delay of the wave as the ledges of the groove are so narrow that their contribution to the response is small. However as the porosity ratio reduces the slit-pore model loses effectiveness in the whole frequency band indicating that the slit-pore model has an operating limit upon its porosity parameter as well as the general frequency limit imposed by the proliferation of scattering.

Observe that the general trend of increasing pitch d does not greatly effect the position of EA minima features but rather affects their amplitude. Intuitively this may be explained by the diminishing scattering effect of the grooves as the aperture lessens in proportion to the ledge extent of the structure causing the ground to tend to a hard ground plane at $z=0$ with increasing pitch d for fixed aperture width.

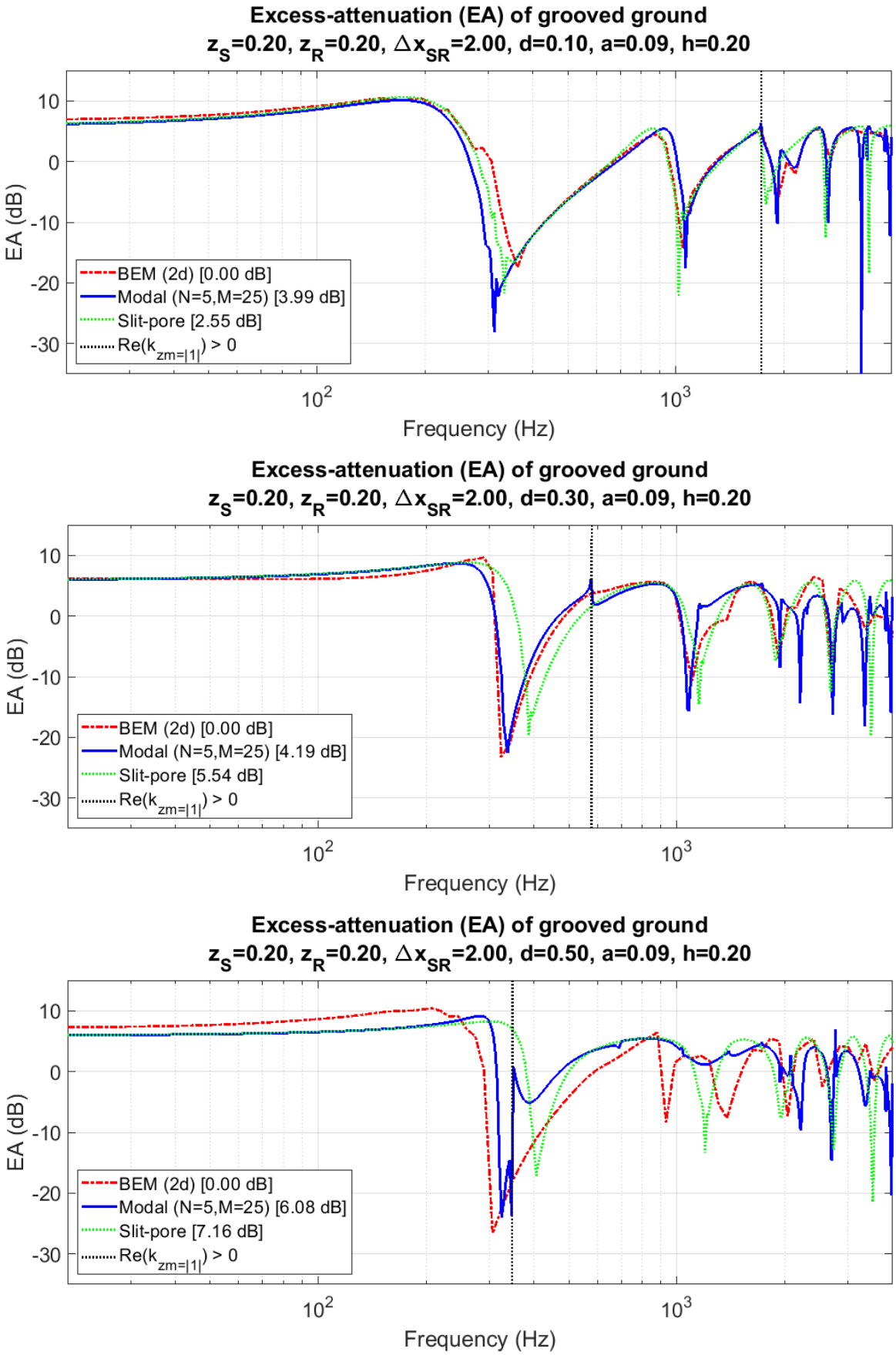

Figure 6.11a-c Excess-attenuation plots with varying grating pitch d in the range 0.1 m to 0.5 m with aperture a=0.09 m and groove depth h=0.2 m.

6.3.4 The effect of aperture width, *a*

Following are plots showing the variation in response to varying aperture width *a*. Once again this has the effect of altering the *a*/*d* ratio but in this instance *d* remains constant while *a* is swept. The geometry of the scene will be kept constant with source-receiver heights of 0.2 m and a horizontal source-receiver separation of 2 m. The grating structure will have a fixed pitch, *d* of 300 mm and groove depth *h* of 200 mm. Aperture width *a* will be swept from *d*/3 up to just under *d*.

As one would expect this sweep has little effect on the first EA minima which is governed primarily by the time-of-flight phase shift caused by the plane wave mode propagating the depth of the groove.

However increasing the aperture width has caused the higher order waveguide modes ($n>0$) to be excited at lower frequencies. This is because the cut-off frequency of each *n*-mode is lowered with increasing aperture width. Consequently the higher order EA peaks are reduced in frequency with increasing aperture width as a direct result of the higher order waveguide *n*-modes being excited lower down in the frequency band and coupling with the free-space scattered modes.

Once again the slit-pore model is in agreement for the first EA minima but fails to hold beyond this in the frequency band as would be expected for such large grating feature sizes. The groove grating structure in this case is comparable in magnitude to the exciting incident wave and so significant scattering behaviour is observed and the assumption of porous ground for the slit-pore certainly does not apply. The scattering behaviour being caused by significant excitation of higher order waveguide modes within the aperture and their associated coupling to the scattered free-space modes and associated free-space diffraction from the apertures.

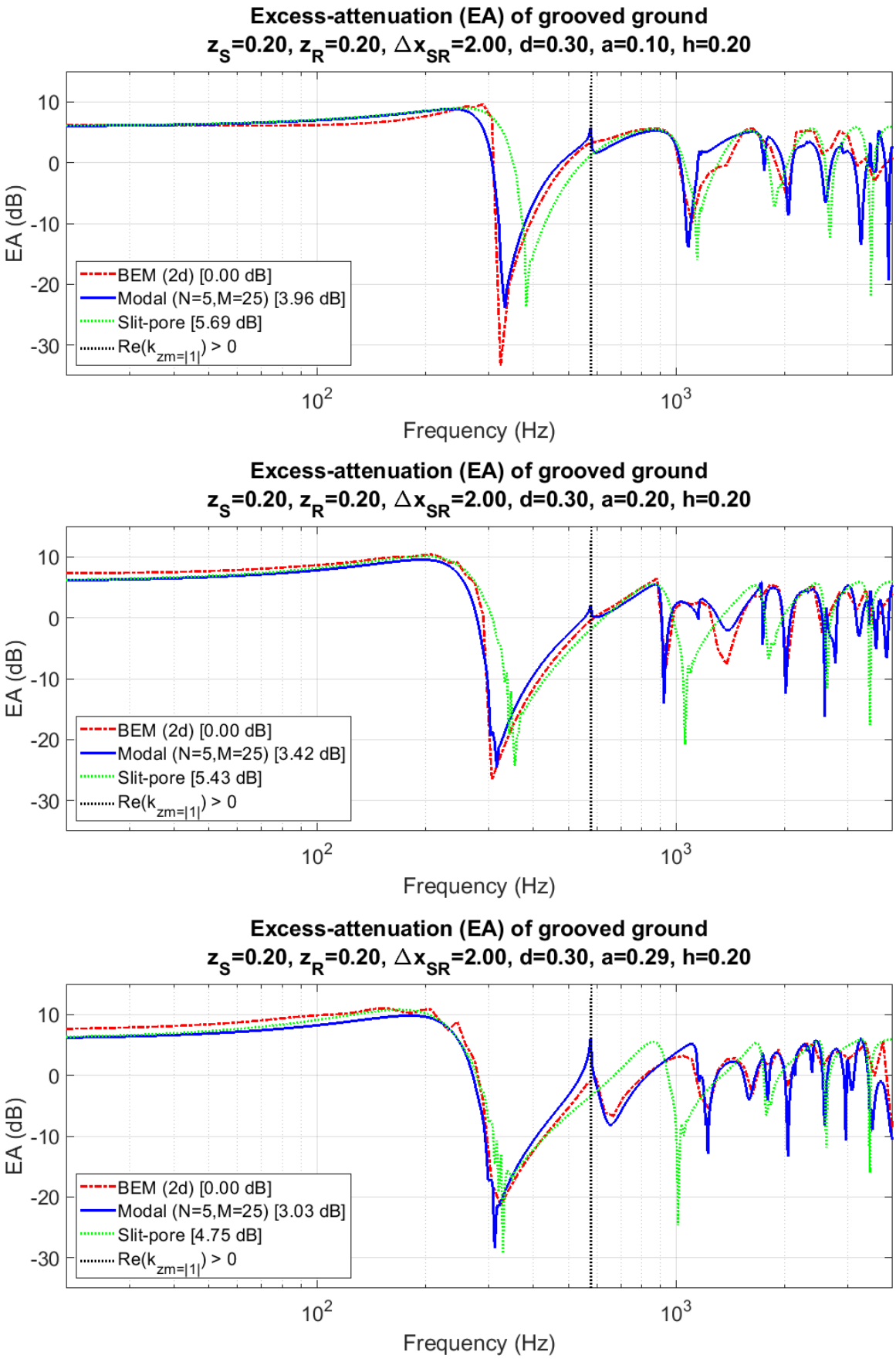

Figure 6.12a-c Excess-attenuation plots with varying aperture a from 0.1 m to 0.29 m.

6.3.5 The effect of groove depth, *h*

Finally the groove depth h was varied from 0.1 m up to 0.3 m with a fixed pitch d of 0.3 m and aperture width a of 0.2 m. The ratio a/d is held constant and the effects of the ratios a/h and d/h by inference are shown.

Notice that altering the groove depth does not affect the first m-mode cut off frequency because it is dependent upon only the grating pitch d. However the amplitude of the n-and m-modes will be affected by the depth. The groove depth relative to the incident wavelength will affect the amplitude of any given mode due to the time-of-flight of the mode in the groove and the interaction this causes at z=0 between the down going incident and up going reflected wave. As h tends to zero the response tends to hard ground response as the modal amplitudes are so small because of near field effects and at zero depth not allowing any modal normal velocity amplitude due to no phase shift between the incident and reflected components. As h is increased the impedance at z=0 will vary periodically due to the phase difference caused by traversing the groove. This effect may also cause a corresponding EA peak to vary periodically with h. As h increases from zero the EA peak will lower in frequency until h reaches a given fraction (or multiple depending upon the order of the mode) of incident wavelength. This represents an EA frequency minima where further increasing h will cause the EA peak to increase in frequency until it reaches its original location when h was zero and the equivalent phase shift of the reflected wave at z=0 is a multiple of 360 degrees. This periodic behaviour continues ad infinitum with increasing h.

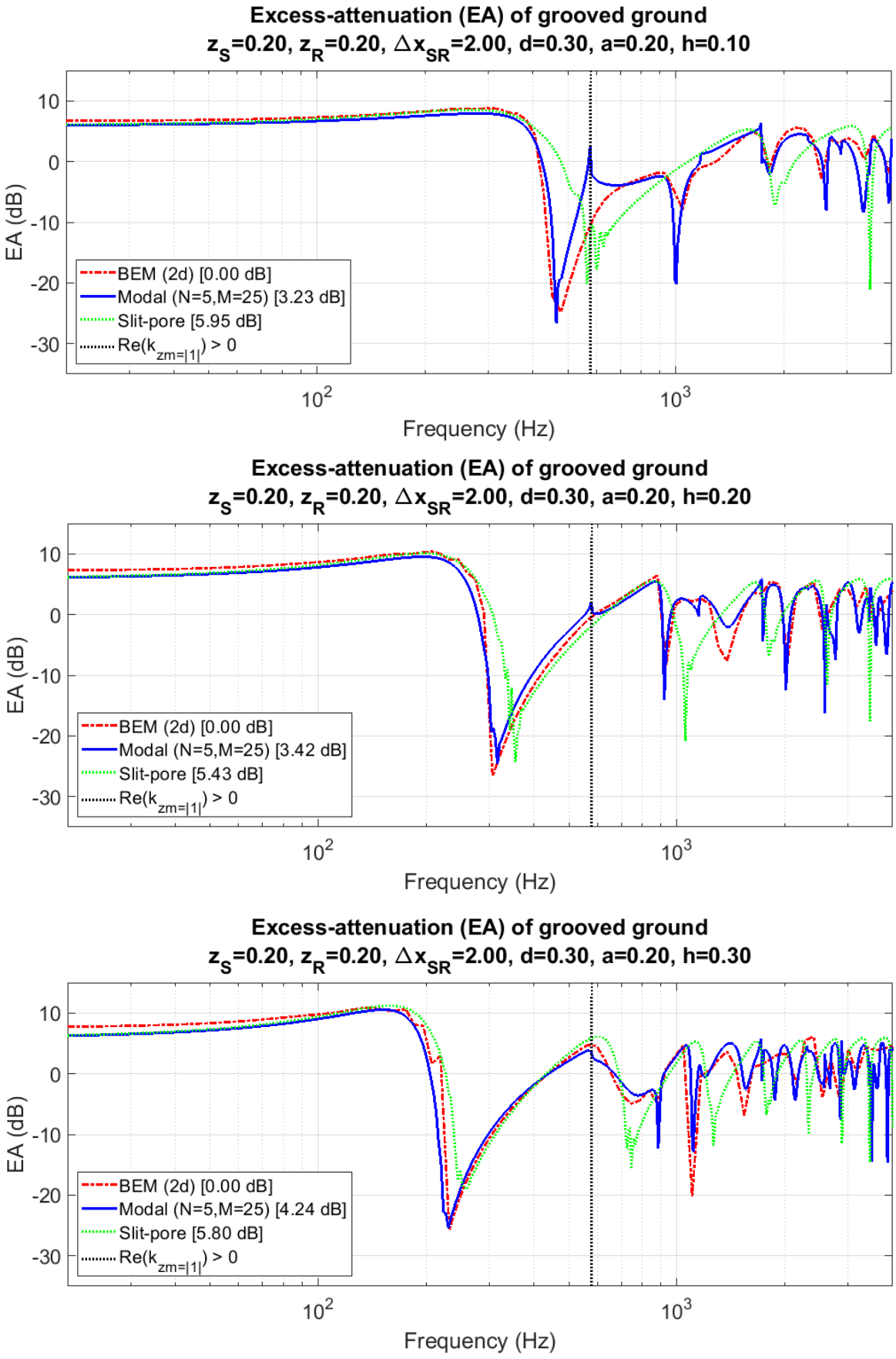

Figure 6.13a-c Excess-attenuation plots with varying groove depth h from 0.1 m to 0.3 m.

6.3.6 Effects due to scattering

The effect of altering the frequency at which scattering occurs f_{LS} will be investigated and while the results show this not to be particularly significant for the modal and BEM models it is so for the slit-pore model. Extensive testing shows the condition of Eq. (6.90) to hold as a high frequency limit of the slit-pore model, above which it may be in significant error due to the onset of scattering. Presented is a representative sample of results in the frequency range 100 to 4000 Hz where the vertical cursor represents the scattering limit, f_{LS}, condition of Eq. (6.90). The chosen source-receiver geometry is similar to that used in several outdoor measurements [31, 46-48] and the grating dimensions chosen to result in a primary EA minimum near 1 kHz which would be relevant to reducing road/tyre noise. The symbol Omega Ω represents the porosity ratio a/d.

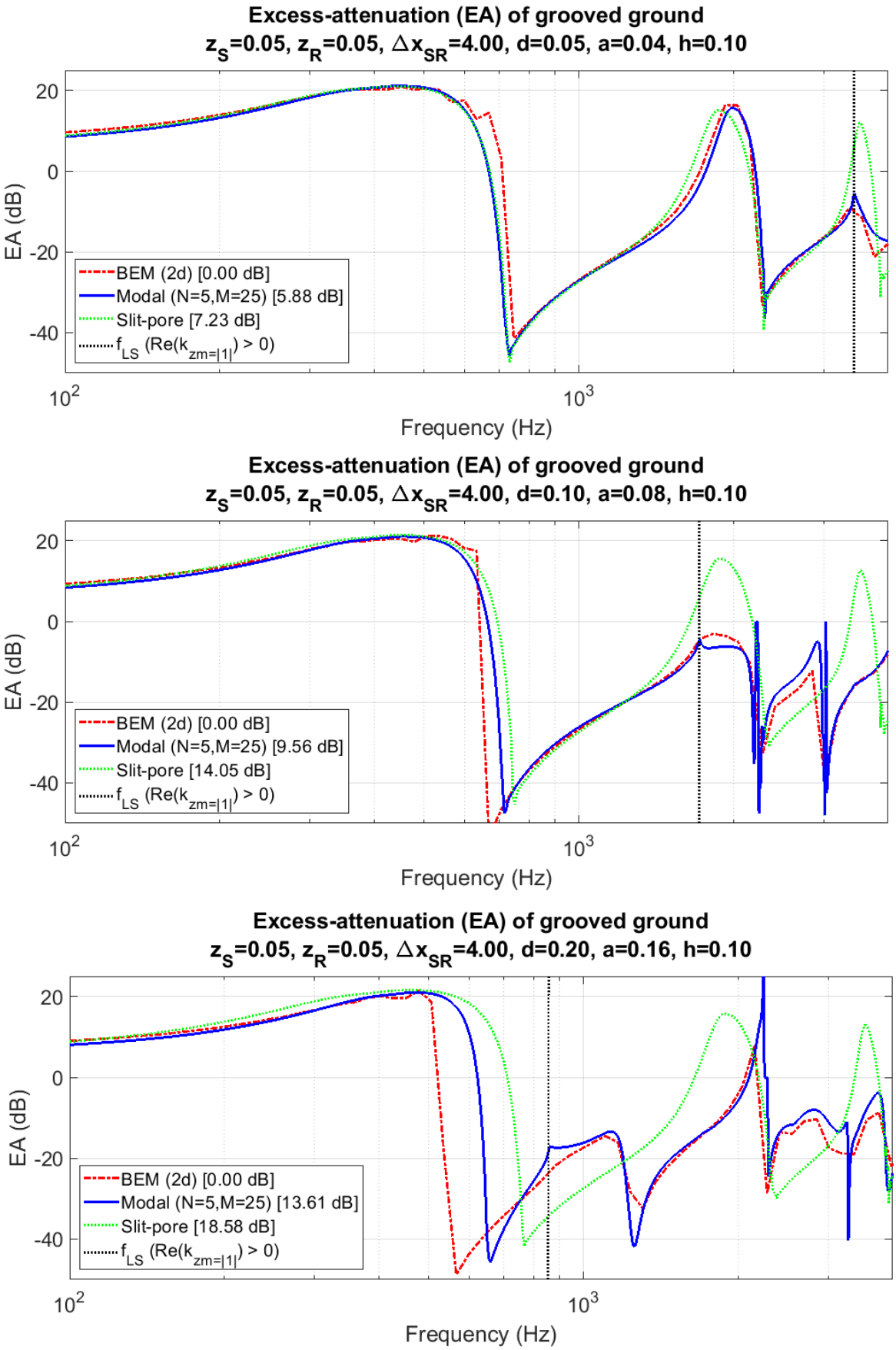

Figure 6.14a-c.EA Spectrum results for a) Ω=0.8, d=0.05, a=0.04, h=0.1, b) Ω=0.8, d=0.1, a=0.08, h=0.1 and c) Ω=0.8, d=0.2, a=0.16, h=0.1.

It can be seen generally that the slit-pore prediction may fail beyond f_{LS}, but is reliable at frequencies below this. For figure 6.14a all models agree up to around 3 kHz where the limit of scattering is reached and the homogeneous ground assumption ceases to hold. The thermo-viscous losses implicit in the slit-pore model may be observed in the lesser magnitude first EA minima when compared with the BEM and modal models. For the mid-sized ground features of figure 6.14b the BEM, modal and slit-pore models are largely in agreement to just above f_{LS}. In the predictions for the largest scale of structure in figure 6.14c the modal model and BEM predict the complex nature of the EA curve caused by the extensive scattering behaviour. They differ by around 100 Hz in predicting the first EA minima but this magnitude of difference is about as large as we have seen throughout our research. Furthermore we have consistently encountered unresolved issues with modal-model and BEM agreement for very low source-receiver heights as seen in figure 6.14c. The prediction of the first EA minima of the slit-pore model also differs slightly yet the response agrees in shape with the modal model below f_{LS}, but thereafter there is little in common with the BEM or modal curves.

Bashir [31] concluded empirically that the slit-pore model is applicable for rectangular grooved gratings at incidence angles near grazing so long as 1) the wave-length corresponding to the first EA minima is four times larger than *a,* and 2) that $a<h$. Condition 1 is independent of *h,* but it cannot be valid for all values of *h* since the first EA minimum frequency f_{EAmin} and magnitude depend on *h*. As *h* is reduced from a multiple of half of the incident wavelength, f_{EAmin} increases towards f_{LS} (which is *h* independent) and the slit-pore model will become inaccurate. However, condition 1 will still be satisfied regardless of *h* and the resulting proximity of f_{EAmin} to f_{LS}. Condition 1 is therefore unreliable and is proven so by figure 6.15, where the true first EA minimum f_{EAmin} as predicted by the modal-model and BEM is coincident with f_{LS} to within 100 Hz. Yet the slit-pore model is clearly in error while both condition 1 and 2 are comfortably met (slit-pore predicted $\lambda_{EAmin} \approx 13a$ & $a=h/3$). Furthermore condition 1 is posed in terms of *a* rather than *d* which is the truly dependent variable for scattering phenomena, creating a reliability dependence on porosity.

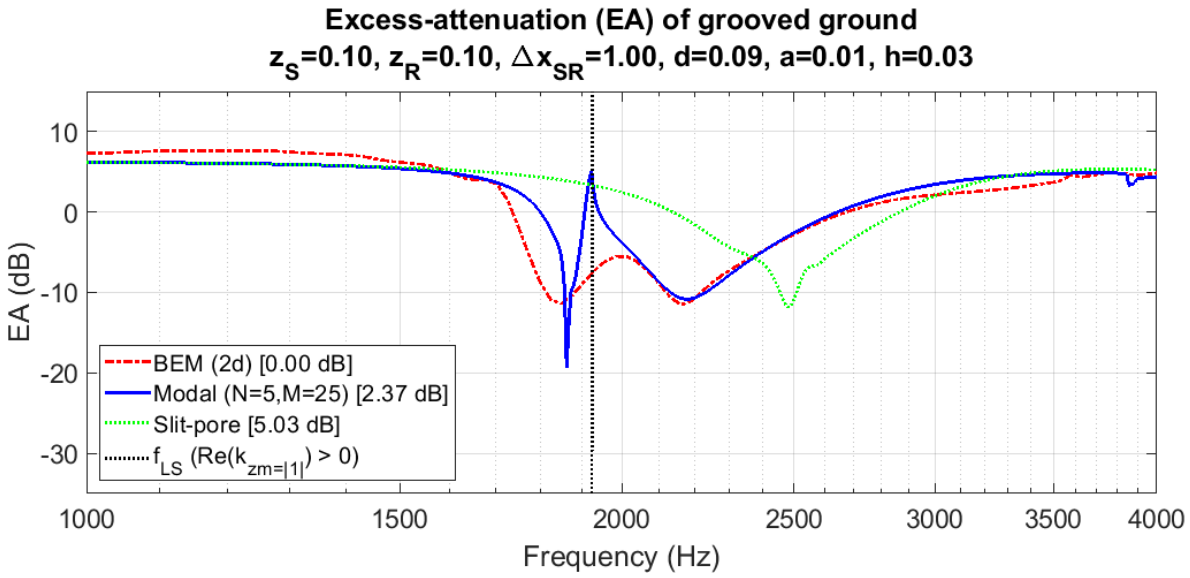

Figure 6.15.EA Spectrum where $f_{EAmin} \approx f_{LS}$ with 1m source-receiver separation, $z_S=z_R=0.1m$, $d=0.09$, $a=0.01$ and $h=0.03m$.

Condition 2 may be more robust, even though it is still posed in terms of a, thereby creating once more a reliability dependence upon porosity. The $a<h$ relationship tends to result in f_{EAmin} being less than f_{LS}, because f_{EAmin} reduces as h increases (up to half the incident wavelength or multiple thereof) and $f_{LS} \rightarrow \infty$ as $a \rightarrow 0$, for a given porosity. The $a<h$ condition assists the slit pore model to be valid near or beyond the first EA minimum. Both conditions are satisfied for figures 6.13a) and b) where the slit-pore model is accurate over bandwidths of 3.3 kHz and 1.7 kHz respectively. For figure 6.14c neither condition is satisfied. The wavelength corresponding to f_{EAmin}, ~0.5 m is less than $4a$ which is 0.64 m and $a>h$. This is consistent with the failure of the slit-pore model beyond f_{EAmin} of ~700 Hz.

Two numerical errors can be seen in the figure 6.14b response curve at just over 2 kHz and at around 3 kHz. The occurrence of such errors is reduced significantly by including the pseudo-finite grating approximation as this helps to eliminate modes which would not reach the receiver for the given geometry. This approximation is added to the model because the core modal-model assumes, in fact requires, that the grating extends infinitely. However this causes a contradiction when the equivalent impedance is derived and applied to a spherical wave ground-plane model where the grating structure does not extend into infinity and the waves are spherical or cylindrical in nature. The numerical errors manifest when the effective impedance of the ground has a negative imaginary part greater in magnitude than the real which causes the complex error function in the spherical reflection

coefficient to operate in the region of an infinite peak causing unrealistic reflection coefficients. It is believed that this error is due to the magnitude of scattered mode energy reaching the source being in excess of what is physically possible and hence violation of energy conservation causes the equations to become unstable. This is partially alleviated by removing modes which would not reach the receiver by means of the pseudo-infinite grating approximation which ensures energy is more accurately conserved. The path length difference approximation also helps in this respect to better predict the energy at the receiver. However both are simple approximations and while not resolving the inherent conflicts they offer a significant improvement.

Evident in the majority of results from the extended modal-model is the discontinuity in the EA response at f_{LS} and is particularly noticeable in figure 6.15. This is caused because at this frequency the first scattered mode becomes free-space propagating and will have a significant influence upon the field at the receiver in two ways. Firstly as the mode becomes free-space propagating it transmits energy and as a consequence of the conservation of energy its proportion must be shared with the zeroth mode. The total energy being that of the incident and for our lossless system all incident energy must be transferred to all propagating modes in proportions given by the solution of the modal-model. Below f_{LS} all incident energy is transferred to the m=0 specular reflection mode but above this the energy will be shared between the multiple propagating modes. The second potential cause for discontinuities at or above f_{LS} is purely geometric and caused by the hard cut-off of modes in the finite grating approximation of the extended modal-model. Modes are included or excluded in the initial plane-wave summation based upon whether their propagation geometry causes their intersection with the receiver which may cause discontinuities due to the sudden cut-on or off of modes.

6.3.7 Surface Wave response

In this section results are presented that relate to the abundance of surface waves which are supported by the grooved grating.

The EA minima are caused by the destructive interference of the incident and ground reflected waves at the receiver. The surface wave is governed by the geometry of the grating and will always manifest as an additional energy contribution at the receiver because it has a different propagation speed from the propagating waves and so does not

have a constant phase relationship with the incident and reflected waves and so will not cause time independent points of constructive or destructive interference with the incident and reflected waves.

It appears from the approaches taken thus far in this research that there will be two discrete but related evanescent wave mechanisms present in our analysis. First there are the evanescent mode terms arising from the incident field to satisfy the boundary conditions at the ground surface and exist only within the presence of the incident field [41,68]. The spherical incident field is non-homogeneous in space and so the horizontal propagation constant of each evanescent mode will vary in sympathy. The incident wavelength projected onto the ground surface increases with horizontal distance from the source in order to satisfy the boundary conditions imposed by the ground surface. The evanescent terms may therefore be considered as a kind of surface mode set and not true surface waves as they would not exist in the absence of the incident field and they have propagation characteristics which vary in space. As an analogy they would be akin to forced-waves as they are created by a forcing source interacting with the ground surface. Secondly the grating structure is itself capable of supporting propagating surface waves in the absence of an incident field which may be thought of as free-waves as they are supported by the geometry of the ground structure itself and in the absence of an incident field. These are true surface waves or boundary modes that will propagate the ground surface in the absence of an incident field. The frequency response of the surface wave will be dependent upon the geometry of the grating (d, a and h). Initially the surface wave is excited by an incident disturbance which creates a complex interaction within the grating, resulting in a self sustaining surface wave. The incident source will setup surface modes which together may act as an energy source to excite the dominant surface wave of the grooved grating structure causing a propagating surface wave that will traverse indefinitely so long as the grating structure remains to support it. The two separate but related mechanisms are therefore the evanescent modes induced by satisfying the boundary conditions in the presence of an incident wave which will vanish in the absence of an incident field and the true surface waves or boundary modes supported by the geometry of the rough surface alone but excited initially by an incident source. Tolstoy [41] considers the distinction between the two evanescent mechanisms in some detail. The dominant surface wave characteristics for a given rectangular grooved grating geometry have been explored using the modal-model by Kelders Allard and Lauriks [8] and more generally by Parrott et al.

[53] amongst many others.

In order to explore the surface wave behaviour its effect must be isolated as far as is practical. The method of expressing the grating as an effective impedance does not allow the free field to be plotted, as the effective impedance depends upon the geometry of the problem so Z_{eff} will change if either the source or receiver points are moved. The surface wave behaviour will therefore have to be inferred by modelling several geometries and collating the results. Ideally the angle-of-incidence will be kept constant because the grating is externally reacting while varying the height of the receiver but the spherical reflection coefficient [37] will assume spherical propagation for the direct and reflected waves but cylindrical propagation for the surface wave so this method would be problematic due to the relative scaling with distance. As a compromise the source-receiver horizontal separation will be kept constant and the height of the receiver varied. This will cause Z_{eff} to vary in each case but this is preferable to the constant AOI method as it exhibits a clear surface wave response which may be approximately characterised. Care must be taken to ensure the surface wave is far lower in frequency than the onset of scattering by using a 'small' grating pitch. The magnitude of the surface wave in each case will be estimated as follows. At frequencies far below the onset of scattering the grating structure may be approximated by a hard flat surface at $z=-h$ providing that the ratio of a/d is close to unity. Given this, then the magnitude of the surface wave can be estimated by subtracting the response were the ground a hard flat plane which will account for the phase shift between the incident and reflected paths at the receiver. Therefore at low frequencies any response above that of hard ground (approximately 6 dB) may be attributed to a surface wave. This assumption does not hold once scattering occurs because the response will no longer be similar to that of hard ground. The geometry for the results in this section will be chosen to satisfy this condition in order to explore the behaviour of the surface wave in relative isolation. To prove that this contribution is indeed a surface wave the excess magnitude beyond that of specular reflection versus receiver height is plotted in figure 6.16 using the equation,

$$\left|SW\right|_{dB} = 20\log\left(\left|1+\frac{\Gamma_S L_S(R_{ref})\exp(ikR_{ref})}{L_S(R_{inc})\exp(ikR_{inc})}\right|\right) - 20\log\left(\left|1+\frac{L_S(R_{ref})\exp(ik(R_{ref}+2h))}{L_S(R_{inc})\exp(ikR_{inc})}\right|\right) \tag{6.92}$$

The result exhibits an exponential decay in magnitude with receiver height approximately

proportional to $exp(8x)$ which is consistent with the behaviour of a surface wave.

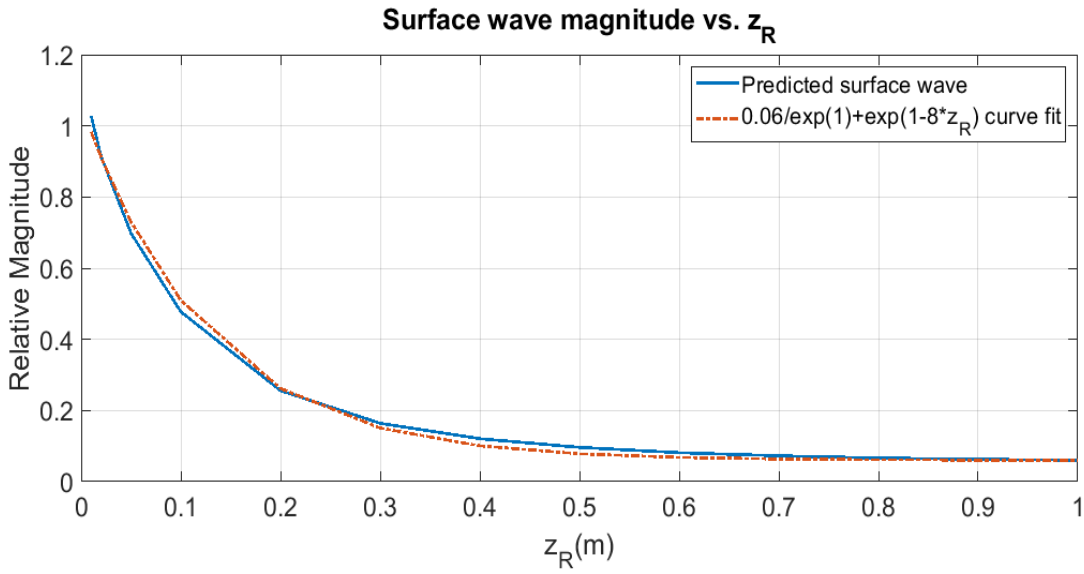

Figure 6.16 Surface magnitude versus height z_S=0.1m, Δx_{SR}=2m, z_R=0.01, 0.02, 0.05. 0.1, 0.2, 0.3, 0.4, 0.5, 0.6. 0.7, 0.8, 0.9, 1.0 m, d=0.05, a=0.049, h=0.05.

Figure 6.18 shows EA plots with agreement in surface wave prediction between the extended modal model, the slit-pore, BEM and the prediction of surface wave component according to Thomasson [52]. The effects that *d*, *a* and *h* have upon the surface wave frequency was explored by applying Z_{eff} to Eq (4.30) of Thomasson, for a sweep of each of the groove grating geometry parameters. The resulting surface wave pressure magnitude $|p|$ at the receiver location (x_R,z_R) given a unity amplitude source, is shown in figure 6.17 for a sweep of each groove parameter.

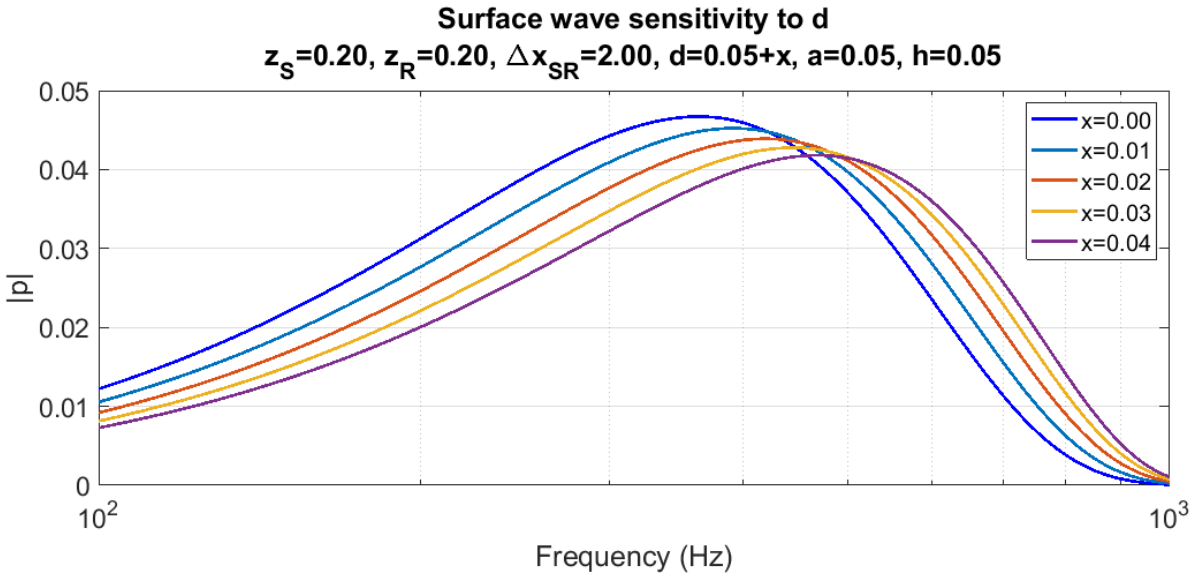

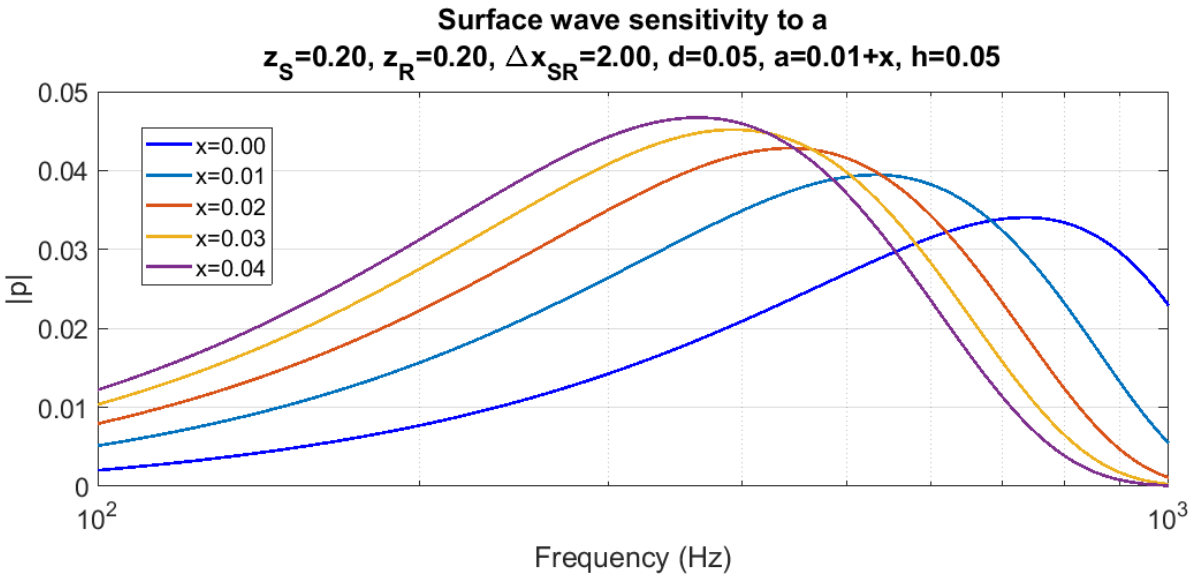

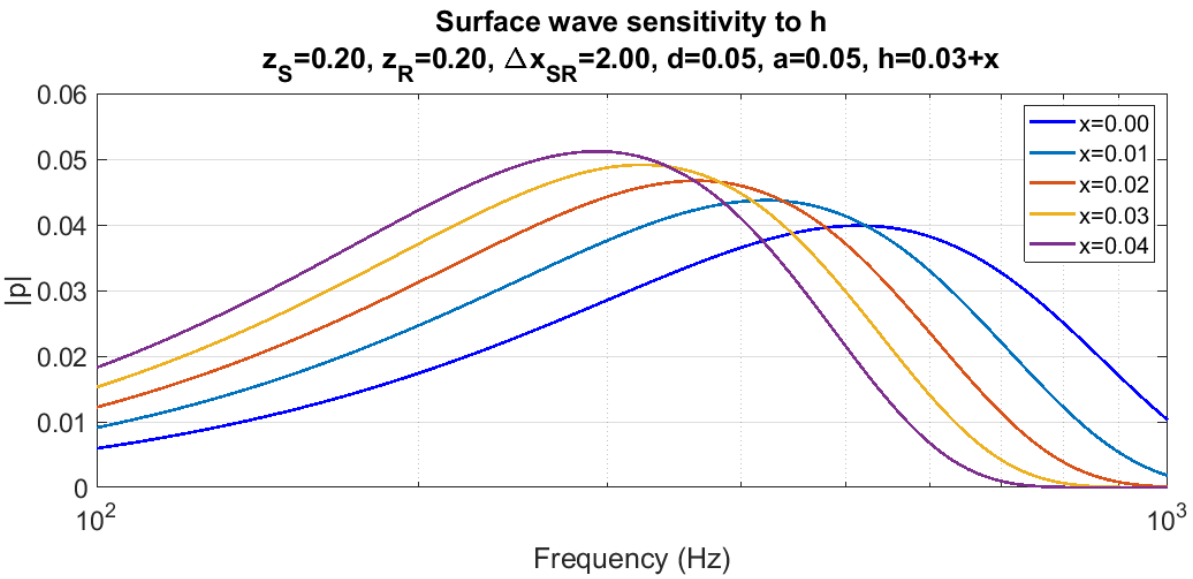

Figure 6.17 a-c Thomasson equation predictions of surface wave frequency for groove geometry parameter sweep.

From figure 6.17, the least sensitive parameter appears to be the grating pitch *d* but there is still an effect of increasing the surface wave frequency peak with increasing *d*. Both *a* and *h* show the opposite effect of decreasing surface wave frequency with increasing size and appear more sensitive to changes in dimension. The magnitude at resonance also changes for all sweeps as the effective 'Q-factor' of the resonant system is altered. Evidently increasing porosity increases the magnitude of the surface wave peak as does increasing the depth of the groove within the given range.

The $|p|$ result from Thomassons surface wave magnitude formula of Eq. (4.30) is normalised in figure 6.18 to allow direct comparison with the EA curves of the models under investigation. The additional numeric values in this figure around the surface wave peak approximate the contribution in dB from to the surface wave calculated by subtracting the flat hard ground response. The contribution of surface waves can be seen to diminish with increasing receiver height due to their evanescent nature where the amplitude falls off with increasing height, *z*. Figure 6.18 shows generally good agreement between the extended modal model and the slit-pore model up to several kHz due to the feature size of the grating structure being small when compared to the incident wavelength in this frequency band. Under these conditions the homogeneous ground assumption has validity and hence the slit-pore model may be effective in the frequency band where this remains true. The results show clear attenuation of the surface wave with increasing receiver height and good agreement with the predictions of Thomasson (see section 4.2). Notice that in figure 6.18c the onset of the first EA minima begins before the frequency of the surface wave peak and hence the surface wave term is further attenuated.

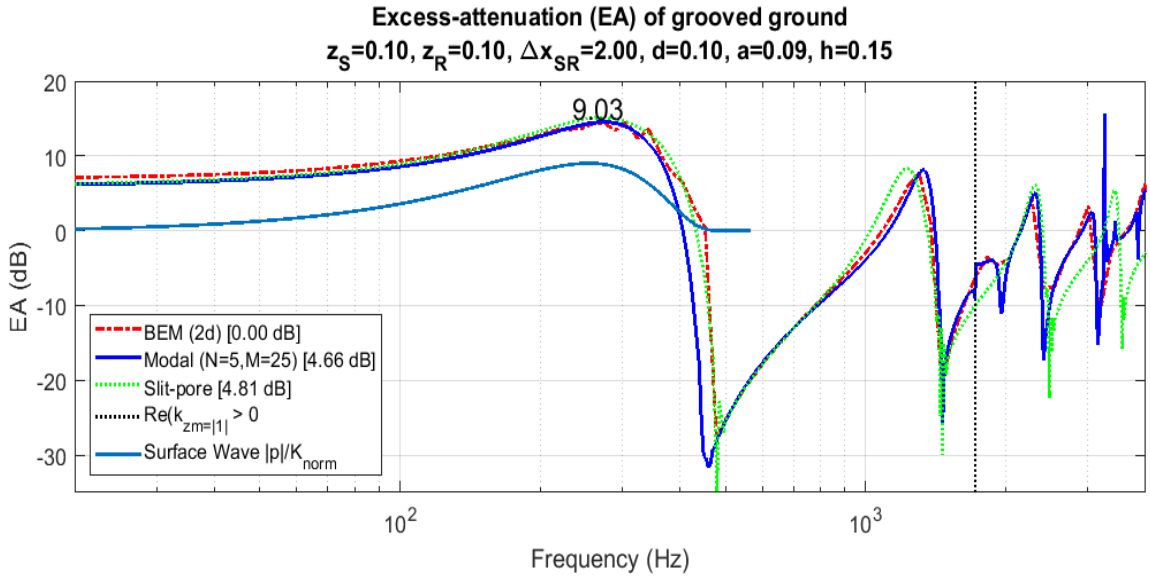

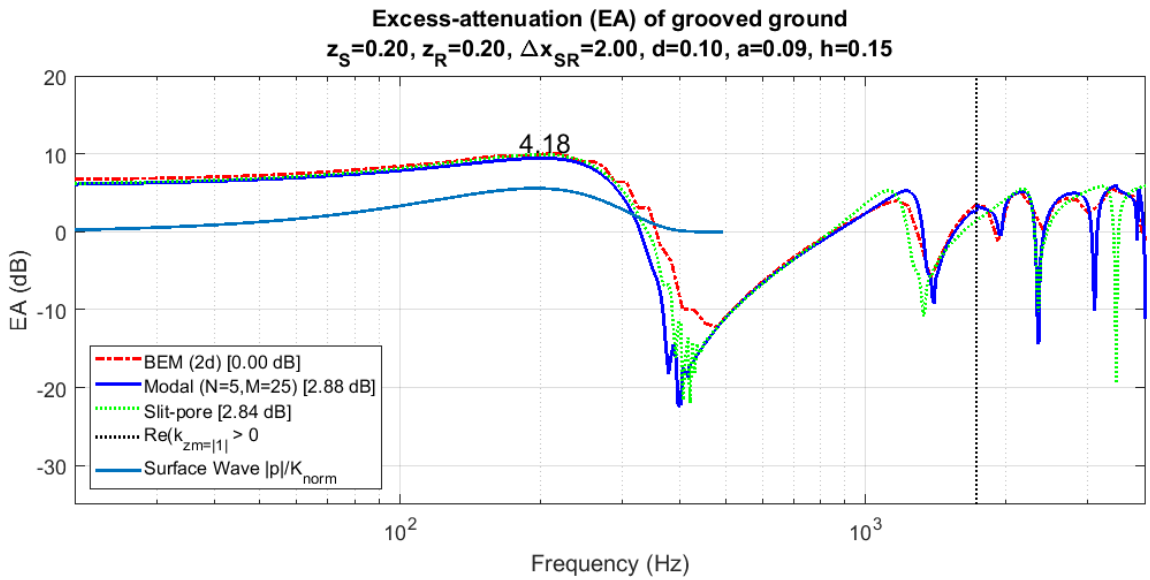

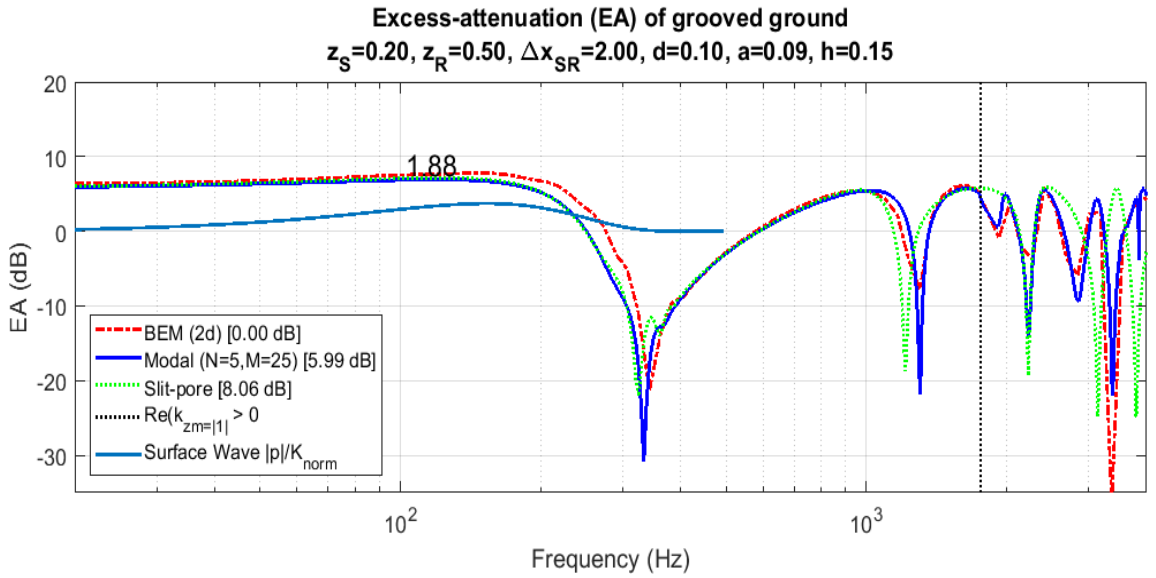

Figure 6.18 a-c Excess-attenuation plots for grating with period 100mm, aperture 90mm and groove depth of 150mm.

6.3.8 Variation in source-receiver height

The variance of characteristic response for different source-receiver heights is explored in this section. This will cause a reduction in the angle of incidence with increasing source-receiver heights for a given horizontal separation. The *x*-component wavelength of the incident wave will decrease with increasing source-receiver height thereby reducing the modal excitation within the grooves for a given frequency span. Examples of this may be seen in the first group of plots for low-source receiver heights of 0.1 to 0.3 m which are showing significant scattering effects caused by the modal excitation within the grooves at the high angles of incidence. Under these conditions the *x*-component of incident wavelength is very similar to the incident wavelength. Conversely where the source-receiver height is large and the corresponding angle of incidence is small as in the latter plots the response more resembles that of hard ground because the elongation of the *x*-component incident wavelength reduces the modal excitation across the given frequency band.

Increasing the source-receiver height also increases the path length difference between the direct and reflected components causing the EA minima features to reduce in frequency with increasing source-receiver height.

The high frequency agreement between BEM and the modal model are good throughout the results but it may be observed that the low frequency agreement is variable. It appears that the correlation is not directly related to source-receiver height but appears somewhat cyclic across the tested range. Figure 6.16a) shows the modal-model underestimating the magnitude of the first EA minimum with respect to BEM while b) and c) show good agreement. Subsequently figure 6.20 shows an onset of the modal model overestimating the magnitude of the first EA minima, tending to good agreement in figure 6.21c). From then on the situation reverses to the modal-model underestimating the magnitude of the first EA. The cause of this phenomenon is not clear but it being cyclic in nature may point to a cause which itself is repetitive such as multiples of wavelength or end effects which may manifest in the BEM predictions but will be lost by the modal-model due it fundamentally assuming a homogeneous field with an infinite extent grating. The truncation to a finite field in the modal model is purely geometric and so end effects and similar will not be reproduced. However the frequency agreement between BEM and

modal models for the first EA minimum is generally good with the worst cases being shown in figures 6.18a) and c) and figures 6.19a) and b).

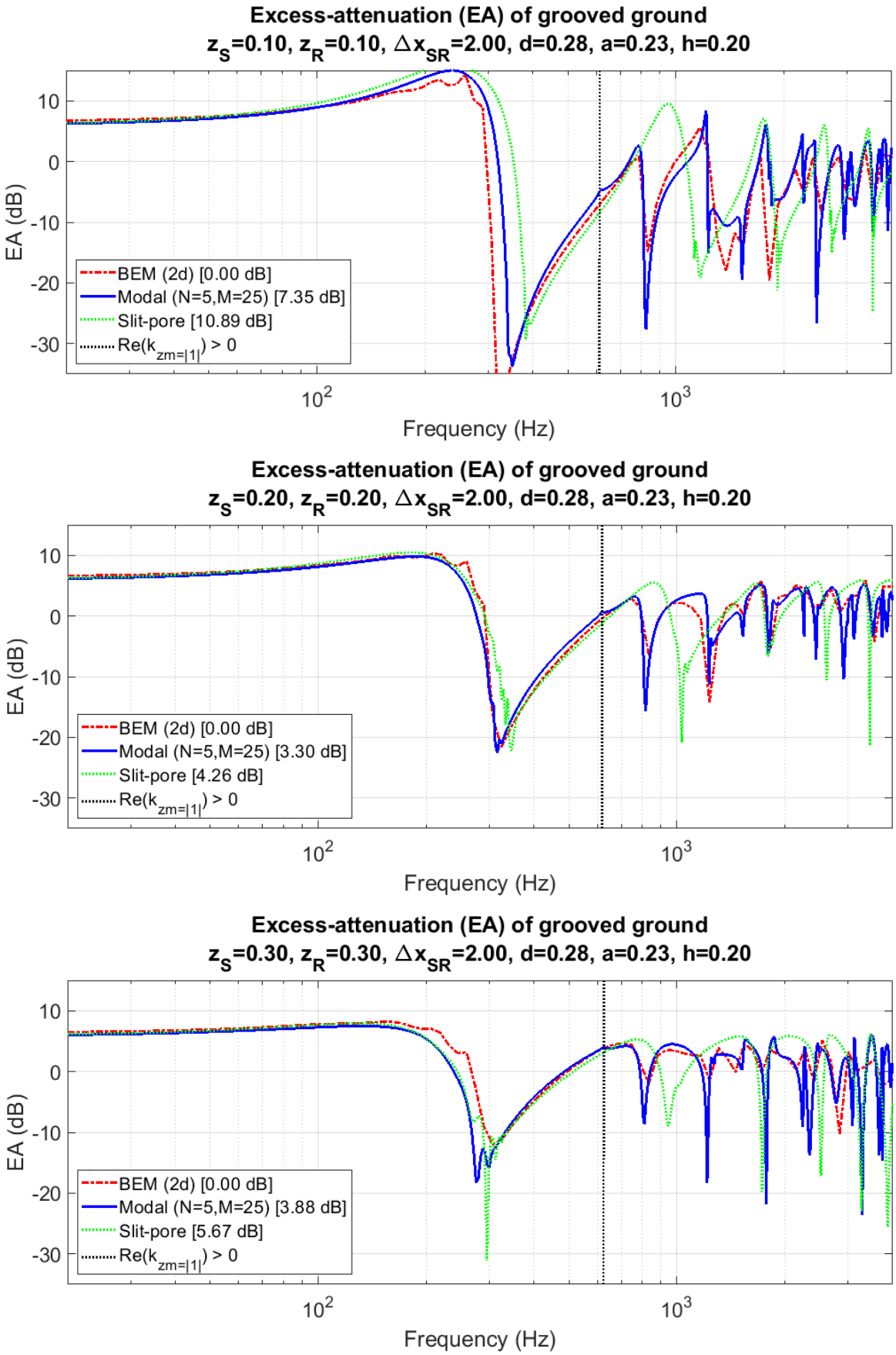

Figure 6.19a-c The effects of source-receiver height. Grating period 280mm, aperture 230mm and groove depth of 200mm.

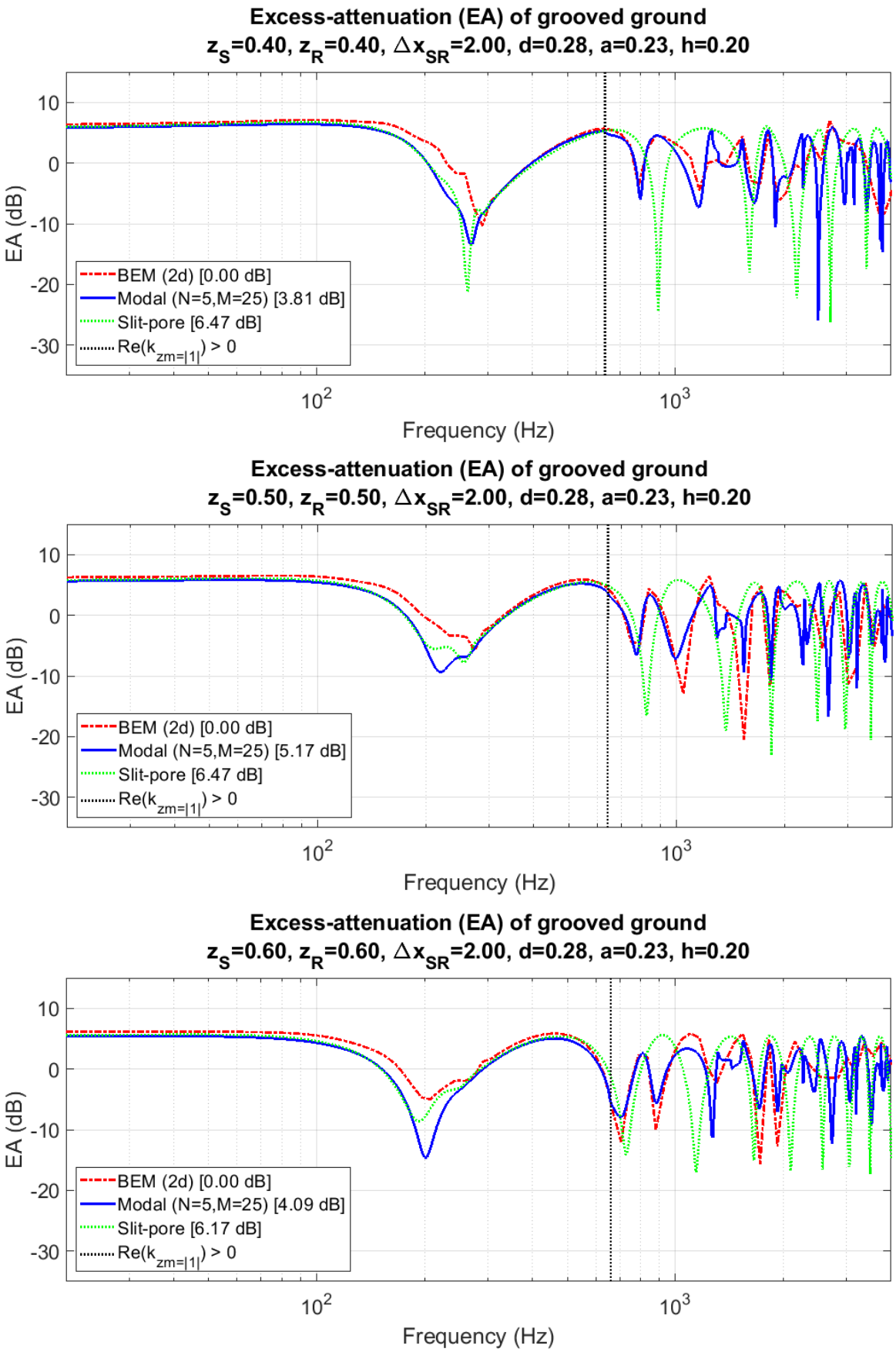

Figure 6.20a-c The effects of source-receiver height. Grating period 280mm, aperture 230mm and groove depth of 200mm.

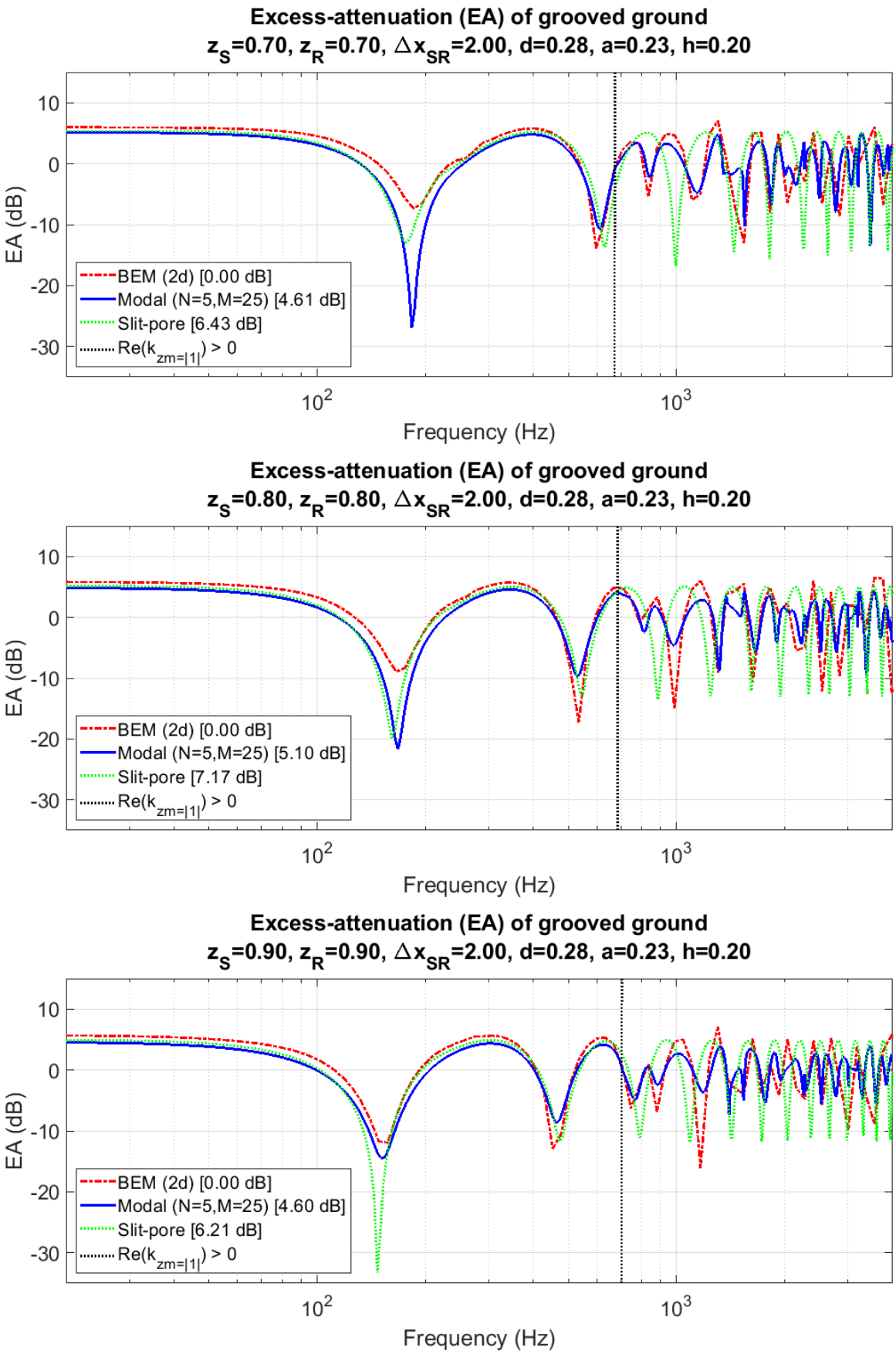

Figure 6.21a-c The effects of source-receiver height. Grating period 280mm, aperture 230mm and groove depth of 200mm.

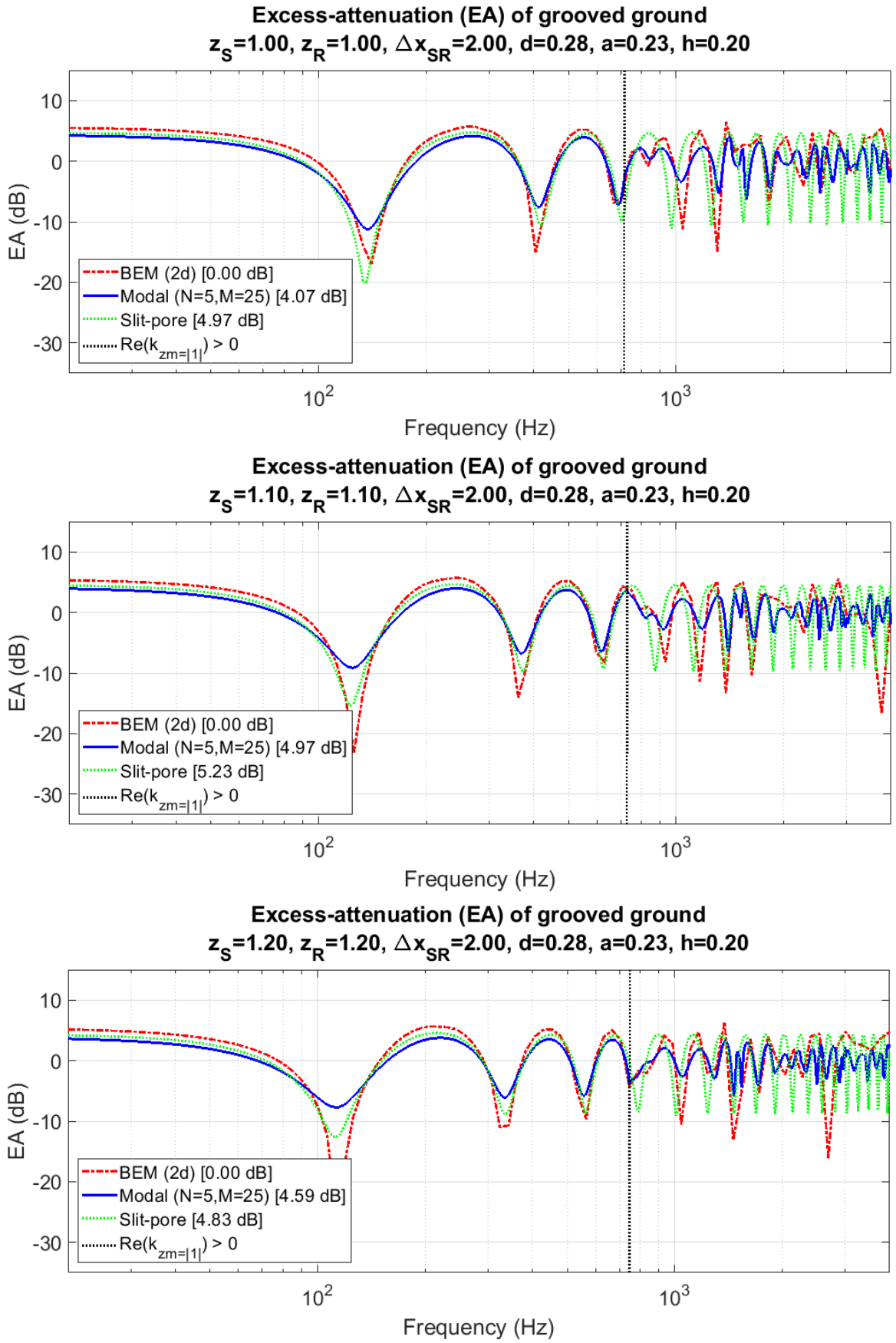

Figure 6.22a-c The effects of source-receiver height. Grating period 280mm, aperture 230mm and groove depth of 200mm.

6.3.9 Comparison with measurement

The 2d extended modal-model is compared with measurements made by Bashir [31] over aluminium strips. The strips were laid on an MDF surface and spaced at regular intervals to form a rectangular grooved structure. Each strip was 1 m in length with cross sectional dimensions of 0.0254 m x 0.0126 m so with the strips laid on their shortest edge this gave a depth h, of 0.0254 and pitch d of 0.0126 m greater than the chosen edge-to-edge spacing a, which was the variable in these measurements. The source and receiver were placed 0.02 m above the top of the strips at a spacing of 0.7 m. Figure 6.23 shows the setup created by Bashir [31] using a hard MDF board as a hard ground surface with the aluminium strips placed upon it to create a rectangular grooved grating. Notice that the structure extends slightly beyond the source and receiver.

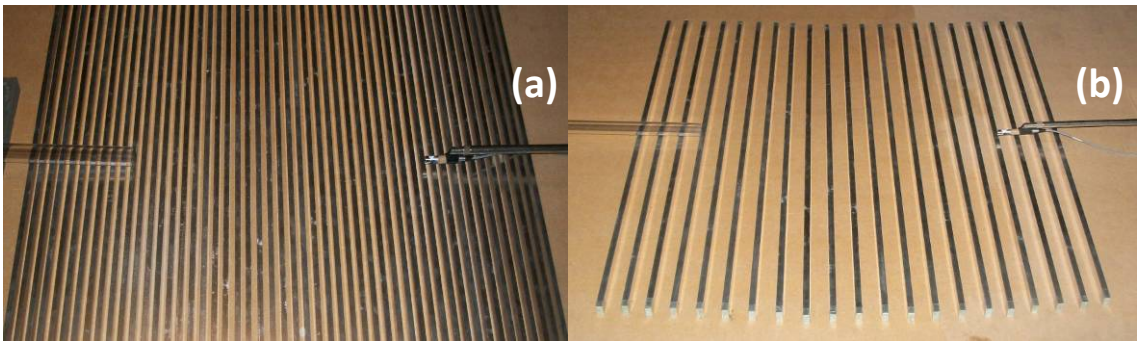

Figure 6.23 Pictures of rectangular grooved ground structures created by Bashir with edge-to-edge spacings a, of a) 0.012m, b) 0.067m. (pictures courtesy of Bashir [31])

The results are shown in figures 6.23 and 6.24 for increasing values of a and d. In general the modal-model predictions agree well with measurements especially in the region beyond the first EA minima. In general the predictions are over estimating the slope and peak magnitude in the region of the surface wave and first EA minima but this is generally attributable to measurement errors. Losses occur due to the materials falling short of the ideal in terms of acoustic hardness and the finite extent of the structures and air gaps which inevitably occur where the strips are laid onto the MDF surface also affect the measurement as does the fact that not matter how carefully one constructs the scene, it can never be geometrically perfect. Significant differences worthy of particular note, occur in figures 6.23b and 6.24c. The former shows a disagreement in the frequency of the first EA

by a greater margin than the other results with a difference approaching 600 Hz. Furthermore the magnitude of the second EA minima is also in severe disagreement with the measurement showing a much deeper trough for whatever reason. However the obvious discrepancies do not manifest significantly in the SE figure which suggests that the general agreement is still good. The latter case of figure 6.25c) posses an SE value much larger than the rest which appears primarily due to the misalignment by around 500 Hz of the second EA minimum, even though both data and prediction show a sharp double trough in the second EA minima. The agreement is good across the remaining spectrum. Interestingly, in figure 6.25a) the modal-model prediction shows a significant EA minimum feature of magnitude in excess of -20 dB at just over 10 kHz which is missing from the measurement. Detail which appears in the predictions of ideal mathematical models are often not observed in measurement due to visco-thermal effects such as air absorption or boundary layer losses which are not included in the theoretical predictions, compounded with measurement errors.

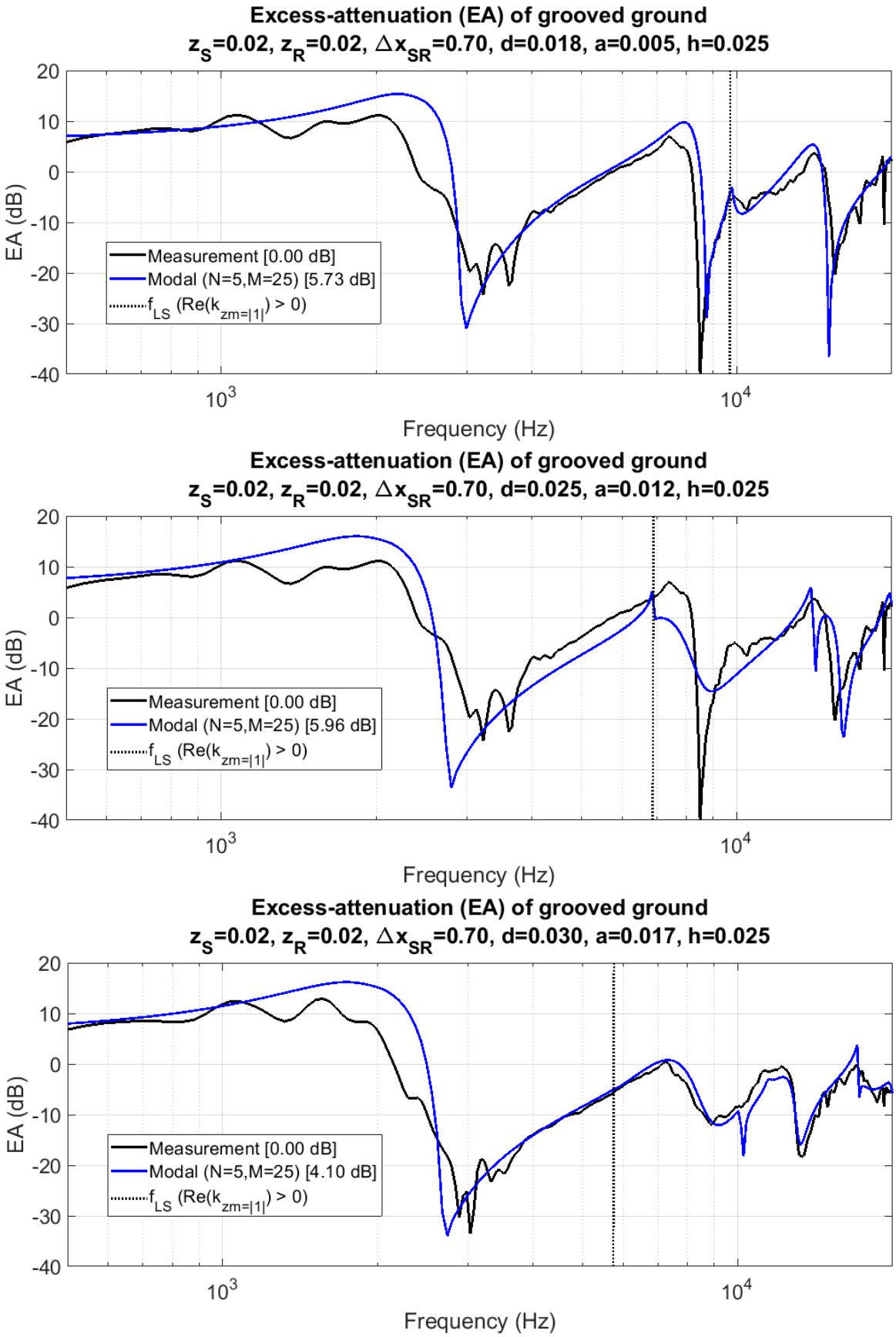

Figure 6.24a-c Comparison of the extended modal-model with measurement for h=0.025m and a) d=0.018m, a=0.005m, b) d=0.025m, a=0.012m, c) d=0.030m, a=0.017m. (Measurements courtesy of Bashir [31])

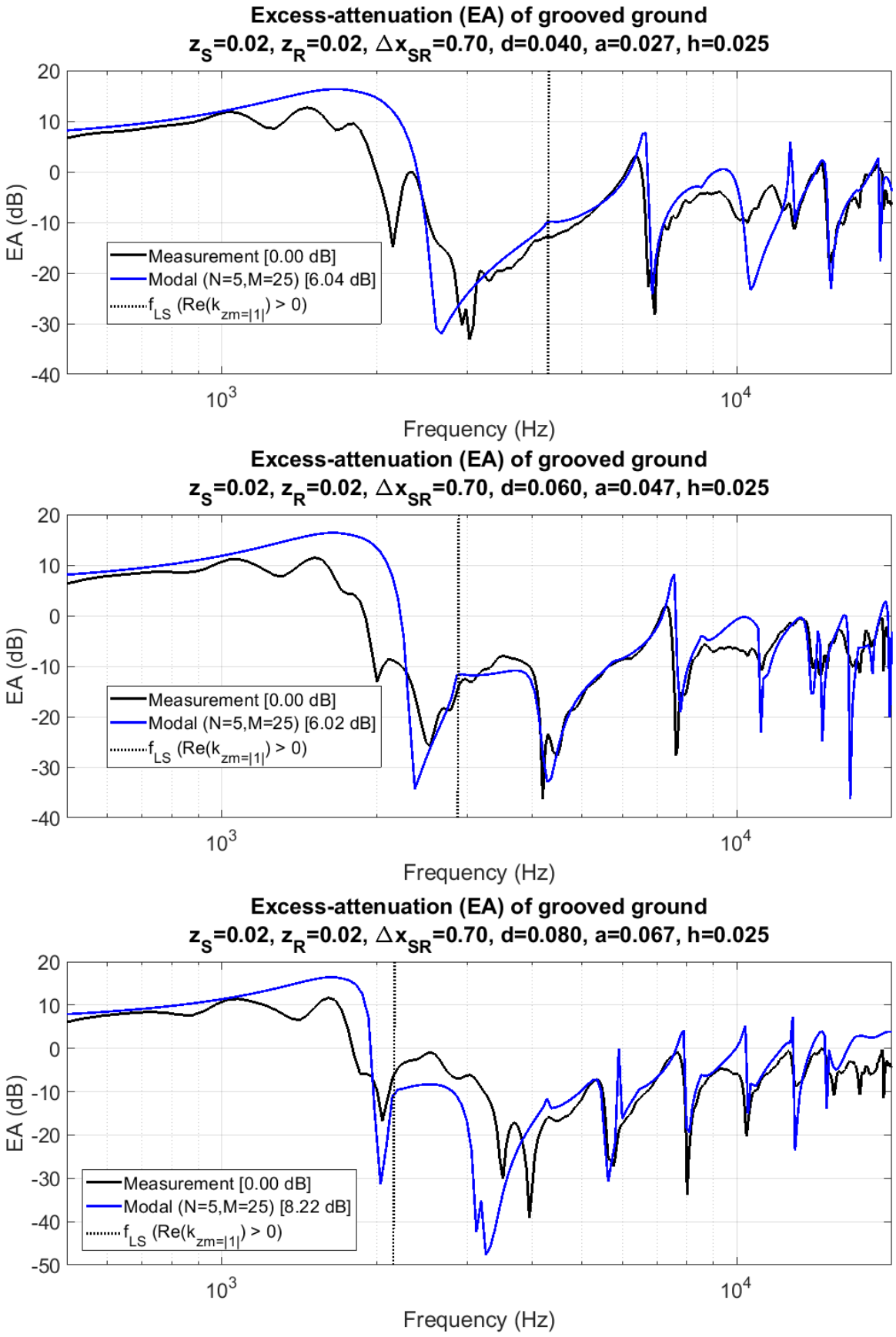

Figure 6.25a-c Comparison of the extended modal-model with measurement for h=0.025m and a) d=0.040m, a=0.027m, b) d=0.060m, a=0.047m, c) d=0.080m, a=0.067m. (Measurements courtesy of Bashir [31])

6.3.10 Effective impedance characteristics

The effective impedance derived from the extended modal-model Z_{eff} was calculated and plotted for a range of angles of incidence (AOI) as shown in figure 6.26. The parameter '*R*' is the radius of the circle on which the source and receiver points lie. It can be seen that the impedance is chaotic for situations of low AOI where the excitation of modes is at its greatest due to the high spatial frequency of the incident mode projected in the *x*-axis on to the ground surface. Consequently significant scattering can be expected. As the AOI is reduced the apparent spatial frequency of the incident wave in *x* and on the ground surface reduces and so the impedance tends involve less scattering and be more hard ground like. This effect may be seen quite clearly in the EA plots figures 6.18 to 6.21 also.

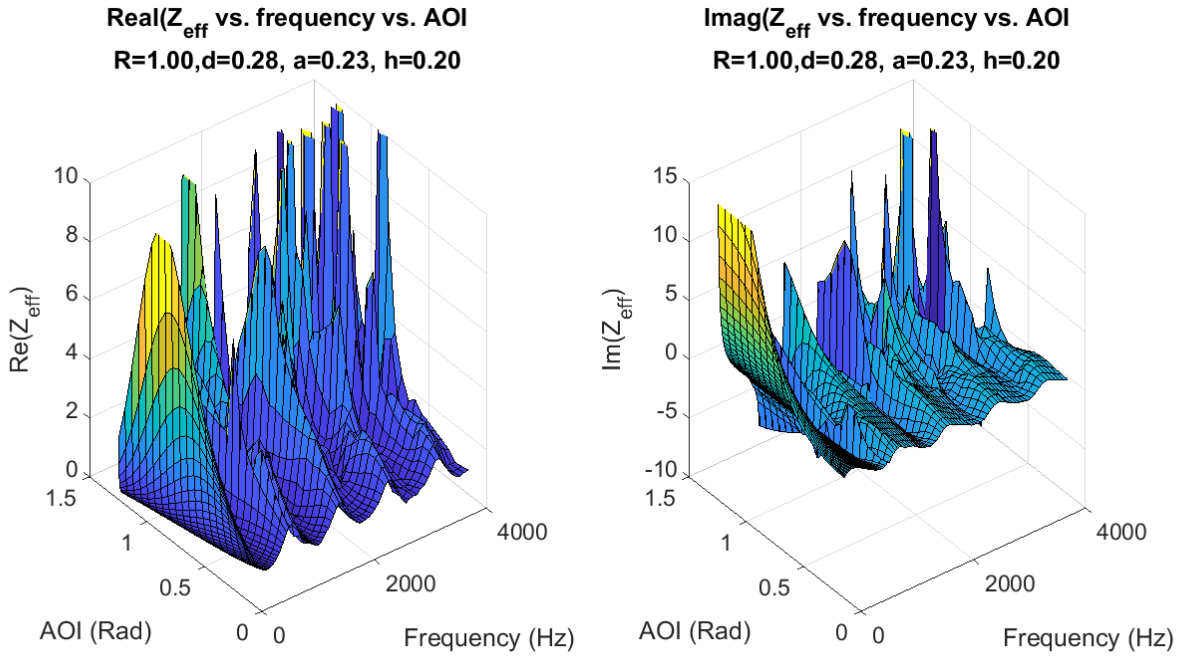

Figure 6.26 Effective impedance Z_{eff} surface vs. frequency vs. AOI for d=0.28, a=0.23 and h=0.2m.

Figure 6.27 shows the real and imaginary parts of Z_{eff} for the same grating geometry but with z_S=z_R=0.2 m. It is presented to show that the onset of a real part to the impedance coincides with the cut-on of the first propagating free-space mode which is *m*=-1 in this example. The real part is denoting an apparent loss due to scattering.

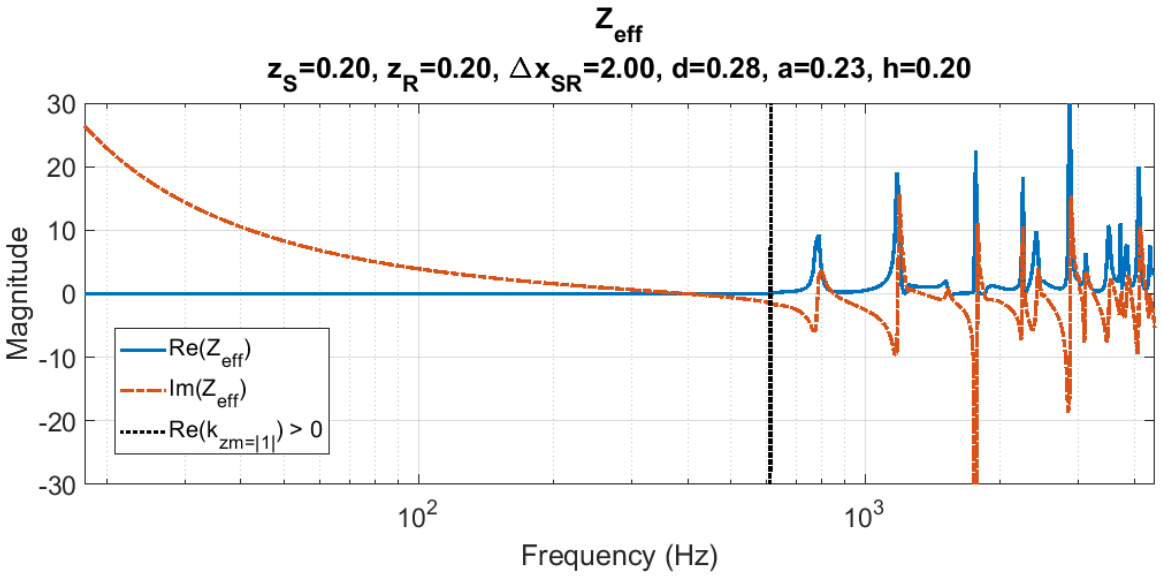

Figure 6.27 Effective impedance Z_{eff} for d=0.28, a=0.23, h=0.2m.

6.3.11 Results summary

It has been shown that the extended 2d modal-model mostly agrees well with established BEM techniques for a wide range of geometries and grating structure dimensions. Computation times for the modal-model are in general significantly less than for BEM. In addition the modal-model has been shown to agree well with measurement for a range of geometries.

Limitations on the range of validity of the slit-pore model have been shown. In general one cannot expect to rely on the slit-pore model at frequencies beyond the cut-off frequency of the first free-space scattered mode. Furthermore there appears to be a lower limit on the porosity below which the slit-pore model begins to fail.

CHAPTER 7 –The 3d modal model

7.1 Theory

7.1.1 Introduction

The 2d modal-model as explained in the previous chapter will be extended to 3d and although this has been achieved by Allard [39] it was derived independently by the author prior to knowledge of Allard's work. Whereas Allard assumed square cells and cavities, we allow for rectangular ones but the difference is trivial. The resulting structure changes from a grooved grating to a regular lattice structure comprised of rectangular cavities of a uniform depth as shown in figure 7.1.

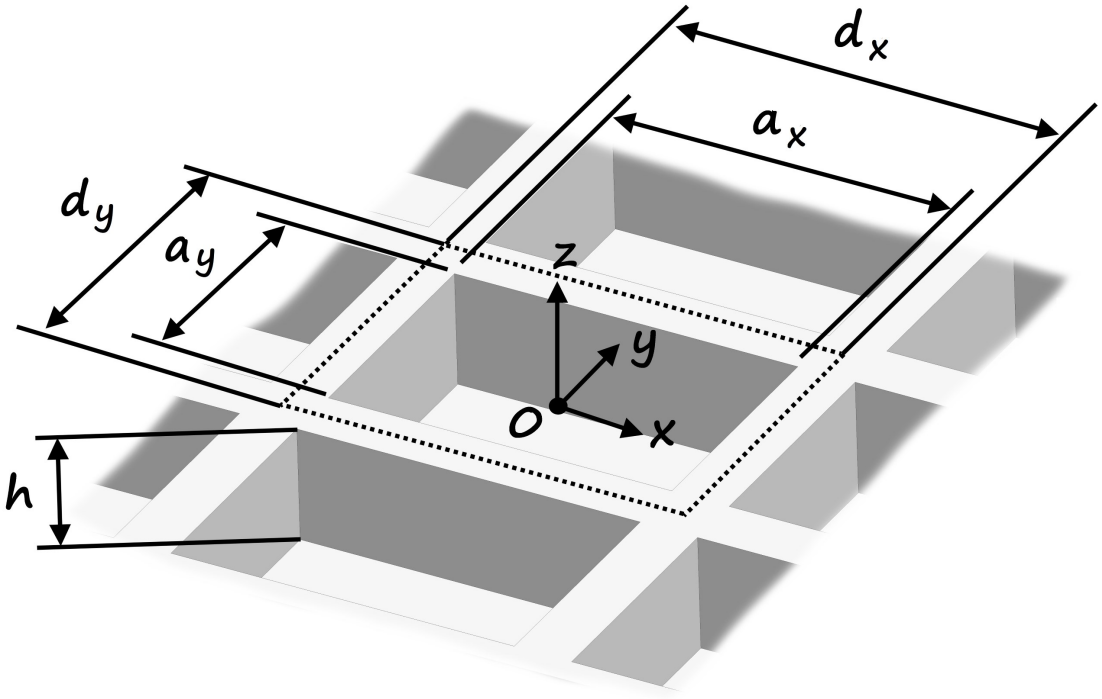

Figure 7.1 Latticed grating structure of 3d model.

The depth of the cavity is h, while the pitch of the cavities in the x and y directions are termed d_x and d_y respectively with the corresponding aperture sizes given by a_x and a_y. The angle of incidence of the plane wave source (with wave-number k) is θ and calculated by assuming notional point source and receiver locations. The azimuthal angle that the incident plane wave makes with the x-axis is φ as in figure 7.2.

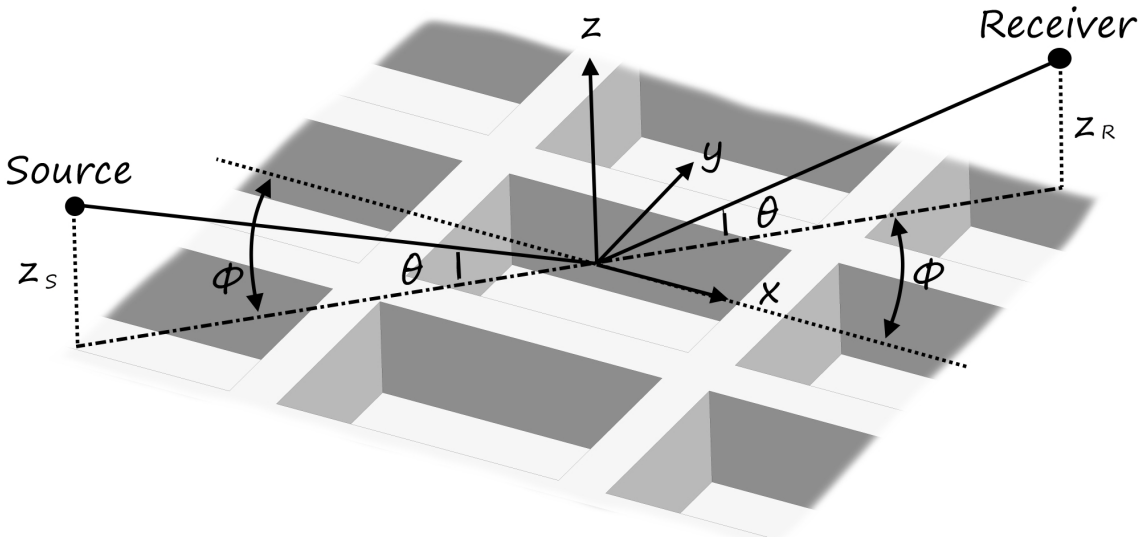

Figure 7.2 Angle of Incidence (AOI) and azimuthal angle of incident wave.

The modal-model is formulated by considering the free-space field above the grating surface $z>0$ and the space occupied by the latticed grating structure $z<0$ separately and equating the two regions at the boundary $z=0$. The characteristics of the incident wave along with the geometry of the lattice structure are the known parameters of the problem and the numerical solution yields the amplitudes of the infinite set standing wave modes, *n*-modes, within the rectangular apertures of the lattice cavities at $z=0$. The infinite set of harmonic *n*-modes within the cavity provide the boundary conditions at $z=0$ within the aperture of the cavity where $|x,y|<a_{x,y}/2$. For the remainder of the cell outside of the aperture window, $d_{x,y}/2>|x,y|>a_{x,y}/2$, the boundary conditions at $z=0$ are those for an acoustically hard surface. The boundary conditions are given from the numerical solution of the modal-model and subsequently the amplitudes of the infinite set of free-space diffraction modes are calculated analytically.

The diffraction grating will induce an infinite set of diffraction modes, *m*-modes, in free-space. As the grating is assumed to be infinitely periodic in x and y the resultant free-space field may be expressed as the superposition of an infinite set of discrete orthonormal 3d Bloch wave modes. As with the 2d case the periodicity of the problem allows solution by considering just one cell in isolation at the origin. Were the problem finite in extent then the diffraction modes would be a continuous infinite set and not discrete. Hence the

assumption of an infinite extent grating simplifies the problem significantly. The geometry of the diffraction modes is given solely by the grating pitch d and the incident wave. Figure 7.3 gives an example of the propagating free-space diffracted fields for the first 3 $m_{x,y}$ modes with an incident wave at normal incidence. Most m-modes will be surface modes which are evanescent in z but under appropriate conditions will propagate into free space which correspond to the diffraction modes. Each array at the tip of each vector is the m-mode index $[m_x,m_y]$. Evanescent modes will have an imaginary z-axis wave-number and so do not lend themselves to depiction on a this diagram which shows only the geometry of propagating modes.

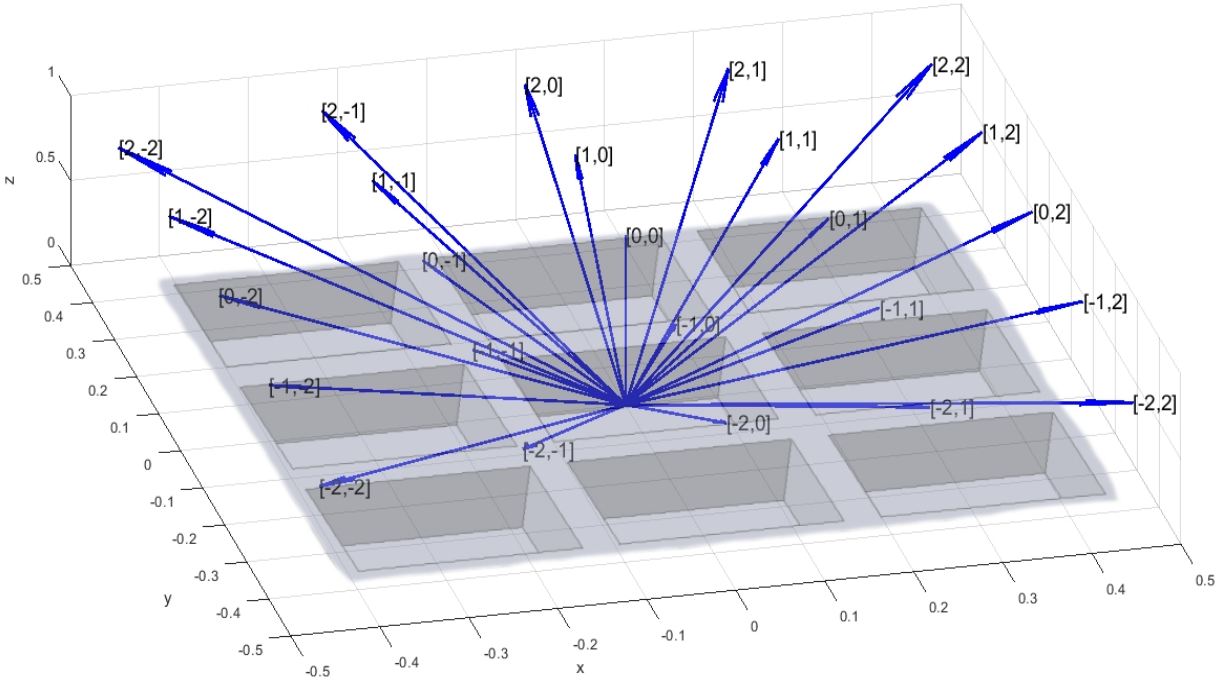

Figure 7.3 Free-space diffraction modes of periodic grating.

The m-modes are pseudo periodic Bloch waves [26] with 2d periodicity of the cell periods, $d_{x,y}$, multiplied by a common phase term due to the incident wave in x and y. This represents Floquet periodicity in x and y as,

$$\Psi(x+C_x d_x, y+C_y d_y) = \exp\left(i\left[k_{xm}x + k_{ym}y\right]\right)\psi(x+C_x d_x, y+C_y d_y) \quad C_{x,y} = 0,1,2...\infty \tag{7.1}$$

Where the *exp()* term is the periodic in d term representing the modes induced by the grating with wave-numbers k_{xm}, k_{xm} and $\psi()$ is the incident term which is not periodic in d.

The 3d problem remains orthonormal so each *m*-mode may be approximated by the inner product[2]of its own mode function and sum of all *n*-modes thus, where *f(x,y)* and *g(x,y)* are spatial functions of an *m* or *n* mode in 2d.

$$< f(x,y), g(x,y) >= \int_{-a_x/2}^{a_x/2} \int_{-a_y/2}^{a_y/2} f(x,y).g(x,y)\, dxdy \tag{7.2}$$

At the boundary *z*=0 and across one cell of the grating, the surface-normal velocity *vz*, of the complete set of free space *m*-modes are matched with the boundary conditions imposed by the *n*-modes induced within each cavity to yield the free-space scattered field which may be expanded as,

$$\begin{aligned}
\Psi(x,y,z) &= V_i\psi_i + V_r\psi_r + \sum_{m\neq 0} V_m\psi_m \\
\Psi(x,y,z) &= V_i \exp\left(ik\left[x\left(\sin\theta.\cos\varphi\right) + y\left(\sin\theta.\sin\varphi\right) - z\cos\theta\right]\right) \\
&\quad + V_r \exp\left(ik\left[x\left(\sin\theta.\cos\varphi\right) + y\left(\sin\theta.\sin\varphi\right) + z\cos\theta\right]\right) \\
&\quad + \sum_{m\neq 0} V_m \exp\left(i\left[\alpha_{xm}x + \alpha_{ym}y + \beta_m z\right]\right) \quad z \geq 0, t = 0
\end{aligned} \tag{7.3}$$

The subscripts '*i*' and '*r*' refer respectively to a parameter of the incident and specularly reflected (*m*=0) wave components. The $\alpha_{x,y}$ and β are the modal propagation constants in *x,y* and *z*. The Floquet periodic nature of the problem is such that the field at *z*=0 exhibits a periodicity in *d,* combined with a phase constant term of the incident wave, evident in the definition of α and β.

$$\begin{aligned}
\alpha_{xm_x} &= k(\sin\theta.\cos\varphi) + \frac{2m_x\pi}{d_x} \\
\alpha_{ym_y} &= k(\sin\theta.\sin\varphi) + \frac{2m_y\pi}{d_y} \\
\beta_m &= \pm\sqrt{k^2 - \left(\alpha_{xm}{}^2 + \alpha_{ym}{}^2\right)}
\end{aligned} \tag{7.4}$$

The modal indices *n* and *m* are themselves 2d, having independent *x* and *y* components so will be expressed as follows.

2 This differs from the standard inner product definition where *g(x,y)* is conjugated, but is used to ensure continuity with previous work.

$$
\begin{aligned}
m = m_{x,y} &= \left[m_x, m_y \right] \quad -M \le x, y \le M \\
n = n_{x,y} &= \left[n_x, n_y \right] \qquad 0 \le x, y \le N
\end{aligned}
\tag{7.5}
$$

Symmetric truncations of x and y will become necessary once the modal-model is solved. A time dependence of $exp(-i\omega t)$ is once more assumed but henceforth omitted for brevity.

7.1.2 Deriving the 3d modal-model for acoustic applications

The 3d model is constructed in the same manner as the 2d case, from the fundamental consideration of the boundary conditions given by a single cell of the grating structure as defined by the dotted line boundary of figure 7.1 which consists of the cavity surrounded by half of the extent of the flat 'ledges'. The boundary conditions at z=0 are posed with respect to continuity of surface normal velocity which is once again z-axis velocity v_z. This is expressed as follows for the horizontal region within the cavity and the surrounding ledge respectively,

$$
\begin{aligned}
v_z(x, y, 0 - \delta_z) &= v_z(x, y, 0 + \delta_z) \qquad |x, y| \le a_{x,y} / 2 \\
v_z(x, y, 0) &= 0 \qquad\qquad\qquad d_{x,y} / 2 > |x, y| > a_{x,y} / 2
\end{aligned}
\tag{7.6}
$$

The δ_z is an infinitesimally small increment in the z-axis and serves to convey that v_z must be continuous at z=0 within the bounds of the cavity and vanish on the hard surround. Once more the horizontal component of velocity $v_{x,y}$, need not be constrained due to the inviscid fluid assumption which exerts no viscous forces.

Correspondingly the acoustic pressure p, boundary conditions for the cavity and hard surround regions are,

$$
\begin{aligned}
p(x, y, 0 - \delta_z) &= p(x, y, 0 + \delta_z) \qquad |x, y| \le a_{x,y} / 2 \\
\frac{d}{dz} p(x, y, 0) &= 0 \qquad\qquad\qquad d_{x,y} / 2 > |x, y| > a_{x,y} / 2
\end{aligned}
\tag{7.7}
$$

At the bottom of the closed cavity at z=-h the pressure gradient must vanish as must v_z. This causes the down-going component of mode n to be reflected form the bottom surface to form an equivalent up-going component which will interfere at the opening of the cavity at z=0 to define the impedance relationship as in Eq. (7.24).

7.1.3 Acoustic free space field, z>0

The free-space field in which $z>0$ is expressed as the superposition of the incident wave and the infinite set of discrete Bloch-Floquet [26] m-modes. The aim of the modal-model is to solve for the set of complex amplitudes $\hat{V}_m$ relating to the free-space m-modes which combined give the solution of the free-space field. As in previous sections the free-space field variables will be denoted by the hat '^' to distinguish them from their namesake counterparts in the lower-space of $z<0$. The free-space field will be expressed in the form,

$$v_z(x,y,z\geq 0)=\hat{V}^i_{0,0}\,\hat{e}_{0,0}\exp(-i\,\hat{k}_{z0,0}\,z)+\hat{V}^r_{0,0}\,\hat{e}_{0,0}\exp(i\,\hat{k}_{z0,0}\,z)+\sum_{m\neq 0,0}^{x}\sum^{y}\hat{V}_m\,\hat{e}_m\exp(i\,\hat{k}_{zm}\,z) \tag{7.8}$$

The '*i*' and '*r*' annotations (incident and reflected) have moved to superscript to avoid confusion with set indices m or n. On the surface of the grating at $z=0$ this reduces to,

$$v_z(x,y,0)=\hat{V}^i_{0,0}\,\hat{e}_{0,0}+\hat{V}^r_{0,0}\,\hat{e}_{0,0}+\sum_{m\neq 0,0}^{x}\sum^{y}\hat{V}_m\,\hat{e}_m \tag{7.9}$$

The function $\hat{e}_m$ is the free-space m-mode v_z characteristic in the x-y horizontal plane at $z=0$ and $\hat{V}_m$ is the corresponding complex amplitude. The wave-number $\hat{k}_{zm}$ is the z-axis wave-number of mode m which is defined in the 3d model as,

$$\hat{k}_{zm}=+\sqrt{k^2-k_{xm_x}{}^2-k_{ym_y}} \tag{7.10}$$

where $\hat{k}_{zm}$ is taken as the positive root because the propagating free-space scattered modes will do so in the $+z$ direction. Those modes which do not propagate free-space due to their horizontal wave-numbers exceeding the resultant for free-space will be evanescent in z and $\hat{k}_{zm}$ will be imaginary. Furthermore mode $m=0$ is the combination of the incident wave and specular reflected component as they share the same magnitude of horizontal wave-number components. The x and y component wave-numbers for mode m are given by,

$$\begin{aligned}\hat{k}_{xm_x}&=k(\sin\theta.\cos\varphi)+\frac{2m_x\pi}{d_x}\\ \hat{k}_{ym_y}&=k(\sin\theta.\sin\varphi)+\frac{2m_y\pi}{d_y}\end{aligned} \tag{7.11}$$

Where the *sin* and *cos* terms represent the projection of the incident wave on the x-y plane

at z=0 given their angle of incidence and azimuthal angle. The quotient term is the modal contribution from the grating with periodicity in m/d. The sign of the $\hat{k}_{x,ym}$ terms may be positive or negative signifying the direction of propagation in each given axis.

The normalised mode function for the 3d case is as follows, where the normalising constant is the product of normalising factors in both axes.

$$\hat{e}_m = d_x^{-\frac{1}{2}} d_y^{-\frac{1}{2}} . \exp\left(i \hat{k}_{xm_x} x \right) . \exp\left(i \hat{k}_{ym_y} y \right) \quad z = 0 \tag{7.12}$$

The amplitude of each mode m is given by the unknown set $\hat{V}_m$ and the instantaneous value for mode m will hence be $\hat{V}_m \hat{e}_m$ at z=0. To provide a complete solution for the acoustic field both velocity and pressure components must be considered. Pressure may be deduced from the impedance relation,

$$\hat{p}_m = \hat{Z}_m \hat{V}_m \hat{e}_m \quad z = 0 \tag{7.13}$$

The value of Z_m will be unique to each mode m and will be defined as follows, given the characteristic of the inviscid air medium,

$$Z_C = \rho_0 c_0 \tag{7.14}$$

where ρ_0 is the density and c_0 the speed of sound of air. The impedance of each mode m which relates v_z to pressure is given by the ratio of wave-numbers thus,

$$\hat{Z}_m = \frac{Z_C k}{\hat{k}_{zm}} \tag{7.15}$$

It is once again useful for clarity of later derivation to separate mode m=0 into its incident and reflected components recalling that mode m=0 represents the combination of the incident and specularly reflected waves. The incident wave impedance is as below and has the leading negative sign to respect the fact that it propagates in the -z direction.

$$\hat{Z}^i_{0,0} = -\frac{Z_C k}{\hat{k}_{z0,0}} \tag{7.16}$$

As the specularly reflected component shares the same propagation characteristics as the incident wave except for inversion in z, it's impedance is just the negative of the incident,

$$\hat{Z}^{r}_{0,0} = \frac{Z_C k}{\hat{k}_{z0,0}} \tag{7.17}$$

This result allows the amplitudes of the pressure *m*-modes $\hat{I}_m$, to the related to the set of free-space v_z amplitudes thus,

$$\hat{I}_m = \hat{Z}_m \hat{V}_m \quad m \neq 0 \tag{7.18}$$

The pressure amplitude for mode m=0 comprises both the incident and the specular reflected components which have opposing directions of z-direction propagation as denoted by the sign of the corresponding impedance. The amplitude of the incident wave $\hat{V}^{i}_{0,0}$ is given as an initial condition of the model and is generally set to unity as the absolute value is arbitrary when the quantities of interest are relative acoustic field magnitudes. The resultant pressure and velocity amplitudes $\hat{I}_{0,0}$ and $\hat{V}_{0,0}$ are the combination of the incident and reflected wave components. The pressure amplitude $\hat{I}_{0,0}$ at z=0 is given by,

$$\hat{I}_0 = \hat{Z}^{i}_{0,0}\left(\hat{V}^{i}_{0,0} - \hat{V}^{r}_{0,0}\right) \tag{7.19}$$

The expression for the free space pressure field is then,

$$p(x, z \geq 0) = \hat{I}^{i}_{0,0}\,\hat{e}_{0,0}\exp\left(-i\,\hat{k}_{z0,0}\,z\right) + \hat{I}^{r}_{0,0}\,\hat{e}_{0,0}\exp\left(i\,\hat{k}_{z0,0}\,z\right) + \sum_{m\neq 0,0}^{x}\sum^{y}\hat{I}_m\,\hat{e}_m\exp\left(i\,\hat{k}_{zm}\,z\right) \tag{7.20}$$

which at the boundary z=0 reduces to,

$$p(x,0) = \hat{I}^{i}_{0,0}\,\hat{e}_{0,0} + \hat{I}^{r}_{0,0}\,\hat{e}_{0,0} + \sum_{m\neq 0,0}^{x}\sum^{y}\hat{I}_m\,\hat{e}_m \tag{7.21}$$

The free-space acoustic field is described by equations (7.8) and (7.20) for vertical velocity v_z and pressure respectively. As with the 2d case this requires the solution of the infinite set $\hat{V}_m$.

7.1.4 Acoustic waveguide region, z<0

The 3d nature of the problem gives rise to a latticed structure which consists of rectangular pockets as opposed to grooves in the 2d case. This constrains modes within the rectangular cavities in both x and y dimensions due to the hard boundary walls on all sides meaning

that modes will consist of a standing wave of order n_x and n_y in both x and y which will combine to form a modal surface at the aperture as shown in the examples of figure 7.4. If either n_x or n_y are 0 the mode will be axial, having invariance in the axis for which the order is 0 but for all other cases the mode will be transverse with the periodicity in both axes combining to form a spatial 2d standing wave pattern.

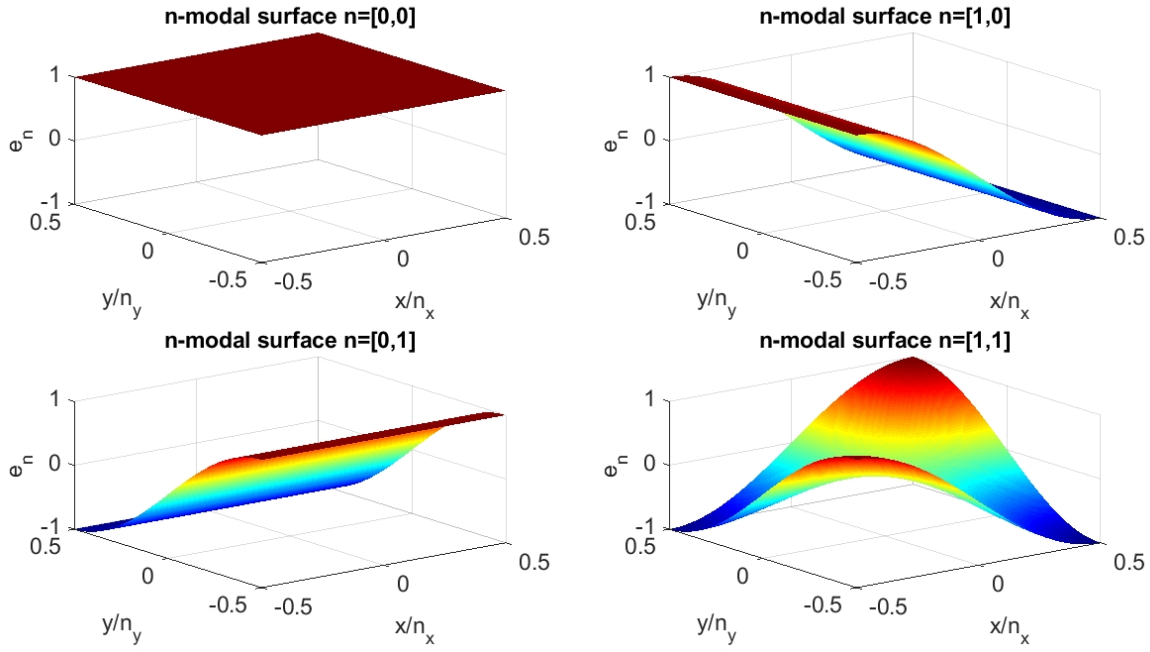

Figure 7.4 Waveguide n-mode characteristics at z=0, V_n=1 and t=0.

The weighting factor for each n-mode V_n is complex where the magnitude gives time independent amplitude and angle describes its temporal phase. The infinite V_n set is found from the numerical solution of the modal-model matrix.

The boundary conditions imposed by the rectangular cavities give rise to the following set of supported spatial modes within the cavities in the perpendicular x and y directions,

$$k_{xn_x} = \frac{n_x \pi}{a_x} \quad n_x = 0,1,2...\infty$$
$$k_{yn_y} = \frac{n_y \pi}{a_y} \quad n_y = 0,1,2...\infty \tag{7.22}$$

Given that the normal velocity and pressure gradient must vanish on the side walls the

normalised characteristic mode function for each *n*-mode is as follows, where the function is normalised by the product of the individual normalising constants in *x* and *y*.

$$e_n = B\cos\left(\left[\frac{n_x\pi}{a_x}\right]\left[x+\frac{a_x}{2}\right]\right)\cdot\cos\left(\left[\frac{n_y\pi}{a_y}\right]\left[y+\frac{a_y}{2}\right]\right) \quad |x|\le\frac{a_x}{2},|y|\le\frac{a_y}{2}$$

$$B=\begin{bmatrix}\sqrt{1/a_x}\cdot\sqrt{1/a_y} \text{ if } n_x=n_y=0\\ \sqrt{1/a_x}\cdot\sqrt{2/a_y} \text{ if } n_x=0 \;\&\; n_y>0\\ \sqrt{2/a_x}\cdot\sqrt{1/a_y} \text{ if } n_x>0 \;\&\; n_y=0\\ \sqrt{2/a_x}\cdot\sqrt{2/a_y} \text{ else}\end{bmatrix} \tag{7.23}$$

The impedance for each mode is determined by the interaction of the down-going and up-going modes within the cavity which is dependent upon the vertical wave-number of the mode k_{zn} and depth of the cavity *h* thus,

$$Z_n = -i\frac{Z_C k}{k_{zn}}\cot(k_{zn}h) \tag{7.24}$$

with the negative sign to maintain consistency with the defined positive axis directions as per figure 7.1. The vertical *z*-axis wave-number for each mode *n* is given by the residual from the resultant of the horizontal wave-numbers,

$$k_{zn} = \pm\sqrt{k^2 - {k_{xn_x}}^2 - {k_{yn_y}}^2} \tag{7.25}$$

The k_{zn} wave number will either be real signifying a mode which will propagate the rectangular cavities in *z* or positive imaginary if the mode is evanescent. As the model is assumed to be lossless k_{zn} will be either real or imaginary and not a combination of both.

7.1.5 Acoustic boundary conditions and equations at z=0

The 3d modal model equations are formed by matching the upper and lower space modal surfaces at the boundary z=0 for both pressure *p* and surface normal velocity v_z. Continuity of normal velocity is maintained by equating the equation for v_z at z=0 Eq. (7.9) with the lower half space *n*-modes as,

$$\begin{aligned}
&\hat{V}^i_{0,0}\,\hat{e}_{0,0}+\hat{V}^r_{0,0}\,\hat{e}_{0,0}+\sum_{m\neq 0,0}^{x}\sum^{y}\hat{V}_m\,\hat{e}_m=\sum_{n\neq 0,0}^{x}\sum^{y}V_n e_n \qquad |x,y|\le a_{x,y}/2\\
&\hat{V}^i_{0,0}\,\hat{e}_{0,0}+\hat{V}^r_{0,0}\,\hat{e}_{0,0}+\sum_{m\neq 0,0}^{x}\sum^{y}\hat{V}_m\,\hat{e}_m=0 \qquad d_{x,y}/2>|x,y|>a_{x,y}/2
\end{aligned} \tag{7.26}$$

Separate equalities are required for the space within the extents of the cavity and the surrounding hard ledges. From Eq. (7.21) continuity of pressure is ensured by satisfying,

$$\begin{aligned}
&\hat{I}^i_{0,0}\,\hat{e}_{0,0}+\hat{I}^r_{0,0}\,\hat{e}_{0,0}+\sum_{m\neq 0,0}^{x}\sum^{y}\hat{I}_m\,\hat{e}_m=\sum_{n\neq 0,0}^{x}\sum^{y}I_n e_n \qquad |x,y|\le a_{x,y}/2\\
&\frac{d}{d\mathbf{n}}\left(\hat{I}^i_{0,0}\,\hat{e}_{0,0}+\hat{I}^r_{0,0}\,\hat{e}_{0,0}+\sum_{m\neq 0,0}^{x}\sum^{y}\hat{I}_m\,\hat{e}_m\right)=0 \qquad d_{x,y}/2>|x,y|>a_{x,y}/2
\end{aligned} \tag{7.27}$$

The pressure continuity equations automatically include consideration of v_z through the use of the pressure amplitudes $\hat{I}_m$ and I_n which are calculated from the relationships,

$$\begin{aligned}
I_n &= Z_n V_n\\
\hat{I}_m &= \hat{Z}_m \hat{V}_m
\end{aligned} \tag{7.28}$$

Making use of the orthonormality of each modal set the corresponding modal amplitudes may be expressed as,

$$\hat{V}_m=\sum_{n\neq 0,0}^{x}\sum^{y}V_n<e_n,{}^*\hat{e}_m> \tag{7.29}$$

$$V_n=\sum_{m\neq 0,0}^{x}\sum^{y}\hat{V}_m<e_n,\hat{e}_m> \tag{7.30}$$

The e_n function vanishes outside of the cavity aperture so the limits of integration may be truncated to $-a/2$ to $a/2$ as opposed to the full extents of $d_{x,y}$. Substituting Eq. (7.28) into (7.30) gives an expression for the pressure amplitude of each lower half space n-mode in terms the entire free-space field. The m=0 mode must be treated separately as it comprises the combination of the incident and specularly reflected components.

$$\begin{aligned}
I_n &= \hat{I}_{0,0}<e_n,\hat{e}_{0,0}>+\sum_{m\neq 0,0}^{x}\sum^{y}\hat{I}_m<e_n,\hat{e}_m>\\
&= \hat{Z}^i_{0,0}\left(\hat{V}^i_{0,0}-\hat{V}^r_{0,0}\right)<e_n,\hat{e}_{0,0}>+\sum_{m\neq 0,0}^{x}\sum^{y}\hat{Z}_m\hat{V}_m<e_n,\hat{e}_m>
\end{aligned} \tag{7.31}$$

Absorbing the zeroth term into the major summation for elegance by adding the term into summation and subtracting it outside yields,

$$I_n = 2\hat{Z}^i_{0,0}\hat{V}^i_{0,0} < \hat{e}_n, \hat{e}_{0,0} > + \sum_{m\neq 0,0}^{x}\sum^{y} \hat{Z}_m \hat{V}_m < \hat{e}_n, \hat{e}_m > \tag{7.32}$$

Where the subtle details of this step are explained in detail in the 2d modal-model chapter as the rationale is identical. The equation must be recomposed in terms of V_n as the only unknown, so V_m may be eliminated by substituting it with Eq. (7.29),

$$\begin{aligned} I_n &= 2\hat{Z}^i_{0,0}\hat{V}^i_{0,0} < \hat{e}_n, \hat{e}_{0,0} > + \sum_{m_y}\sum_{m_x} \hat{Z}_m \left(\sum_{n\dagger_y}\sum_{n\dagger_x} V_{n\dagger} < \hat{e}_{n\dagger}, {}^*\hat{e}_m > \right) < \hat{e}_n, \hat{e}_m > \\ &= 2\hat{Z}^i_{0,0}\hat{V}^i_{0,0} < \hat{e}_n, \hat{e}_{0,0} > + \sum_{n\dagger_y}\sum_{n\dagger_x} V_{n\dagger} \left[\sum_{m_y}\sum_{m_x} \hat{Z}_m < \hat{e}_{n\dagger}, {}^*\hat{e}_m > < \hat{e}_n, \hat{e}_m > \right] \end{aligned} \tag{7.33}$$

A local index $n\dagger$ has appeared in the equation to separate a local summation loop with the primary value of n to which the subject of the equation relates. Making use of $I_n = Z_n V_n$ isolates V_n on the left hand side and allows Z_n to be expanded by its full expression of Eq. (7.24) leading to,

$$\begin{aligned} -i\frac{Z_C k}{k_{zn}}\cot(k_{zn}h) V_n &= 2\hat{Z}^i_{0,0}\hat{V}^i_{0,0} < \hat{e}_n, \hat{e}_{0,0} > + \sum_{n\dagger_y}\sum_{n\dagger_x} V_{n\dagger} \left[\sum_{m_y}\sum_{m_x} \hat{Z}_m < \hat{e}_{n\dagger}, {}^*\hat{e}_m > < \hat{e}_n, \hat{e}_m > \right] \\ -2\hat{Z}^i_{0,0}\hat{V}^i_{0,0} < \hat{e}_n, \hat{e}_{0,0} > &= i\frac{Z_C k}{k_{zn}}\cot(k_{zn}h) V_n + \sum_{n\dagger_y}\sum_{n\dagger_x} V_{n\dagger} \left[\sum_{m_y}\sum_{m_x} \hat{Z}_m < \hat{e}_{n\dagger}, {}^*\hat{e}_m > < \hat{e}_n, \hat{e}_m > \right] \end{aligned} \tag{7.34}$$

The final step to format the equation into a form suitable for expression as a matrix is to absorb the '*cot*' term into the *n*-dagger summation. Use of a Kronecker delta with definition,

$$\delta^n_{n\dagger} = \begin{bmatrix} 1 \text{ if } n_x = n\dagger_x \text{ and } n_y = n\dagger_y \\ 0 \text{ else} \end{bmatrix} \tag{7.35}$$

enables the final recomposition of the primary equation to,

$$\sum_{n\dagger_y}\sum_{n\dagger_x} V_{n\dagger} \left[\sum_{m_y}\sum_{m_x} \hat{Z}_m < \hat{e}_{n\dagger}, {}^*\hat{e}_m > < \hat{e}_n, \hat{e}_m > + \delta^n_{n\dagger} i\frac{Z_C k}{k_{zn}}\cot(k_{zn}h) \right] = -2\hat{Z}^i_{0,0}\hat{V}^i_{0,0} < \hat{e}_n, \hat{e}_{0,0} > \tag{7.36}$$

To complete the 3d modal-model $[n_x, n_y]$ is truncated to $[N_x, N_y]$ and $[m_x, m_y]$ to $[\pm M_x, \pm M_y]$

and the resulting set of equations is formed into the ($N_x.N_y$) x ($N_x.N_y$) element matrix of Eq. (7.37) which is solved numerically to yield the V_n set of lower space modal amplitudes. The free-space amplitude set $\hat{V}_m$ is then found analytically from the V_n set by applying Eq. (7.29).

$$
\begin{pmatrix}
A_{N=[0,0],N\dagger=[0,0]} & A_{[0,0],[1,0]} & \cdots & A_{[0,0],[N\dagger_x,0]} & A_{[0,0],[0,1]} & A_{[0,0],[1,1]} & \cdots & A_{[0,0],[N\dagger_x,1]} & \cdots & \cdots & A_{[0,0],[N\dagger_x,N\dagger_y]} \\
A_{N=[1,0],N\dagger=[0,0]} & A_{[1,0],[1,0]} & \cdots & A_{[1,0],[N\dagger_x,0]} & A_{[1,0],[0,1]} & A_{[1,0],[1,1]} & \cdots & A_{[1,0],[N\dagger_x,1]} & \cdots & \cdots & A_{[1,0],[N\dagger_x,N\dagger_y]} \\
 & & & & & \vdots & & & & & \\
A_{N=[N_x,0],N\dagger=[0,0]} & A_{[N_x,0],[1,0]} & \cdots & A_{[N_x,0],[N\dagger_x,0]} & A_{[N_x,0],[0,1]} & A_{[N_x,0],[1,1]} & \cdots & A_{[N_x,0],[N\dagger_x,1]} & \cdots & \cdots & A_{[N_x,0],[N\dagger_x,N\dagger_y]} \\
A_{N=[0,1],N\dagger=[0,0]} & A_{N=[0,1],[1,0]} & \cdots & A_{[0,1],[N\dagger_x,0]} & A_{[0,1],[0,1]} & A_{[0,1],[1,1]} & \cdots & A_{[0,1],[N\dagger_x,1]} & \cdots & \cdots & A_{[0,1],[N\dagger_x,N\dagger_y]} \\
A_{N=[1,1],N\dagger=[0,0]} & A_{N=[1,1],[1,0]} & \cdots & A_{[1,1],[N\dagger_x,0]} & A_{[1,1],[0,1]} & A_{[1,1],[1,1]} & \cdots & A_{[1,1],[N\dagger_x,1]} & \cdots & \cdots & A_{[1,1],[N\dagger_x,N\dagger_y]} \\
 & & & & & \vdots & & & & & \\
A_{N=[N_x,1],N\dagger=[0,0]} & A_{N=[N_x,1],[1,0]} & \cdots & A_{[N_x,1],[N\dagger_x,0]} & A_{[N_x,1],[0,1]} & A_{[N_x,1],[1,1]} & \cdots & A_{[N_x,1],[N\dagger_x,1]} & \cdots & \cdots & A_{[N_x,1],[N\dagger_x,N\dagger_y]} \\
 & & & & & \vdots & & & & & \\
 & & & & & \vdots & & & & & \\
A_{N=[N_x,N_y],N\dagger=[0,0]} & A_{N=[N_x,N_y],[1,0]} & \cdots & A_{[N_x,N_y],[N\dagger_x,0]} & A_{[N_x,N_y],[0,1]} & A_{[N_x,N_y],[1,1]} & \cdots & A_{[N_x,N_y],[N\dagger_x,1]} & \cdots & \cdots & A_{[N_x,N_y],[N\dagger_x,N\dagger_y]}
\end{pmatrix}
\begin{pmatrix}
V_{N_x=0,N_y=0} \\
V_{1,0} \\
\vdots \\
V_{N_x,0} \\
V_{0,1} \\
V_{1,1} \\
\vdots \\
V_{N_x,1} \\
\vdots \\
\vdots \\
V_{N_x,N_y}
\end{pmatrix}
=
\begin{pmatrix}
X_{N_x=0,N_y=0} \\
X_{1,0} \\
\vdots \\
X_{N_x,0} \\
X_{0,1} \\
X_{1,1} \\
\vdots \\
X_{N_x,1} \\
\vdots \\
\vdots \\
X_{N_x,N_y}
\end{pmatrix}
\tag{7.37}
$$

Where,

$$A_{[n_x,n_y],[n\dagger_x,n\dagger_x]} = \sum_{m_y}\sum_{m_x} \hat{Z}_m < e_{n\dagger}, {}^*\hat{e}_m > < e_n, \hat{e}_m > + \delta^n_{n\dagger}\, i \frac{Z_C k}{k_{zn}} \cot(k_{zn} h)$$

$$X_{[n_x,n_y]} = -2\hat{Z}^i_{0,0}\, \hat{V}^i_{0,0} < e_n, \hat{e}_{0,0} > \tag{7.38}$$

7.2 Implementation

7.2.1 Introduction to 3d implementation

The 3d modal-model is applied to simulating point-to-point acoustic problems above a doubly-periodic rectangular latticed ground surface in the same manner as the 2d modal-model has been applied in previous sections to a rectangular grooved ground. As such the process for 3d and 2d is similar and in the interests of brevity only the differences and specifics for 3d will be discussed in detail in this section. However, a short recap on the method follows.

The modal-model is solved for a given latticed ground surface geometry under homogeneous plane-wave excitation. The plane-wave field is then known in the presence of an infinite extent latticed ground surface.

Simple approximations are then applied to resulting plane-wave field to approximate a latticed grating which is finite in extent.

From this, an effective impedance for the lattice and particular geometry is calculated from a plane-wave reflection coefficient.

The effective impedance is then used with a spherical or cylindrical reflection coefficient in a point-to-point geometry to yield an approximate spherical or cylindrical wave solution for the excess-attenuation spectrum.

The process for solving the 3d modal-model itself is similar to the 2d case and does not warrant further comprehensive explanation. The reader is referred back to the Implementation section of the 2d modal-model. In 3d the resulting matrix is much larger than for 2d and parameters of *n* and *m* become two-dimensional with *x* and *y* components

so summations in *n* and *m* are necessarily double summations.

7.2.2 Plotting the 3d free-space field

The solution of the 3d modal-model yields the plane wave free-space field which can be plotted at any given point in space for z>0. In this section the equations for pressure and acoustic velocity of the plane-wave free-space field are presented. Once again the normalising constants of the modal characteristic functions are omitted as they are not required for plotting the resulting fields. The time convention of exp(-*iωt*) is once again assumed and henceforth all expressions are shown for time *t*=0.

The pressure field of the incident plane-wave source is given by,

$$p_i(x,y,z\geq 0) = \hat{Z}^i_{0,0}\,\hat{V}^i_{0,0}\exp\left(ik\left[x\left(\sin\theta.\cos\varphi\right)+y\left(\sin\theta.\sin\varphi\right)\right]\right).\exp\left(-i\,\hat{k}_{z0,0}\,z\right) \tag{7.39}$$

and for the specularly reflected mode *m*=[0,0],

$$p_r(x,y,z\geq 0) = \hat{Z}^r_{0,0}\left(\hat{V}_{0,0}-\hat{V}^i_{0,0}\right)\exp\left(ik\left[x\left(\sin\theta.\cos\varphi\right)+y\left(\sin\theta.\sin\varphi\right)\right]\right).\exp\left(i\,\hat{k}_{z0,0}\,z\right) \tag{7.40}$$

where *k* is once again the propagation constant for the free-space medium. Each mode *m* for which *m*≠[0,0] is a scattered mode induced by the diffractive effects of the latticed ground surface and given by,

$$p_m(x,y,z\geq 0) = \hat{Z}_m\,\hat{V}_m\exp\left(i\left[\hat{k}_{xm_x}\,x+\hat{k}_{ym_y}\,y\right]\right).\exp\left(i\,\hat{k}_{zm}\,z\right)\quad m\neq[0,0] \tag{7.41}$$

The scattered field is therefore the sum of modal contributions,

$$p_{sct}(x,y,z\geq 0) = \sum_{m\neq 0,0}^{x}\sum^{y}\hat{Z}_m\,\hat{V}_m\exp\left(i\left[\hat{k}_{xm_x}\,x+\hat{k}_{ym_y}\,y\right]\right).\exp\left(i\,\hat{k}_{zm}\,z\right) \tag{7.42}$$

and the total pressure field is given by the superposition of all components as follows, with the truncation $-M\leq m_{x,y}\leq M$.

$$p_{tot}(x,y,z\geq 0) = p_i + p_r + \sum_{m\neq 0,0}^{x}\sum^{y}\hat{Z}_m\,\hat{V}_m\exp\left(i\left[\hat{k}_{xm_x}\,x+\hat{k}_{ym_y}\,y\right]\right).\exp\left(i\,\hat{k}_{zm}\,z\right) \tag{7.43}$$

Now consider ray path point-to-point propagation above a ground plane as if the source and receiver were discrete points in space. In the 3d coordinate space of the point-to-point propagation problem the origin $O(x,y,z)=(0,0,0)$ is defined as the point of specular reflection on the surface given the notional angle of incidence obtained from the spatial locations of the point source $S(x_S,y_S,z_S)$ and receiver $R(x_R,y_R,z_R)$ as shown in figure 7.5. The modal-model is solved at the origin and all plane-wave modal components are defined with reference to the origin.

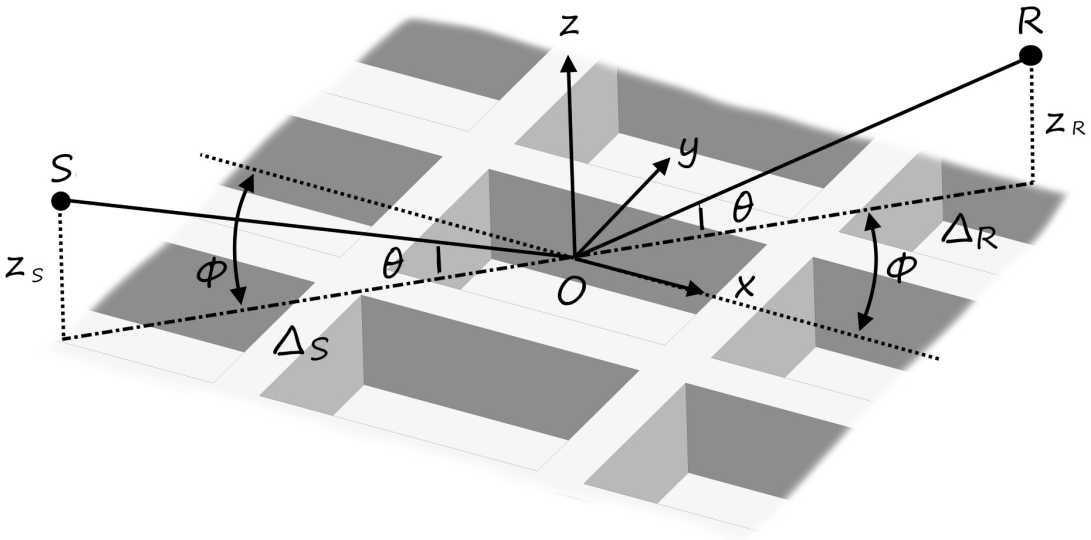

Figure 7.5 3d Geometry of point-to-point propagation model over lattice.

The horizontal distances between the origin and the source Δ_S and the origin and receiver Δ_R are calculated by the numerical solution of the two equations,

$$\frac{\Delta_R}{z_R}-\frac{\Delta_S}{z_S}=0 \text{ and } \Delta_R+\Delta_S=\Delta_{SR}$$

which may be formed into the matrix,

$$\begin{bmatrix} \frac{1}{z_R} & - & \frac{1}{z_S} \\ 1 & + & 1 \end{bmatrix} \begin{bmatrix} \Delta_R \\ \Delta_S \end{bmatrix} = \begin{bmatrix} 0 \\ \Delta_{SR} \end{bmatrix} \tag{7.44}$$

This then allows the absolute x,y component location of the source S and receiver R in our co-ordinate space to be calculated from the azimuth angle by,

$$S\left(x_S = -|\Delta_S|\cos\varphi,\ y_S = -|\Delta_S|\sin\varphi,\ z_S\right)$$
$$R\left(x_R = |\Delta_R|\cos\varphi,\ y_R = |\Delta_R|\sin\varphi,\ z_R\right) \tag{7.45}$$

The horizontal distances are factored by cos φ and sin φ to obtain the projected distances in x and y respectively. The source and receiver heights in z as well as their horizontal separation Δ_{SR} are given as parameters of the model.

7.2.3 Finite grating extents approximations

The modal-model assumes homogeneous plane-wave fields which extend infinitely in all spatial dimensions. The point-to-point acoustic propagation model which has more widespread practical application than the infinite plane-wave scenario assumes that the source and receiver are point locations giving rise to spherical wave propagation. The two cases are significantly different so transferring the modal-model field to the point-to-point case is a large assumption which requires some geometric manipulation. The plane-wave field extends infinitely without loss which is clearly not compatible with the point-to-point model where spherical (or cylindrical) spreading is assumed and so the field must be constrained in space to include only modes which will have a significant effect on the acoustic field at the receiver. This is achieved by assuming that the grating structure has finite extents and only the modes with propagation angles that would cause them to intersect the receiver are included in the initial plane-wave field summation prior to calculating the effective impedance of the surface. The principle is the same as for the 2d case except the geometry in 3d is complicated slightly by the added dimension and the azimuthal angle. Some schemes for achieving this will be presented each with subtle differences as to how they model the extents of the latticed grating which itself is assumed to be rectangular in extent. Although the geometry is not complex it is involved, so the reader is referred to the list of symbols for definitions. As a general rule absolute coordinates will be signified by a capital letter in the form $X=X(x,y,z)$ and relative dimensions which are mostly horizontal by a leading delta as in ΔX.

The path length difference compensation applied in the 2d case will not be implemented in 3d as the effective ray paths from source to receiver are numerous and complex. Although calculating the related geometry is arduous but not difficult, applying a reasonable amplitude scaling is. Rays with equivalent paths in one plane will have different paths in

the other and so just assuming a loss based upon path length alone may be highly erroneous. This is due to the assumption this makes that all modes will be excited by a uniform plane wave which will not hold in the 3d case where excitation will diminish away from the source receiver plane given a spherical source. Therefore a weighting function would then be required to be applied to the path length compensation based upon how far away from the source receiver plane the intersecting mode was apparently excited.

A number of implementation methods for approximating the point-to-point geometry with a finite sized lattice structure are presented henceforth. They are formulated around the measurement set-up used to produce the measurements against which the 3d modal-model will be compared and allows the methods to be tested against measurement in the absence of any theoretical reference methods. Many other variations are possible but we are unable to test these against other theoretical methods and so their validity cannot be tested. The relations for determining whether each mode is to be included in the plane-wave field summation are common to all methods. As there are two horizontal dimensions the propagation angle of each mode must be projected in both the *x*-*z* and *y*-*z* planes to determine if the mode will intersect the receiver in both planes. Only if the mode is propagating (real $\hat{k}_{zm}$ value) and the angle of propagation is such that it intersects the receiver in both planes will the mode be included in the plane-wave field summation. The accompanying diagrams for each method are shown later in their respective sections which specifically define the critical parameters in each approach as they may have subtle differences.

Mathematically this geometric cut-off method is achieved with Kronecker delta functions of the propagation angle for each mode θ_m projected in *x* and in *y* and θ_1 and θ_2 which are the angles from the start and end of the grating respectively to the receiver in each projection. In the *x* projection the delta function is,

$$\delta_{\theta 1x}^{\theta 2x} = \begin{bmatrix} 1 \text{ if } \Re\left(\hat{\mathrm{k}}_{\mathrm{zm}}\right) > 0 \text{ and } \theta_{2x} \geq \theta_{mx} \geq \theta_{1x} \\ 1 \text{ if } \Im\left(\hat{\mathrm{k}}_{\mathrm{zm}}\right) > 0 \\ 0 \text{ else} \end{bmatrix} \tag{7.46}$$

and in *y* it becomes,

$$\delta_{\theta 1y}^{\theta 2y} = \begin{bmatrix} 1 \text{ if } \Re\left(\hat{\mathrm{k}}_{\mathrm{zm}}\right) > 0 \text{ and } \theta_{2y} \geq \theta_{my} \geq \theta_{1y} \\ 1 \text{ if } \Im\left(\hat{\mathrm{k}}_{\mathrm{zm}}\right) > 0 \\ 0 \text{ else} \end{bmatrix} \tag{7.47}$$

The projected propagation angles for mode *m* is given in *x* by,

$$\theta_{mx} = \cos^{-1}\left(\frac{\hat{k}_{xm_x}}{\sqrt{\hat{k}_{zm}^{\,2} + \hat{k}_{xm_x}^{\,2} + \hat{k}_{ym_y}^{\,2}}}\right) \tag{7.48}$$

and in *y* by,

$$\theta_{my} = \cos^{-1}\left(\frac{\hat{k}_{ym_y}}{\sqrt{\hat{k}_{zm}^{\,2} + \hat{k}_{xm_x}^{\,2} + \hat{k}_{ym_y}^{\,2}}}\right) \tag{7.49}$$

Surface modes must also be considered which will be included in the summation if the grating extends beyond the receiver in both *x* and *y* projections and omitted otherwise which gives rise to the additional Kronecker deltas in *x* of,

$$\delta_{xG}^{xR} = \begin{bmatrix} 1 \text{ if } \Im\left(\hat{\mathrm{k}}_{\mathrm{zm}}\right) > 0 \text{ and } x_{G2} > x_R \\ 1 \text{ if } \Re\left(\hat{\mathrm{k}}_{\mathrm{zm}}\right) > 0 \\ 0 \text{ else} \end{bmatrix} \tag{7.50}$$

and in *y* of,

$$\delta_{yG}^{yR} = \begin{bmatrix} 1 \text{ if } \Im\left(\hat{\mathrm{k}}_{\mathrm{zm}}\right) > 0 \text{ and } \mathrm{y}_{G2} > y_R \\ 1 \text{ if } \Re\left(\hat{\mathrm{k}}_{\mathrm{zm}}\right) > 0 \\ 0 \text{ else} \end{bmatrix} \tag{7.51}$$

The field summation of Eq. (7.43) with the addition of the finite grating approximation

delta functions then becomes,

$$p_{tot}(x,y,z\geq 0) = p_i + p_r + \sum_{m\neq 0,0}^{x}\sum^{y}\delta_{\theta 1x}^{\theta 2x}\delta_{\theta 1y}^{\theta 2y}\delta_{xG}^{xR}\delta_{yG}^{yR}\hat{Z}_m\hat{V}_m \exp\left(i\left[\hat{k}_{xm_x}x+\hat{k}_{ym_y}y\right]\right).\exp\left(i\hat{k}_{zm}z\right) \tag{7.52}$$

Remember that this is the plane-wave field summation from the solution of the modal-model but modified by the finite grating approximation to remove modes which would not geometrically intersect the receiver were the grating only finite in extent.

7.2.3.1 Type I – Floating rectangular grating

For this variant the extents of the lattice are defined by the two corner co-ordinates G_1 and G_2. It allows the size of lattice to be defined relative to the origin, which is the point of notional specular reflection. The geometrical scheme is shown below both in plan view (the *x*-*y* plane) and the horizontal projection for *x* or *y*.

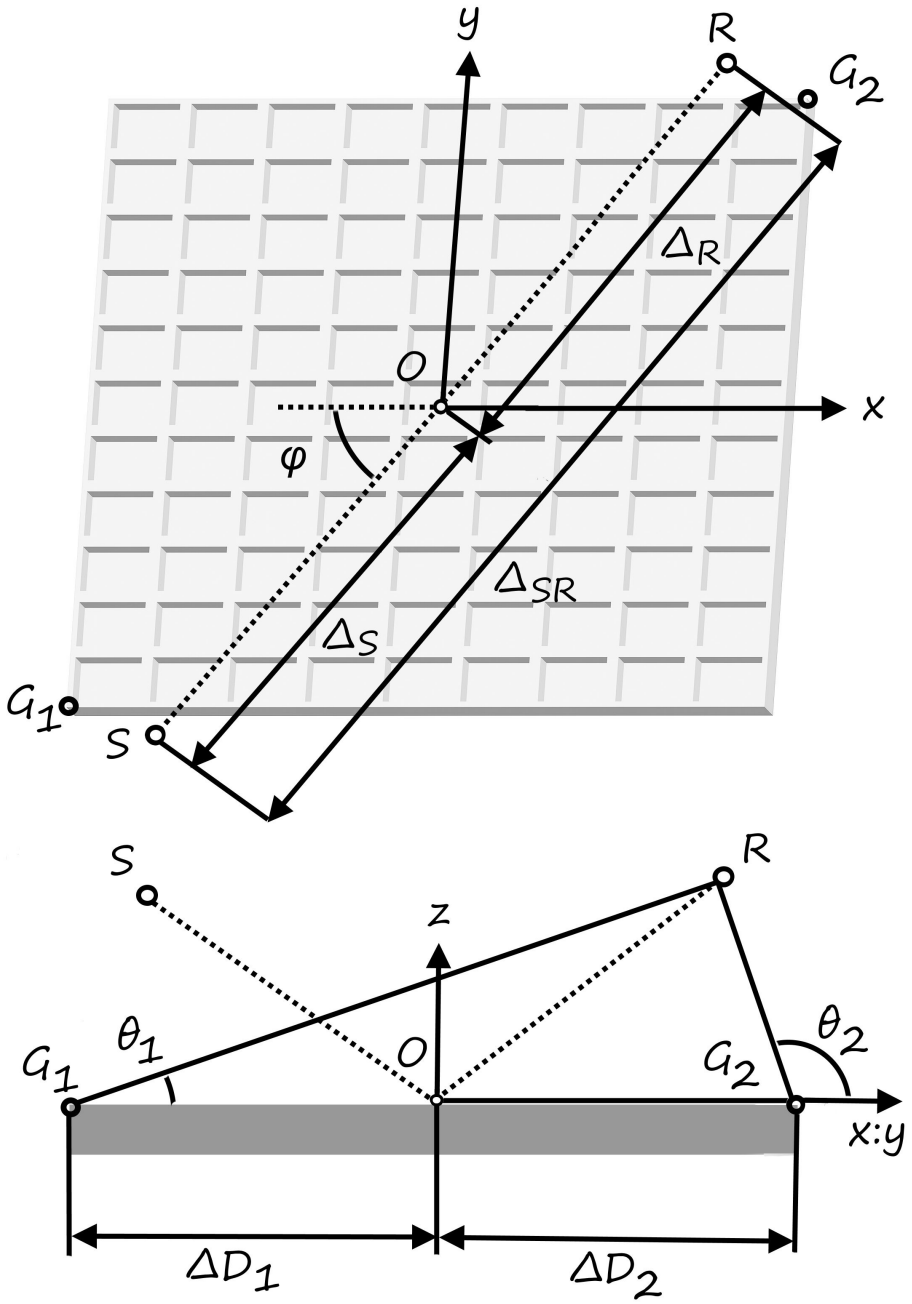

Figure 7.6 Finite grating assumption scheme for type I.

In order to calculate whether the *m*'th mode will intersect the receiver, the bounding angles θ_1 and θ_2 are calculated and compared with the propagation angle of mode *m* (Eq. (7.48)) and Eq. (7.49)) using the relation of Eq. (7.46) in *x* and Eq. (7.47) in *y*. If mode *m* is evanescent then Eq. (7.50) solely determines whether the mode will be included in the plane-wave field summation in the *x*-*z* plane and Eq. (7.51) in the *y*-*z* plane. The projected distance from the start of the grating to the receiver Δ_{D1} is given in *x* and *y* by,

$$\Delta_{D1x} = x_R - x_{G1} \tag{7.53}$$

$$\Delta_{D1y} = y_R - y_{G1} \tag{7.54}$$

Projecting the horizontal distance form the end of the grating to the receiver is achieved with,

$$\Delta_{D2x} = x_R - x_{G2} \tag{7.55}$$

$$\Delta_{D2y} = y_R - y_{G2} \tag{7.56}$$

With reference to figure 7.6 the bounding angles in the *x*-*z* plane projection are,

$$\theta_{1x} = \tan^{-1}\left(\frac{z_R}{\Delta_{D1x}}\right) \tag{7.57}$$

$$\theta_{2x} = \tan^{-1}\left(\frac{z_R}{\Delta_{D2x}}\right) \qquad \Delta_{D2x} \geq 0 \tag{7.58}$$

$$\theta_{2x} = \tan^{-1}\left(\frac{z_R}{\Delta_{D2x}}\right) + \pi \quad \Delta_{D2x} < 0 \tag{7.59}$$

which for the *y*-*z* plane are,

$$\theta_{1y} = \tan^{-1}\left(\frac{z_R}{\Delta_{D1y}}\right) \tag{7.60}$$

$$\theta_{2y} = \tan^{-1}\left(\frac{z_R}{\Delta_{D2y}}\right) \qquad \Delta_{D2y} \geq 0 \tag{7.61}$$

$$\theta_{2y} = \tan^{-1}\left(\frac{z_R}{\Delta_{D2y}}\right) + \pi \quad \Delta_{D2y} < 0 \tag{7.62}$$

Use the Kronecker delta functions of Eq. (7.46) in *x* and (7.47) in *y* with θ_1 and θ_2 as the parameters to determine whether the given modes will geometrically intersect the receiver in both planes and thus be included or not in the plane-wave field summation.

7.2.3.2 Type II – Centred rectangular grating

This scheme assumes that the latticed grating is centred horizontally upon the geometric mid-point between the source and receiver and may be different from the origin which is the notional point of specular reflection. The extents of the grating are then defined by its length Δ_G in the *x* and *y* directions as shown in figure 7.7.

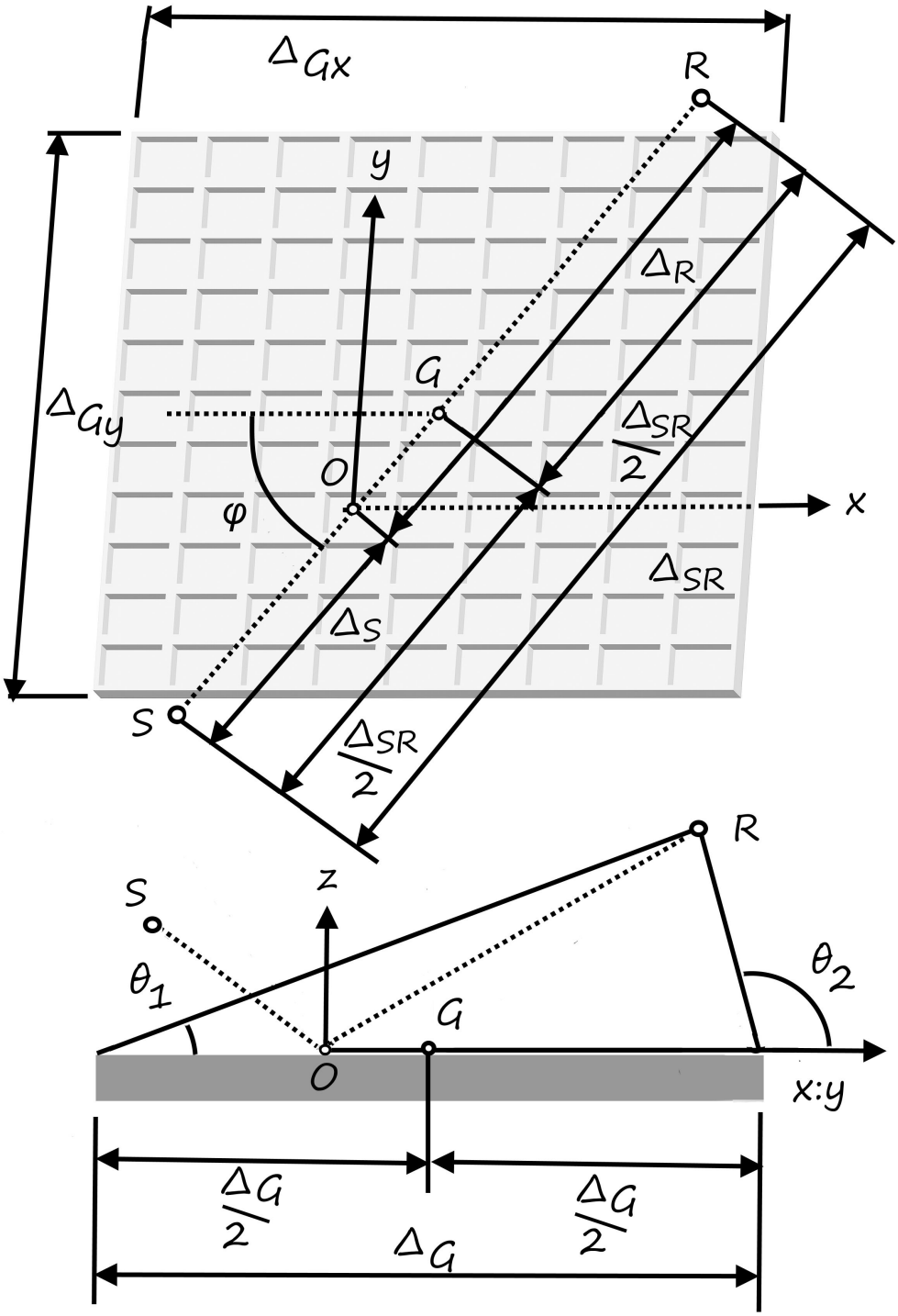

Figure 7.7 Finite grating assumption scheme for type II.

The intent is to model a situation similar to that used for making the measurements where the source and receiver are separated by the given distance Δ_{SR} and the lattice structure rotated around its centre point G (not the origin) to create the required azimuthal angle φ.

As the centre of the latticed grating $G(x_G,y_G,0)$ does not coincide with the origin, its absolute location with respect to the origin $O(0,0,0)$ must be calculated thus,

$$x_G = \frac{\Delta_{SR}}{2}\cos\varphi - |\Delta_S|\cos\varphi \tag{7.63}$$

$$y_G = \frac{\Delta_{SR}}{2}\sin\varphi - |\Delta_S|\sin\varphi \tag{7.64}$$

From figure 7.7 the horizontally projected distance between the start of the grating and the receiver for x and y is,

$$\Delta_{D1x} = \left(|\Delta_R|\cos\varphi - x_G\right) + \frac{\Delta_{Gx}}{2} \tag{7.65}$$

$$\Delta_{D1y} = \left(|\Delta_R|\sin\varphi - y_G\right) + \frac{\Delta_{Gy}}{2} \tag{7.66}$$

The horizontal distance from the end of the grating to the receiver is as follows,

$$\Delta_{D2x} = \left(|\Delta_R|\cos\varphi\right) - \left(x_G + \frac{\Delta_{Gx}}{2}\right) \tag{7.67}$$

$$\Delta_{D2y} = \left(|\Delta_R|\cos\varphi\right) - \left(y_G + \frac{\Delta_{Gy}}{2}\right) \tag{7.68}$$

The bounding angles are then given by the same equations as in type I which in the x projection is Eqs. (7.57-59) and in y is Eqs. (7.60-62).

7.2.3.3 Type III – Bound grating

In this type of the finite grating approximation it will be assumed that the latticed grating is bounded by the horizontal extents of the source and receiver as in figure 7.8 which shows the x-z and y-z horizontal projections. A plan view in this instance is omitted as it does not add any information, the lattice is just bounded by the horizontal extents of the source and receiver in both projections. Therefore, in the limit φ=0° the grating will have 0 length in y, and vice versa for φ=90° where the x extent of the grating will be 0.

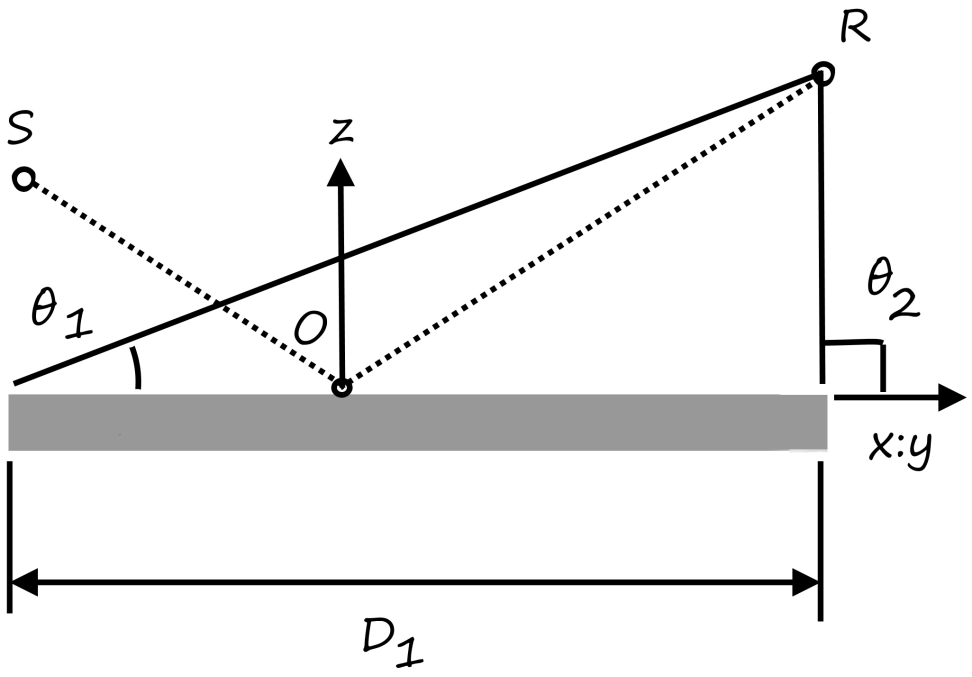

Figure 7.8 Finite grating assumption scheme for type III.

For this type the horizontal distance from the end of the grating to the receiver is always zero as the two points are horizontally coincident. The distance from the start of the grating to the receiver in the horizontal plane is given in *x* by,

$$\Delta_{D1x} = \left|\Delta_{SR}\right| \cos\varphi \tag{7.69}$$

and in *y* as,

$$\Delta_{D1y} = \left|\Delta_{SR}\right| \sin\varphi \tag{7.70}$$

These give rise to the bounding angles of,

$$\theta_{1x} = \tan^{-1}\left(\frac{z_R}{\Delta_{D1x}}\right) \tag{7.71}$$

$$\theta_{1y} = \tan^{-1}\left(\frac{z_R}{\Delta_{D1y}}\right) \tag{7.72}$$

as $\Delta_{D2} = 0$,

$$\theta_{2x} = \theta_{2y} = \frac{\pi}{2} \tag{7.73}$$

which as before are used in Eq. (7.46) and Eq. (7.47) to determine whether the

corresponding mode intersects the receiver in the plane-wave summation.

7.2.4 Deriving an effective surface impedance

From the resulting 3d plane-wave summation of Eq. (7.52) an effective impedance Z_{eff} for the latticed surface may be derived. The process is the same as for 2d and so requires only a brief recap. The plane wave pressure field at every point in the free-field is known from the solution of the 3d modal-model and Eq. (7.52) as is the geometry of the problem in terms of source-receiver location and separation. It is therefore possible to calculate the effective plane-wave reflection coefficient Γ_P given by Chien and Soroka [37] as,

$$\Gamma_P = \frac{\cos\theta - 1/Z_{eff}}{\cos\theta + 1/Z_{eff}} \tag{7.74}$$

from the plane-wave pressure field and problem geometry thus,

$$\Gamma_P = \frac{p_r(x_R, y_R, z_R) + \sum_{m\neq 0,0}^{x}\sum^{y} p_m(x_R, y_R, z_R)}{p_i(x_R, y_R, z_R).\exp\left(ik\left[R_{ref} - R_{inc}\right]\right)} \tag{7.75}$$

The *exp*() term is required to remove the phase difference due to path length difference between the incident and reflected components to leave just the effects of the ground surface itself. The terms R_{ref} and R_{inc} are the straight line ray path lengths of the incident and 'specularly reflected' components reaching the receiver from the point source. These are given in the 3d point-to-point propagation geometry by,

$$R_{inc} = \sqrt{\Delta x_{SR}{}^2 + (z_R - z_S)^2} \tag{7.76}$$

$$R_{ref} = \sqrt{(\Delta_S + z_S)^2 + (\Delta_R + z_R)^2} \tag{7.77}$$

Rearranging Γ_P of Eq. (7.74) allows Z_{eff} to be calculated as follows.

$$Z_{eff} = \frac{(1+\Gamma_P)\sec\theta}{1-\Gamma_P} \tag{7.78}$$

It is valid only for the geometry and frequency used to calculate it and as such cannot be considered as an inherent property of the latticed surface.

7.2.5 The excess-attenuation spectrum for the latticed grating-structure

The problem is reduced to that of simple point-to-point propagation above an impedance plane of the form of figure 7.9 in order to approximate the response were the source point-like. This is the same as for 2d because in both cases once the ground has been characterised by Z_{eff} the problem may be analysed as a simple point-to-point ray path problem above an impedance plane.

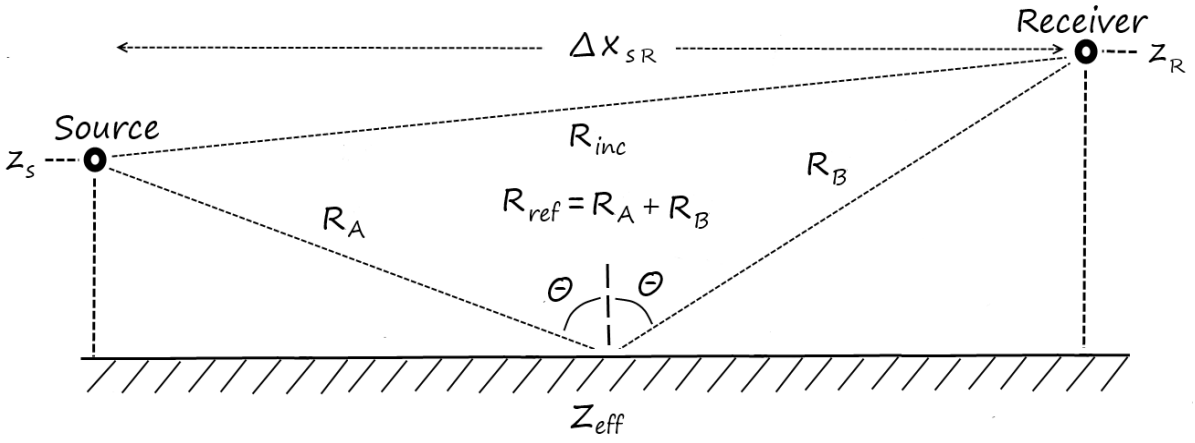

Figure 7.9 Point-to-point acoustic propagation above an impedance ground plane.

The transition from plane-wave to spherical propagation is made by using Z_{eff} in the spherical reflection coefficient [37] Γ_S as Z_{eff} may be considered largely independent of wave type for this application as justified in section 6.2.9. The equation for excess-attenuation is the same as for the 2d case which for spherical wave spreading is,

$$EA_{dB}(f) = 20\log\left(\left|1+\frac{\frac{\Gamma_S}{4\pi R_{ref}}\exp(ikR_{ref})}{\frac{1}{4\pi R_{inc}}\exp(ikR_{inc})}\right|\right) \tag{7.79}$$

The details and derivations have been omitted here for brevity but the reader is referred to the 2d implementation section for a thorough discussion of this process.

What we have achieved is to take the plane-wave homogeneous field from the modal-model and convert it to find a solution of a point-to-point spherical field for a given geometry. The key to this method is calculating Z_{eff} for the plane wave field and then applying it within a spherical reflection coefficient to approximate a point source and

receiver which is of more practical use in outdoor acoustics. This method is an approximation and is limited to the geometry for which it is solved but has run times orders of magnitude faster than the equivalent direct analysis techniques such as BEM or finite element analysis.

7.3 Results

7.3.1 Comparison with measurement

The section compares the predictions of the extended 3d modal-model with measurements made in the anechoic chamber. Due to the complexity of the lattice structure it was not possible to obtain results from any other theoretical method, however the predictions will be compared in later sections with the 2d extended modal-model which bear some equivalence at azimuthal angles of 0 and 90 degrees. As discussed in previous sections a 3d BEM program was modified for this application but the computing resources required for the solution of the lattice problem with sufficient resolution were far beyond those available to us. Furthermore COMSOL (a finite element analysis software suite) was evaluated but it is not ideally suited to such problems by nature and the resources required to solve the problem were also not realistic.

The measurements were made in the Open University's anechoic chamber using the methods described in chapter 3. A 1 m^2 square lattice structure was made from four equal sections of laser cut MDF which was placed upon a thick sheet of plywood to make the hard cavity bottoms. The lattice was then rotated around the centre point between the source and receiver to achieve an azimuthal angle. A picture of the measurement set up is shown below at an azimuth angle φ of 83 degrees,

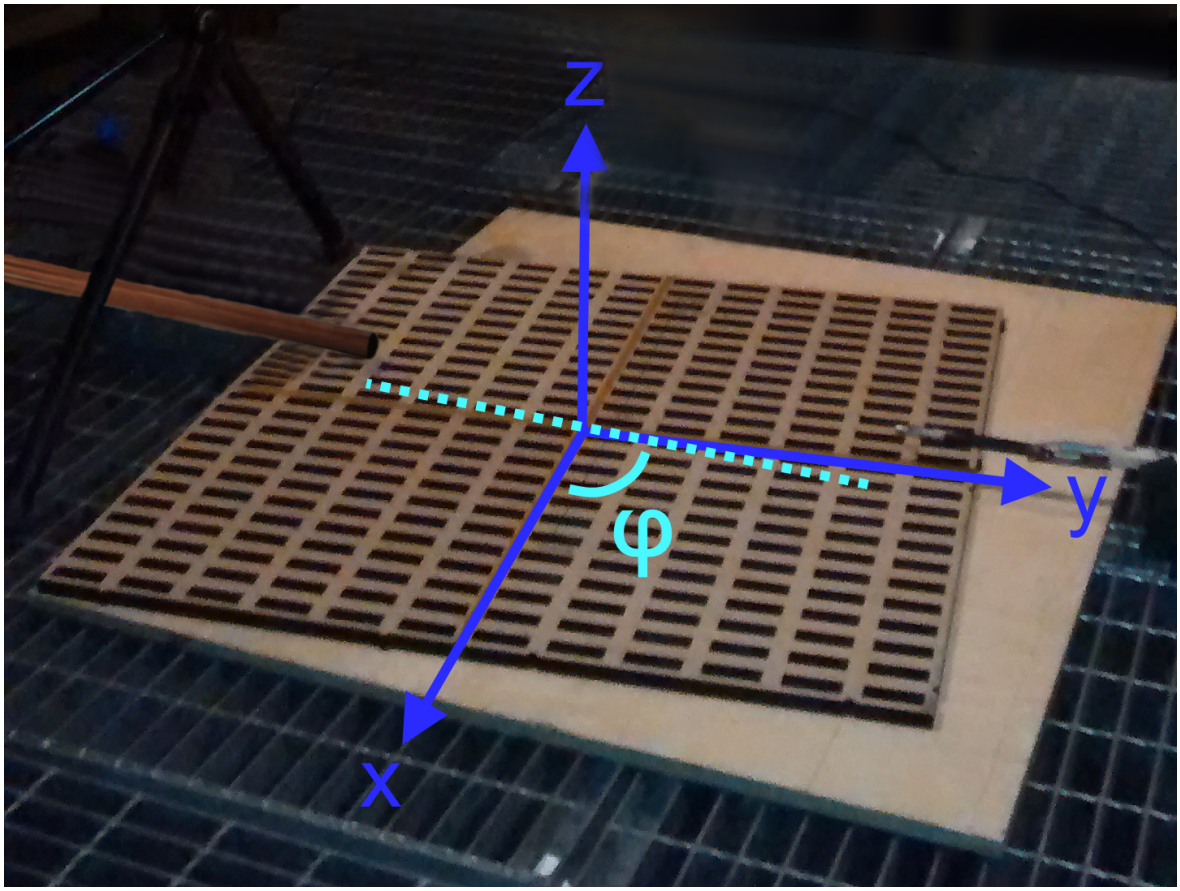

Figure 7.10 Lattice structure measurement setup φ=83°.

The parameters of the MDF lattice were as follows,

Lattice pitch in x, d_x = 0.04 m.

Lattice pitch in y, d_y = 0.08 m.

Aperture in x, a_x = 0.02 m.

Aperture in y, a_y = 0.06 m.

Lattice height, h = 0.018 m.

The source-receiver separation distance was set to 0.7 m with source and receiver heights above the lattice surface of 0.04 m and 0.045 m respectively. The overhang of the lattice structure beyond the source and receiver was kept approximately equal which is 0.15 m either end at φ=0° and φ=90° owing to the 1 m square lattice size and source-receiver separation of 0.7 m.

Measurements were taken in the approximate range 40 Hz to 40 kHz but the dimensions of the lattice cavities and the source-receiver geometry cause the majority of the discernible

effects to lie in the range 1 kHz to 10 kHz and so the results will be presented for this bandwidth. A set of nine measurements were taken for the stated source-receiver geometry at azimuthal angles of 0º, 7º, 15º, 30º, 45º, 60º, 75º, 83º, 90º. The first set of three is shown in figure 7.11. The figures in square brackets [ ] for each legend entry is the standard error calculated with the following formula with reference to the measurement.

$$SE = \sqrt{\frac{1}{n}\sum_{f_n}\left|EA_{reference}(f_n) - EA_{predicted}(f_n)\right|^2} \tag{7.80}$$

For each result the measurement is plotted along with the extended 3d modal-model prediction for all three types of finite grating approximation discussed in the previous section which will be summarised again here for clarity. Type I defines the extents of a square grating surface by the absolute *x*-*y* co-ordinates of its two corners G_1 and G_2 which in this instance are G_1=(-0.5, -0.5) and G_2=(0.5, 0.5). Type II defines the length of the lattice in *x* and *y* by Δ_{Gx} and Δ_{Gy} which will both be 1 m in this section, with its centre placed at the mid-point between the source and receiver and not the origin as in Type I. For the measurement setup used in this example Types I and II will be similar. Type III assumes that the grating extends only between the source-receiver when projected onto the *x*-*z* or *y*-*z* plane so at the limit φ=0º the grating will have 0 length in *y,* 0.7 m length in *x* and vice versa for φ=90º. The truncations for the 3d modal-model are *N*=1 and *M*=5 unless otherwise stated and 200 frequency points are used.

The EA plots throughout this section are defined relative to a flat hard ground surface at *z*=0 and hence the response will tend to 0 dB as frequency tends to zero.

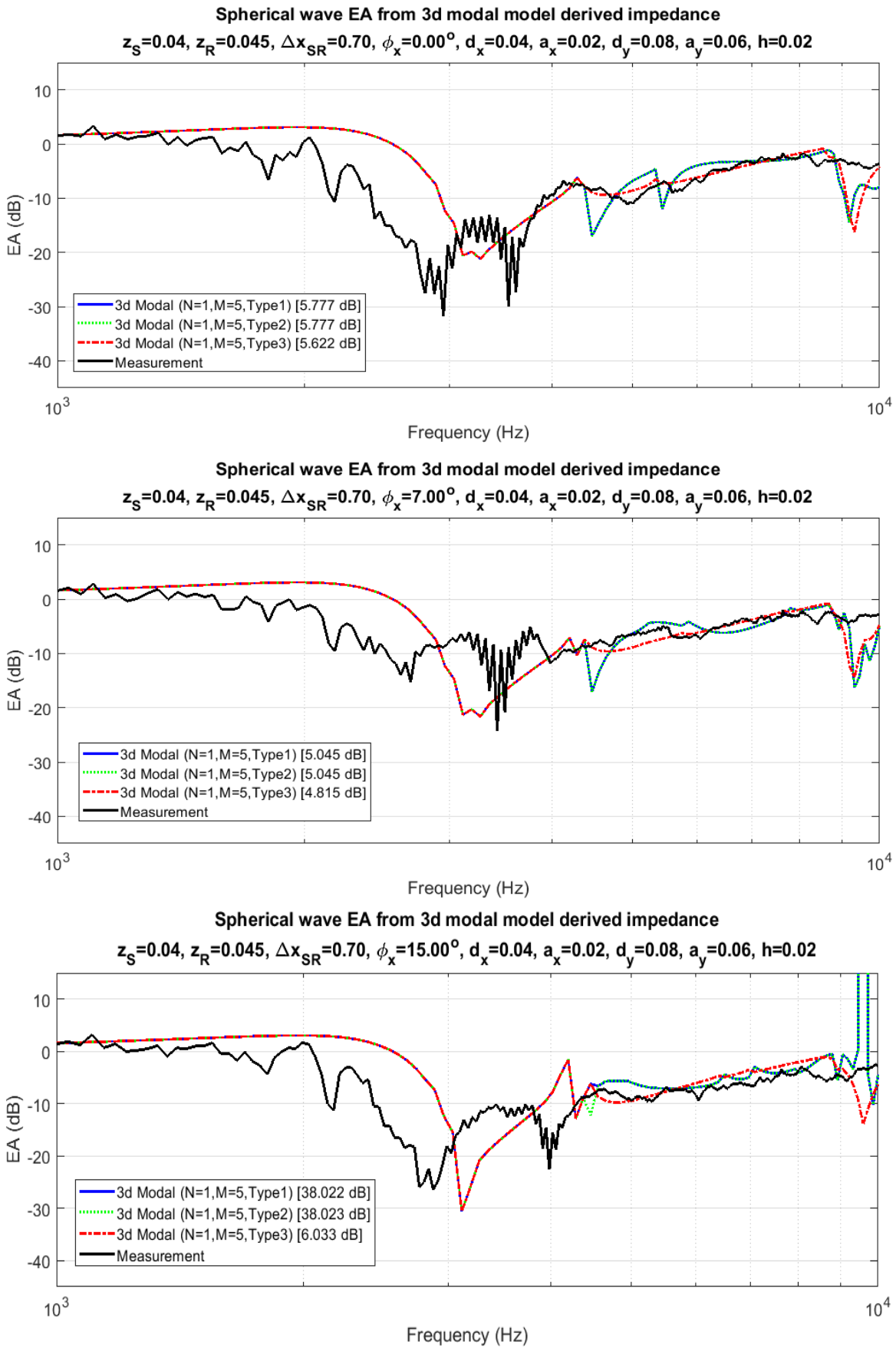

Figure 7.11 Excess-attenuation spectra for latticed structure at azimuthal angles of a) φ=0°, b) φ=7°, c) φ=15°.

It is immediately apparent that Type I and II produce very similar results which is to be expected as for this measurement setup the two share close equivalency. This is because the grating has been defined in the simulations to extend equally either side of the source and receiver which places the mid-point of the grating and horizontal mid-point between the source and receiver almost coincident because the source and receiver heights are very similar. Therefore the approximations of Type I and Type II have close equivalency in this case but for different geometries they would be expected to diverge to some extent. Type III is also very similar to the other two up to around 2 kHz where is differs slightly and tends to show smoother characteristics which agree better with the measurement than Types I and II. Hence the slightly lower SE figures for Type III in figures 7.11 a) and b). The errant SE results for Types I and II in figure 7.11c) are due to the numerical errors which can be seen as positive saturating EA values at just below 10 kHz. They are caused by the complex error function *cef* () of the spherical reflection coefficient going out of bounds which occurred also for the 2d models and has been attributed to approximation errors which cause Z_{eff} values which signify an overestimation of energy reaching the receiver and violation of energy conservation. Type III does not suffer the same effects for this geometry which perhaps may be due to the fact that the grating never exceeds the horizontal extents of the source and receiver and so may be less susceptible to erroneously showing excess energy.

In figure 7.11a) Types I and II exhibit two local EA minima at 4500 Hz and 5400 Hz and in b) a single dip at 4500 Hz which are not evident in the measurements nor in Type III. These could be due to diffracted modes from the far extents of the lattice which are not evident in the measurement or type III because in reality such modes would be attenuated by spherical spreading losses. They would be highly attenuated upon reaching the receiver in measurement and for Type III simply may not be there as the grating is more severely truncated and would be excluded by the finite grating approximation. For φ=15^{o} in figure 7.11c) all three predictions exhibit a response peak at just over 4200 Hz whereas the measurement is suggesting a corresponding dip at 4000 Hz. Also throughout figure 7.11 all of the extended modal-model predictions show extra EA minima at just under 10kHz which is not evident in measurement. It is difficult to postulate upon these latter two anomalies due to a lack of another reference method as all of the predictions are acting in unison.

The measurements are not showing a clear surface wave preceding the first EA minimum. It is suspected, as consistently seen in figures 6.24 and 6.25, that our measurement system does often underestimate surface wave magnitudes in this area which results in the gradual roll-off towards the first EA minimum rather than the resonant response one may expect. The cause is not known for sure at this time and so the problem is yet to be resolved. It appears that either the surface wave is not being excited or it is being dissipated by losses in the surface structures under test. The MDF material used for the lattice structure is acoustically 'softer' than other materials such as plastic or metal and so may not be a satisfactory approximation to an acoustically hard material. Cost constraints meant that MDF was the best available compromise as fabricating such structures from metal or plastic was found to be prohibitively expensive. It is therefore difficult to say to what extent the discrepancy between the measurements and predictions in the low frequency area is caused by measurement error or by the performance of the 3d extended model-models. However it appears that the frequency of the first EA minimum agrees between the measurements and predictions to within approximately 300 Hz. It is interesting to note that between φ=0° and φ=15°, the predicted frequency of the first EA minimum remains fairly constant at around 3100 Hz but becomes more pronounced in magnitude at φ=15°.

The measurements in all three cases show a double EA dip in the region up to 4000 Hz which is not reproduced in the predictions. Only a single dip is predicted which lies in between the two dips present in the measurements. The measurements show a trend where the separation between the two dips widens with increasing azimuthal angle.

The next three results in figure 7.12 are with azimuthal angles of φ=30°, φ=45° and φ=60°.

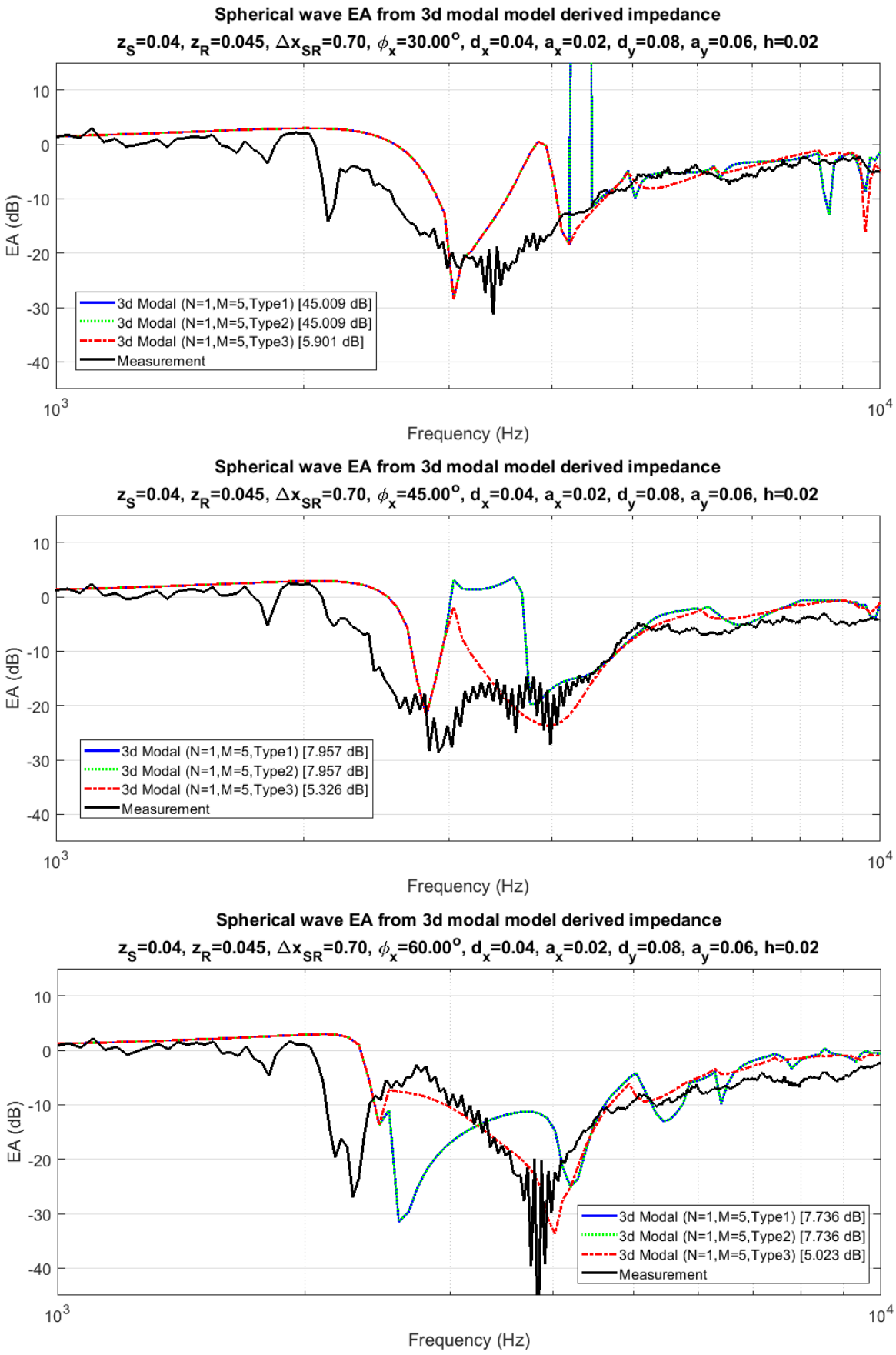

Figure 7.12 Excess-attenuation spectra for latticed structure at azimuthal angles of a) φ=30°, b) φ=45°, c) φ=60°.

Once again the measurements are showing a generally lower magnitude than the predictions at frequencies up to the first EA minimum. As previously discussed the cause of this cannot be attributed to one particular effect due to our measurement uncertainties in this region. From φ=30º to φ=60º the measurement is showing a transition from a broad single dip response to a sharp double dip characteristic. Notice that the measurement shows a double EA minimum dip in figure 7.11c) for φ=15º, a single and gentle dip for figure 7.12a) φ=30º then returns to a double dip characteristic in figures 7.12b) and c) which then can be seen to persist for remaining sweep of azimuthal angle up to φ=90º. The energy distribution between modes will be complex for the lattice and this will manifest as the apparent chaotic nature of the response. The interaction of supported modes within each cavity will be far more complex in nature than for the 2d grooves because of the extra dimension involved in the lattice.

The response below 4000 Hz changes significantly between figure 7.12b) φ=45º and figure 7.12c) φ=60º. The measurements show that from figure 7.12b) to c) the second dip remains similar in frequency but increases in magnitude while the first dip reduces significantly in frequency yet remains similar in magnitude at approximately -30 dB. The intervening response is then lifted to nearly 0 dB. The predictions of Type III loosely track this trend while Types I and II do not follow the measurements at all well.

Worthy of note is the reducing discrepancy between measurement and prediction in the low frequency and surface wave region below the first EA minimum with increasing azimuthal angle. The magnitude of the surface wave component in the predictions remains fairly constant with azimuthal angle but the measurements are showing a trend towards increasing magnitude with increasing azimuthal angle in the realm below the first EA minimum. This may be suggesting that the surface wave related measurement problems are less when the lattice is orientated towards φ=90º or that the lattice itself more readily supports surface waves in this orientation but this does not manifest in the predictions. For the results we have it is difficult to say for certain if either hypothesis has merit.

For figures 7.12a) and b) Type III proves to be significantly superior to the other two. In b) Types I and II significantly over predict the response between the two low frequency EA dips while Type III exhibits the same problem but to a lesser extent. For c) Types I and II

predict entirely the wrong slope for the response between 2600 Hz and 4200 Hz combined with incorrect predictions of the frequencies of the two low frequency dips. Type III fares significantly better, predicting the correct slope direction and the two predicted low frequency dips are closer to the measurement, especially the second at around 4000 Hz.

Once again a numerical error can be seen in figures 7.12a) for Types I and II at just over 4000 Hz which is corrupting the SE figures. Type III is once again unaffected by this phenomenon.

The final set of measurement results are presented in figure 7.13 which consists of the azimuthal angles of φ=75^{o}, φ=83^{o} and φ=90^{o}.

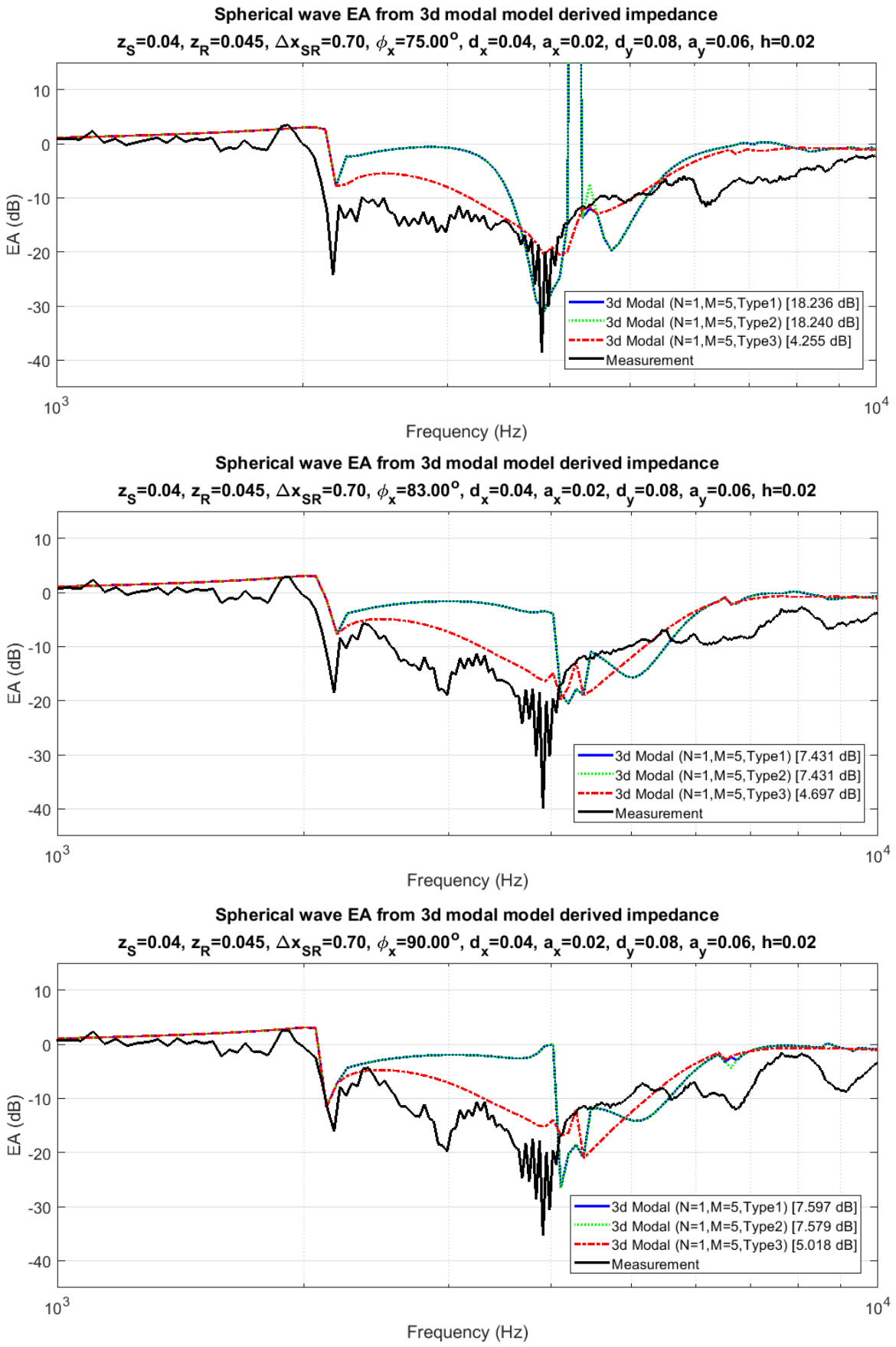

Figure 7.13 Excess-attenuation spectra for latticed structure at azimuthal angles of a) φ=75°, b) φ=83°, c) φ=90°.

This group of results represents the closest agreement between measurement and prediction. The response in each case of figure 7.13 shows a clear double dip characteristic in the low frequency range up to around 4000 Hz. The second dip remains largely unperturbed throughout the range of φ=60° to φ=90° at a frequency of 4000 Hz and with a magnitude which dwindles slightly from -45 dB to just over -40 dB. The frequency of the first EA minimum dip remains fairly constant across figure 7.13 at around 2200 Hz but the magnitude reduces noticeably from figure 7.13a) to c). The low frequency region below the first EA minimum agrees well with predictions further suggesting the assertion made earlier that this frequency region may be suffering less experimental error when the lattice is orientated towards φ=90°, for whatever reason. This of course could be a false assertion, but discrepancies are known to exist with our measurements taken in the low frequency region below and up to the first EA minimum underestimating the response and the magnitude of the surface wave compared with what would be expected.

The predictions of all three types are in good agreement with measurements up to the first EA minimum at about 2200 Hz with the exception that the magnitude of the first EA minimum is underestimated by the predictions in figure 7.13a) and to a lesser extent b). Beyond this in the spectrum Type III exhibits much closer agreement with measurement than do the other two predictions. However all three types predict the frequencies of the two major EA minima with reasonable accuracy.

Another numerical error manifests in figures 7.13a) for Types I and II making the SE figures unreliable for these but again Type III is not affected.

In summary it is evident that the predictions offer significantly better agreement with measurement as the azimuthal angle tends to 90°. It is difficult to determine the root causes of this without reference to other theoretical methods or data with which to compare. However the obvious difference between the two azimuthal angle limits is that the lattice when projected onto the plane of the source and receiver appears very different between φ=0° and φ=90°. For φ=0° the response of the lattice will likely be dominated by the d_x and a_x dimensions which are relatively small with an effective porosity of 0.5. Whereas at φ=90° the d_y and a_y dimensions are in the same plane as the source-receiver which are larger dimensions and have a much higher effective porosity of 0.75.

Type III has shown to give the best agreement for this particular lattice and measurement setup. This may be somewhat surprising as intuitively it is the type with least resemblance to the laboratory setup because it assumes no extension of the lattice beyond the horizontal extents of the source and receiver, which in fact there was as can be seen in the photo of figure 7.10. However this does suggest that in practice the response for a spherical source is dominated by the ground surface structure directly between the source and receiver and the influence of the ground off angle from the direct horizontal line from source to receiver diminishes rapidly with distance. For types I and II modal contributions from the whole truncated latticed surface have equally weighted influence because the modal field summation is planar with no spreading loss. Where in reality contributions from the farther extents of the lattice will be diminished due to spreading losses. This suggests that the 3d scenario is less tolerant of the initial plane wave field assumption than the 2d case and more sensitive to the appropriate application of the finite grating approximation. Type III effectively ignores contributions from the far extents of the lattice by truncating it to the projected horizontal extents between the source and receiver which appears to be the most effective approach of the three types tested in this study.

7.3.2 Comparison with the 2d extended modal-model

At the perpendicular azimuthal angles of φ=0° and φ=90° the 3d extended modal-model may be approximately compared with the results from the 2d extended modal-model. The lattice pitch d in the perpendicular direction relative to the source-receiver plane is set to a small value with an a/d ratio of close to unity so that the diffractive properties in that direction are shifted somewhat beyond the upper frequency of interest while also appearing similar to infinite grooves with the high porosity. The lattice should then behave predominantly as if it were a 2d grooved surface with dimensions of those in the direction of the source-receiver plane. The truncations of N=1 and M=5 were used for both the 2d and 3d simulations for consistency. The truncations being severe due to the computation time of the 3d model, which is significantly longer than for 2d because of the relative sizes of the modal matrix as discussed in the corresponding theory sections.

Figure 7.14 shows the results of the comparison between the 3d and 2d extended modal-models for φ=0° and the equivalent values of d=0.04, a=0.02, h=0.018 for the 2d modal and x-axis lattice dimensions of d_x=0.04, a_x=0.02, h=0.018 for the 3d model with the

perpendicular y-axis lattice dimensions of d_y=0.008, a_y=0.0079 in an attempt to minimise their effect.

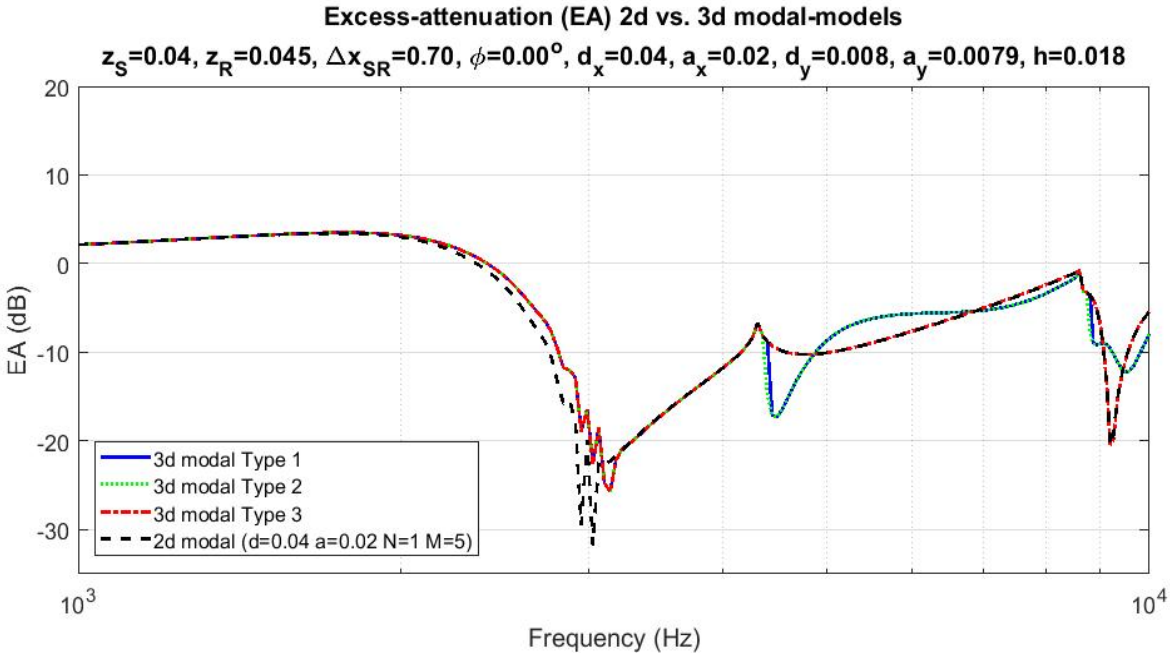

Figure 7.14 3d vs. 2d modal model for φ=0°.

Figure 7.15 shows the equivalent plot but with an azimuthal angle of φ=90°. The equivalent values for the 2d modal were d=0.08, a=0.06, h=0.018 and d_y=0.08, a_y=0.06, h=0.018 for the 3d model lattice y-axis dimensions and perpendicular x-axis dimensions of d_x=0.004, a_x=0.0039.

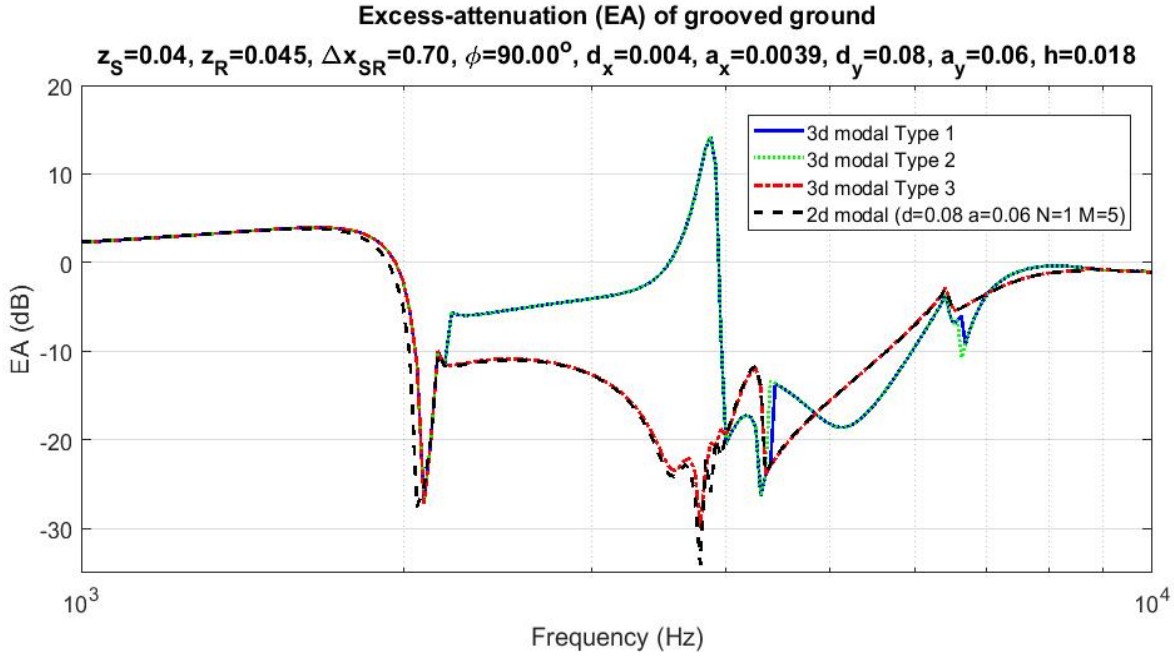

Figure 7.15 3d vs. 2d modal model for φ=90°.

In both instances the agreement between the 2d result and the trio of 3d types is good up to the first EA minimum. Only Type III retains good agreement with the 2d prediction throughout the remainder of the spectrum.

For φ=0° the agreement with 2d and Type III is excellent with only a slight overestimation of the magnitude of the EA minimum just below 10 kHz by the 3d Type III model and slight rippling of the response up to the first EA minimum being the only significant differences. Types I and II fare better in respect of agreement as to the magnitude of the EA minimum near 10 kHz but predict an extra EA minimum between 4000 and 5000 Hz which is not present for 2d or Type III. It is difficult to determine which method is the most correct because we do not have another reference method for the response of the latticed ground with which to compare. We are merely observing the performance of the models relative to each other under conditions of relative equivalence.

At φ=90° it is immediately apparent that Types I and II do not agree at all well with the 2d prediction. Type III shows good agreement with 2d up to around 4000 Hz. At φ=90° the surface will exhibit more scattering effects than at φ=0° for the given bandwidth because the size of d in the direction of source-receiver is larger and hence f_{LS} will be lower and the response will be dominated more by scattering with the accompanying 'chaotic' looking EA response at higher frequencies.

It appears that once again the Type III extended 3d modal-model is proving to be the most successful of the three in this study and for this geometry. It reinforces the earlier assertion that it is the ground surface in the immediate vicinity of the horizontal straight line between the source and receiver which has the greatest influence upon the response. In fact at the cardinal cases of φ=0° and φ=90° Type III assumes that the lattice is infinitely thin in the perpendicular direction so only the ground surface lying directly on the line between source and receiver will have any effect. Although the results of this section do not provide definitive proof of the accuracy of the 3d extended modal-model it does add a degree of confidence in the Type III method and the underlying kernel of the 3d model itself because of its close agreement with the 2d model-model under approximately equivalent conditions. The 2d model having been proved to show good agreement with existing methods and so constitutes a credible reference.

7.3.3 Sensitivity to the truncation of *M* and *N*

It is important to explore the sensitivity of the results to the truncations of M and N for the 3d case because of the implications for computation time. For the 2d extended modal-model it is not so critical in this respect because the computation time is so rapid that large values of M and N can be used by default that will encompass the audible spectrum for virtually any practical problem. The same cannot be said for 3d because the resulting modal-model matrix is N times larger than for 2d and is proportional to N^2 so the computation times soon become unreasonable with even modest values of N. The truncation of M does not alter the size of the matrix but it does affect the number of program loops required to calculate each element giving rise to a program loop proportionality of something like $2M^2 \times N^2$. The relative computation time impact M and N will have will therefore depend to some extent upon the particular software and hardware implementation.

Hence it is desirable to choose smaller truncations for the 3d model which are just enough include the required detail over the bandwidth of interest. Figure 7.16 shows a plot of results obtained from various truncations. As an example on a mid-range 2015 vintage personal computer running a crude and unoptimised MATLAB implementation (which is notoriously slow with discrete program loops) the computation times for 200 frequency points ranged from many minutes for N=1, M=2 to around an hour for N=3, M=2, a couple of hours for N=3, M=5 and in the order of 24 hours for N=3, M=10. However a more optimised implementation or using a compiled programming language would reduce these times enormously.

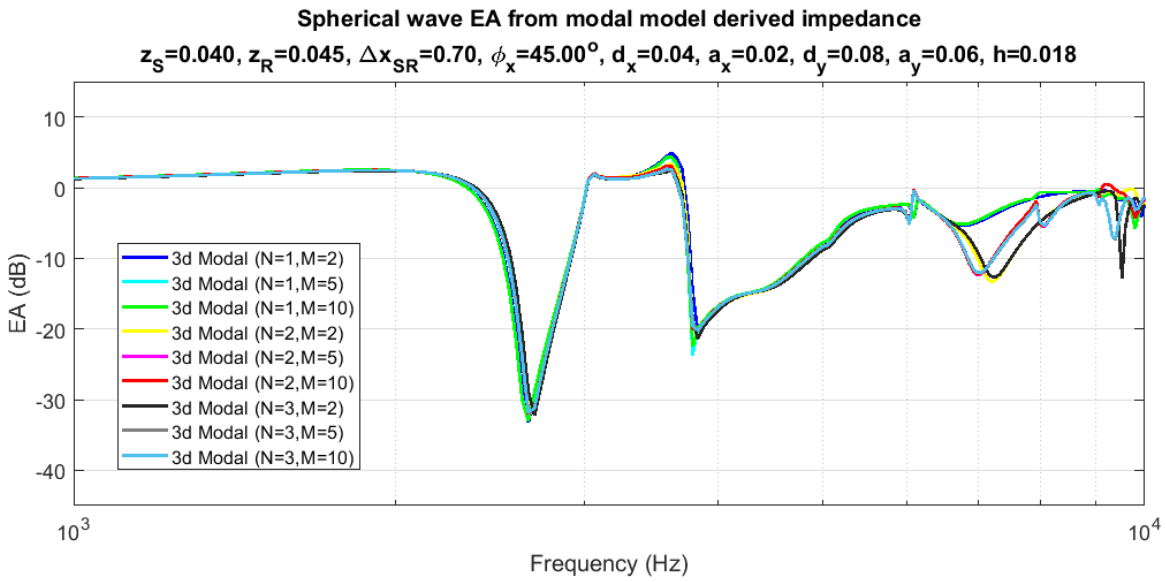

Figure 7.16 Sensitivity sweep of M and N for 3d lattice reference geometry at φ=45°.

Notice that up to 6000 Hz all curves agree closely and so within this frequency band and for the given reference geometry a truncation of N=1, M=2 would suffice in the interests of computation time. The N=1 examples show a noticeable resonant peak at 3600 Hz which flattens down to a consistent level for N>1.

For the truncation N=1, both the zeroth plane wave mode n=[0,0] and the first order modes n=[1,0], n=[0,1] and n=[1,1] will be included. The three curves for which N=1 (blue, cyan and green) exhibit responses which are virtually indistinguishable and in fact the cyan trace for N=1, M=5 is hidden from view behind the other two. The N=1 trio are missing a local EA minimum at around 7000 Hz which given the apparent independence of M must be caused by a cavity n-mode with order >1 which is not included with a truncation of N=1. So, for N=1 the choice of M beyond a value of 2 is not critical as the performance in this instance is limited by N.

When N>1 the EA minima at 7000 Hz is represented for all cases and the characteristic response is largely stable for all tested values of M. The frequency of said EA minima reduces by around 300 Hz for when N is increased from 2 to 3.

For this example the minimum truncation required in order to obtain a largely stable response is N=2, M=2 which had a solve time on our setup of around 30 minutes.

7.3.4 Summary

The 3d extended modal-model has been compared with measurement and has shown promise but requires further work. A proven theoretical reference method will be required to further investigate the performance and diagnose any problems.

However the Type III model compared favourably with its 2d equivalent at the two perpendicular angles which suggests that the core of the 3d modal-model and the methods used are fundamentally sound.

It can be inferred from Type III showing the best performance throughout that for this geometry at least, it is the portion of grating directly between the source and receiver which dominates the field at the receiver for the spherical wave propagation problem.

CHAPTER 8 – Direct Impedance Models for 2d groove grating

Methods will be presented for approximating the effective impedance of a periodic 2d rectangular grooved ground surface posed in terms of normal velocity as with the modal model. This is achieved by considering the interaction of the incoming incident wave with the discrete set of modes supported by the groove given by its dimensions as in figure 8.1.

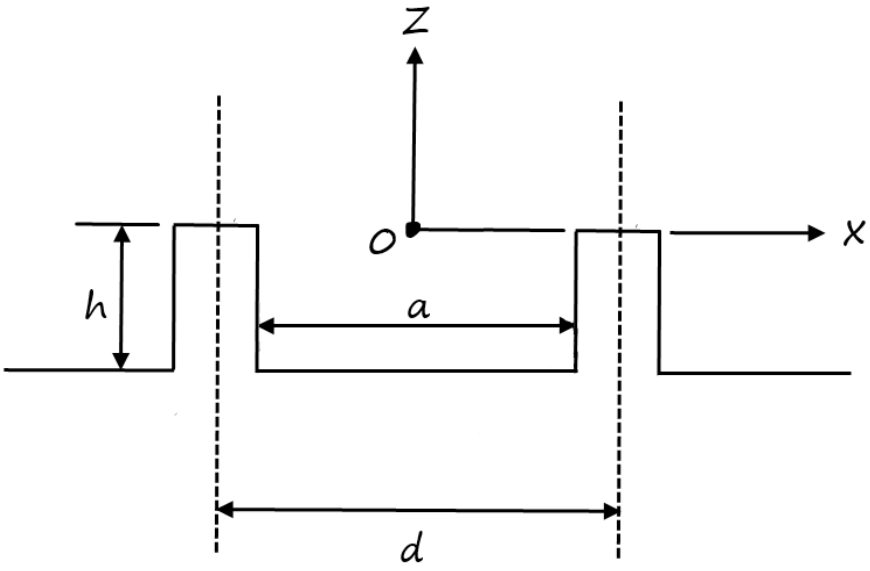

Figure 8.1 Periodic rectangular grooved surface.

8.1 Simplified causal summation model

A simplified impedance model, with similarities to the Fraunhofer model proposed by Cox etal. [63], is derived by first considering the time dependent causal interactions of the incoming (down-going in z) and outgoing (up-going) waves within an individual groove at the origin. Each amplitude weighted mode may be considered separately and linearly combined to approximate an average lumped impedance at the centre of the aperture, $x=z=0$. The assumption of unit porosity will be made where $a=d$ in order to simplify the analysis. Hence the walls between grooves will be assumed present but of zero thickness. Incidentally Zhu et al. [40] considered a similar comb-like structure but solved for tangential velocity differences at the cell boundaries to explore surface wave behaviour. For convention the positive direction of propagation is assumed to be defined as the positive direction of each respective axis. This, as before, defines the sign of impedance quantities and propagation constant components.

The effective impedance of a surface in the plane z=0 is by definition,

$$Z = \frac{p}{v \bullet d\mathbf{n}} \quad z = 0 \tag{8.1}$$

and will define the impedance within the groove aperture at z=0. Where p is pressure, v is particle velocity (positive in positive direction of associated axis) and $d\mathbf{n}$ is the surface normal unit vector pointing into the surface [38]. For this application $d\mathbf{n}$ is orientated in the -z direction as the surface is by definition perpendicular to the z-axis and parallel to x. Therefore,

$$v \bullet d\mathbf{n} = \text{vertical velocity into surface} = -v_z \tag{8.2}$$

Reference will be made to the modal model set of z-axis wave numbers for the modes within the groove, $k_{zn,}$. Where the sets k_{zn}^{+} and k_{zn}^{-} refer respectively to the positively valued up-going and the negatively valued down-going components for mode n. In line with convention k_{zn}^{+} propagates upwards towards z=∞ and k_{zn}^{-} downwards towards z=-∞ . Henceforth the superscript sign convention will be used to denote parameters referring to up or down-going wave components. Several other terms already defined in the modal-model will be used and referred to subsequently.

The lossless and inviscid assumptions are invoked and as such the impedance for each groove mode n at z=0, can be approximated thus, by considering the down and up-going components separately and on the basis that the spatial frequency of mode n is invariant and hence the impedance will be constant in x within the aperture.

$$Z_{Seff}(n) = \frac{p_n^- + p_n^+}{(v_{zn}^- + v_{zn}^+) \bullet d\mathbf{n}} \quad z = 0 \tag{8.3}$$

The p and v terms will be expanded at the origin x=z=0. For this the amplitude of each down-going groove mode n is required at the aperture on z=0 and will be approximated by the amplitude C_n. This is different from V_n of the modal-model because C_n represents an approximated amplitude of the down-going groove mode n whereas V_n is the resultant amplitude of the combination of the down-going and reflected up-going components of mode n. Here the up and down-going components are considered separately whereas in the

modal-model they are not.

In order to approximate C_n it will be assumed that the n modal component in the incident wave will excite the associated down-going n-mode within the groove with amplitude given by the inner product. It will be assumed that the mode will be excited with the full v_z amplitude of the component present the incident wave. In reality this could only occur when the mode has the same impedance as the incident wave and $a=d$. Else there will be a component transmitted to the associated groove mode and a component reflected at the groove aperture, the proportions given by the relative impedances. Furthermore it is also assumed that the amplitudes of the groove based n-modes are dependent only upon the incident wave and not on the remaining set of free-space m-modes. While the sets of n and m-modes are themselves orthonormal their relationship to each other is not. The excitation amplitude of each mode n is dependent upon the amplitude of all m-modes (including the incident wave contained in $m=0$) which themselves are dependant upon the amplitude of each mode n, and so on. The approximation C_n is therefore a critical parameter to the forthcoming simplifications because it allows the decoupling of the complex inter-dependence of the full problem to make possible an analytic approximation. Treatment of the problem in this way is similar to the approach taken by Cox et al. in their Fraunhofer model for Schroeder Diffusers [63].

Given the stated simplifications, let C_n be approximated by the inner product of the n-modal characteristic and the incident wave normalised to a in order to retain correct amplitude scaling as in Eq. (8.4). With the aid of Wolfram Alpha [42], the integral forms can be evaluated analytically as shown.

for $n = 0$,

$$C_0 = \int_{-a/2}^{a/2} \frac{1}{\sqrt{a}} \cos\left(\left[\frac{n\pi}{a}\right]\left[x + \frac{a}{2}\right]\right) . \frac{1}{\sqrt{a}} \exp(ikx \sin\theta)\, dx \quad n = 0 \tag{8.4a}$$

which evaluates to,

$$C_0 = \frac{\exp(-0.5iak \sin\theta)\left(-iak\left(-1 + \exp(iak \sin\theta)\cos\left(n\pi\right)\right)\sin\theta - \exp(iak \sin\theta) n\pi \sin\left(n\pi\right)\right)}{\left(-n\pi + ak \sin\theta\right)\left(n\pi + ak \sin\theta\right)} \tag{8.4b}$$

for $n > 0$,

$$C_n = \int_{-a/2}^{a/2} \sqrt{\frac{2}{a}} \cos\left(\left[\frac{n\pi}{a}\right]\left[x + \frac{a}{2}\right]\right) . \sqrt{\frac{2}{a}} \exp(ikx \sin\theta)\, dx \quad n > 0 \tag{8.4c}$$

which evaluates to,

$$C_n = \frac{\exp(-0.5iak \sin\theta)\left(-2iak\left(-1 + \exp(iak \sin\theta)\cos\left(n\pi\right)\right)\sin\theta - 2\exp(iak \sin\theta) n\pi \sin\left(n\pi\right)\right)}{\left(-n\pi + ak \sin\theta\right)\left(n\pi + ak \sin\theta\right)} \tag{8.4d}$$

The down-going component of velocity at the origin, v_{zn}^- is simply,

$$\begin{aligned} v_{zn}^- &= C_n \exp(ik_{zn}^- z) \\ &= C_n \qquad x = z = 0 \end{aligned} \tag{8.5}$$

With knowledge of the impedance of the *n'th*-mode within the groove cavity, also from the modal model, the corresponding pressure quantity at the origin is defined thus where k is the positive signed wave number of the incident wave,

$$p_n^- = v_{zn}^- Z_C \frac{k}{k_{zn}^-} \quad x = z = 0 \tag{8.6}$$

The down-going wave is denoted by the k_{zn}^- term, maintaining the correct inverse sign relationship between p_n^- and v_n^- for down-going propagation.

The up-going components are the reflections from the bottom surface of the groove and hence will have traversed the full depth of the waveguide like groove twice. The reflected component of velocity is expressed as follows where the -1 factor accounts for the phase inversion upon reflection from the bottom surface of the groove and the two *exp*() phase factors accounting for the downward and upward traverse respectively,

$$\begin{aligned} v_{zn}^+ &= C_n \exp(ik_{zn}^-(-h)) \exp(ik_{zn}^+ h)(-1) \\ &= -C_n \exp(ik_{zn}^+ 2h) \end{aligned} \tag{8.7}$$

The expansion is completed with the reflected pressure component where the Z (k/k_{zn}^+)

term remains positive as this component is up-going,

$$\begin{aligned} p_n^+ &= v_{zn}^+ Z_C \frac{k}{k_{zn}^+} \\ &= v_{zn}^+ Z_C \frac{k}{k_{zn}^+} \end{aligned} \tag{8.8}$$

Throughout the expansion, the sign of k_{zn} wave number components has been maintained to agree with propagation direction. Remember too that the velocity is defined as positive when in the positive direction of the axis. This ensures that the effective impedance results will be correctly signed. Substituting the expansions into Eq. (8.3) provides an approximate expression for each modal effective impedance Z_S within the groove.

$$\begin{aligned} Z_{Seff}(n) &= \frac{C_n Z_C \frac{k}{k_{zn}^-} - C_n \exp(ik_{zn}^+ 2h) Z_C \frac{k}{k_{zn}^+}}{\left(C_n - C_n \exp(ik_{zn}^+ 2h)\right) \bullet d\mathbf{n}} \\ &= \frac{C_n \left(Z_C \frac{k}{k_{zn}^-} - \exp(ik_{zn}^+ 2h) Z_C \frac{k}{k_{zn}^+} \right)}{C_n \left(1 - \exp(ik_{zn}^+ 2h)\right) \bullet d\mathbf{n}} \end{aligned} \tag{8.9}$$

The impedance across the x extents of the aperture for each mode n in isolation will be constant because of the single spatial frequency. However when multiple modes are combined the impedance will be dependant upon x within the extents of the aperture because of the combination of the different spatial frequencies of each mode. An average lumped impedance across the aperture combining all modes may be given by the integral,

$$Z_{Seff} = \int_{-a/2}^{a/2} \left(\frac{\sum_{n=0}^{n=\infty} e_n(x).C_n \left(Z_C \frac{k}{k_{zn}^-} - \exp(ik_{zn}^+ 2h) Z_C \frac{k}{k_{zn}^+} \right)}{\sum_{n=0}^{n=\infty} e_n(x).C_n \left(1 - \exp(ik_{zn}^+ 2h)\right) \bullet d\mathbf{n}} \right) .dx \tag{8.10}$$

As the n-modal characteristic function $e_n(x)$ and C_n are already normalised to a the integral does not require a normalising factor. Relative phase information between each mode is retained in this process because of the inner product method of obtaining C_n but it remains a significant simplification over the full modal-model. No regard is made of the boundary conditions at each period of the grating nor to the implications these have on the discrete set of free-space modes or in turn their interaction with the modes within each groove. An

a/*d* ratio of unity is also assumed. The inter-dependency of the system has been broken in order to obtain this simplification.

This expression is for the absolute impedance where for this application a normalised impedance is required for use in the reflection coefficient formula [37] which is achieved by dividing through by the free-space medium characteristic impedance, Z_C. The resulting normalised impedance is,

$$Z_{Seff} = \int_{-a/2}^{a/2} \left(\frac{\sum_{n=0}^{n=\infty} e_n(x).C_n \left(\frac{k}{k_{zn}^-} - \exp(ik_{zn}^+ 2h) \frac{k}{k_{zn}^+} \right)}{\sum_{n=0}^{n=\infty} e_n(x).C_n \left(1 - \exp(ik_{zn}^+ 2h) \right) \bullet d\mathbf{n}} \right) .dx \tag{8.11}$$

Recalling the definition of Eq. (8.2) the velocity components are already posed in terms of vertical velocity so the $\bullet d\mathbf{n}$ term equates to -1 in order that the surface normal points into the surface in the -*z* direction. This gives,

$$Z_{Seff} = \int_{-a/2}^{a/2} \left(\frac{\sum_{n=0}^{n=\infty} e_n(x).C_n \left(\frac{k}{k_{zn}^-} - \exp(ik_{zn}^+ 2h) \frac{k}{k_{zn}^+} \right)}{\sum_{n=0}^{n=\infty} e_n(x).C_n \left(\exp(ik_{zn}^+ 2h) - 1 \right)} \right) .dx \tag{8.12}$$

A drawback of this simplification is the tendency to predict negative real parts to the effective impedance once above the cut off frequency of the first non-plane mode *n*=1. This is physically incorrect and is believed to be caused by losing properties of energy conservation as a result of the simplifying assumptions. Because the behaviour of the modes within the groove have been simplified the subtle interference of modes within the groove will be only an approximation and liable to error in inferring erroneous sources of energy. In these cases of positive real part, the simplified formula is suggesting more energy outflow from the cavity than inflow. In such cases the real part is set to zero using a simple conditional statement thus,

```
if Real(Zeff) < 0, then Real(Zeff)=0.
```

For practical application n must be truncated to N, so for instance truncating to N=2 will model the first three modes within the groove, n=0, n=1 and n=2. Truncation of N should be chosen such that the upper frequency bound of interest is lower than the cut-off frequency of mode N+1. The upper frequency limit of the simplified model for a given truncation N is therefore,

$$f_{\max} = \frac{c_0 (N+1)}{2a} \tag{8.13}$$

Intuitively this simply ensures that all propagating cavity modes are included within the frequency range of interest.

The Causal model was tested with the corrected groove depth formula of Hurd [2] which states that $h{:}h^H = h - a/\pi \, log 2$ and while it improved agreement with the modal-model when $h \ll a$ when applied only to the zeroth mode n=0, it was detrimental to performance when h was comparable or greater than a. In the interests of clarity the Hurd correction was therefore not applied to the Causal model and all results henceforth use the actual value of h for the groove depth.

8.1.1 Similarity to hard backed layer and groove mode wave impedance Z_n of modal-model

Under certain conditions one may expect the simplified single mode model of Eq. (8.9) to resemble the impedance of a hard backed homogeneous porous layer with inherent porosity of unity, which has a normalised impedance given by,

$$\frac{Z}{Z_C} = \pm i \cot (k_l \, h_l) \tag{8.14}$$

with the leading sign chosen to agree with the time-space conventions of the problem at hand. Where k_l is the wave number in the porous medium, h_l the depth of the layer and Z_C the characteristic impedance of inviscid air. The hard backed layer is locally reacting where the speed of sound in the layer medium is significantly less than that in free air so propagation in the porous layer may be assumed normal to the surface. Furthermore as the layer is homogeneous at the scale of wavelengths concerned, only the plane wave mode of

propagation exists in the layer. This is equivalent to the simplified model when kd <<1 allowing the truncation of N=0 and considering only the plane wave term in the summation. From the single mode simplified model Eq. (8.9) the impedance for each mode n is as follows where once again $\bullet d\,\mathbf{n}$ has the value -1 and the impedance is normalised to Z_C.

$$Z_{Seff}(0) = \frac{C_0\left(\frac{k}{k_{z0}^-} - \exp(ik_{z0}^+ 2h)\frac{k}{k_{z0}^+}\right)}{C_0\left(\exp(ik_{z0}^+ 2h) - 1\right)} \tag{8.15}$$

Considering only the plane wave mode n=0, then k_{z0} will equal the wave number of the incident wave k and so the associated quotient will always be unity. Furthermore k_{z0} is always real as the plane wave mode will always be propagating. This leads to the quotient,

$$Z_{Seff}(0) = \frac{C_0\left(-1 - \exp(ik_{z0}^+ 2h)\right)}{C_0\left(\exp(ik_{z0}^+ 2h) - 1\right)} \quad N = 0 \tag{8.16}$$

The model is lossless and as such all of the energy from the incident wave will be retained in the plane wave mode because N=0. The inner product C_0 now cancels giving,

$$\begin{aligned} Z_{Seff}(0) &= \frac{-1 - \exp(ik_{z0}^+ 2h)}{-1 + \exp(ik_{z0}^+ 2h)} \quad N = 0 \\ &= i\cot(k_{z0}\, h) \end{aligned} \tag{8.17}$$

Which shows equivalency between the simplified causal model and the hard backed homogeneous layer under the homogeneous ground assumption and hence non-scattering conditions. Intuitively for this special case of N=0 it makes sense that C_n will cancel because it is assumed that all of the energy entering the groove will be contained solely in the n=0 mode and therefore for unity incident amplitude, C_n should therefore also equate to unity given also that a=d. In other words the incident energy is not shared between n-modes as this is precluded by the N=0 assumption which is valid for when the incident wavelength is much longer than the width of the aperture, a. For when N >0, C_n will not cancel as energy will be distributed from the incident mode across the N modes according to the excitation of each mode by the incident wave.

It is also possible to derive the impedance of each n-mode within the groove as stated in

the full modal model from our simplified causal model. Begin with Eq. (8.9) of the causal model which includes contributions from evanescent modes and is not normalised to Z_C consistent with the modal-model. In this case the $\bullet d\,\mathbf{n}$ term is removed from the denominator because the equation is now expressing the impedance of the groove mode wave and not the impedance of a surface. For each mode *n* this becomes,

$$Z_n = \frac{C_n\left(Z_C\frac{k}{k_{zn}^-} - \exp(ik_{zn}^+ 2h)\,Z_C\frac{k}{k_{zn}^+}\right)}{C_n\left(1-\exp(ik_{zn}^+ 2h)\right)} \tag{8.18}$$

The $Z_C(k/k^+_{zn})$ term in the numerator may be factored while noting that the first term is negatively signed due to it involving k^-_{zn} while also cancelling C_n gives,

$$Z_n = \frac{Z_C k}{k_{zn}^+}\frac{-1-\exp(ik_{zn}^+ 2h)}{1-\exp(ik_{zn}^+ 2h)} \tag{8.19}$$

Using the relationship in Eq. (8.17) the formula for Z_n as defined in the modal-model is obtained with the sign being arbitrary and chosen accordingly to the particular direction conventions.

$$Z_n = -i\frac{Z_C k}{k_{zn}^+}\cot(k_{zn}^+ h) \tag{8.20}$$

8.2 Heuristic summation series model

This section introduces a series of heuristic steps so the result is a simplified heuristic analytical effective impedance model. By taking the simplified causal model of Eq. (8.9) as a basis and taking advantage of its reduction to the standard *cot* () formula of Eq. (8.17) for the plane-wave mode, an *N+1* term series based approximation may be formed to include higher order groove modes beyond just the planar. In order to achieve this each term becomes independent, decoupling interaction between modes within the grooves. Consequently any inherent real part to the resultant effective impedance is lost due to the decoupling precluding direct interference between modes. The series becomes a weighted impedance summation as opposed to wave superposition as in the causal case.

Begin with the result of Eq. (8.20), normalise by Z_c and vector multiply by the surface

normal $d\mathbf{n}$ as once again the impedance of a surface is being expressed, to yield,

$$Z_{Heff}(n) = -i\frac{k}{k_{zn}^{+}}\cot(k_{zn}^{+}h) \bullet d\mathbf{n} \tag{8.21}$$

The approximate effective impedance Z_H may therefore be expressed as the sum of all n-modes, weighted by some coefficients $W_n(\omega)$. The weighting required to account for the frequency dependant excitation of each mode which depends upon the energy transferred to each mode by the incident wave and the modal impedance. Which noting the inversion the $\bullet d\mathbf{n}$ gives due to it pointing in the $-z$ direction gives,

$$Z_{Heff} = \sum_{n} iW_n(\omega)\frac{k}{k_{zn}^{+}}\cot(k_{zn}^{+}h) \tag{8.22}$$

When Allard [39] presented a simplified impedance formula, which has the same form as above in Eq. (8.21) but for the zeroth mode only, an a/d term was included to represent an effective porosity given by the ratio of aperture width a to grating pitch d. We may do the same for each term in our series to remove the assumption of $a=d$ and improve the range of applicability of the model. Intuitively, reducing the porosity will increase the effective impedance due to the reduced aperture in comparison to side wall ledge at z=0 so each term is multiplied by the reciprocal of porosity and as such,

$$\begin{aligned} Z_{Heff} &= \sum_{n} iW_n(\omega)\frac{1}{(a/d)}\frac{k}{k_{zn}^{+}}\cot(k_{zn}^{+}h) \\ &= \sum_{n} W_n(\omega)\frac{d}{a}.\frac{k}{k_{zn}^{+}}i\cot(k_{zn}^{+}h) \end{aligned} \tag{8.23}$$

The real part of the propagation impedance term k/k_{zn} for each n-mode will be at a peak just as the mode becomes propagating and will tend to unity as frequency tends to infinity. This is because the mode will be propagating primarily in the x-axis in the region just above cut-off and hence the propagation impedance, posed in terms of v_z, will also be at its highest. It may also be observed that given grazing incidence, the highest order propagating n-mode has the potential to receive the most excitation energy from the incident wave. This is because the highest frequency propagating n-mode and the incident wave at or near grazing incidence will be similar in x-axis spatial frequency and hence show a peak in their inner product just above the cut-off frequency. As the inner product is a line integral in this 2d case, the peak value will in fact occur when the incident projected wavelength is slightly

longer than that of mode n, with this factor Λ decreasing from around 1.37 for n=1 towards unity as n tends to infinity. Although lower order modes may still be excited, their potential excitation energy will be ever decreasing with frequency due to their inner product being only proportional to the area of one incident half cycle. Given this the simplifying assumption can be made that that the highest order propagating mode will dominate the local response, at or near to grazing incidence. The resultant impedance of each n-mode at the groove aperture is then the combination of the down and up-going components within the groove.

8.2.1 Weighting functions

It now remains to define frequency dependant weighting functions $W_n(\omega)$ for each n. Two definitions will be discussed and their performance compared in the results section. Each variant will be denoted by a superscript Roman numeral increment (I, II etc) to distinguish the various implementations. However, each variant is substituted in the same way into Eq. (8.23) to form the heuristic model.

8.2.1.1 Variant I - Inner product weighting

The C_n function may be used to approximate the frequency dependant amplitude and relative scaling of each mode. As the modes are fully decoupled the relative phase of C_n is redundant so we need take only the magnitude to provide a scalar weighing envelope for each mode. Another consequence of the modal decoupling is that the summation may be overwhelmed by modal terms equating to infinity at resonances of the *cot* () terms. In the causal representation Eq. (8.12) this problem did not arise because all terms were coupled by summation of the modal pressure and velocity quantities and not by impedance summations as in the heuristic model. Exploiting the fact that the highest propagating mode tends to dominate the response, contributions from lower order modes can be removed by forcing $W_n(\omega)$ to zero. In its crudest form this may be achieved by cancelling any contribution from mode n when mode n+1 is propagating as signified by a real z-axis wave number. Expressing this gives us the following weighting function set which shall be called variant 'I' and denoted as a superscript,

$$W_n^I(\omega) = |C_n| \frac{i\,\mathrm{Im}\left\{k_{zn+1}^+\right\}}{k_{zn+1}^+} \tag{8.24}$$

where,

$$\frac{i\,\mathrm{Im}\left\{k_{zn+1}\right\}}{k_{zn+1}} \equiv \begin{cases} 0 & \left|\mathrm{Re}\left\{k_{zn+1}\right\}\right| > 0 \\ 1 & else \end{cases} \tag{8.25}$$

which has the effect of removing the contribution of mode n, once the next highest mode n+1 becomes propagating. It is expected that near field effects become significant when h is small when compared with a as behaviour is likely to be complex and dominated by near field or end effects within the diffraction zone. Another practical effect of when $h<a$ is that it tends to reduce the frequency gap between the first EA minima caused by simple ray path length difference and the onset of scattering effects because the path length difference minima will be dominated by h while scattering effects by a. The smaller the depth of the groove h, the higher in frequency the first path length difference EA minima will be. Conversely increasing a (assuming a proportional change in d) will lower the frequency at which scattering effects occur. So increasing a and reducing h will close the frequency gap between the first path length difference EA minima and the manifestations of scattering.

8.2.1.2 Approximating the inner product

As an engineering model the full inner product formulation of C_n in Eq.(8.4), both in its integral form (Eq. (8.4a) and (8.4c)) and evaluated form (Eq. (8.4b) and (8.4d)), is cumbersome to implement due to the need to compute the integral numerically or code the evaluated form. While this is not a difficult task it does not lend itself well to widespread implementation. We shall therefore explore methods of approximating the C_n set beginning with the case of the plane wave mode within the groove for which n=0. It has a simple analytic approximation especially if one assumes grazing incidence so that the $sin\ \theta$ term vanishes. In addition unit porosity is also assumed for the C_n set as porosity has already been considered in the series summation itself Eq. (8.23). Unit porosity of a=d means that the incident and n-mode component use the common normalising constant posed in terms of aperture width a, otherwise the incident component would be normalised with respect to the grating pitch d. Incidentally it would be interesting for future work to investigate

whether porosity could be successfully accounted for using this method instead of the specific factor. Given this we have the grazing incidence approximation for C_0 of,

$$C_0 = \int_{-a/2}^{a/2} \frac{1}{\sqrt{a}} \cos\left(\left[\frac{n\pi}{a}\right]\left[x+\frac{a}{2}\right]\right) . \frac{1}{\sqrt{a}} \exp(ikx)\, dx \quad n = 0, \theta = \pi/2 \tag{8.26}$$

which has the analytic equivalent,

$$C_0 = \frac{2\sin\left(\frac{a\,k}{2}\right)}{a\,k} \quad n = 0, \theta = \pi/2 \tag{8.27}$$

Attention is now turned to simplifying the expression for the magnitude of C_n for n>0. Taking the magnitude of the integral form of Eq. (8.4) gives,

$$\left|C_n\right| = \left| \int_{-a/2}^{a/2} \sqrt{\frac{2}{a}} \cos\left(\left[\frac{n\pi}{a}\right]\left[x+\frac{a}{2}\right]\right) . \sqrt{\frac{2}{a}} \exp(i\,x\,k\sin\theta)\, dx \right| \quad n > 0 \tag{8.28}$$

As only the magnitude is required, the distinction between real and imaginary components caused by relative modal phasing and odd/even relationships no longer matters. It may be deduced intuitively from this that C_n may be simplified to a working approximation by considering the relationship purely in terms of relative x-axis projected wavelength of the incident wave λ_i and that of mode n within the groove aperture λ_n. The $|C_n|$ function is proportional to the sine of the ratio of the two wavelengths, possessing a peak when the two wavelengths are near equal. The inner product is a line integral so the peak value does not occur when the wavelengths are exactly the same except for the limiting case where the inner product is conducted over an infinite number of cycles. A wavelength factor Λ_n must therefore be included to account for this fact. Our wavelength posed approximation to $|C_n|$ is derived as follows. Consider that the inner product is approximately proportional to the sine of the two wavelength components thus,

$$\left|C_n\right| \sim \propto \sin\left(\frac{\lambda_n}{\lambda_i}\right)$$

adding the factor $\pi / 2$ to correct the phase to give a peak when $\lambda_n = \lambda_i$ leads to,

$$\left|C_n\right| \sim \propto \sin\left(\left[\frac{\lambda_n}{\lambda_i}\right]\frac{\pi}{2}\right)$$

finally, to compensate for the inner product maximum occuring when $\lambda_n > \lambda_i$, the factor Λ_n is added to yield,

$$\left|C_n\right| \approx \sin\left(\left[\frac{\lambda_n}{\Lambda_n \lambda_i}\right]\frac{\pi}{2}\right) \quad n > 0 \tag{8.29}$$

where the *x* projected wavelengths are given by,

$$\lambda_n = 2a / n$$
$$\lambda_i = \left(\frac{k \sin\theta}{2\pi}\right)^{-1} \tag{8.30}$$

Combining these gives a simplified expression for $|C_n|$ for n>0 of,

$$\begin{aligned}\left|C_n\right| &\approx \sin\left(\left[\frac{2a / n}{\Lambda_n\left(\frac{k \sin\theta}{2\pi}\right)^{-1}}\right]\frac{\pi}{2}\right) \\ &\approx \sin\left(\frac{a\, k \sin\theta}{2\Lambda_n\, n}\right) \quad n > 0\end{aligned} \tag{8.31}$$

The constant Λ_n must be solved and has periodic solutions but the relevant solution is the peak value in the region of equality of λ_i and λ_n and is given by the solution of,

$$\frac{d\left|C_n\right|}{d\Lambda_n} = 0 \quad n > 0 \tag{8.32}$$

To determine this relationship the full equation for $|C_n|$ as in Eq. (8.28) must be solved. Bear in mind that Λ_n is a wavelength factor of *k*. The solution is independent of *a* so we may arbitrarily set *a*=2 for convenience as this cancels the leading $(2/a)^{0.5}$ terms giving,

$$\frac{d}{d\Lambda_n}\left|\int_{-1}^{1}\cos\left(\left[\frac{n\pi}{2}\right]\left[x+1\right]\right).\exp(i\,x\Lambda_n k\sin\theta)\,dx\right|=0 \quad a=2 \tag{8.33}$$

Setting λ_i and λ_n to be equal in order to allow the solution of Λ_n requires that,

$$\lambda_n=\lambda_i$$
$$\frac{2a}{n}=\left(\frac{k\sin\theta}{2\pi}\right)^{-1}$$
$$\frac{\pi n}{a}=k\sin\theta \tag{8.34}$$

Substituting Eq. (8.34) into *sin* θ terms of Eq. (8.33) gives the equation of Λ_n, which is solved within the given interval to remain in the region of interest and exclude periodic higher order correlation peaks.

$$\frac{d}{d\Lambda_n}\left|\int_{-1}^{1}\cos\left(\left[\frac{n\pi}{2}\right]\left[x+1\right]\right).\exp(i\,x\Lambda_n\frac{\pi n}{2})\,dx\right|=0 \quad a=2,\quad 1.5\geq\Lambda_n\geq 1 \tag{8.35}$$

With the aid of wolfram alpha [42] the approximate solutions are shown below in table (8.1) for n=1 to n=5. They clearly shows the tendency to unity with increasing n as to be expected as the correlation window of $\pm a$ encompasses ever more cycles.

n	**~Λ_n**
1	1.367
2	1.125
3	1.06
4	1.035
5	1.025
6	1.02

Table 8.1 Approximate solutions of Λ_n.

The completed variant I heuristic approximation is comprised of Eq. (8.23) and Eq. (8.24) as summarised below. For practical engineering purposes one would use the approximation to $|C_n|$ as in Eq.(8.27) for n=0 and Eq.(8.29) for n>0.

$$Z_{Heff} = \sum_n W_n(\omega)\frac{d}{a}.\frac{k}{k_{zn}^+} i\cot(k_{zn}^+ h)$$

where,

$$W_n^I(\omega) = |C_n|\frac{i\,\mathrm{Im}\left\{k_{zn+1}^+\right\}}{k_{zn+1}^+} \tag{8.36}$$

8.2.1.3 Variant II – Flat weighting

The weighting $|C_n|$ derived in the previous section is relatively complicated. A further approximation that $|C_n|=1$ might be useful when $h \geq a$ where the effects of path length difference and scattering will be significantly separated in frequency and near field effects within the aperture of the groove are negligible. The weighting function for Variant II therefore simplifies to,

$$W_0^{II}(\omega) = \frac{i\,\mathrm{Im}\left\{k_{zn+1}^+\right\}}{k_{zn+1}^+} \tag{8.37}$$

8.2.2 Slit-pore model zeroth term

To improve accuracy the zeroth term is replaced with the slit-pore effective impedance model Z_{SP} [28], which includes visco-thermal effects, albeit only for the plane wave term. This in reality is likely to be the realm where such effects are at their most significant, when the wavelength is large compared to the groove diameter. Although it may be argued that higher order modes with a large transverse components may fit this criteria due to the apparently long wavelength they project on the vertical groove sides. Incorporating the slit-pore term removes the low frequency or small aperture width limit of the series which would otherwise be encountered due to visco-thermal effects. It was found to be advantageous to the Heuristic model to use the Hurd groove depth correction of $h{:}h^H = h - a/\pi log 2$ for the plane wave mode $n=0$ term. However applying it to higher order modes $n>0$ generally degraded the performance as would be expected as this condition was obtained by Hurd under the assumptions that $a=d$ and $\lambda >> a$ which allows only for the plane wave-mode. This correction was presented by Hurd [2] and applied by Allard et al. [39] to correct for near field effects when the groove depth is smaller than aperture width, $h<a$. It is not required for the full modal-model because such effects are implicit in its

comprehensive formulation. Substituting the slit-pore model with the Hurd corrected depth h^H into the series gives,

$$Z_{effs} = Z_{SP}(h^H)W_0(\omega) + \sum_{n>0} W_n(\omega)\frac{d}{a}.\frac{k}{k_{zn}^+} i\cot(k_{zn}^+ h) \tag{8.38}$$

This represents a single model for a rectangular grooved grating with a potentially limitless useful frequency range for a given groove geometry and appropriate truncation of N. In the realm of long incident wavelength when compared to groove dimensions, visco-thermal effects will be significant but only the plane wave mode will be dominant and scattering effects negligible. Conversely, when the wavelength is short compared to the groove dimensions, diffractive, scattering and modal behaviour will be dominant and visco-thermal effects of less significance.

A subtle weakness of this simplified approach is worthy of mention. Except for leading porosity term which does not affect the scattering behaviour, the model it is posed in terms of a rather than d which causes the model to predict the onset of scattering effects at the frequency at which the first higher mode n=1 becomes propagating within the groove. This is technically incorrect. Scattering effects will begin when the first free-space diffraction mode m=±1, becomes propagating which is dependent only upon the pitch of the grating d and the geometry and frequency of the incident wave. When $a<d$ (a physical necessity), the onset of scattering will occur when just the planar mode propagates the grooves due to free-space diffraction effects alone. The only case of parity will occur when $a=d$, a physical impossibility of infinitely thin walls where the onset of free-space scattering and the propagation of the first non-planar mode within the groove coincide at the same frequency. The modes within the grooves do not affect the geometry of free-field diffraction modes, but do affect their amplitude with ever increasing complexity as higher orders are excited.

We therefore expect there to be a frequency band between the true onset of scattering and the propagation within the groove of the first higher order mode n=1 where the results of the heuristic model may be unreliable in its characteristic. In other words it will tend to overestimate the cut-on frequency of scattering effects with ever increasing error as a/d decreases.

8.2.3 Truncating N

The truncation of N should be chosen such that the maximum frequency of interest is lower than the cut-off frequency of mode $N+1$. This ensures that all modes capable of propagation within the grooves are included in the series across the bandwidth of interest. With reference to Eq. (8.13), the following inequality is derived and should be satisfied to estimate a sensible truncation of N. Mode n may propagate within the groove whenever the incident wavelength λ_i is shorter than $2a$ because aperture modes are resonant at each half cycle. For a chosen maximum frequency f_{max}, an inequality is formed around N and f_{max} as follows.

$$\lambda_i < \frac{2a}{N+1}$$
$$\lambda_i = \frac{c_0}{f_{\max}} \quad \therefore$$
$$f_{\max} < \frac{c_0\left(N+1\right)}{2a}$$
$$N > \frac{2a\, f_{\max}}{c_0} - 1 \quad N = 0,1,2... \tag{8.39}$$

N should be rounded up to the next highest integer to ensure there are sufficient series terms for a given f_{max}.

8.3 Testing the inner product approximations

In this brief section the simplifications of Eq. (8.27) and (8.31) are tested against the evaluated forms of the full inner products of Eq. (8.4b and 8.4d). The rationale for simplification is that neither the integral form nor the evaluated form are straightforward to implement in practical acoustics engineering where only basic numerical tools may be to hand. Figure 8.2a) shows the error of the approximations to the inner products with respect the full expressions which is calculated as the difference Eq. (8.4b) - Eq. (8.27) for n=0 and Eq. (8.4d) - Eq. (8.31) for n>0. The cut-off frequency for each mode n is denoted by a vertical cursor.

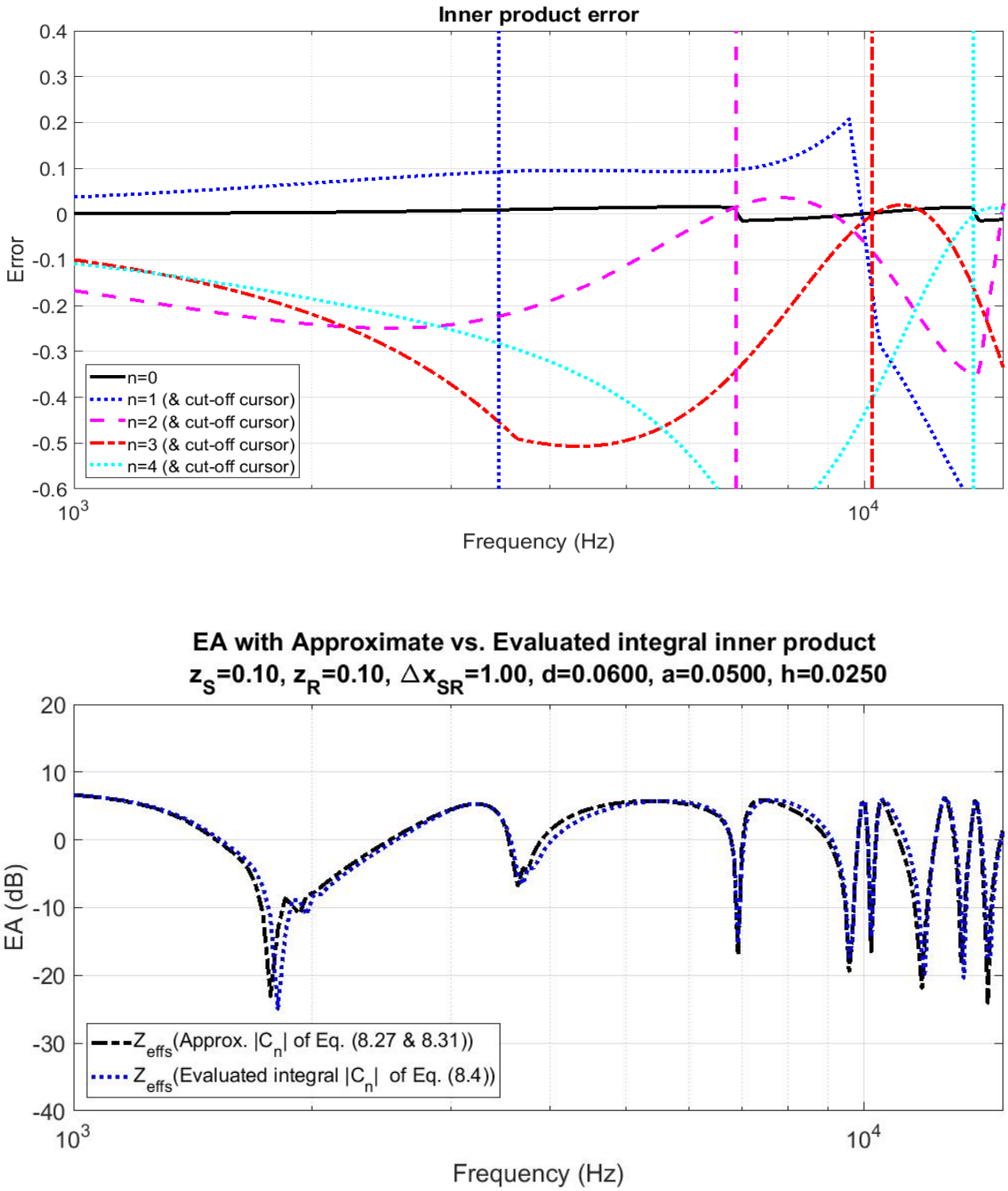

Figure 8.2 Error curves for approximated inner products with respect to the full inner product for the first 5 n-modes. b) Comparison of EA curve predictions of summation model with the full inner products and simplified versions.

In the region near the modes own cut-off frequency and upto the cut-off frequency of the next higher mode, the errors of the approximate inner products of figure 8.2a) are small.

However, across the remaining spectrum the approximations exhibit large error. In spite of this, the predicted EA curves from both the full and approximate inner products in figure 8.2b) show close agreement. This suggests that the local response is dominated by the highest order propagating mode and the approximations to the inner product presented here are reasonable.

8.4 Effective impedance comparison with modal-model

The simplified models were implemented in MATLAB and tested with a truncation of $N=5$ giving the first six waveguide mode terms n=0, n=1 to n=5. Figure 8.3 shows a plot of the effective impedance as predicted by the 2d extended modal-model, the causal and both variants of the heuristic models. The frequency scale shows from 200 Hz to 2000 Hz for clarity and the y-axis scale is asymmetrically truncated to represent finer detail around zero at the expense of clipping at the peaks.

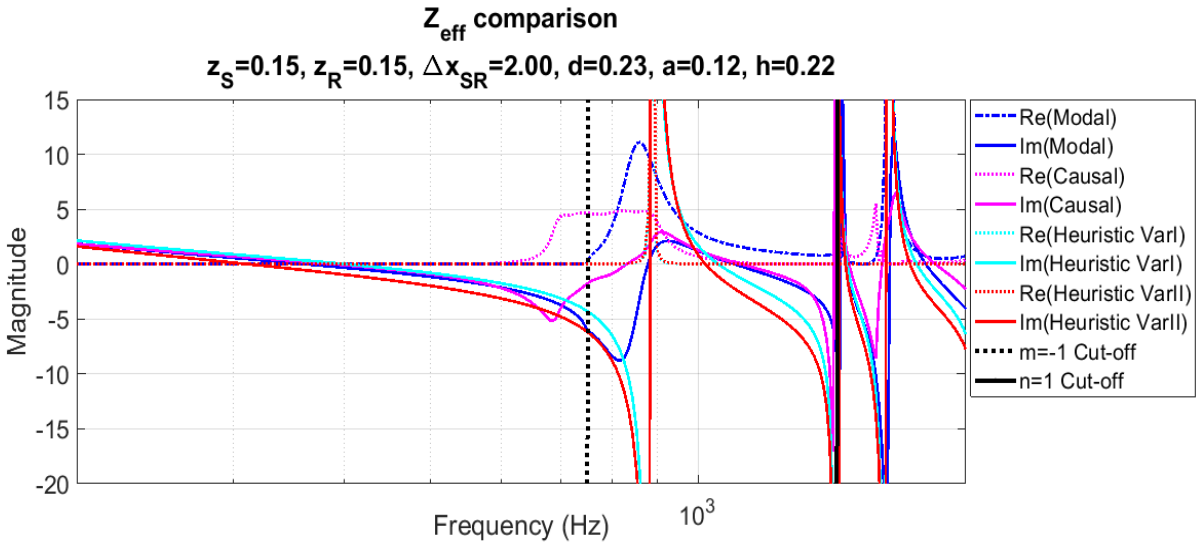

Figure 8.3 Z_{eff}, Modal-model vs. Simplified models for d=0.23, a=0.12, h=0.22 and source receiver at 0.15 m separated by 2 m.

It is immediately apparent from figure 8.3 that none of the simplified models agree particularly well with the modal model in respect of the imaginary part of the normalised impedance. Nonetheless, this large disparity does not translate (generally) into equivalently large errors in the excess attenuation predictions presented in the next section. The answer to this lay in the nature of the discrepancy. The simplified models predict the characteristic

shape of the imaginary impedance curve reasonably well, which aids the prediction of the correct characteristic in the excess-attenuation result. In terms of magnitude, the models exhibit their best agreement at lower magnitudes where the reflection coefficient will be at its most sensitive to error. Around the periodic peaks and troughs the magnitude errors are large but the reflection coefficient is less sensitive to the absolute magnitude of the impedance in these regions, which is why the excess attenuation results are better than would be expected at first glance from the imaginary impedance predictions.

It is clear to see that the onset of a real part predicted by the causal simplified model is premature. As the Causal model is inviscid any real part will be attributed to scattering loses. Therefore it would be expected that the real part manifest beyond the cut-off frequency of the first scattered free-space mode which is m=-1 in this instance. This is correctly predicted by the full modal model where the onset of a real part coincides with the first scattered mode m=-1 becoming propagating and hence interfering with the specular reflected mode and the incident wave at the receiver to show an apparent loss. Due to the core of both the causal and heuristic models being independent of d except for the simple porosity factor which is not frequency dependent, their impedance predictions in the frequency band 500 – 1000 Hz which is around the onset of the first diffraction mode m=-1 is poor. As a result it is expected that the performance of the causal and heuristic models will degrade as a reduces relative to d and the aforementioned frequency band widens, not because of the porosity per se or the leading porosity term, rather due to the fundamental discrepancy in predicting the onset of scattering. Outside of this frequency band the general agreement between the causal model and the modal-model is reasonable for both real and imaginary parts. The heuristic models both have a real part due to the visco-thermal effects from the slit-pore zeroth term which show a sharp peak at around 900 Hz for both Variant I and Variant II. The higher order scattering terms generate only imaginary values related to the interference of down and up-going modal components. The modes are fully decoupled and therefore interference between them which would lead to an apparent loss is not possible. Agreement between the imaginary parts of the heuristic and modal-model is again reasonable once beyond the chaotic region between 500 and 1000 Hz. Once beyond the chaotic region after 1000 Hz the response settles and the agreement between the causal and modal-model is good while the heuristic models are fair and appear to improve with increasing frequency. The heuristic Variant I fares better than Variant II due to its added complexity in calculating the modal weighting values. At low frequencies

all models agree well with the causal mode tracking the model-model up to around 550 Hz where it prematurely predicts scattering effects while the two variants of heuristic track well up to 1000 Hz. The real part of the heuristic models due to the visco-thermal effects of the slit-pore zeroth-term is present but is too low in magnitude to show on the plots.

The modal curves can be seen to be smoother and less abrupt in response as well as showing generally smoother peaks than the causal or heuristic models. This is attributed to the more complex nature of the full modal-model which fully considers the modal interactions with the grating structure as opposed to being dominated by simple *cot* () function resonances.

Both simplified models, the causal and heuristic, consider merely one periodic cell of a notionally infinite grating. The full modal-model assumes infinite extents and as such accounts for interaction between cells in terms of the free-space modes and cell boundaries which ensure continuity at the intersection of each cell. Neither the causal nor heuristic models cater for continuity at the boundaries of each grating cell which is another source of error due to the simplifying premises.

Furthermore both simplified models cater for finite thickness of the groove walls with only the simple a/d factor which does not model the true effects giving rise to a further source of error as a/d tends to 0.

Visco-thermal effects aside, the real part of impedance may become non-zero positive whenever anything other than the specular reflection mode propagates in free-space as a result of scattering from the grating causing an apparent loss at the receiver. In our case this occurs when either the m=-1 or m=+1 mode becomes propagating as signified by a real z-axis wave number component. This is because the free-space modes in the scattered field can then interfere causing an apparent scattering loss at the receiver, signified by a real part to the effective impedance. Boulanger et al. [34] attributed the real part of effective impedance of a rough surface to non-coherent scattering. The real part may only ever be positive signifying an apparent loss which will occur when the free-space modes destructively interfere. A negative real part is invalid as it would signify an extra energy source, violating energy conservation. Any apparent loss in the effective impedance is therefore expected to represent destructive interference of free-space scattered modes at the

receiver for the specific source receiver geometry. This however does not represent a true loss as all energy is conserved, rather it just models the spatial constructive and destructive interferences present in the scattered field. As discussed in previous sections, the notion of applying a lumped impedance to a scattering surface is not rigorous so it simply models the overall effect for a given problem geometry as opposed to modelling the fundamental physics.

The propagation geometry of scattered free-space modes is dependent only upon the pitch of the grating d and the incident wave, not the size of the cavity aperture a. Higher order free-space scattered modes ($|m|>0$) may propagate and be excited even when only the plane wave mode $n=0$ is excited within the cavities of the grating. Exciting higher order cavity modes does not change the propagation geometry of the free-space modes, rather it just affects the mutual excitation amplitudes. The causal model is capable of predicting a real part related to scattering loss where the heuristic models cannot. Because no reference to free-space modes is made the onset frequency of scattering losses for the causal model will be in error as seen in figure 8.3. The heuristic models are not capable of producing a real part due to scattering losses because of the complete decoupling of modes but they crudely model the interferences at the receiver from scattered modes via the imaginary element. Using the slit-pore model as the zeroth term will cause real parts but because of visco-thermal effects alone.

Finally, let us briefly consider the modes within the cavities of the grating, which will broadly hold for most non-tortuous and continuous shapes. A proportion of the incident exciting energy is distributed amongst the modes excited within the groove. For lossless and inviscid conditions and in steady state the energy leaving the cavity into free-space cannot exceed the excitation energy of the incident wave entering the cavity. Indeed, when the cavity is acoustically hard the incident energy entering the cavity must equal the energy leaving once steady state conditions are reached.

8.5 Results

The following figures present excess-attenuation (EA) spectra for the stated geometries obtained from BEM, the 2d extended modal-model and the causal and heuristic models along with the slit-pore model. All standard error (SE) values will be referenced to BEM and calculated as stated in previous sections. The modal model has the truncations of N=5,

M =25 and the casual and heuristic models N=5. The vertical cursor represents the cut-off frequency of n=6 which, if within the bandwidth of the plot, will indicate the maximum frequency limit of the series based models for the truncation N=5. The source-receiver geometry is given for each result. For the modal-model the finite grating approximation has been set such that the grating extends horizontally between the source and receiver and the path length compensation has been applied. The BEM has been run with a mesh to produce the grating of given geometry which extends horizontally between the source and receiver with nothing but free-space beyond this. End effects may therefore taint the BEM results slightly due to the abrupt extents of the grating structure.

The first example of figure 8.4 shows a grating with a pitch of 0.05 m, aperture of 0.04 m and a depth of 0.05 m.

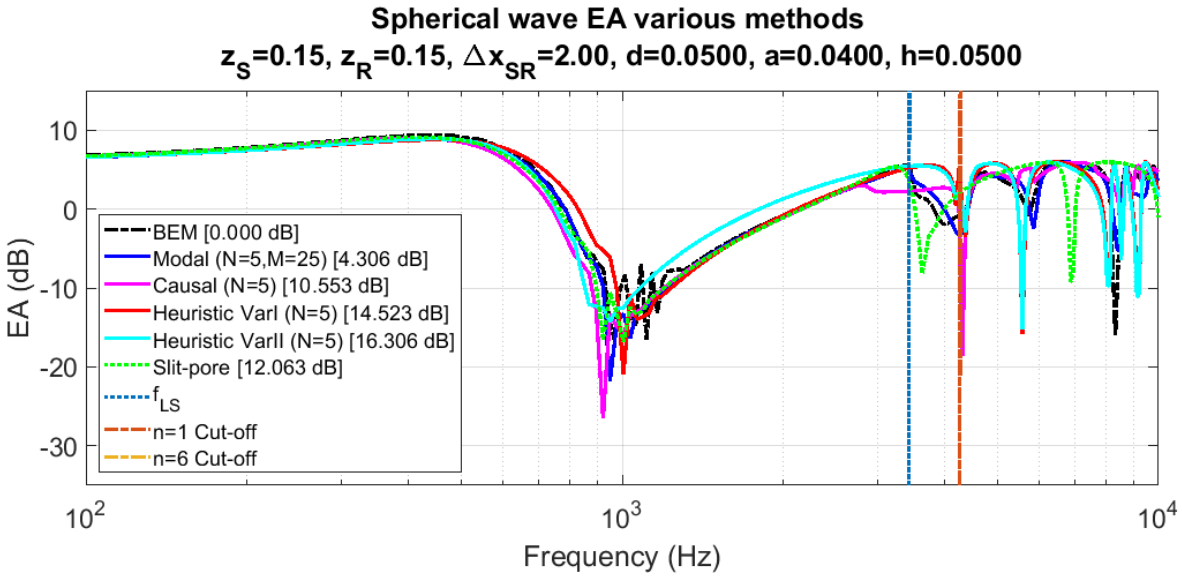

Figure 8.4 Theoretical EA plot for d=0.05, a=0.04, h=0.05.

For this example only cursors are visible for the frequency at which the first diffraction mode propagates f_{LS} signifying the onset of scattering at 3.4 kHz and the cut-off frequency of the first higher order mode within the groove n=1, at 4.3 kHz. As the cut-off for n=6 is beyond the upper frequency of this plot, the choice of N=5 is more than adequate for this example. The BEM and modal-model results are in good agreement throughout. As expected, the causal and heuristic models are characteristically in error within the band between f_{LS} and n=1 cut-off due to them being fundamentally posed in terms of the n-modes within the groove. Each plot will exhibit this error with varying severity, this example being particularly stark. We may expect the situation to deteriorate as a reduces

compared to d but it appears to be mitigated somewhat by the general tendency for the ground to tend towards a hard flat surface as porosity approaches unity and so the performance does not degrade to the extent that may be expected.

Below f_{LS} and above n=1 cut-off, both causal and heuristic models of both variants agree well with the BEM and modal-model reference although the simple Variant II predicts the frequency of the first EA minima with greater accuracy than Variant I despite its inferior SE figure. As expected the slit-pore model does not agree well with the references beyond f_{LS} because of the assumption of purely planar propagation within the groove and a homogeneous ground gives rise to the incorrect characteristic response in terms of minima and maxima despite the favourable SE value. At lower frequencies significantly below the scattering limit one would consider the slit-pore to be the most appropriate of the presented models due to its inclusion of visco-thermal effects.

Figure 8.5 shows a sweep of effective porosity (a/d). Immediately apparent is the close agreement between all models throughout figure 8.5a) where the porosity is at its lowest and the ground is behaving like a hard surface at z=0. Despite the fact that f_{LS} is just over 1000 Hz the scattering behaviour is simply not being excited by the narrow aperture which doesn't support the first high order mode n=1 until around 8500 Hz. The causal model performs well across the entire range of effective porosities being the best of the simplified models for this geometry. In all but figure 8.5a) the more complex Variant I heuristic model outperforms Variant II in terms of the SE figures even though the simple Variant II implementation is more accurately predicting the frequency of the first EA minimum in figure 8.5a). As the effective porosity is increased and the scattering effects become more significant the slit-pore model agreement with BEM and the modal-model worsens even though figure 8.5c) shows a good SE figure the characteristic shape is incorrect once scattering occurs beyond f_{LS}. As is to be expected the frequency gap between f_{LS} and the n=1 cut-off narrows as the effective porosity ratio a/d tends to unity as f_{LS} remains constant and the n=1 cut-off frequency decreases towards it as a/d tends to unity. Agreement between the BEM and 2d extended modal-model is once again good although the BEM is predicting a somewhat higher surface wave magnitude than the modal-model in the first instance of figure 8.5a), a sharper slope towards the first EA minimum in b) and a higher frequency first EA minimum in c) with some ringing in the response. It is difficult to address such subtle differences because BEM is such a comprehensive model that it is

highly sensitive to how the mesh is implemented which has a bearing on factors such as diffraction and reflection from the ends of the mesh and other related subtleties which occur from the necessary truncation of the geometry.

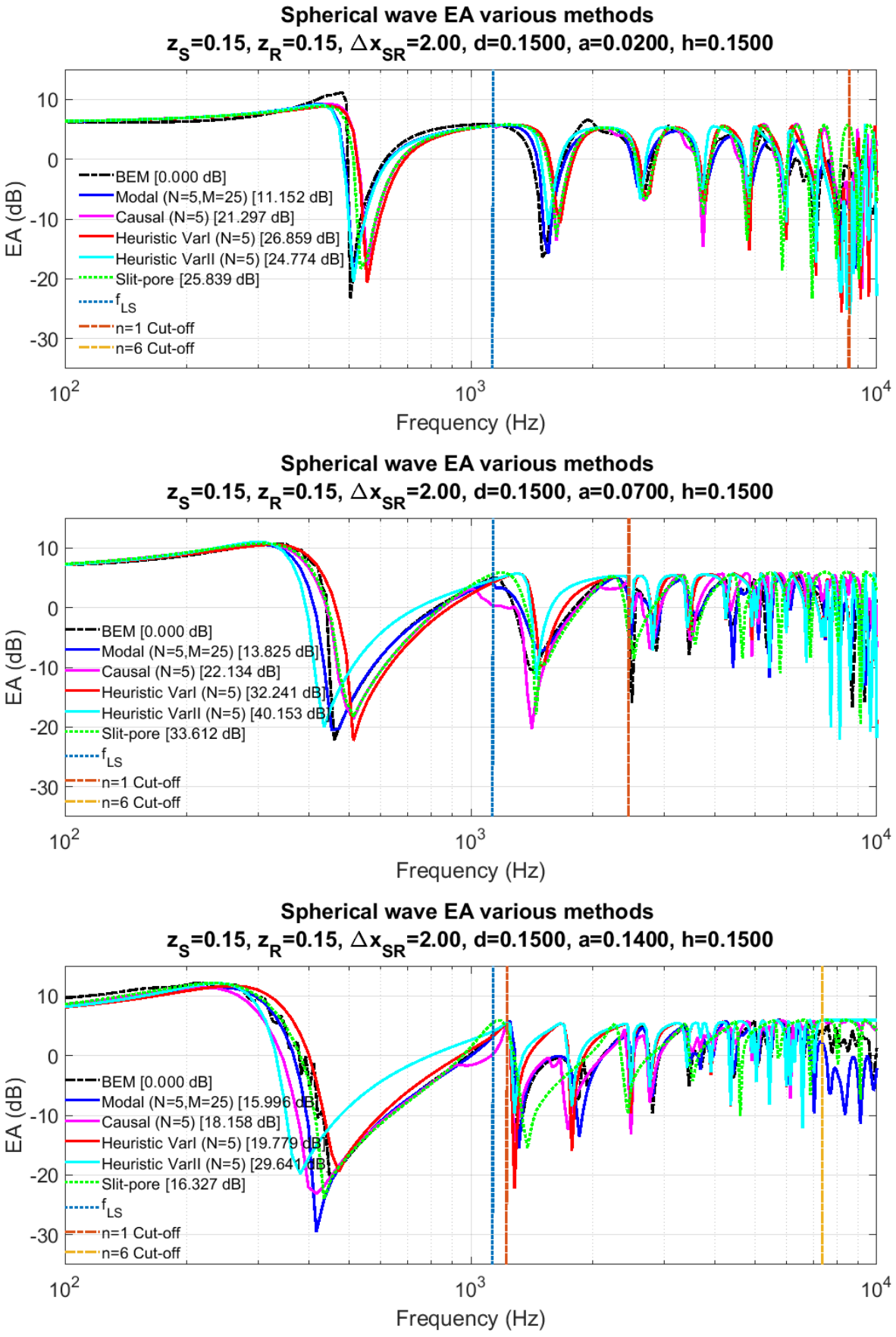

Figure 8.5 EA plots for d=0.15, h=0.05 and effective porosities of a) 0.13, b) 0.47 and c) 0.93.

In figure 8.6 the behaviour of the predictions is shown for a variety of groove depths h in order to explore the effects of the ratio h/a. As expected from previous works on the subject [31] the slit-pore model does not perform well when $h<a$ as in a) and b) but for the case of $h>a$ as in c) it agrees well with BEM and the modal-model and has a lower SE figure than the simplified models even though it does not track the EA characteristic in the realm of scattering behaviour above 1000 Hz. The causal model is the best of the simplified models for a) where h is small but still fails to track the highly chaotic nature of the response in the region of f_{LS}. It then performs less well as h is increased in b) and c). Whereas the heuristic models are poor for the smallest h in a) they improve as h is increased with the more complex Variant I giving better results than Variant II by some margin in figures 8.6b) and c). The exact reasons for the poor performance of the simplified models when $h<a$ are not fully apparent to the author and further investigation into the physics would be required, perhaps with the aid of time domain models and further insight into the work of Hurd [2] and near-field wave theory.

As a general trend the heuristic models have a tendency to overestimate the response which is likely due to their inability to model scattering losses as a real part of impedance and also the fact that the modes are decoupled and so the full extent of their interaction is lost.

The relatively large groove geometry in this instance means that the cut-off frequency of n=6 falls within the bandwidth of interest at around 4400 Hz meaning that the chosen truncation of N =5 gives a useful bandwidth of 4400 Hz for the simplified models. As such and in the interests of not distorting the SE values the frequency range has been reduced to 100 Hz to 5000 Hz. This frequency is dependent only upon the aperture width a and so it is invariant across the sweep of h in figure 8.6.

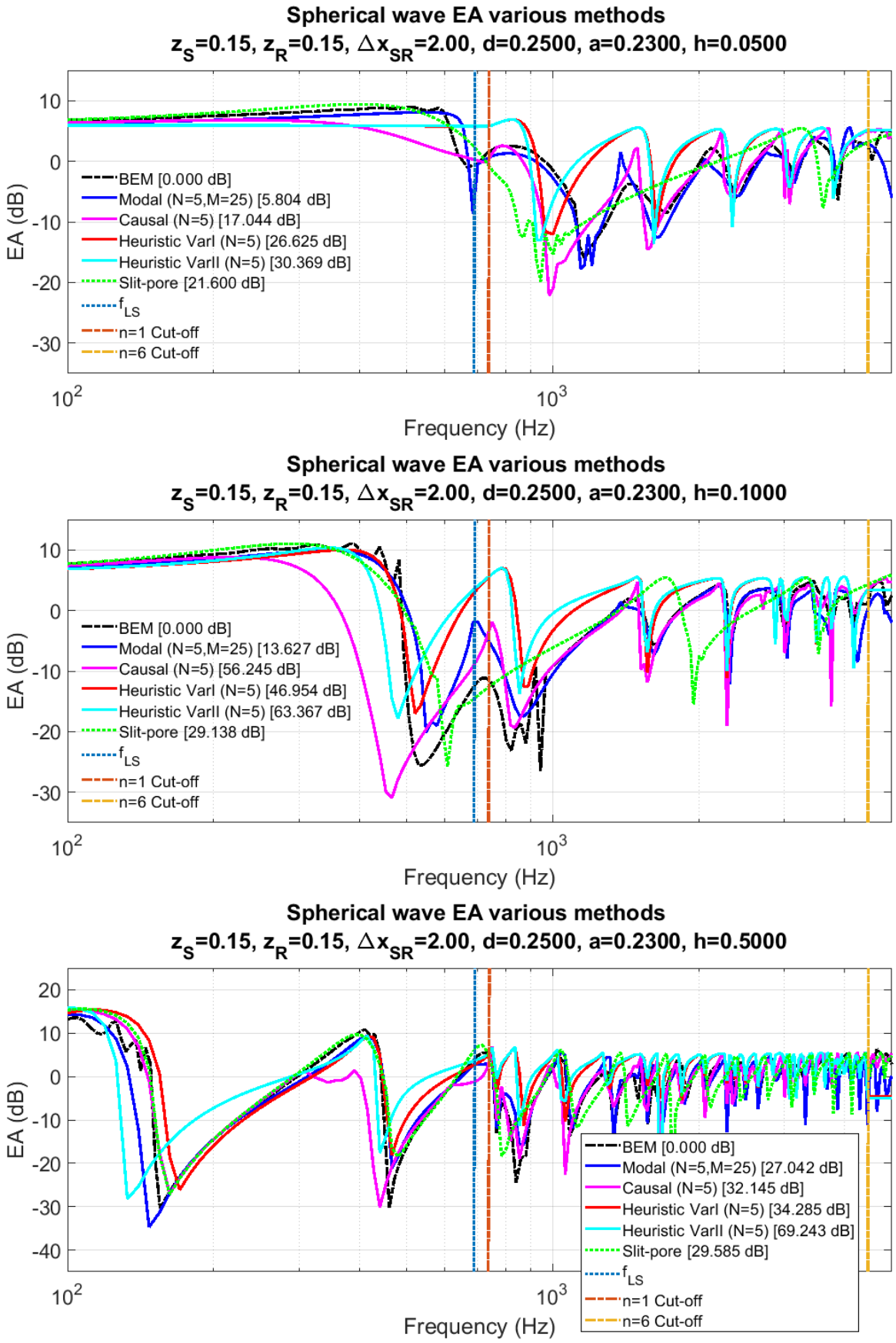

Figure 8.6 EA plots for d=0.25, a=0.23 and groove depths of a) 0.05, b) 0.10 and c) 0.50.

Finally the effect of angle of incidence (AOI) is explored in figure 8.7. Once again the agreement between BEM and the modal-model is good with a minor discrepancy between the magnitude and frequency of the first EA minima in a) and in magnitude for c). In a) the slit-pore model is over predicting the frequency and under estimating the magnitude of the first EA. The frequency of the first EA minimum is at 700 Hz and f_{LS} at 1700 Hz so the two are separated by some margin as the slit-pore model has been shown to be unreliable when the two events are close together in frequency due to the onset of scattering effects (see figures 8.6a and b). However in this instance it appears that diffractive effects are effecting the slit-pore prediction as its agreement with BEM and the modal-model improves in b) and c) where frequency separation of the first EA minimum along with f_{LS} are increased along with decreasing AOI.

The causal model performs well throughout the AOI sweep with good SE values and characteristics.

Once again the heuristic models underestimate the magnitude of the first EA minimum in figure 8.7a) as they have tended to do in previous results also. This is attributed to the fact that the heuristic models do not fully account for the complex interaction between modes, both free-space and within the groove and as such are not fully expressing the constructive and destructive effects which occur at such peaks. In fact this problem may also manifest as overestimations too as seen in the second EA minima of b) at 2600 Hz. The simpler Variant II model is unsuitable for the AOI angle of 87^{o} as in a) as it fails to represent the first EA dip whereas Variant I is far closer in agreement at low frequency. Both track the high frequency characteristics well in terms of predicting the frequencies of EA minima and maxima even if the magnitudes are often over estimated.

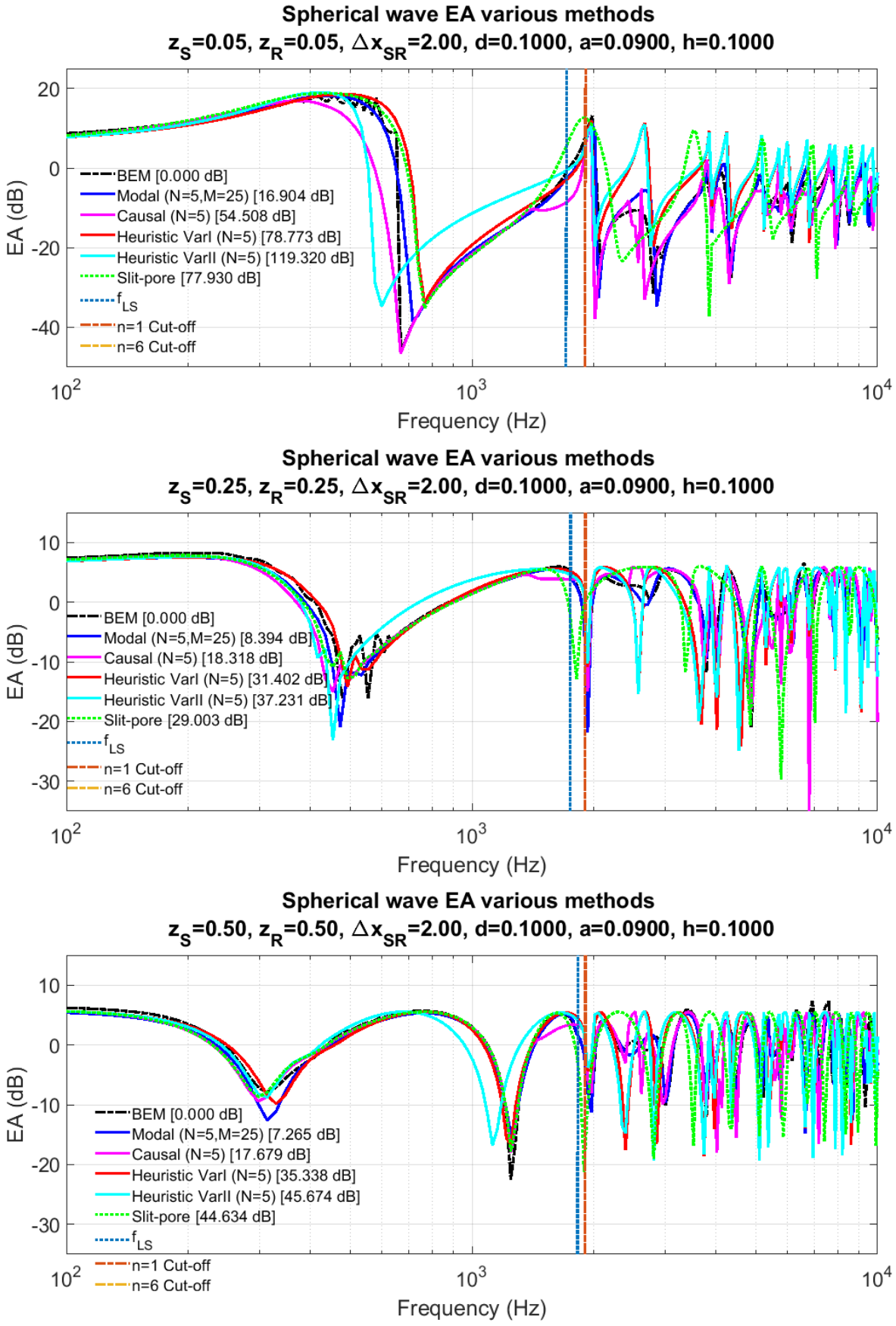

Figure 8.7 EA predictions for d=0.01, a=0.09, h=0.10 with AOI of a) 87°, b) 76° and c) 63°.

8.6 Comparison with measurements

The various simplified impedance models are compared with measurement and the existing slit-pore model in order to gain further insight into their accuracy and where they may offer advantages over the slit-pore model. Once again the measurements used are those of Bashir [31] using aluminium strips to form a rectangular grooved ground surface.

Figures 8.8 and 8.9 show the results for an increasing range of values of d and a which corresponds to a decreasing f_{LS} showing more scattering behaviour as the figures progress. In appraising these results we must be especially careful to consider both the quantitative aspect of the SE values as well as the qualitative measure of how well the curves fit the characteristic shape of the response. This is because the models are now approximations and so the fits will not be so close as with the more complex theoretical models and so a greater degree of qualitative judgement will be required to assess the results. As would be expected the slit-pore mode is effective in figures 8.8a) and b) where the values of d and a are at their smallest and scattering behaviour does not occur until high frequencies. For the remaining results the slit-pore does not reliably predict the chaotic characteristics of the response despite some favourable SE figures when compared with the other models. Due to the causal model taking some account of modal interaction, it consistently agrees better with measurement with respect to magnitude than the Heuristic methods because it may better model scattering losses. The modal decoupling of the Heuristic models cause them to consistently overestimate the magnitude, even though they may generally predict the characteristics of the response. It may be argued that the causal model offers the best overall agreement with the data save for the case of figure 8.9c) where the agreement is poor in the region of the first and second EA minimum. Variant I is the superior of the two heuristic models overall because Variant II is unreliable at predicting the frequency of the first EA minimum whereas Variant I agrees much better with measurement in this respect.

Notice that for the final case of figure 8.9c) both heuristic models flat line near the end of the spectrum which is because the truncation of N=5 is not sufficient for this large geometry.

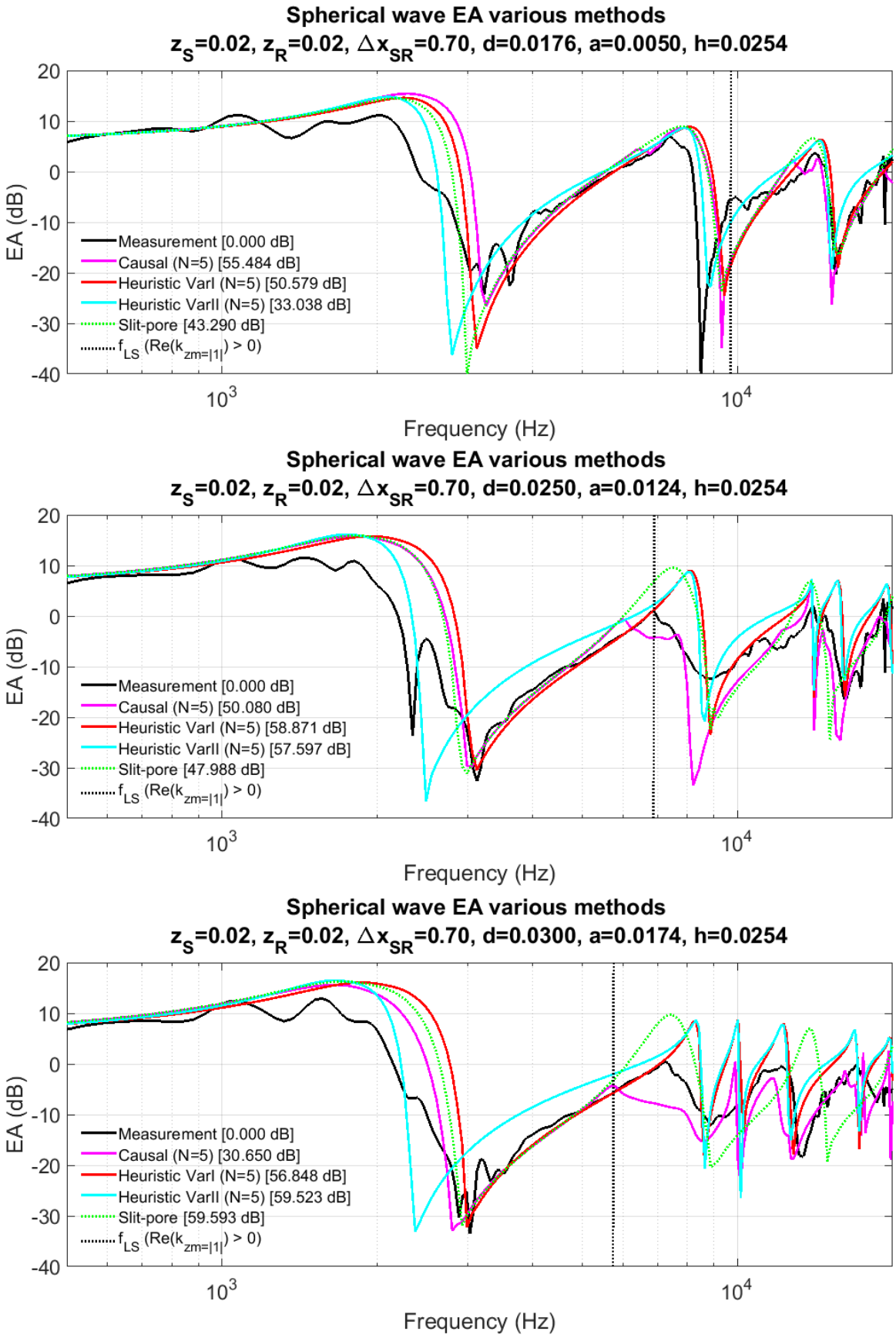

Figure 8.8a-c Comparison of the simplified models with measurement and slit-pore for h=0.025m and a) d=0.018m, a=0.005m, b) d=0.025m, a=0.012m, c) d=0.030m, a=0.017m. (Measurements courtesy of Bashir [31])

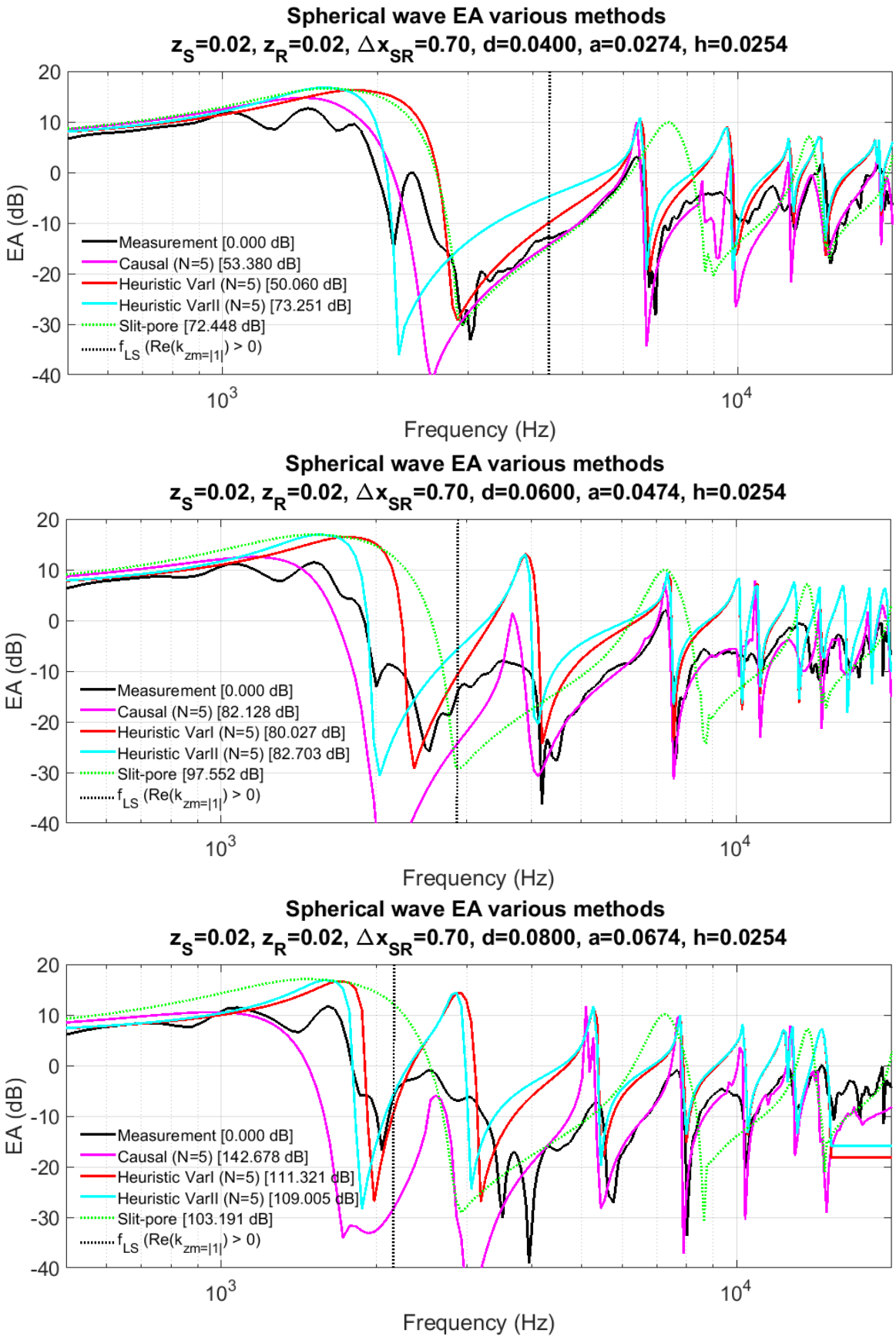

Figure 8.9a-c Comparison of the simplified models with measurement and slit-pore for h=0.025m and a) d=0.040m, a=0.027m, b) d=0.060m, a=0.047m, c) d=0.080m, a=0.067m.(Measurements courtesy of Bashir [31])

8.7 Summary

The 2d extended modal-model has been used as a starting point from which to deduce analytic formulae which model the effective impedance of a rectangular grooved ground surface of given dimensions and for a given AOI. Initially a semi-rigorous approach was applied with accompanying simplifying assumptions to create the causal model based upon the physical interaction of modes within a groove. From this a heuristic approach was then applied resulting in a weighted series in which each term represents the impedance of each mode within a groove with the slit-pore model itself as the zeroth term. Two means of implementing the weighting functions for each term were presented.

Each of the three methods, the causal and both variants of the heuristic series model, were tested against a BEM and 2d-extended modal-model prediction and also with the slit-pore model and a Standard Error (SE) calculated for each plot with reference to the BEM prediction. The cumulative SE for each method across all figures from 8.5 to 8.9 inclusive are presented in the table below in order of decreasing performance,

Rank	Model	ΣSE (dB)
1	Modal-model	117
2	Causal	250
3	Slit-pore	275
4	Heuristic Variant I	311
5	Heuristic Variant II	430

Table 8.2 Cumulative SE results.

From the low SE and the qualitative agreement which can be seen in the plots with BEM the modal-model is the most effective of the quintet which is no surprise as it is a complex numerical model, hence our wish to explore simple analytic simplifications. From the SE results the causal model is next best followed closely by the slit-pore model. At this point the qualitative agreement in EA characteristic response must be considered in terms of how well the prediction tracks the shape and frequency location of each local maximum and minimum and the slope of the curve around them. In this respect the slit-pore model fails to predict the correct characteristic just beyond f_{LS} in every case except in figure 8.5a) where

the effective porosity is very low and scattering effects are thus negligible.

Qualitatively the heuristic Variant I model with the inclusion of the more thorough weighting functions than Variant II performs reasonably well in terms of predicting the location and characteristic shape of each major EA event even though the magnitude is often over estimated which contributes somewhat to the relatively poor SE figures. The Variant I model therefore appears to be an acceptable engineering model for real-world point-to-point acoustic problems involving rectangularly grooved ground surfaces whose dimensions would cause significant scattering in the audio range, striking a sensible balance between complexity and accuracy.

In comparison with measurement the slit-pore model agrees well with the data when the grooved structure is small in comparison with incident wavelength and scattering does not dominate the response. For instances where scattering is significant, the casual simplified model appears most appropriate but it is complex and the heuristic Variant I model may be best suited for acoustic engineering applications.

An important consideration for practical application is the computation time which is shown in table 8.3 for each method presented with 200 frequency points and all run on the same notebook computer. As would be expected the direct impedance models compute in the shortest time but they also exhibit the lowest accuracy for the grooved gratings, but are well suited to use in practical acoustic engineering due to their ease of implementation. The computation time for the modal model is essentially independent of the chosen geometry and the 10 s solve time is for an unoptimised MATLAB implementation. Far faster solve times would easily be achieved with implementation in a more efficient manner. The computation time of the BEM depends upon the geometry of the problem because this impacts the size of the resulting mesh. The fastest and slowest examples are shown. Notice that the simplest case of the result from figure 6.13a solves in a mere 8 s whereas the much larger mesh involved with figure 6.14a takes around 2 hours. The modal model therefore has clear advantages in terms of time saving over BEM with little loss in accuracy.

Method (200 frequency points)	Computation time
Direct impedance (Slit-pore, Heuristic and Causal)	< 1 s
Modal model (N=5, M=25)	~ 10 s
BEM simplest (figure 6.13a)	~ 8 s
BEM most complex (figure 6.14a)	~ 2 hours

Table 8.3 Relative computation times.

For future work the heuristic model may be improved by the addition of terms to generate a real part to the impedance to more rigorously account for scattering losses. Existing work [59-61] suggests that for layered ground the real and imaginary parts are related and so perhaps this could be used as the basis to calculate a real part based upon the imaginary. Furthermore the simplified models may be extended to 3d to predict the behaviour of rectangular cavity latticed structures for a given azimuthal angle.

Plotting the results in 1/3 octave bands may also produce better agreement between the heuristic approximations and the modal and BEM models as some of the fine detail would be smoothed. But this would be of benefit to practical application, whereas we are concerned with more detailed comparisons.

CHAPTER 9 – Conclusions and future work

Specific solutions have been proposed to the questions posed at the very beginning of this thesis and so this research can be considered as successful even though it opens up many more avenues for investigation. As with any scientific pursuit, in seeking the answer to one question many more spring up along the way. This has been no different and opportunities for improvement or further work will be considered in these concluding remarks. It has been shown that for a specific case, a periodic rectangular grooved structure can be characterised by an effective surface impedance when predicting point-to-point acoustic propagation and on this basis a simple analytic model has been proposed.

The measurements referenced throughout this work have been a combination of those conducted specifically for this research and those made by others. In general the measurements have provided a good reference with which to compare our models and in general the agreement between data and theory has been good and having data from separate sources adds confidence to the conclusions. Improvements could be made to our general measurement procedure specifically at low frequencies where we have tended to see unexpected attenuation of the surface wave. This could be due to the materials used to construct the structures amongst other factors, but investigations into these matters is somewhat outside of the scope of this research as significant knowledge already exists.

The Boundary Element Method (BEM) has once again proven to be reliable means of predicting the acoustic field in the presence of shaped ground structures. However problems have been experienced when the source and receiver are placed very close to the ground, the exact cause of which has not been identified and for most practical applications this limitation will not be encountered. All of the BEM excess-attenuation spectra presented have been in 2d, but a 3d program was realised which due to computational and human resource limitations could not be applied to the point-to-point acoustic propagation problem even though preliminary results showed it would be capable. In order to reduce the computation resource demands, future work with the BEM could be focussed upon understanding then implementing the complex 'fast multipole' method.

The modal-model originally developed for rectangular grooved diffraction grating problems in the electromagnetic domain was adapted for acoustics some time ago in order to study surface wave phenomena. It is somewhat surprising that the method was not then widely applied to acoustic propagation and field problems, but this research has focused upon this and a successful method has been presented for using the modal-model solutions to predict acoustic fields for point-to-point acoustic propagation. This has been achieved by using the plane wave solution from the modal-model for a given geometry to attribute an equivalent impedance to the grooved ground surface which in turn is applied to well known reflection coefficients to yield approximations to point-to-point acoustic problems for spherical or cylindrical wave sources. While the modal-model is existing knowledge, the additional methods of applying the results to point-to-point propagation is believed to be original work. The calculated effective impedance is valid only for the geometry for which the model was solved and so any changes in angle of incidence, source-receiver placement or grating size would require the model to be re-run in its entirety. The method was tested extensively against BEM predictions, the slit-pore impedance model and data for a wide range of geometries. Agreement with BEM was shown to be good while agreement with measurement was also good save for the frequency region in the vicinity of the surface wave. Both BEM and the extended modal-models tended over predicted the magnitude of the surface wave, but this discrepancy is likely due to measurement errors which are not reproducing surface waves of the expected magnitude. Agreement of the slit-pore model with predictions and data is good so long as the frequency bandwidth of interest does not include scattering effects because the slit-pore model assumes homogeneity which breaks down with the onset of scattering. While the modal-model is still a numerical method its computation time is not dependent upon the dimensions of the grooved grating unlike BEM, so its solve time for given truncations is invariable and in all but the simplest cases faster than BEM. However a major drawback of the modal-model is that it assumes a rectangular grooved structure and so it does not have the flexibility offered by BEM to cater for arbitrary shapes. It would be interesting in the future to investigate how effective the modal-model would be for different shapes and how tolerant the model would be to deviations from strictly rectangular grooves.

The original modal-model was posed in two spatial dimensions which limited its application to groove structures. In order to explore doubly periodic lattice like structures and to cater for horizontal azimuthal angles as well as the vertical angle of incidence, the

modal-model was expanded to 3d. This was undertaken independently by the author but had already been achieved prior to this. Like the 2d case, the 3d model was extended to calculate an effective impedance for the surface which was then applied to a reflection coefficient formula to predict point-to-point acoustic propagation for spherical waves. The success of this is undetermined because for technical reasons explained in detail previously, we were limited to a small number of measurements with which to compare the predictions. The agreement was dubious but nonetheless encouraging as the characteristic response curves shared significant similarities. Another reference method, such as 3dBEM, would be advantageous in order to investigate where the discrepancies lie. Furthermore the location of EA peaks and troughs are highly sensitive to geometry and so it should be investigated if some of the discrepancy is caused by a mismatch in geometry between the data and predictions. This is very much work for the future as the author is confident that the method does have merit for 3d applications.

For the case of 2d rectangular grooves the findings from studying the model-modal and its application to acoustic propagation were applied to constructing a direct analytic formula to approximate the effective impedance of the grooved surface, given only its geometry. Fundamental to this was to decouple the fields within the grooves from that of free-space because it is this complex interaction which endows the modal-model with the power to solve the complex interdependent fields but at the cost of an analytic solution. In taking this assumption it was possible to express the impedance of the surface as that at the opening of a single cavity multiplied by a porosity factor. However the impedance will vary across the aperture whenever one considers any more than just a single mode in isolation and so the resultant impedance is averaged as a weighted sum of the impedance for each mode within the groove. The predictions from this method show reasonable agreement with BEM and data in terms of characteristic but the magnitude tends to be generally overestimated due to the decoupling. It represents a usable model for practical acoustic engineering applications as the model is simple enough to implement even in a spreadsheet program, which was an original aim of this research.

REFERENCES

[1] J.W. Strutt (Lord Rayleigh), “On the dynamical theory of gratings”, Proc. R. Soc, Lond. A 79 (1907) 399-416.

[2] R.A. Hurd, “The propagation of an electromagnetic wave along an infinite corrugated surface”, Can. J. Phys., (1954), Vol. 32, 727-734.

[3] L.A. Vajnshtejn, “Electromagnetic surface waves on a comblike structure”, Zh. Tekh. Fiz, (1956), Vol 26, 385-397.

[4a] V. Twersky, “On the scattering of waves by an infinite grating”, IEEE Trans. Antennas Propag., (1956), AP-4, 330-345.

[4b] V. Twersky, ‘‘Scattering and reflection by elliptically striated surfaces’’, J. Acoust. Soc. Am. 40, 883–895 (1966).

[4c] V. Twersky, ‘‘Multiple scattering of sound by correlated monolayers’’, J. Acoust. Soc. Am. 73, 68–84 (1983).

[5] K.M. Ivanov-Shits, F.V. Rozhin, “Investigation of surface waves in air”, Sov. Phys. Acoust., (1960), Vol. 5, 510-512.

[6] A. Hessel, J. Schmoys, D.Y. Tseng, “Bragg-angle blazing of diffraction gratings”, Journal of the optical society of America, (1975) Vol 65, No.4, 380-384.

[7a] J.A. DeSanto, “Scattering from a perfectly reflecting arbitrary periodic surface: An exact theory”, Radio Science, (1981) Vol 16, No. 6, 1315-1326.

[7b] J.A. DeSanto, “Scattering from a sinusoid: Derivation of linear equations for the field amplitudes”, J. Acoust. Soc. Am., (1975) Vol 57, 1195-1197.

[8] L. Kelders, J.F. Allard, W. Lauriks, “Ultrasonic surface waves above rectangular-groove gratings”, Acoustic society of America, (1998) 103 (5) Pt.1, 2730-2733.

[9] W. Zhu, M.R. Stinson, G.A. Daigle, “Scattering from impedance gratings and surface wave formation”, Acoustic Society of America, (2002) 111 (5), Pt. 1, 1996-2012.

[10] C.M. Linton, I. Thompson, “Resonant effects in scattering by periodic arrays”, Elsevier Wave Motion 44 (2007), 165-175.

[11] G. Kirchoff, “Ueber den Einflufs der Warmeleitung in einem Gase auf die Schallbewegung”, Ann. Phys. Chem., (1868), Vol 134, 177-193.

[12] J.W. Strutt (Lord Rayleigh), “The Theory of Sound”, Dover, New York (1945), Vol. II, 89-96.

[13] C. Zwicker, C.W. Kosten, “Sound absorbing materials”, Elsevier Amsterdam, (1949).

[14] M.A. Biot, “Theory of propagation of elastic waves in a fluid-saturated porous solid”, Parts I and II., J. Acoustic. Soc. Am., (1956), Vol. 28, 168-191.

[15] K. Attenborough, “Acoustical characteristics of porous materials”, Phys. Rep., (1982), Vol. 82, 179-227.

[16] M.R. Stinson, “The propagation of plane sound waves in narrow and wide circular tubes, and generalization to uniform tubes of arbitrary cross-sectional shape”, J. Acoust. Soc. Am., (1991), Vol. 89, 550-558.

[17] Y. Champoux, M.R. Stinson, “On acoustical models for the sound propagation in rigid frame porous materials and the influence of shape factors”, J. Acoust. Soc. Am., (1992), Vol. 92, 1120-1131.

[18] R.F. Millar, “On the Rayleigh assumption in scattering by a periodic surface”, Proc. Cambridge Philos. Soc., (1969) Vol. 65, 773-791.

[19] N.R. Hill, V. Celli, “Limits of convergence of the Rayleigh method for surface scattering”, Phys. Rev. B, (1978) Vol. 17, 2478-2481.

[20] P.M. van den Berg, J.T. Fokkema, “The Rayleigh hypothesis in the theory of diffraction by a perturbation in a plane surface”, Radio Science, (1980) Vol. 14, No.4, 723-732.

[21a] J.L. Uretsky, “Scattering of plane waves from periodic surfaces”, Ann. Phys. (N.Y.), (1965) Vol. 33, 400-427.

[21b] J.L. Uretsky, “Reflection of a plane sound wave from a sinusoidal surface”, J. Acoust. Soc. Am., (1963) Vol. 35, 1293-1294.

[22] R.L. Holford, “Scattering of sound waves at a periodic pressure release surface: An exact solution”, Technical report (1971), Bell Teleph Lab., Whippany, N.J. USA.

[23] P.C. Waterman, “Scattering by periodic surfaces”, J. Acoust. Soc. Am., (1975) Vol. 57, 791-802.

[24] Chr. Huygens, Traitė de la Lumiere (completed in 1678, published in Leyden in 1690).

[25] A. Fresnel, Ann Chim et Phys, (2), 1 (1816), Oeuvres, Vol. 1, 89, 129.

[26] F. Erdogan, “Approximation solution of systems of singular integral equations”, SIAM (Soc. Ind. Appl. Math.), (1969) J. Appl. Math. 17, 1041-1059.

[27] D. Hilbert, Nordheim, W. Lothar, J. von Neumann, "Über die Grundlagen der Quantenmechanik", Mathematische Annalen 98 (1927), 1–30,

[28] K. Attenborough, K. M. Li, K. Horoshenkov, “Predicting the acoustical properties of outdoor ground surfaces”, Predicting Outdoor Sound (2007), 63-65.

[29] D.T. Blackstock, “Fundamentals of physical acoustics”, Wiley Interscience, (2000), 240 & 428-432.

[30] D.J. Griffiths, “Introduction to Electrodynamics”, St. Martin Books (2014), 393-396.

[31] I. Bashir, “Acoustical Exploitation of Rough, Mixed Impedance and Porous Surfaces Outdoors”, Open University PhD Thesis (2013). a) Fig. 6.17, chapter 6, 30-31.

[32] World Health Organization (WHO), Burden of Disease from Environmental Noise: Quantification of Healthy Life Years Lost in Europe, Copenhagen (2011).

[33] J. Forssen, Courtesy of the Open University and HOSANNA, “Toolbox from the EC FP7 HOSANNA project for the reduction of road and rail traffic noise in the outdoor environment”, (April 2013).

[34] P. Boulanger, K. Attenborough, S. Taherzadeh, T. Walters-Fuller, K. Ming Li, “Ground effect over hard rough surfaces”, J. Acoust. Soc. Am., (1998), Vol. 104 (3), 1474-1482.

[35] P. Boulanger, K. Attenborough, Q. Qin, C.M. Linton, “Reflection of sound from random distributions of semi-cylinders on a hard plane: models and data”, J. Phys. D: Appl. Phys., (2005), Vol. 38, 3480-3490.

[36] H. Bougdah, I. Ekici, J. Kang, “A laboratory investigation of noise reduction by riblike structures on the ground”, J. Acoust. Soc. Am., (2006), Vol. 120 (6), 3714-3722.

[37] C.F. Chien, W.W. Soroka, “Sound propagation along an impedance plane”, Journal of sound and vibration 43(1), (1975), 9-20.

[38] S.W. Rienstra, A. Hirschberg, “An Introduction to Acoustics”, Extended and revised edition of IWDE 92-06, Eindhoven University of Technology, 8th August 2016, Page 36.

[39] J.F. Allard, L. Kelders, W. Lauriks, “Ultrasonic surface waves above a doubly periodic grating”, J. Acoust. Soc. Am., (1999), Vol. 105 (4), 2528-2531.

[40] W. Zhu, M.R. Stinson, G.A. Daigle, “Scattering from impedance gratings and surface wave formation”, J. Acoust. Soc. Am., (2002), Vol. 111 (5).

[41] I. Tolstoy, “Smoothed boundary conditions, coherent low-frequency scatter, and

boundary modes”, J. Acoust. Soc. Am., (1984), Vol 75 (1).

[42] www.wolframalpha.com

[43] Whye-Teong Ang, "A beginner's Course in Boundary Element Methods", Universal Publishers Boca Raton, Florida, 2007, ISBN 158112974-2.

[44] F. Goos and H. Hänchen, “Ein neuer und fundamentaler Versuch zur Totalreflexion,” Ann. Phys. (436) 7–8, 333–346 (1947).

[45] D.T. Blackstock, “Fundamentals of physical acoustics”, Wiley Interscience, (2000), 457.

[46] S. Taherzadeh, I. Bashir, T. Hill, K. Attenborough, M. Hornikx, “Reduction of surface transport noise by ground roughness”, Applied Acoustics 83 (2014), 1-15.

[47] I. Bashir, S. Taherzadeh, K. Attenborough, “Surface waves over periodically spaced strips”, J. Acoust. Soc. Am. 134 (2013), 4691 – 4697.

[48] I. Bashir, S. Taherzadeh, K. Attenborough, “Diffraction-assisted rough ground effect: models and data”, J. Acoust. Soc. Am. 133 (2013), 1281 – 1292.

[49] D.T. Blackstock, “Fundamentals of physical acoustics”, Wiley Interscience, (2000), 151.

[50] K. Attenborough, K. M. Li, K. Horoshenkov, “Predicting the acoustical properties of outdoor ground surfaces”, Predicting Outdoor Sound (2007), Section 8.2.3.

[51] D.C. Hothersall and J.N.B. Harriott, "Approximate models for sound propagation above multi-impedance plane boundaries", J. Acoust. Soc. Am. 97, 918-926 (1995).

[52] S.I. Thomasson, "A Powerful Asymptotic Solution for Sound Propagation above an Impedance Boundary", ACUSTICA, Vol. 45 (1980), 123-125.

[53] T.L. Parrott, G.L. McAninch, I.A. Carlberg, "Evaluation of a Scale-Model Experiment To Investigate Long-Range Acoustic Propagation", NASA Technical Paper 2748 (1987).

[54] S. Chandler-Wilde and S. Langdon, "Boundary element methods for acoustics", Department of Mathematics, University of Reading, July 18, 2007.

[55] Y. Liu, "Fast Multipole Boundary Element Method", Cambridge University Press (2014).

[56] D. Berry, S. Taherzadeh and K. Attenborough, “Acoustic Surface Wave Generation over Rigid Cylinder Arrays on a Rigid Plane”, submitted to JASA (2019).

[57] H.A. Kramers, "La diffusion de la lumière par les atomes", Atti del Congresso Internazionale dei Fisici, Como 2 (1927).

[58] R.D.L. Krönig, "On the theory of dispersion of X-rays", Journal of the Optical Society of America 12, 547-557 (1926).

[59] HOSANNA, “APPENDIX 3 Causality and Ground Impedance Models”, WP4, (April 2013).

[60] R.W. Wood, "On a remarkable case of uneven distribution of light in a diffraction grating spectrum", Philos. Mag. 4 (1902) 396–408.

[61] C.M. Linton and P.A. Martin, "Multiple scattering by random configurations of circular cylinders: second-order corrections for the effective wave number", J. Acoust. Soc. Am. 117 3413–23 (2005).

[62] M.R. Schroeder, "Binaural dissimilarity and optimum ceilings for concert halls: More lateral diffusion", J. Acoust. Soc. Am. 65 958-963 (1979).

[63] T.J. Cox, Y.W. Lam, "Prediction and evaluation of the scattering from quadratic residue diffusers", J. Acoust. Soc. Am. 95 297-305 (1994) .

[64] T. Wu, T.J. Cox, Y.W. Lam, "From a profiled diffuser to an optimized absorber", J. Acoust. Soc. Am. 108 643-650 (2000) .

[65] T. J. Cox, P. D'Antonio, "Acoustic Absorbers and Diffusers: Theory, Design and Application." 2nd ed. Taylor & Francis; 2009.

[66] S. Taherzadeh, K.M. Li, K. Attenborough, "A hybrid BIE/FFP scheme for predicting barrier efficiency outdoors", J. Acoust. Soc. Am. 110 918-924 (2001).

[67] J. A. Hargreaves, Y. W. Lam, S. Langdon, "A transformation approach for efficient evaluation of oscillatory surface integrals arising in three-dimensional boundary element methods", Int. J. Numer. Methods Eng. 108(2):93–115 (2016).

[68] T. F. W. Embleton, "Tutorial on sound propagation outdoors", J. Acoust. Soc. Am. 100(1) 31-48 (1996).